The Dissertation Committee for Feng Yuan Certifies that this is the approved version of the following Dissertation:

Intrinsically Disordered Proteins as Mechanistic Drivers of Membrane Remodeling and Endocytosis

Committee:

Jeanne Stachowiak, Supervisor

Eric Senning

Sapun Parekh

Evan Wang

Intrinsically Disordered Proteins as Mechanistic Drivers of Membrane Remodeling and Endocytosis

by

Feng Yuan

Dissertation

Presented to the Faculty of the Graduate School of

The University of Texas at Austin

in Partial Fulfillment

of the Requirements

for the Degree of

Doctor of Philosophy

The University of Texas at Austin

December 2023

Acknowledgements

Time flies! Five years of graduate studies in the University of Texas at Austin have passed in the blink of an eye. As I close this dissertation, my wonderful PhD journey also comes to an end. Looking back, I have gained so many invaluable experiences, and there are so many people and events to express my gratitude to.

First and foremost, I would like to thank my PhD advisor, Dr. Jeanne Stachowiak, for providing me the exciting opportunity to work with her. Over the past five years, she is always there to give me patient guidance, insightful feedback, and motivating encouragement in research whenever I need, which enabled me to achieve significant research outcomes. Moreover, she truly cares about our career development and provides us tremendous support to thrive in academia, such as attending different kinds of conferences each year and networking with people in relevant fields. It has been a privilege to work alongside such a supportive mentor. Her unwavering passion for research, efficient working style and supportive mentorship style have been inspiring me and shaping me throughout my PhD. She is a great role model of how to become a successful PI and I hope I can be a PI like her in the future when I have my own lab and students.

I would also like to thank the past and current members of Stachowiak lab for their support and friendship. I am especially grateful to Dr. Kasey Day, Grace Kago, and Dr. Wade Zeno for teaching me all the basic techniques to help me get started with my experiment and patiently giving me suggestions in troubleshooting. I would like to thank Dr. Kristin Graham and Dr. Sadhana Gollapudi for being the same cohort in the lab and encouraging each other during our PhD journey. I would like to thank Grant Ashby for the instructions in data analysis using Matlab. I am also deeply thankful for Dr. Carl Hayden,

Dr. Chi Zhao, Brandon Malady, Caleb Walker, Advika Kamatar, Ketsia Zinga, Dr. Yohan Lee, Dr. Susovan Sarkar and Dr. Haoyang Liu for being a source of support both in and out of lab. Big thanks to my undergrad Arjun Sangani for being an amazing helper in conducting experiment. His hard work and dedication have been instrumental in my academic achievements.

Further, I would like to recognize other incredible mentors and collaborators. I would like to thank Dr. Sapun Parekh, Dr. Evan Wang and Dr. Eric Senning for serving on my dissertation committee and providing continued support and feedback. I would like to especially thank Dr. Padmini Rangamani and her students, Dr. Haleh Alimohamadi and Dr. Christopher Lee, in the University of California San Diego for the wonderful collaboration in modeling, which has led to two impactful publications. I would like to also thank our collaborators, Dr. Eileen Lafer and Liping Wang in the University of Texas at San Antonio for consistently purifying various proteins for my study and giving me guidance on protein purification. Besides, I also appreciate Dr. Jon Huibregtse for providing insightful suggestions on protein ubiquitylation.

In addition, I would like to thank all the wonderful people and things I have encountered during my time at the University of Texas for making my journey through graduate school memorable. I thank Lacy White for being a super responsible graduate coordinator and helping me get through the problems when I just got into the department as an international student. I thank my friends Dr. Zaixi Shang and Dr. Wenbai Huang for supporting each other both in graduate school and in life, for exploring various foods together and for planning the unforgettable trips all around the US. I thank all the people who regularly played badminton with me during the past four years for keeping me happy and fit in my free time. I would also thank the University of Texas at Austin, the department

of Biomedical Engineering for giving me the opportunity to study abroad and bringing me to the wonderful city of Austin. I could not have such an enjoyable and colorful life if it were not in Austin.

Lastly, I would like to sincerely thank my family, including mom, dad, and my sister. It is their twelve-year consistent understanding, encouragement and support that helps me get through college and graduate school. They are always the driving force behind my ability to overcome challenges and keep moving forward.

Abstract

Intrinsically Disordered Proteins as Mechanistic Drivers of Membrane Remodeling and Endocytosis

Feng Yuan, PhD

The University of Texas at Austin, 2023

Supervisor: Jeanne C. Stachowiak

Membrane bending is a ubiquitous cellular process that is required for membrane traffic, cell motility, organelle biogenesis, and cell division. Proteins that bind to membranes using specific structural features, such as wedge-like amphipathic helices and crescent-shaped scaffolds, are thought to be the primary drivers of membrane bending. However, many membrane-binding proteins have substantial regions of intrinsic disorder which lack a stable three-dimensional structure. Recently, our group and others have reported that intrinsically disordered proteins can also be potent drivers of membrane bending. Specifically, when noninteracting disordered domains are crowded together in cellular structures, steric repulsion among them drives the membrane to buckle outward, taking on a curved shape. Interestingly, rather than repelling one another, many of these disordered domains have recently been found to form networks stabilized by weak, multivalent contacts, leading to assembly of protein liquid phases on membrane surfaces. In my thesis, I first characterized the impact of protein liquid-liquid phase separation (LLPS) on membrane curvature. Specifically, I have demonstrated that protein phase

separation on the surfaces of synthetic and cell-derived membrane vesicles creates a substantial compressive stress in the plane of the membrane. This stress drives the membrane to bend inward, creating protein-lined membrane tubules. Discovery of this mechanism, which may be relevant to a broad range of cellular protrusions, illustrates that membrane remodeling can also be driven by the rapidly emerging class of liquid-like protein networks that assemble at membranes. To further understand how repulsive and attractive domains work together to apply bending stresses to the membrane surface, I then investigated series of disordered protein chimeras, which combine protein domains previously shown to drive either convex or concave membrane curvature. Using these chimeras, I demonstrated that disordered protein layers with opposite curvature preferences can either work together to amplify curvature or can oppose one another to create context-dependent control of membrane shape. This work outlines a set of design rules that can be used to understand the impact of disordered proteins on membrane curvature.

Furthermore, I studied how LLPS impacts endocytosis. I examined the influence of ubiquitin on the stability of the liquid endocytic protein network. In vitro, I found that recruitment of small amounts of polyubiquitin dramatically increased the stability of Eps15 condensates, suggesting that ubiquitylation could nucleate endocytic sites. In live cell imaging experiments, a version of Eps15 that lacked the ubiquitin-interacting motif failed to rescue defects in endocytic initiation created by Eps15 knockout. Furthermore, fusion of Eps15 to a deubiquitinase enzyme destabilized nascent endocytic sites within minutes. These results suggest that ubiquitylation drives assembly of the flexible protein network responsible for catalyzing endocytic events. Collectively, my thesis work has illustrated biophysical mechanisms by which intrinsically disordered proteins could regulate membrane bending and endocytosis.

Table of Contents

List of Tables

List of Figures

Chapter 1: Introduction[1]

Disordered proteins are ubiquitous in endocytic network.

The assembly of endocytic vesicles is an essential cellular process that is required for cell signaling, nutrient uptake, and receptor and lipid recycling[1]. Trafficking vesicles assemble when cargo molecules, such as lipids and transmembrane receptors, come together at membrane surfaces with the components of the vesicular coat, which typically consists of proteins that bind peripherally to membrane surfaces[2-4]. The components assemble together to create an endocytic vesicle through a series of overlapping steps, which include (1) initiation of the vesicle assembly site, (2) induction of membrane curvature, (3) sensing of the curvature by additional protein components, leading to the growth of the vesicle, (4) recruitment of the vesicular coat, (5) scission of the vesicle neck, leading to separation from the parent membrane, and (6) disassembly of the vesicular coat in preparation for fusion of the vesicle with its target membrane (Figure 1.1).

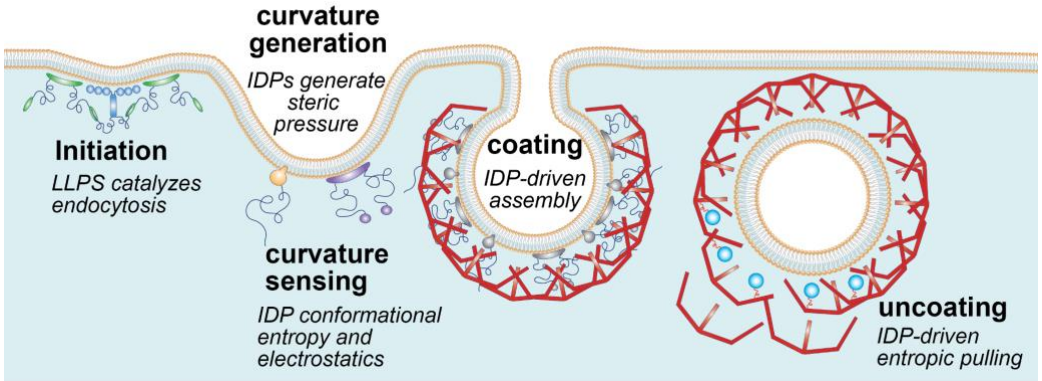

[1] This chapter is published as a book chapter: Zeno WF, Yuan F, Graham KD, Stachowiak JC, Disordered protein networks as mechanistic drivers of membrane remodeling and endocytosis. *Structure and Intrinsic Disorder in Enzymology*, 2023, p. 427-454.

Figure 1. 1 Disordered proteins play important roles in many stages of trafficking vesicle biogenesis including: (i) Initiation of endocytic sites, where liquid-liquid phase separation plays a catalytic role; (ii) generation and sensing of membrane curvature, where disordered proteins use steric and electrostatic mechanisms to modulate membrane shape; (iii) coating of vesicular carriers, where disordered proteins drive coat assembly; and (iv) uncoating, where disordered domains use an entropic-pulling mechanism to drive the disassembly of vesicular coats.

Our understanding of the protein machinery that drives endocytosis has emerged over the past 40 years, in parallel with major advances in high resolution structural biology[5]. Importantly endocytic proteins have been the subject of ground breaking structural studies including identification of membrane-penetrating amphipathic helices[6], visualization of complex icosahedral protein coats[7,8], and resolution of membrane-shaping scaffolds[9,10] and scission machines[11,12]. Driven by these discoveries, the "structure-function paradigm" in which biophysical mechanisms are attributed to specific protein structures, has played a major role in our understanding of endocytic mechanisms. However, over the past two decades, it has become increasingly clear that the machinery responsible for membrane traffic includes many proteins with substantial intrinsically disordered domains, including prominent components of the clathrin-mediated endocytic machinery[13-16]. Overall, a recent review of yeast and mammalian proteins involved in endocytosis concluded that more than 20 % of the amino acids in these proteins are found within intrinsically disordered domains[16].

Many of these disordered regions contain conserved sequence motifs which bind specifically to other structured or disordered elements within the network of endocytic proteins[13,14,17,18]. In this way, disordered domains participate in linking together endocytic proteins, helping them to assemble at endocytic sites with spatial and temporal resolution [18]. However, over the past few years it has become increasingly clear that disordered

domains also play critical physical roles in specific steps of trafficking vesicle biogenesis. Here, we discuss these physical mechanisms in the context of discrete membrane trafficking functions including: (i) initiation and catalysis of trafficking vesicle assembly, (ii) membrane curvature, (iii) curvature sensing, and (iv) vesicle coating and uncoating, Figure 1.1. In the following sections, we bring together recent experimental and computational evidence to help explain how the inherent conformational entropy of disordered peptide sequences, along with their propensity for forming weak, multi-valent networks, leads to new mechanisms for organizing and remodeling membrane surfaces. Collectively, this body of emerging work provides a new biophysical picture of endocytosis as a stochastic process driven by collaborations between structured and disordered proteins, which assemble into dynamic and adaptable networks. More broadly, principles revealed in the study of endocytic vesicles are shedding light on the broader roles of disordered proteins in diverse membrane structures involved in cell motility, division, sensing, and signaling.

Disordered proteins as sensors of membrane curvature

Intrinsically disordered protein regions are ubiquitous in endocytosis and are often coupled with structured domains within the same full-length protein[19]. These bulky disordered regions often accounting for more than 50% of the total amino acid sequence of a single protein. It has been discovered recently that disordered domains are potent sensors of membrane curvature[20,21]. While small, disordered segments (< 30 amino acids) often form amphipathic helices that interact with membrane defects and sense membrane curvature[22,23], larger disordered regions (> 200 amino acids) typically do not undergo structural changes in the presence of membranes. Instead, these large disordered domains are tethered in close proximity to the membrane surface via serially encoded structured

domains that have biochemical affinity for the membrane[14]. Due to their extended peptide chain conformation, disordered domains utilize biophysical interactions to sense membrane curvature. But how does this curvature sensitivity arise? To understand the origins of this biophysical phenomenon, one must examine the structural behavior of disordered domains through the lens of polymer physics. Bulky disordered domains that sense curvature exhibit behavior akin to polymers in good solvent. Structural hallmarks of these proteins include high proline content[24], polar and charged amino acids residues[25,26], low hydrophobicity[27], and high net charge[28]. A variety of theoretical predictions and experimental techniques have been developed and implemented to characterize the polymer-like structure and behavior of disordered proteins, including small angle x-ray scattering (SAXS)[29] and NMR spectroscopy[30]. However, single molecule Förster resonance energy transfer (single molecule FRET or smFRET) has been particularly instrumental in providing insight about structural and dynamic information about disordered proteins.

The Schuler lab has developed and utilized smFRET and correlation spectroscopy techniques to examine disordered proteins that were fluorescently labeled with donor and acceptor fluorophores at each terminus[31]. Their results showed that disordered proteins underwent nanosecond-scale structural reconfigurations. This type of dynamic behavior is akin to conformational fluctuations associated with random polymers. They then used smFRET to further probe the applicability of polymer theory to disordered proteins by evaluating polymer scaling laws[32]. The radii of gyration (R_g) for various disordered sequences were found to scale directly with $N^{3/5}$, where N represents the number rigid segments. In the context of disordered proteins, N is closely related to the number of amino acids. Folded proteins, which typically scale with $N^{1/3}$, exhibited $N^{3/5}$ scaling once they

became denatured after exposure to guanidinium chloride. These scaling relationships were in agreement with scaling laws for random coil polymers[33], thus this work demonstrated that polymer models can accurately reflect the conformation and behavior of disordered proteins. Work by the Kumar lab expanded the structural understanding of disordered proteins by perturbing net charge within the chain. Specifically, they developed polymer brush coatings that were derived from disordered proteins within the neurofilament proteins, and monitored expansion/contraction of the film as a function of ionic strength or pH[26]. These stimuli-responsive, disordered protein-derived polymer brush coatings demonstrated that charged disordered proteins behave like polyampholytes.

Since water-soluble disordered proteins behave like polymers and highly flexible polymers are associated with high degrees of conformational entropy[34], disordered proteins must also contain a high degree of conformational entropy. But how does tethering of disordered proteins to membrane surfaces, as occurs during endocytosis, affect chain entropy? Early work by Dimarzio and McCrackin investigated the flexibility of polymers that were tethered to surfaces[35,36]. Together, they derived analytical relationships that describe the end-to-end distance distribution of freely jointed, tethered polymer chains, as well as the relationship between the number of rigid segments in a polymer and the number of resulting configurations. This theoretical framework illustrated the profound loss of conformational entropy that polymers experience when they become tethered to a solid surface. When Boltzmann's equation is considered, $S = k_B \ln(W)$, where W is the number of configurations, it is clear that a reduction in W leads to a thermodynamically unfavorable decrease in entropy, S. Interestingly, work from Lipowsky several decades after Dimarzio and McCrackin, suggested that curved surfaces can alleviate the thermodynamic penalty associated with tethered polymers. Specifically, Lipowsky developed a theory for polymers

tethered to lipid bilayer surfaces and predicted that the entropy loss associated with polymer tethering is compensated by the curvature gained by the membrane surface[37]. From a physical perspective, this theory predicts that the most highly curved surfaces will permit the highest degrees of configurational freedom for the tethered polymer, Figure 1.2a. Based on this logic, polymers should be able to sense the curvature of the substrates to which they become tethered. Since disordered proteins are structurally and functionally analogous to these types of polymers, is it possible for tethered, disordered proteins to utilize an entropically driven mechanism to sense membrane curvature?

This theory was first tested experimentally by Zeno *et al.* in 2018, where disordered C-terminal domains (CTDs) of the endocytic proteins AP180, epsin1, and amphiphysin1 were isolated and purified with artificial membrane affinity tags[20]. These purified disordered proteins were then incubated with synthetic lipid vesicles that were tethered to a glass coverslip and ranged in diameter from 20-200 nm, Figure 1.2b. Protein-lipid binding was monitored using fluorescence microscopy, Figure 1.2c. Zeno *et al.* found that these disordered proteins were potent sensors of membrane curvature, as they preferentially partitioned to the smallest vesicles. The CTD of AP180 was the strongest curvature sensor observed among the three disordered domains, exhibiting a 10-fold increase in partitioning to 20 nm vesicles relative to 200 nm vesicles, Figure 1.2d. This level of curvature sensitivity was comparable to the ENTH domain from epsin1, which is a well-established sensor of membrane curvature[38]. These findings represented a substantial departure from the structure-function paradigm, as these bulky disordered regions had been previously neglected in curvature sensing studies based on the assumption that only structured proteins could sense membrane curvature. Due to the -31 net charge within AP180CTD, its residues undergo intramolecular electrostatic repulsion. Therefore, ionic strength was tuned to

modulate the rigidity, and thereby R_g, of AP180CTD. These changes in R_g and rigidity were facilitated by changes to the effective Kuhn length (l_k) of the polymer-like protein. By changing l_k, the magnitude of the hypothesized entropic curvature sensing mechanism was perturbed. Relative to physiological conditions, an increase in ionic strength caused a decrease in l_k and an increase in protein flexibility, while a decrease in ionic strength caused an increase in l_k and an increase in protein rigidity. When the ionic strength of the solution was perturbed, the curvature sensitivity of AP180CTD was responsive in a manner consistent with the entropic curvature sensing mechanism, where curvature sensitivity increased as the chain became more flexible and decreased when the chain became more rigid. These experimental findings were corroborated by Monte Carlo simulation, where polymer conformations were generated on surfaces with varying curvature and the corresponding entropies were calculated using Boltzmann's Equation. Using temperature, these entropies were converted to free energies, which could then be converted to experimentally measurable thermodynamic partitioning data via Boltzmann distributions. In the simulation, the contour length of the polymer (i.e., $N*l_k$) was fixed and l_k was varied. Therefore, l_k was treated as a regression parameter. The values of l_k that yielded the closest agreement between simulations and experiments were on the order of 0.4-0.7 nm, which are consistent with the length scale of amino acids – the monomer units in these polymer-like disordered proteins. In addition to curvature sensitivity, the R_g of the simulated polymers, which scales with $l_k N^{3/5}$ was in quantitative agreement with protein radii measured via fluorescence correlation spectroscopy. This combination of experimental and theoretical techniques demonstrate that disordered proteins are capable of utilizing an entropic mechanism to sense membrane curvature.

The disordered domain of AP180, as well as many other membrane trafficking proteins, contains a substantial degree of net negative charge. When examining curvature sensitivity, net charge of the disordered domain is an important consideration, as biological membranes also tend to be negatively charged. Therefore, an appreciable amount of electrostatic repulsion can be generated when negatively charged disordered domains are tethered to anionic membranes. Relative to flatter membranes, highly curved membranes increase the average separation between anionic amino acids and lipids, leading to a decrease in electrostatic repulsion. This decreased repulsion would lead to a preference for highly curved membranes, Figure 1.2a. Zeno *et al.* investigated the existence of this electrostatic mechanism by utilizing truncation mutants of AP180CTD[21]. In particular, curvature sensing was compared between AP180CTD and the N-terminal third of this domain (AP180CTD-1/3), which contains the highest density of negatively charged amino acids. When the ionic strength was varied, AP180CTD-1/3, exhibited changes in its curvature sensitivity that were opposite of those observed for AP180CTD and consistent with an electrostatic mechanism. Specifically, the curvature sensitivity of AP180CTD-1/3 increased with decreasing ionic strength, indicating that, as electrostatic screening was reduced, electrostatic repulsion between the protein and membrane became greater.

This work suggests that the entropic and electrostatic mechanisms are two distinct mechanisms by which disordered proteins can sense membrane curvature, ultimately making them robust and potent curvature sensors. Qualitatively, the entropic mechanism is favored by larger disordered proteins with low net charge, while the electrostatic mechanism is favored by smaller disordered proteins with high net negative charge.

During endocytosis, disordered domains are recruited to membrane surface by serially encoded structured domains within the same proteins[14]. Several of these structured

domains have been isolated and shown to sense membrane curvature. How might the presence of a disordered domain influence the curvature sensitivity of the full-length proteins? Interestingly, full-length epsin1 exhibited a substantial increase in curvature sensitivity when compared to either of its constitutive parts, the ENTH domain and the isolated disordered domain[20], Figure 1.2e. A similar result was observed for full-length amphiphysin1 when it was compared to its isolated N-BAR domain and its isolated disordered domain, Figure 1.2f. In both cases, the full-length protein was more sensitive to curvature than its component domains combined, suggesting synergy between structured and disordered domains during curvature sensing. Other recent work has demonstrated that this synergy is particularly relevant in epsin1, where the disordered domains is necessary for facilitating clathrin-mediated endocytosis in environments where the plasma membrane is under high tension[39]. This synergy is also essential in caveolar endocytosis, where it has been suggested that the disordered domain of Cavin1 facilitates its partitioning to highly curved caveolar pits[40]. Another fascinating example of this synergy can be found in proteins responsible for cortical wave formation in cells, where it has been recently discovered that the curvature sensitivity of the F-BAR-containing protein FBP17 is largely derived from its disordered domain[41]. Taken together, this work illustrates the important contributions of intrinsically disordered domains to curvature sensing during endocytosis and more broadly in membrane remodeling processes throughout the cell.

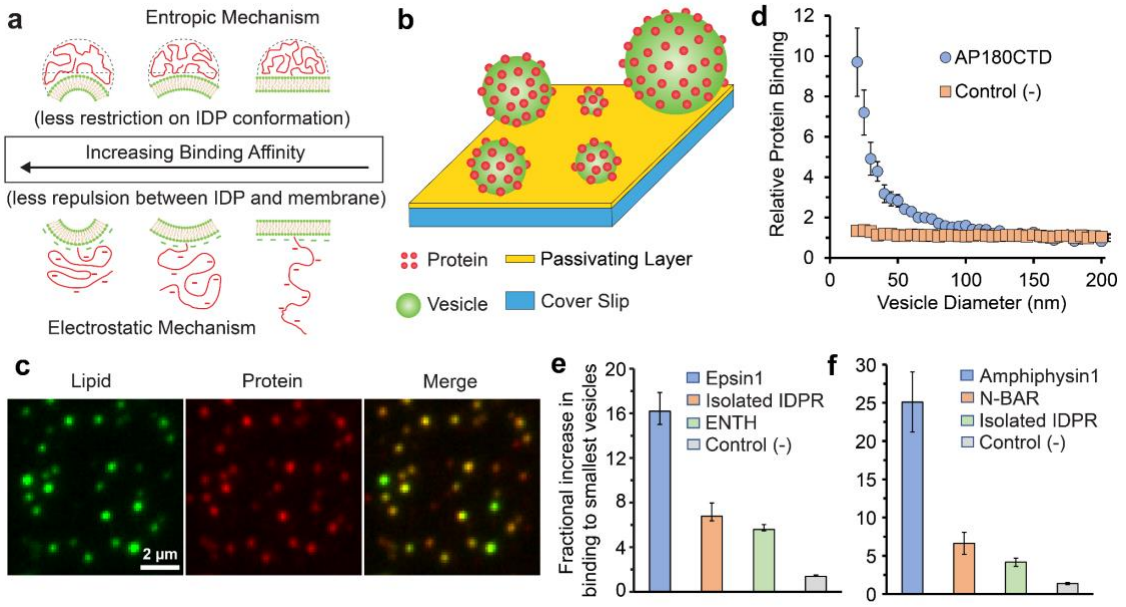

Figure 1. 2 (a) Schematic showing entropic and electrostatic mechanisms, (b) schematic of tethered vesicle assay. (c) representative fluorescence micrograph of proteins bound to tethered vesicles, (d) curvature sensitivity of AP180CTD compared to a non-sensing negative control protein, (e) curvature sensitivity of epsin1 and its constitutive domains, (f) curvature sensitivity of amphiphysin1 and its constitutive domains[20]. IDPR stands for intrinsically disordered protein region.

Disordered proteins as drivers of membrane curvature

Once the site of a nascent trafficking vesicle is initiated, proteins must assemble together at the membrane surface to drive formation of a highly curved bud[18,42]. How protein networks produce highly curved membrane geometries is a fundamental question that has interested cell biologists and biophysicists for the past several decades[10,43-45]. One of the earliest insights into this question was proposed by Sheetz and Singer in 1974, and is known as the bilayer couple model[46]. This model suggests that asymmetries in geometry or surface pressure can drive membrane curvature. In particular, Sheetz and Singer observed that binding of amphipathic drug molecules to one leaflet of a membrane bilayer could drive changes in membrane curvature, presumably by expanding the surface area of

the leaflet in contract with the drug. In this way, mechanical coupling of the two bilayers, owing to the hydrophobicity of the juxtaposed tails, requires that if one leaflet is expanded, the other must contract, leading to coupled bending of the bilayer. In principle, the fundamental asymmetry required for bending in the bilayer couple model can be created by any mechanism that changes the geometry or surface pressure of one membrane leaflet, relative to the other leaflet.

Multiple mechanisms for creating this asymmetry have been identified and characterized in recent years, Figure 1.3a. The two most broadly recognized are bending by (i) insertion of amphipathic motifs, and (ii) binding of the membrane surface by inherently curved protein scaffolds. Amphipathic insertions often consist of alpha helices characterized by a hydrophobic face and an opposing hydrophilic face. Such helices often float on membrane surfaces, analogously to a log floating on a river, with the hydrophobic face oriented toward the lipid tails and the hydrophilic face oriented toward the surrounding aqueous environment. Amphipathic helices are found in membrane-binding proteins throughout the cell[47] and have been hypothesized to drive membrane bending by several membrane trafficking proteins[6,48,49], though notably the protein concentrations required for such a mechanism may not be physiological[50]. In contrast, protein scaffolds with inherently curved membrane interacting surfaces can impose their curvature on the membrane when they assemble on the surface of one of its leaflets. The BAR (Bin/Amphiphysin/Rvs) superfamily form banana-shaped dimers that are thought to drive the curvature of tubule-like morphologies in endocytosis, cytokinesis, and filopodia formation[9,51,52].

Collectively, a significant body of work has illustrated that specific structural motifs are capable of generating membrane curvature. However, more recent work has shown that curvature can also be driven by less specific effects, such as steric pressure at membrane

surfaces[53-55], which can be generated by almost any membrane-bound protein, including intrinsically disordered domains. Specifically, as protein become crowded on membrane surfaces, collisions between them generate steric pressure that stretches the membrane surface, Figure 1.3a. If this steric pressure is not balanced on the opposite side of the membrane, then the bilayer will bend toward the more crowded surface such that the area available per protein on this surface is increased. The ability to generate steric pressure has been shown to be independent of both protein structure and the mechanism that proteins use to attach to membrane surfaces. In particular, membrane bending by the ENTH domain of the endocytic protein, Epsin1, which had previously been thought to bend membrane via amphipathic insertion[6], was shown to correlate with coverage of the membrane surface by proteins[56] and steric pressure[57], regardless of whether an amphipathic helix or an engineered tag was used to recruit the protein to the membrane surface. These ideas have been extended to help explain the role of steric pressure in budding of lipid droplets from the membranes of the endoplasmic reticulum[58].

Repulsive interactions drive convex curvature

Given the independence of steric pressure on protein structure, we would expect that any protein, even intrinsically disordered proteins, which lack a well-defined three-dimensional fold, could be drivers of membrane curvature, provided they repel each other sterically on membrane surfaces. In particular, the large hydrodynamic radii of many intrinsically disordered proteins could make them efficient drivers of steric pressure on membrane surfaces. This idea builds on earlier work in the field of polymer physics, which suggested that synthetic polymers, when tethered to membrane surfaces, can generate substantial steric pressure[59,60]. Notably, the hydrodynamic radius of a globular, folded molecule typically increases with its molecular weight to the 1/3 power. In contrast,

polymeric molecules, owing to their random configurations, typically have hydrodynamic radii that increase as the 2/5 to 3/5 power with molecular weight[61], allowing them to cover more of the membrane surface using a lower total molecular mass.

As discussed in the introduction, intrinsically disordered domains are a common feature of proteins involved in endocytosis. Many of these domains carry significant net negative charge[13,16], which leads to repulsive interactions among the domains, ideal for amplifying steric pressure at membrane surfaces. Recently, the disordered domains of several endocytic proteins (Epsin1, AP180, Amphiphysin) have been found to drive dramatic increases in membrane curvature when recruited to membrane surfaces[62], leading to formation of membrane tubules and fission of larger vesicles into a population of smaller vesicles[56,63]. Studies of the endocytic protein, Epsin1, showed that the membrane deforming abilities of the structured N-terminal domain (ENTH) were greatly exceeded by those of the disordered C-terminal domain, and that the two domains had a synergistic impact on membrane remodeling[62], Figure 1.3b.

Similarly, experiments with Amphiphys1 illustrated that the presence of a disordered domain can dramatically alter a protein's function[63]. Specifically, the N-terminal BAR domain of Amphiphysin1 had long been thought to shape tubular geometries within the cell, including the neck of clathrin-coated pits[9,51]. However, exposure of membrane vesicles to the full-length protein, which contains a substantial disordered domain, resulted in a striking degree of membrane fission and fragmentation, causing a significant reduction in vesicle diameter (Figure 1.3c)[63], a result which was confirmed using live cell imaging. Based on these results, Amphiphysin appears to be a component of the membrane fission machinery, rather than a stabilizer of tubular membrane geometries. In agreement with these findings, alpha synuclein, which associates with membrane bilayers using two N-

terminal amphipathic helices, has been shown to drive membrane remodeling by using its C-terminal intrinsically disordered domain to generate steric pressure (Figure 1.3d)[64].

Extending the idea to the outer surface of the plasma membrane, recent experiments suggest that steric pressure generated by the disordered extracellular domain of the Mucin protein, MUC1, generate steric pressure that can drive assembly of filopodia-like protrusions, when expression level is sufficiently high[65], Figure 1.3e. Interestingly, this effect persisted when glycosylation of MUC1 was suppressed, suggesting that steric pressure arises primarily from interactions between the disordered peptide backbone of the protein's extracellular domain. Collectively, a recent body of work illustrates that steric, repulsive interactions among disordered proteins that are crowded on membrane surfaces can drive membrane curvature away from the crowded surface, generating protein-coated buds and membrane tubules. These findings greatly expand the family of potential curvature driving proteins to include domains of arbitrary structure and intrinsically disordered domains.

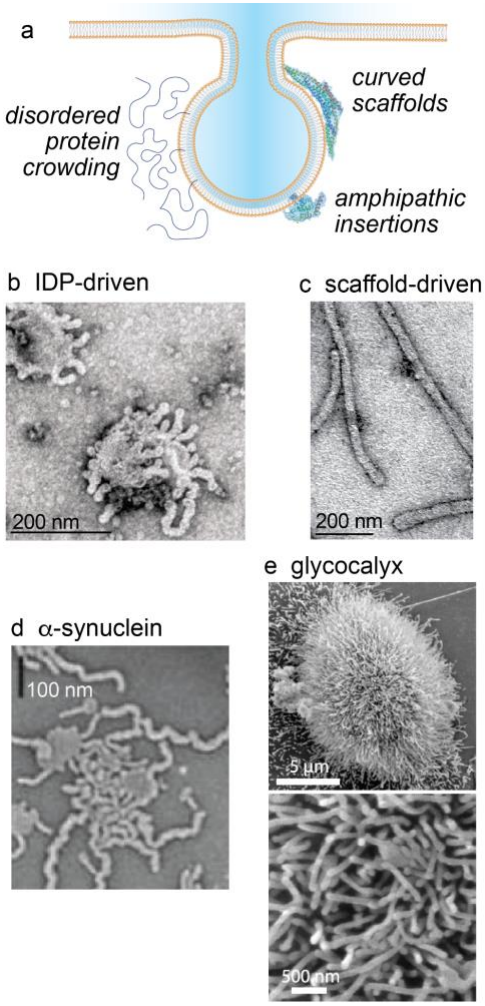

Figure 1. 3 Repulsive interactions between disordered protein domains drive membrane bending. (a) overview of mechanisms by which structured and disordered domains drive membrane bending. (b) disordered protein crowding generates membrane tubules with pearled, isotropic curvature.[56] (c) BAR domain scaffolds generate tubules with anisotropic, cylindrical curvature.[63] (d) a-synuclein generates membrane tubules through steric, repulsive interactions driven by its disordered C-terminal domain.[64] (e) disordered, glycosylated extracellular protein domains (Muc1 tandem repeat domain) generate steric pressure that drives outward, filopodia-like protrusions from cells.[65]

Attractive interactions drive concave curvature

Most recently, numerous studies have highlighted the role of disordered protein networks as major drivers of intracellular phase transitions. These phase transitions are typically defined as liquid-liquid phase separation (LLPS), a phenomenon resulting in the demixing of proteins into discrete condensates that demonstrate liquid-like behavior. This condensation is predominantly mediated by weak, conformationally flexible, multivalent interactions[66]. As polymers of amino acids, disordered proteins can participate in numerous intermolecular interactions, such as electrostatic interactions, cation-π, and π-π stacking interaction[67]. Disordered proteins also inherently exhibit a high degree of conformational flexibility due to their chain entropy, and therefore can adopt numerous spatial arrangements. Finally, the presence of multimerization domains can increase the overall multivalency of the system, allowing for the assembly of networks. In heteromeric phase separating systems, the presence of weakly interacting motifs such as SH3-PRD, SUMO-SUM, RRM-RNA, allows for the formation of higher order protein networks with the complementary binding partner, also contributing to multivalency[68-70]. Overall, the ability of proteins to form higher order, flexible networks is a major driver for phase separation.

In contrast to disordered proteins with steric repulsive interactions, more and more disordered domains are found to have attractive interactions through multivalency as the roles of LLPS are being discovered throughout the cell. Importantly, two-dimensional membranes promote LLPS at significantly lower protein concentrations compared to LLPS in three-dimensional solution[71,72], likely owing to local concentration of proteins on the membrane surface. However, we are just beginning to understand the impact of the attractive interactions between disordered domains on membrane shape.

In chapter 2, I have demonstrated that LLPS of disordered domains at membrane surfaces is capable of bending the lipid membrane in an opposite manner to the bending

caused by repulsive interactions[71]. Specifically, several well-studied domains that are known to undergo LLPS, including the N-terminal low complexity domain of Fused in Sarcoma (FUS LC) and its variants, the low-complexity domain of a heterogeneous nuclear ribonucleoprotein (hnRNPA2 LC) and the arginine/glycine-rich domain (RGG) of a P-granule protein LAF-1 (LAF-1 RGG), were assembled on the surfaces of synthetic and cell-derived membrane vesicles, with the goal of understanding how LLPS influences membrane curvature. N-terminal histidine-tags were fused to the proteins to achieve binding to lipids with Ni-NTA head groups, Figure 1.4a. As these proteins accumulated on the surfaces of giant unilamellar vesicles (GUVs), two-dimensional LLPS was observed, Figure 1.4b, following by the emergence of protein-lined tubules that began at the GUV surface and protruded inward toward the GUV lumen, Figure 1.4 a and c. Interestingly, the tubules showed an undulating morphology like a string of pearls, Figure 1.4d, which is typically associated with an area mismatch between the two membrane leaflets[73,74]. Therefore, the inward protrusion suggested the LLPS reduced the area of the outer leaflet relative to that of the inner leaflet. The proposed mechanism of the reduction in area is that the attractive interaction between the proteins creates a compressive force at the membrane surface, which likely arises from the gradient of protein segments density as a function of distance from the membrane surface, Figure 1.5e. Specifically, if the membrane were to remain flat, there would be an increasing number of unsatisfied potential protein-protein interactions as distance from the surface increased[36]. These unsatisfied interactions create a driving force for membrane bending, which increases the density of protein segments at a distance from the membrane, so that more of the segment interactions can be satisfied. In addition, a continuum mechanics model was built to recreate the tubule morphology based on the standard Helfrich framework[75], where a compressive stress was imposed on the outer membrane surface in the form of spontaneous curvature, which provides a measure

of membrane asymmetry. Moreover, protein-lined inward tubules were observed when LLPS occurred on the surfaces of cell-derived giant plasma membrane vesicles, suggesting that LLPS is sufficient to deform complex, cell-derived membranes.

In parallel with this work, it has also been recently proposed that the contact between three-dimensional protein condensates and membrane surfaces can drive membrane remodeling through a droplet wetting mechanism[76]. In a typical wetting phenomenon where a droplet is in contact with a smooth, flat and rigid substrate, the shape of the droplet is determined by the balance between three interfacial energies associated with the droplet-substrate (ds), droplet-air (da), and air-substrate (as) interfaces. The total energy can be expressed by the following equation:

$$E = \gamma_{ds}A_{ds} + \gamma_{da}A_{da} + \gamma_{as}A_{as}$$

, where γ and A represent the interfacial tension and interfacial area, respectively. Owing to this balance, a droplet will minimize interfacial area when the interfacial tension is higher, in order to minimize the total surface energy.

When the substrate is a soft elastic lipid membrane, it may undergo deformation due to the interplay between substrate elasticity and droplet surface tension, which is known as elastocapillarity (Figure 1.4f). The characteristic length scale over which elastocapillary phenomena are likely to be observed is defined as elastocapillary length, which is determined by the comparison between substrate bending stiffness (elasticity) and droplet surface tension (capillarity). The membrane bending energy scale corresponds to membrane bending rigidity, κ, while the droplet surface tension energy scales as $\gamma_{da}l^2$, where l is the size of droplet. The elastocapillary length can be derived as $l \sim (\kappa / \gamma_{da})^{1/2}$ by equating both energy scales. Kusumaatmaja et al. have estimated the elastocapillary length $l \sim$ 0.1 - 10μm, using typical lipid membrane bending rigidity scale, $\kappa = 10^{-20} - 10^{-18}\ J$ [77],

and droplet surface tension, γ_{da} = 1 – 100 $\mu N/m$[78,79]. This length scale is within the size range of majority of membrane structures and droplets in cells, indicating that elastocapillary forces are likely capable to shaping cellular membranes[76]. Here the magnitude of membrane remodeling could be tuned by adjusting the physiochemical properties of the system, such as membrane tension, membrane composition, droplet size, and droplet fluidity. The functional importance of droplet wetting has recently been shown by more and more studies, like the remodeling of embryonic vacuoles in plants[80,81] (Figure 1.4g), droplet-mediated autophagy[82-84] (Figure 1.4h), clustering of synaptic vesicles in synapses[85-87] (Figure 1.4i), suggesting that the phenomenon of wetting is a key means of controlling droplet and membrane behaviors.

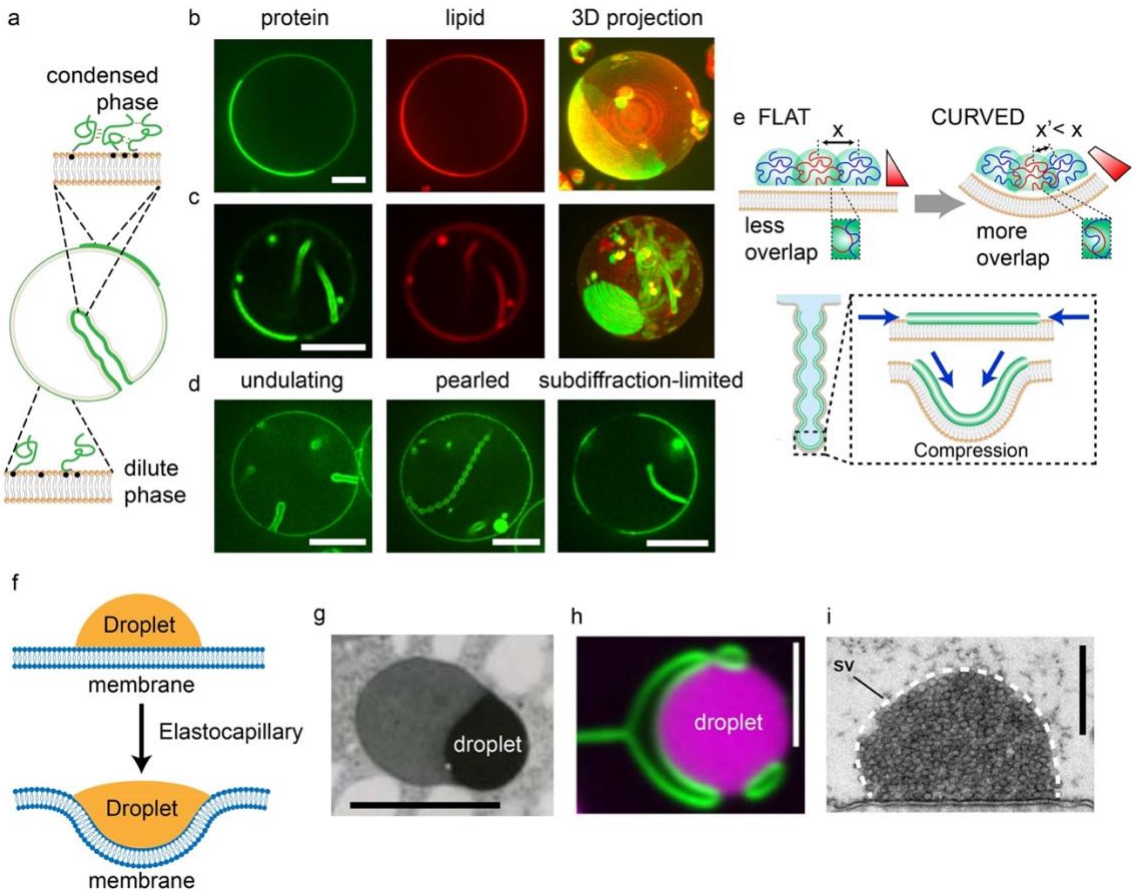

Figure 1. 4 Membrane bending by IDPs with attractive interactions. (a) Schematic of IDP liquid–liquid phase separation (LLPS) on GUV membranes and inward tubule formation. Green lines represent LLPS IDPs. Gray domains indicated 6 × histidine tags, and the black dots indicate Ni-NTA lipids. Bold green lines on GUV indicate two dimensional LLPS region[71]. (b, c) Confocal images (lipid and protein channels) and corresponding maximum intensity projects of GUVs displaying 2D LLPS (b), and protein-lined lipid tubules (c) incubated with 1 μM his-FUS LC in 25 mM HEPES, 150 mM NaCl, pH 7.4 buffer[71]. (d) Representative confocal images of undulating (left panel), pearled (middle panel) and sub-diffraction limited (right panel) tubule morphologies formed by 2D LLPS on GUV membrane surfaces[71]. (e) Schematic depiction of IDP interaction gradient when tethered on membrane (top panel) and membrane tubule formation due to the compressive stresses applied by 2D LLPS on the membrane (bottom panel)[71]. (f) Cartoon displaying the deformation of a soft, elastic membrane by a 3D droplet due to the elastocapillary phenomenon of wetting. (g) Electron microscopy image of a plant vacuole enclosing a wetting droplet[81]. (h) Confocal image of in vitro membrane sheet (green) wetting an autophagosome-related protein droplet surface[82]. (i) Electron microscopy image of droplet-mediated synaptic vesicle (SV) clustering. SVs are clustered in synapsin droplets by complete wetting. And the spherical cap labeled by the white dash line represents partially

wetting of SV clusters on the plasma membrane[86]. Scale bars, 2.5 μm (g), 0.5 μm (i) and 5μm (all other images).

Collectively, we review two ways of membrane bending by phase separation of disordered proteins: (i) compressive stress induced by two-dimensional phase separation, and (ii) the elastocapillary forces created by droplet-membrane interactions. In light of the ongoing discovery of liquid-like behavior in many membrane-bound protein networks, we anticipate that additional functions of LLPS in membrane remodeling will continue to be discovered.

Competition between repulsive and attractive interactions drive controls membrane bending direction

As indicated by the above two sections, the differential stresses induced by a layer of disordered proteins on the membrane surface can be tuned to control the directionality and magnitude of membrane bending. However, disordered domains that are repulsive or noninteracting and disordered domains that attract one another often exist within the same protein and have been characterized as "stickers" and "spacers," respectively[88]. Therefore, to predict the overall impact of an IDP on membrane curvature, we must understand how repulsive and attractive domains work together to apply bending stresses to the membrane surface.

Towards this goal, in chapter 3, I examine a series of disordered protein chimeras, which combine protein domains previously shown to drive either convex or concave membrane curvature. Using these chimeras, I demonstrate that disordered protein layers with opposite curvature preferences can either work together to amplify curvature or can oppose one another to create context-dependent control of membrane shape. In agreement with a simple mechanical model, this work outlines a set of design rules that can be used to understand the impact of disordered proteins on membrane curvature.

Disordered protein networks as catalysts of trafficking vesicle assembly

Once early endocytic proteins have bound to the membrane, they must use interactions between disordered and ordered domains to assemble into an interconnected network[13]. Interestingly, recent work has revealed an emerging role of phase separation in endocytosis, and more broadly in cellular membrane processes and traffic.

The T cell receptor (TCR) activation pathway provided one of the earliest examples of LLPS on membrane surfaces. Like many other membrane receptors, upon stimulation, the TCR forms clusters on the plasma membrane. TCR activation results in phosphorylation of the TCR, resulting in recruitment of ZAP70, which phosphorylates LAT, which recruits Grb2 and then SOS1, potentiating further downstream signaling that can result in activation of intracellular responses such as actin polymerization[89,90]. When reconstituted onto supported lipid bilayers, it was found that the components of the TCR activation pathway assembled into liquid-like clusters in a phosphorylation-dependent manner. Specifically, phosphorylation of LAT, induced by ATP addition, initiated cluster formation, and dephosphorylation, by addition of protein tyrosine phosphatase 1B, dissolved the clusters[91]. By introducing downstream signaling components, N-WASP and Arp2/3, these clusters were sufficient to induce polymerization of actin filaments, indicating that LLPS is capable of supporting signal transduction from receptor to signal output[92]. These protein assemblies also enable kinetic proofreading of the TCR pathway, allowing differentiation between transient interactions and true protein recruitment events. In particular, by increasing the membrane dwell time of SOS in the LAT-Grb2 cluster, LLPS increases the probability of SOS activation, and therefore Ras activation and downstream signaling[93,94]. This allows for signal activation only during TCR activation, rather than transient membrane localizations of SOS. Finally, reconstitution of the LAT-Grb2-SOS condensate onto giant unilamellar vesicles (GUVs) concomitantly induced lipid phase-separation

(Figure 1.5a)[95]. This result suggests that LLPS and lipid phase separation can be functionally coupled. As membrane processes rely on protein-lipid interactions, the ability of LLPS to control lipid organization, and vice versa, may have far reaching implications in cell signaling and trafficking. Overall, these results reveal that LLPS can organize robust signaling events, regulate their activation, and potentially drive rearrangement of membrane lipids.

Clathrin-mediated endocytosis, the most studied endocytic pathway in the cell, is a robust process that relies on an interconnected network of dozens of proteins that organize at the plasma membrane to allow for uptake and encapsulation of cargo[4]. During endocytosis, adaptor proteins recruit transmembrane cargo proteins and the clathrin coat, driving the assembly of coated vesicles. As a growing endocytic structure matures, the protein coat undergoes rearrangements. Many adaptor proteins within the clathrin pathway contain substantial disordered domains[13], which enable the assembly of multi-valent protein networks, which are built upon weak multivalent interactions[96]. The existence of these flexible networks suggests a possible role for LLPS in the clathrin pathway. Indeed, recent work from our lab has shown that the endocytic initiator proteins, Eps15 and Fcho1/2, form liquid-like droplets in solution and on the surfaces of model membranes, Figure 1.5b[72]. Here the authors showed that these liquid-like assemblies are ideal catalysts for vesicle assembly. Specifically, increasing the strength of the network to make it more solid-like resulted in long-lived, stalled endocytic structures. In contrast, reducing the strength of the network, resulted in short-lived, abortive endocytic structures. Complementary findings have been reported in yeast, where Ede1, the yeast homologue of Eps15, was found to form liquid-like condensates that recruit early endocytic proteins in

vivo[97]. It has also been suggested that phase separation may underlie the regulation of actin polymerization at endocytic sites in yeast cells[98].

Given the importance of the endocytic network in the dynamics of endocytosis, in Chapter 4, I set out to understand how cells regulate the stability of the early endocytic network. Many receptors and endocytic proteins are ubiquitylated, while early endocytic proteins such as Eps15 contain ubiquitin-interacting motifs. Therefore, I examined the influence of ubiquitin on the stability of the early endocytic protein network. In vitro, we found that recruitment of small amounts of polyubiquitin dramatically increased the stability of Eps15 condensates, suggesting that ubiquitylation could nucleate endocytic sites. In live cell imaging experiments, a version of Eps15 that lacked the ubiquitin-interacting motif failed to rescue defects in endocytic initiation created by Eps15 knockout. Furthermore, fusion of Eps15 to a deubiquitinase enzyme destabilized nascent endocytic sites within minutes. These results suggest that ubiquitylation drives assembly of the flexible protein network responsible for catalyzing endocytic events.

The significance of a liquid state in the initiation of endocytosis was further suggested by a recent study, which demonstrated that over-stable networks of Ede1 resulted in recruitment of the autophagy machinery to the stalled endocytic site[99]. Autophagosome assembly is preceded by the activation of autophagy receptors that bind to cargo. By showing that Ede1 binds to the autophagy receptor Atg8, this work suggests a role for Ede1 as a sensor for autophagic degradation of nonproductive CME assemblies. Furthermore, they show that in yeast cells with impaired endocytosis, Ede1 localizes into stable clusters with early endocytic proteins that lack the typical dynamics of functioning endocytic pits. These atypical assemblies display characteristics of LLPS, in agreement with the finding that Ede1 forms liquid-like condensates in yeast[97]. Ede1 recruits Atg8 and the autophagy

machinery to the aberrant clusters, facilitating their degradation. Overall, these results suggest that Ede1 assembles via LLPS at endocytic sites, but disruption of the assembly process results in aberrant deposits that are subsequently cleared by the autophagy machinery.

Evidence has mounted for roles of LLPS in clathrin-independent endocytic pathways as well. Caveolae are flask-shaped invaginations of the plasma membrane that are involved in endocytosis, signaling, as well as sensing and responding to plasma membrane stress[100,101]. Caveolae form through the combined effort of caveolin and cavin proteins, which together form a coat around the membrane bud. Caveolins, such as CAV1, are integral membrane proteins that are sufficient for caveolae-like vesiculation in bacteria, but in mammalian cells require the assistance of cavin proteins[102]. Cavins are heteromeric peripheral membrane proteins containing a conserved sequence structure of two helical segments interspersed by three intrinsically disordered regions[102]. Recent work has shown that Cavin1 undergoes LLPS in vitro and in vivo, and that the condensates can recruit CAV1, Figure 1.5c[103]. The intrinsically disordered regions of Cavin1 were found to be essential for mediating phase separation, as well as recruitment of CAV1, membrane remodeling in vitro, and caveolae formation in cells. The authors postulate that LLPS may provide a dynamic platform allowing for generation of caveolae, as well as remodeling of the caveolar coat and subsequent fusion with endosomes. These ideas are consistent with the results of a recent modeling effort, aimed at understanding how transmembrane protein receptors are sorted into endocytic vesicles[104]. Specifically, sorting was modeled as a process of adsorption of proteins into a domain on the membrane, akin to phase separation, which then imposes curvature and drives subsequent vesiculation of the membrane. This process was found to be optimized for intermediate levels of protein aggregation strength,

in agreement with work on the role of Eps15 in clathrin-mediated endocytosis[72]. Overall, recent work suggests that LLPS is leveraged by cells to organize trafficking processes that require dynamic rearrangement of proteins, such as vesicle assembly and fusion.

Autophagy is a cellular process that serves to remove and degrade cellular components for recycling in the lysosome. The most well-studied form of autophagy is macroautophagy, in which a double membrane autophagosome engulfs the molecular cargo, and fuses with the lysosome, releasing its contents for degradation[105]. In yeast, assembly of the autophagosome starts with the assembly of the pre-autophagosomal structure (PAS), which is mainly composed of the five-membered Atg1 complex[105]. These constituent proteins are enriched in disordered domains, and participate in multivalent interactions that allow for self-assembly of the Atg1 complex[106]. Later work demonstrated that the Atg1 complex undergoes LLPS, which is critical for the initiation of the PAS, Figure 1.5d[107]. The liquid state of PAS organization is likely important for recruitment of downstream Atg proteins, as well as dynamic rearrangement to support the growing isolation membrane.

An additional example of LLPS during membrane traffic comes from the organization of synaptic vesicles in nerve terminals. During neuronal synapse, synaptic vesicles containing neurotransmitters fuse with the presynaptic membrane, releasing the neurotransmitter into the synaptic cleft. These synaptic vesicles are stored in clusters in the presynaptic matrix of axon terminals, where they are poised for release. These clusters are dynamic, and vesicles can readily exchange between them. Synapsin, which contains a disordered region and multiple SH3 domains, is the predominant protein in the matrix surrounding these clusters. It has been shown that synapsin phase-separates into liquid-like droplets, due to its disordered domain[85]. Synapsin droplets are capable of localizing

synthetic synaptic vesicles, indicating that the clustering of synaptic vesicles in axon terminals may be mediated by a liquid phase (Figure 1.5e). Upon stimulation by an action potential, voltage-gated calcium channels open, causing an influx of Ca^{2+} and synaptic vesicle release. In order to support fast and efficient neurotransmitter release, neurons contain "active zones" which localize the voltage-gated calcium channels and synaptic vesicles. The active zone contains RIM and RIM-BP proteins, among others, which function in linking the voltage-gated calcium channels to synaptic vesicles. RIM and RIM-BP contain significant intrinsically disordered domains and are capable of undergoing LLPS on supported lipid bilayers, where they effectively cluster the cytoplasmic tail of a voltage-gated calcium channel[108]. Since RIM is networked to SNARE proteins via mutual interactions with other active zone proteins, liquid-like clustering of voltage-gated calcium channels within proximity of SNAREs may be sufficient to facilitate expeditious synaptic vesicle release.

Overall, a growing number of recent reports have contributed to a new understanding of how LLPS of intrinsically disordered proteins at membrane surfaces supports dynamic and flexible cellular functions, which include quality control, productive signaling, robust endocytosis, and generation of membrane vesicles.

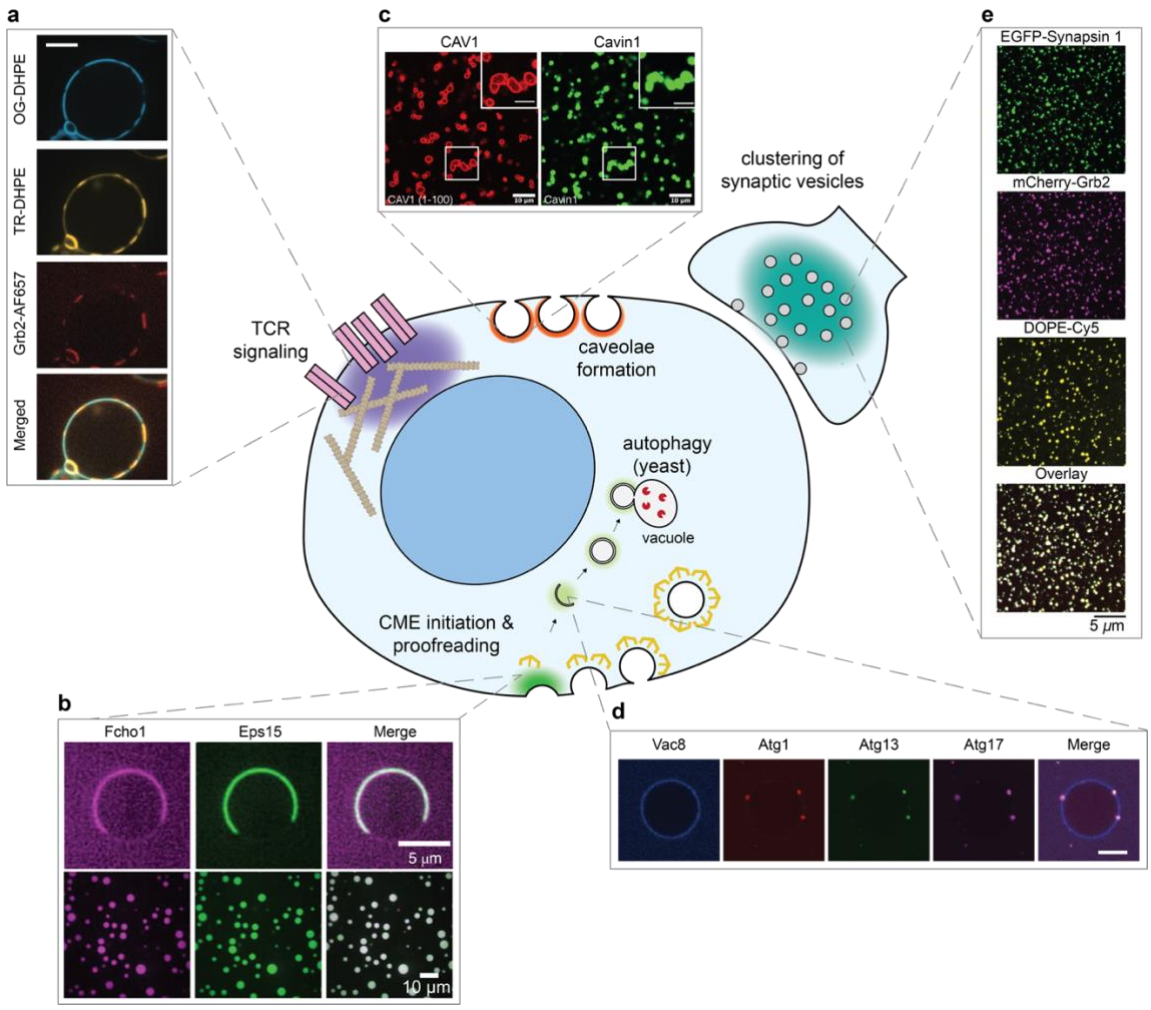

Figure 1. 5 Intrinsically disordered proteins mediate LLPS in membrane trafficking pathways. (a) LAT-Grb2-SOS networks phase-separate on GUV membranes and induce lipid phase-separation. TR-DHPE and OG-DHPE indicate the liquid-disordered and liquid-ordered phases respectively. (b) Fcho1/2 and Eps15 form liquid-like droplets in vitro and phase-separate on GUV membranes[72]. (c) Cavin1 forms droplets that localize Cav1[103]. (d) Droplets of the Atg1 complex proteins assemble onto GUV membranes mimicking the autophagosomal membrane[107]. (e) Synapsin condensates concentrate lipid vesicles that mimic synaptic vesicles.

REFERENCES

1. Elkin, S. R., Lakoduk, A. M. & Schmid, S. L. Endocytic pathways and endosomal trafficking: a primer. *Wiener Medizinische Wochenschrift* **166**, 196-204 (2016).
2. Stachowiak, J. C., Brodsky, F. M. & Miller, E. A. A cost–benefit analysis of the physical mechanisms of membrane curvature. *Nature cell biology* **15**, 1019-1027 (2013).
3. Di Fiore, P. P. & De Camilli, P. Endocytosis and signaling: an inseparable partnership. *Cell* **106**, 1-4 (2001).
4. McMahon, H. T. & Boucrot, E. Molecular mechanism and physiological functions of clathrin-mediated endocytosis. *Nat Rev Mol Cell Biol* **12**, 517-533 (2011).
5. Robinson, M. S. Forty Years of Clathrin-coated Vesicles. *Traffic* **16**, 1210-1238 (2015).
6. Ford, M. *et al.* Curvature of clathrin-coated pits driven by epsin. *Nature* **419**, 361-366 (2002).
7. Fotin, A. *et al.* Molecular model for a complete clathrin lattice from electron cryomicroscopy. *Nature* **432**, 573-579 (2004).
8. Fath, S., Mancias, J. D., Bi, X. & Goldberg, J. Structure and organization of coat proteins in the COPII cage. *Cell* **129**, 1325-1336 (2007).
9. Frost, A., Unger, V. M. & De Camilli, P. The BAR domain superfamily: membrane-molding macromolecules. *Cell* **137**, 191-196 (2009).
10. Johannes, L., Wunder, C. & Bassereau, P. Bending "On the Rocks"-A Cocktail of Biophysical Modules to Build Endocytic Pathways. *Cold Spring Harbor Perspectives in Biology* **6** (2014).
11. Ford, M. G., Jenni, S. & Nunnari, J. The crystal structure of dynamin. *Nature* **477**, 561-566 (2011).
12. Faelber, K. *et al.* Crystal structure of nucleotide-free dynamin. *Nature* **477**, 556-560 (2011).
13. Dafforn, T. R. & Smith, C. J. Natively unfolded domains in endocytosis: hooks, lines and linkers. *EMBO reports* **5**, 1046-1052 (2004).
14. Owen, D. J., Collins, B. M. & Evans, P. R. Adaptors for clathrin coats: structure and function. *Annual review of cell and developmental biology* **20**, 153-191 (2004).

15. Zhuo, Y. *et al.* Dynamic interactions between clathrin and locally structured elements in a disordered protein mediate clathrin lattice assembly. *Journal of Molecular Biology* **404**, 274-290 (2010).
16. Pietrosemoli, N., Pancsa, R. & Tompa, P. Structural disorder provides increased adaptability for vesicle trafficking pathways. *PLoS computational biology* **9**, e1003144 (2013).
17. Schmid, E. M. *et al.* Role of the AP2 beta-appendage hub in recruiting partners for clathrin-coated vesicle assembly. *PLoS Biol* **4**, e262 (2006).
18. Schmid, E. M. & McMahon, H. T. Integrating molecular and network biology to decode endocytosis. *Nature* **448**, 883-888 (2007).
19. Dafforn, T. R. & Smith, C. J. Natively unfolded domains in endocytosis: hooks, lines and linkers. *EMBO Reports* **5**, 1046-1052 (2004).
20. Zeno, W. F. *et al.* Synergy between intrinsically disordered domains and structured proteins amplifies membrane curvature sensing. *Nature Communications* **9**, 4152 (2018).
21. Zeno, W. F. *et al.* Molecular Mechanisms of Membrane Curvature Sensing by a Disordered Protein. *Journal of the American Chemical Society* (2019).
22. Hatzakis, N. S. *et al.* How curved membranes recruit amphipathic helices and protein anchoring motifs. *Nat Chem Biol* **5**, 835-841 (2009).
23. Bhatia, V. K. *et al.* Amphipathic motifs in BAR domains are essential for membrane curvature sensing. *EMBO J* **28**, 3303-3314 (2009).
24. Theillet, F. X. *et al.* The alphabet of intrinsic disorder: I. Act like a Pro: On the abundance and roles of proline residues in intrinsically disordered proteins. *Intrinsically Disord Proteins* **1**, e24360 (2013).
25. Kalthoff, C., Alves, J., Urbanke, C., Knorr, R. & Ungewickell, E. J. Unusual structural organization of the endocytic proteins AP180 and epsin 1. *Journal of Biological Chemistry* **277**, 8209-8216 (2002).
26. Srinivasan, N., Bhagawati, M., Ananthanarayanan, B. & Kumar, S. Stimuli-sensitive intrinsically disordered protein brushes. *Nature communications* **5**, 5145 (2014).
27. Mao, A. H., Crick, S. L., Vitalis, A., Chicoine, C. L. & Pappu, R. V. Net charge per residue modulates conformational ensembles of intrinsically disordered proteins. *Proceedings of the National Academy of Sciences of the United States of America* **107**, 8183-8188 (2010).
28. Uversky, V. N., Gillespie, J. R. & Fink, A. L. Why are "natively unfolded" proteins unstructured under physiologic conditions? *Proteins* **41**, 415-427 (2000).

29. Bernado, P. & Svergun, D. I. Structural analysis of intrinsically disordered proteins by small-angle X-ray scattering. *Molecular biosystems* **8**, 151-167 (2012).
30. Jensen, M. R., Zweckstetter, M., Huang, J.-r. & Blackledge, M. Exploring free-energy landscapes of intrinsically disordered proteins at atomic resolution using NMR spectroscopy. *Chemical reviews* **114**, 6632-6660 (2014).
31. Nettels, D., Hoffmann, A. & Schuler, B. Unfolded protein and peptide dynamics investigated with single-molecule FRET and correlation spectroscopy from picoseconds to seconds. *The Journal of Physical Chemistry B* **112**, 6137-6146 (2008).
32. Hofmann, H. *et al.* Polymer scaling laws of unfolded and intrinsically disordered proteins quantified with single-molecule spectroscopy. *Proceedings of the National Academy of Sciences* **109**, 16155-16160 (2012).
33. Flory, P. J. The configuration of real polymer chains. *The Journal of Chemical Physics* **17**, 303-310 (1949).
34. Phillips, R., Kondev, J., Theriot, J. & Garcia, H. *Physical biology of the cell*. (Garland Science, 2012).
35. DiMarzio, E. A. Proper accounting of conformations of a polymer near a surface. *The Journal of Chemical Physics* **42**, 2101-2106 (1965).
36. DiMarzio, E. A. & McCrackin, F. L. One-Dimensional Model of Polymer Adsorption. *The Journal of Chemical Physics* **43**, 539-547 (1965).
37. Lipowsky, R. Bending of membranes by anchored polymers. *EPL (Europhysics Letters)* **30**, 197 (1995).
38. Capraro, B. R., Yoon, Y., Cho, W. & Baumgart, T. Curvature sensing by the epsin N-terminal homology domain measured on cylindrical lipid membrane tethers. *J Am Chem Soc* **132**, 1200-1201 (2010).
39. Joseph, J. G., Osorio, C., Yee, V., Agrawal, A. & Liu, A. P. Complimentary action of structured and unstructured domains of epsin supports clathrin-mediated endocytosis at high tension. *Communications biology* **3**, 1-16 (2020).
40. Tillu, V. A. *et al.* Cavin1 intrinsically disordered domains are essential for fuzzy electrostatic interactions and caveola formation. *Nature communications* **12**, 1-18 (2021).
41. Su, M. *et al.* Comparative Study of Curvature Sensing Mediated by F-BAR and an Intrinsically Disordered Region of FBP17. *Iscience* **23**, 101712 (2020).

42. McMahon, H. T. & Boucrot, E. Molecular mechanism and physiological functions of clathrin-mediated endocytosis. *Nature reviews. Molecular cell biology* **12**, 517-533 (2011).
43. Hurley, J. H., Boura, E., Carlson, L.-A. & Różycki, B. Membrane budding. *Cell* **143**, 875-887 (2010).
44. Stachowiak, J. C., Brodsky, F. M. & Miller, E. A. A cost-benefit analysis of the physical mechanisms of membrane curvature. *Nature Cell Biology* **15**, 1019-1027 (2013).
45. Baumgart, T., Capraro, B. R., Zhu, C. & Das, S. L. Thermodynamics and mechanics of membrane curvature generation and sensing by proteins and lipids. *Annu Rev Phys Chem* **62**, 483-506 (2011).
46. Sheetz, M. P. & Singer, S. J. Biological membranes as bilayer couples, A molecular mechanism of drug-erythrocyte interactions. *Proceedings of the National Academy of the Sciences of the United States of America* **71**, 4457-4461 (1974).
47. Campelo, F., McMahon, H. & Kozlov, M. The hydrophobic insertion mechanism of membrane curvature generation by proteins. *Biophysical Journal* **95**, 2325-2339 (2008).
48. Lee, M. *et al.* Sar1p N-terminal helix initiates membrane curvature and completes the fission of a COPII vesicle. *Cell* **122**, 605-617 (2005).
49. Miller, S. E. *et al.* The molecular basis for the endocytosis of small R-SNAREs by the clathrin adaptor CALM. *Cell* **147**, 1118-1131 (2011).
50. Kirchhausen, T. Bending membranes. *Nature Cell Biology* **14**, 906-908 (2012).
51. Mim, C. & Unger, V. M. Membrane curvature and its generation by BAR proteins. *Trends Biochem Sci* **37**, 526-533 (2012).
52. Daumke, O., Roux, A. & Haucke, V. BAR domain scaffolds in dynamin-mediated membrane fission. *Cell* **156**, 882-892 (2014).
53. Stachowiak, J., Hayden, C. & Sasaki, D. Steric confinement of proteins on lipid membranes can drive curvature and tubulation. *Proceedings of the National Academy of Sciences of the United States of America* **107**, 7781-7786 (2010).
54. Stachowiak, J. *et al.* Membrane bending by protein-protein crowding. *Nature Cell Biology* **14**, 944-+ (2012).
55. Shi, Z. & Baumgart, T. Membrane tension and peripheral protein density mediate membrane shape transitions. *Nature Communications* **6**, 5974 (2015).

56. Snead, W. T. *et al.* Membrane fission by protein crowding. *Proceedings of the National Academy of Sciences of the United States of America* **114**, E3258-E3267 (2017).
57. Houser, J. R., Hayden, C. C., Thirumalai, D. & Stachowiak, J. C. A Forster Resonance Energy Transfer-Based Sensor of Steric Pressure on Membrane Surfaces. *J Am Chem Soc* **142**, 20796-20805 (2020).
58. Kory, N., Thiam, A., Farese, R. & Walther, T. Protein Crowding Is a Determinant of Lipid Droplet Protein Composition. *Developmental Cell* **34**, 351-363 (2015).
59. Carignano, M. A. & Szleifer, I. On the Structure and Pressure of Tethered Polymer Layers in Good Solvent. *Macromolecules* **28**, 3197-3204 (1995).
60. Lipowsky, R. Bending of Membranes by Anchored Polymers. *Eurphysics Letters* **30**, 197-202 (1995).
61. Gennes, P. G. d. *Scaling concepts in polymer physics*. (Cornell University Press, 1979).
62. Busch, D. J. *et al.* Intrinsically disordered proteins drive membrane curvature. *Nature Communications* **6**, 7875 (2015).
63. Snead, W. T. *et al.* BAR scaffolds drive membrane fission by crowding disordered domains. *J Cell Biol* **218**, 664-682 (2019).
64. Jiang, Z., de Messieres, M. & Lee, J. C. Membrane remodeling by alpha-synuclein and effects on amyloid formation. *Journal of the American Chemical Society* **135**, 15970-15973 (2013).
65. Shurer, C. R. *et al.* Physical Principles of Membrane Shape Regulation by the Glycocalyx. *Cell* **177**, 1757-1770 e1721 (2019).
66. Banani, S. F., Lee, H. O., Hyman, A. A. & Rosen, M. K. Biomolecular condensates: organizers of cellular biochemistry. *Nat Rev Mol Cell Biol* **18**, 285-298 (2017).
67. Brangwynne, Clifford P., Tompa, P. & Pappu, Rohit V. Polymer physics of intracellular phase transitions. *Nature Physics* **11**, 899 (2015).
68. Li, P. *et al.* Phase transitions in the assembly of multivalent signalling proteins. *Nature* **483**, 336-340 (2012).
69. Banani, S. F. *et al.* Compositional Control of Phase-Separated Cellular Bodies. *Cell* **166**, 651-663 (2016).
70. Lin, Y., Protter, D. S., Rosen, M. K. & Parker, R. Formation and Maturation of Phase-Separated Liquid Droplets by RNA-Binding Proteins. *Mol Cell* **60**, 208-219 (2015).

71. Yuan, F. *et al.* Membrane bending by protein phase separation. *Proceedings of the National Academy of Sciences* **118** (2021).
72. Day, K. J. *et al.* Liquid-like protein interactions catalyse assembly of endocytic vesicles. *Nat Cell Biol* **23**, 366-376 (2021).
73. Tsafrir, I. *et al.* Pearling instabilities of membrane tubes with anchored polymers. *Phys Rev Lett* **86**, 1138-1141 (2001).
74. Sanborn, J., Oglęcka, K., Kraut, R. S. & Parikh, A. N. Transient pearling and vesiculation of membrane tubes under osmotic gradients. *Faraday discussions* **161**, 167-176 (2013).
75. Helfrich, W. Elastic properties of lipid bilayers: theory and possible experiments. *Zeitschrift für Naturforschung C* **28**, 693-703 (1973).
76. Kusumaatmaja, H., May, A. I. & Knorr, R. L. Intracellular wetting mediates contacts between liquid compartments and membrane-bound organelles. *Journal of Cell Biology* **220**, e202103175 (2021).
77. Gracia, R. S., Bezlyepkina, N., Knorr, R. L., Lipowsky, R. & Dimova, R. Effect of cholesterol on the rigidity of saturated and unsaturated membranes: fluctuation and electrodeformation analysis of giant vesicles. *Soft Matter* **6**, 1472-1482 (2010).
78. Aumiller Jr, W. M. & Keating, C. D. Experimental models for dynamic compartmentalization of biomolecules in liquid organelles: Reversible formation and partitioning in aqueous biphasic systems. *Advances in colloid and interface science* **239**, 75-87 (2017).
79. Jawerth, L. M. *et al.* Salt-dependent rheology and surface tension of protein condensates using optical traps. *Physical review letters* **121**, 258101 (2018).
80. Kusumaatmaja, H. *et al.* Wetting of phase-separated droplets on plant vacuole membranes leads to a competition between tonoplast budding and nanotube formation. *Proceedings of the National Academy of Sciences* **118** (2021).
81. Zheng, H. & Staehelin, L. A. Protein storage vacuoles are transformed into lytic vacuoles in root meristematic cells of germinating seedlings by multiple, cell type-specific mechanisms. *Plant Physiology* **155**, 2023-2035 (2011).
82. Agudo-Canalejo, J. *et al.* Wetting regulates autophagy of phase-separated compartments and the cytosol. *Nature* **591**, 142-146 (2021).
83. Schultz, S. W. *et al.* Should I bend or should I grow: the mechanisms of droplet-mediated autophagosome formation. *Autophagy* **17**, 1046-1048 (2021).

84. Kageyama, S. *et al.* p62/SQSTM1-droplet serves as a platform for autophagosome formation and anti-oxidative stress response. *Nature communications* **12**, 1-16 (2021).
85. Milovanovic, D., Wu, Y., Bian, X. & De Camilli, P. A liquid phase of synapsin and lipid vesicles. *Science* **361**, 604-607 (2018).
86. Pechstein, A. *et al.* Vesicle clustering in a living synapse depends on a synapsin region that mediates phase separation. *Cell reports* **30**, 2594-2602. e2593 (2020).
87. Park, D. *et al.* Cooperative function of synaptophysin and synapsin in the generation of synaptic vesicle-like clusters in non-neuronal cells. *Nature communications* **12**, 1-10 (2021).
88. Martin, E. W. *et al.* Valence and patterning of aromatic residues determine the phase behavior of prion-like domains. *Science* **367**, 694-699 (2020).
89. Kumari, S., Curado, S., Mayya, V. & Dustin, M. L. T cell antigen receptor activation and actin cytoskeleton remodeling. *Biochim Biophys Acta* **1838**, 546-556 (2014).
90. Hwang, J. R., Byeon, Y., Kim, D. & Park, S. G. Recent insights of T cell receptor-mediated signaling pathways for T cell activation and development. *Exp Mol Med* **52**, 750-761 (2020).
91. Su, X. *et al.* Phase separation of signaling molecules promotes T cell receptor signal transduction. *Science* **352**, 595-599 (2016).
92. Salvi, N. *Intrinsically Disordered Proteins: Dynamics, Binding, and Function*. (Academic Press, 2019).
93. Huang, W. Y. *et al.* Phosphotyrosine-mediated LAT assembly on membranes drives kinetic bifurcation in recruitment dynamics of the Ras activator SOS. *Proceedings of the National Academy of Sciences of the United States of America* **113**, 8218-8223 (2016).
94. Huang, W. Y. C. *et al.* A molecular assembly phase transition and kinetic proofreading modulate Ras activation by SOS. *Science* **363**, 1098-1103 (2019).
95. Chung, J. K. *et al.* Coupled membrane lipid miscibility and phosphotyrosine-driven protein condensation phase transitions. *Biophys J* **120**, 1257-1265 (2021).
96. Smith, S. M., Baker, M., Halebian, M. & Smith, C. J. Weak Molecular Interactions in Clathrin-Mediated Endocytosis. *Front Mol Biosci* **4**, 72 (2017).
97. Kozak, M. & Kaksonen, M. Condensation of Ede1 promotes the initiation of endocytosis. *Elife* **11**, e72865 (2022).
98. Sun, Y. *et al.* Switch-like Arp2/3 activation upon WASP and WIP recruitment to an apparent threshold level by multivalent linker proteins in vivo. *Elife* **6** (2017).

99. Wilfling, F. *et al.* A Selective Autophagy Pathway for Phase-Separated Endocytic Protein Deposits. *Mol Cell* **80**, 764-778 e767 (2020).
100. Parton, R. G. & del Pozo, M. A. Caveolae as plasma membrane sensors, protectors and organizers. *Nat Rev Mol Cell Biol* **14**, 98-112 (2013).
101. Parton, R. G. Caveolae: Structure, Function, and Relationship to Disease. *Annu Rev Cell Dev Biol* **34**, 111-136 (2018).
102. Parton, R. G., Tillu, V., McMahon, K. A. & Collins, B. M. Key phases in the formation of caveolae. *Curr Opin Cell Biol* **71**, 7-14 (2021).
103. Tillu, V. A. *et al.* Cavin1 intrinsically disordered domains are essential for fuzzy electrostatic interactions and caveola formation. *Nat Commun* **12**, 931 (2021).
104. Zamparo, M. *et al.* Optimality in Self-Organized Molecular Sorting. *Phys Rev Lett* **126**, 088101 (2021).
105. Farre, J. C. & Subramani, S. Mechanistic insights into selective autophagy pathways: lessons from yeast. *Nat Rev Mol Cell Biol* **17**, 537-552 (2016).
106. Yamamoto, H. *et al.* The Intrinsically Disordered Protein Atg13 Mediates Supramolecular Assembly of Autophagy Initiation Complexes. *Dev Cell* **38**, 86-99 (2016).
107. Fujioka, Y. *et al.* Phase separation organizes the site of autophagosome formation. *Nature* **578**, 301-305 (2020).
108. Wu, X. *et al.* RIM and RIM-BP Form Presynaptic Active-Zone-like Condensates via Phase Separation. *Mol Cell* **73**, 971-984 e975 (2019).

Chapter 2: Membrane Bending by Protein Phase Separation[2]

ABSTRACT

Membrane bending is a ubiquitous cellular process that is required for membrane traffic, cell motility, organelle biogenesis, and cell division. Proteins that bind to membranes using specific structural features, such as wedge-like amphipathic helices and crescent-shaped scaffolds, are thought to be the primary drivers of membrane bending. However, many membrane-binding proteins have substantial regions of intrinsic disorder which lack a stable three-dimensional structure. Interestingly, many of these disordered domains have recently been found to form networks stabilized by weak, multivalent contacts, leading to assembly of protein liquid phases on membrane surfaces. Here we ask how membrane-associated protein liquids impact membrane curvature. We find that protein phase separation on the surfaces of synthetic and cell-derived membrane vesicles creates a substantial compressive stress in the plane of the membrane. This stress drives the membrane to bend inward, creating protein-lined membrane tubules. A simple mechanical model of this process accurately predicts the experimentally measured relationship between the rigidity of the membrane and the diameter of the membrane tubules. Discovery of this mechanism, which may be relevant to a broad range of cellular protrusions, illustrates that membrane remodeling is not exclusive to structured scaffolds but can also be driven by the rapidly emerging class of liquid-like protein networks that assemble at membranes.

---

2 This chapter is published as: Yuan, F. *et al.* Membrane bending by protein phase separation. *Proceedings of the National Academy of Sciences* **118** (2021)

SIGNIFICANCE STATEMENT

Cellular membranes take on an elaborate set of highly curved and bent shapes which are essential to diverse cellular functions from endocytosis to cell division. The prevailing view has been that membrane bending is driven by proteins with curved shapes, which assemble at the membrane surface to form solid scaffolds. In contrast, here we show that proteins which form liquid-like assemblies on membranes are also potent drivers of bending. These "liquid scaffolds" apply compressive stress to the membrane surface, generating a diverse and dynamic family of membrane shapes. These data, which come at a time when liquid-like protein assemblies are being identified throughout the cell, suggest that protein liquids may play an important role in shaping cellular membranes.

INTRODUCTION

From endocytic buds[109] to needle-like filopodial protrusions[110], curved membrane surfaces play critical roles in many cellular processes[43]. The energetic cost of creating these highly curved surfaces is considerable, such that spontaneous membrane fluctuations are insufficient to establish and stabilize the shapes of cellular membranes[111]. Instead, work during the past two decades has revealed that interactions between proteins and lipids drive membrane curvature[112]. Multiple physical mechanisms underlie the ability of proteins to shape membrane surfaces. These include amphipathic helices that insert like wedges into one leaflet of the membrane, creating an interleaflet area mismatch that drives curvature[113]. Alternatively, proteins with inherently curved membrane binding domains such as BAR domains, dynamin, and ESCRTs act as scaffolds that can stabilize curved membrane geometries[52,114]. While each of these mechanisms relies on structured protein domains, we have recently reported that intrinsically disordered proteins, which lack a stable three-dimensional structure, can also be potent drivers of membrane bending[63,115]. Specifically,

when non-interacting disordered domains are crowded together in cellular structures, steric repulsion among them drives the membrane to buckle outward, taking on a curved shape.

Interestingly, rather than repelling one another, many disordered proteins have recently been found to assemble together via weak, multivalent interactions, forming networks that have the physical properties of liquids[116]. Notably, recent studies have suggested that liquid–liquid phase separation of membrane-bound proteins plays an important role in diverse cellular processes including nucleation of actin filaments[117], immunological signaling[118], and assembly of virions[119].

How might liquid–liquid phase separation of proteins at membrane surfaces impact membrane curvature? To address this question, we examined phase separation of the N-terminal low-complexity domain of fused in sarcoma, FUS LC, on the surfaces of synthetic and cell-derived membrane vesicles. FUS LC was chosen as a model protein for this study because it is among the most thoroughly characterized examples of a domain that undergoes liquid–liquid protein phase separation in solution[120]. Here, we assemble FUS LC on membrane surfaces using an N-terminal histidine tag[121] that binds strongly to lipids with Ni-NTA headgroups. As FUS LC accumulated at the membrane surface, we observed protein phase separation in the two-dimensional plane of the membrane followed by spontaneous inward bending of the membrane, such that protein-lined tubules were created. Similar tubules were observed with two other domains implicated in liquid–liquid phase separation, the low-complexity domain of hnRNPA2[122] and the RGG domain of LAF-1[123]. Interestingly, the tubules had undulating morphologies, similar to a string of pearls. This phenomenon is associated with an area mismatch between the two membrane leaflets[73,74], suggesting that protein phase separation pulls lipids toward one another, creating a net compressive stress on one side of the membrane. In line with this hypothesis, a continuum mechanics model, built on the standard Helfrich framework, recreated the tubule

morphology when a compressive stress was imposed using spontaneous curvature on the outer membrane surface. Further, the model predicted that tubule diameter should increase with increasing membrane rigidity and increasing rigidity ratio, trends confirmed by our experiments. Collectively, these findings suggest that protein phase separation on membrane surfaces generates considerable stresses that can drive the spontaneous assembly of membrane buds and tubules with physiologically relevant dimensions.

RESULTS

Protein Phase Separation on Membranes Drives Assembly of Protein-lined Tubules.

To examine the impact of protein phase separation on membrane surfaces, we combined an N-terminal 6 histidine-tagged version of FUS LC, his-FUS LC, with giant unilamellar vesicles consisting of 93 mol% POPC, 5 mol% Ni-NTA, 2 mol% DP-EG10 biotin for coverslip tethering, and 0.1 mol% Texas Red-DHPE for visualization (Figure 2.1a). The protein was labeled at the N terminus with an N-hydroxysuccinimide (NHS)-reactive dye, Atto 488 for visualization, as described under Materials and Methods. Samples were imaged using multichannel, high-magnification spinning disk confocal microscopy. When a protein concentration of 0.5 μM was applied to the vesicles, a relatively dim, uniform signal from the protein was observed at the membrane surface (Figure 2.1b). In contrast, when the protein concentration was increased to 1 μM, more intense regions of fluorescence in the protein channel were observed around the vesicle periphery (Figure 2.1c). Three-dimensional reconstruction of image stacks revealed that these bright regions formed hemispherical domains on the vesicle surfaces which were surrounded by dimmer regions (Figure 2.1c, protein panel).

The appearance of these vesicles is remarkably similar to vesicles undergoing phase separation into two coexisting lipid phases[124,125]. In particular, the protein-rich regions in

Figure 2.1c and d have smooth, rounded boundaries, suggesting that they enclose an easily deformable liquid[124]. However, the membrane composition used in the present study consisted entirely of unsaturated lipids with melting temperatures well below room temperature, such that phase separation of the underlying lipid membrane was not expected. Furthermore, a control protein that is not involved in protein phase separation, histidine-tagged green fluorescent protein (GFP), covered the surfaces of these vesicles uniformly (SI Appendix, Figure 2.7). These results suggest that the variations in intensity in the his-FUS LC protein channel did not arise from lipid heterogeneity. Instead, the FUS LC protein appeared to organize on the two-dimensional membrane surface into protein-rich and protein-poor phases. Notably, the head-labeled lipid probe, Texas Red-DHPE, was slightly brighter within the protein-rich regions, likely owing to affinity between the aromatic fluorophore on the lipid headgroup and the FUS LC domain which is enriched in aromatic tyrosine residues[120]. However, photophysical effects of FUS LC on Texas Red could also play a role. To separate the lipid label from FUS LC, we also conducted experiments with a tail group–labeled lipid, Texas Red ceramide. Here, enrichment of the labeled lipid in the protein-rich regions was lost, further suggesting that lipid phase separation does not occur in these vesicles (SI Appendix, Figure 2.8).

A few minutes after the addition of his-FUS LC, we observed that many of the vesicles developed lipid tubules spontaneously. These tubules originated at the surfaces of the vesicles and protruded into the vesicle lumen, such that they were lined by the his-FUS LC protein (Figure 2.1d). Some of the tubules had an undulating, wavy appearance (Figure 2.1d and e) while others formed a series of tight spheres, resembling a string of pearls (Figure 2.1f). Still others were so slender that their morphology could not be precisely determined (Figure 2.1g). In some instances, tubules remain associated with protein-rich membrane domains (Figure 2.1g), while in other cases, the domains appear to have been consumed, transforming fully

into tubules (Figure 2.1f). Vesicles were incubated with proteins and given time to come approximately into equilibrium before imaging began. While experiments were performed under isosmotic conditions, the impact of tubule formation on membrane tension was not precisely mapped.

Tubules were observed more frequently as the concentration of his-FUS LC increased (Figure 2.1h and SI Appendix, Table 2.1). Specifically, less than 2% of vesicles formed lipid tubules in the presence of 0.1 μM FUS LC, while 22% and 44% formed tubules after addition of 0.5 μM and 1 μM FUS LC, respectively. However, for protein concentrations above 1 μM, the fraction of vesicles with tubules reached a plateau, likely owing to the appearance of three-dimensional protein droplets in the surrounding solution, which did not appear to be membrane associated (Figure 2.1h, Inset). These droplets likely compete with the membrane surface for protein molecules, limiting the further accumulation of protein on the membrane surface.

Importantly, dynamic changes were observed in the morphology of the tubules over time, suggesting that the protein layer on the membrane surface remained highly deformable rather than assembling into a rigid scaffold (Figure 2.1i and Movie 2.1). Additionally, domains of the protein-depleted phase had rapidly fluctuating boundaries and diffused randomly within the protein-enriched phase, observations which further demonstrate the fluid-like nature of the protein-rich phase (Movie 2.2). To further quantify the relationship between protein concentration and tubule formation, we next varied the strength of protein–protein and protein–membrane interactions and observed the impact on the membrane tubules.

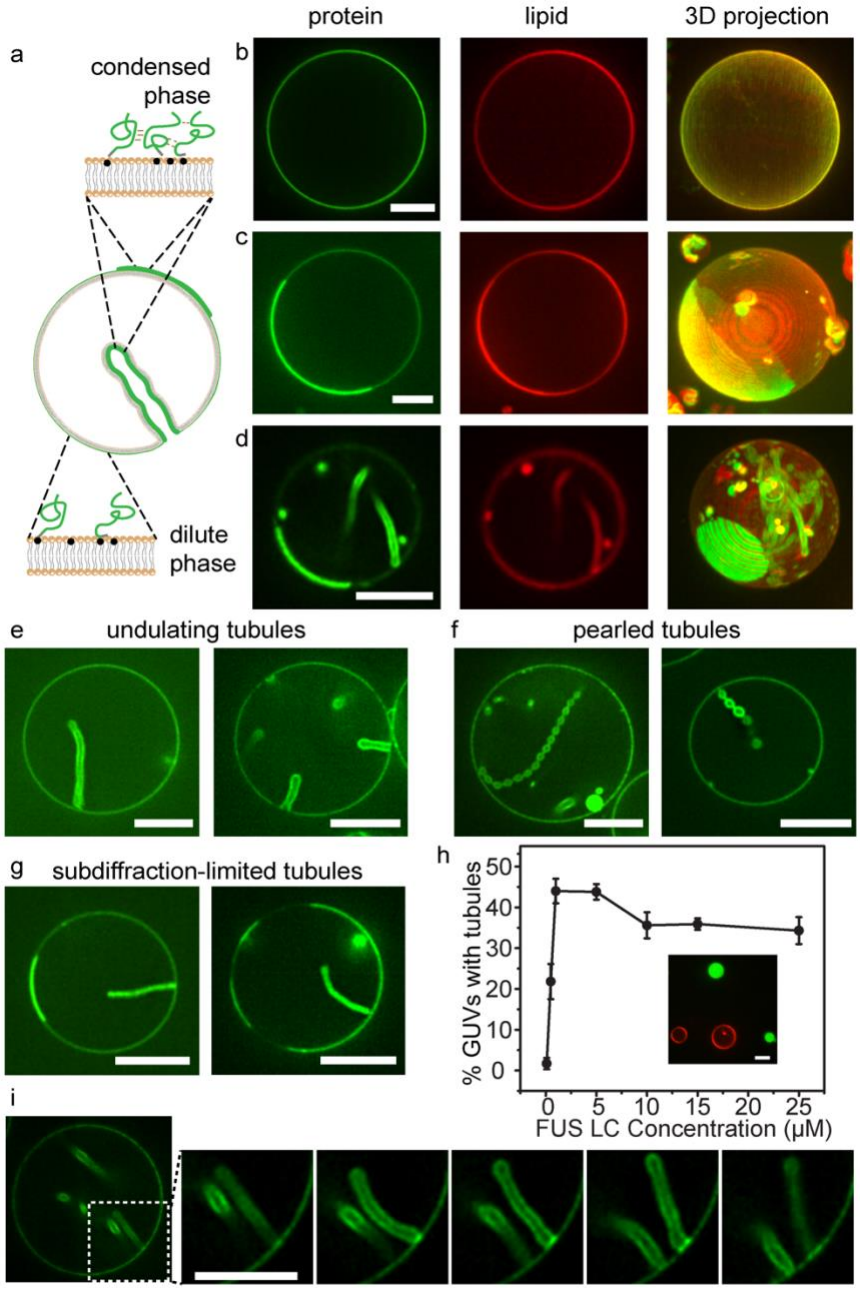

Figure 2. 1 Protein phase separation on membranes drives assembly of protein-lined tubules. (a) Pictorial representation of his-FUS LC liquid-liquid protein phase separation on GUV membranes and inward tubule formation. Green lines represent FUS LC proteins. Grey domains indicated 6×histidine tags, and the black dots indicate Ni-NTA lipids. (b-g) Representative super-resolution images of GUVs incubated with 0.5 μM (b) and 1 μM atto-488 labeled his-FUS LC (c-g) in 25 mM HEPES, 150 mM NaCl buffer, pH 7.4. (b-d)

Representative confocal images (lipid and protein channels) and corresponding maximum intensity projects of GUVs incubated with his-FUS LC. Some GUVs are covered uniformly by the protein (b), while others display 2D liquid-liquid phase separation (c), which is frequently correlated with the formation of lipid tubules (d). (e-g) Three kinds of membrane tubule structures were observed: undulating tubules (e), tubules consisting of a string of pearls (f), and sub-diffraction limited tubules, the structure of which cannot be clearly resolved (g). GUV membrane composition: 93 mol% POPC, 5 mol% Ni-NTA, 2 mol% DP-EG10 biotin and 0.1 mol% Texas Red-DHPE. (h) The fraction of GUVs displaying inward tubules as a function of his-FUS LC concentration. Data represent mean ± standard deviation; n = 3 independent experiments; N > 100 GUVs were acquired in each replicate. When the addition of his-FUS LC was greater than 5 μM, protein droplets were observed in the surrounding medium (inset in h). (i) Confocal image series illustrating dynamic fluctuations in tubule shape. All scale bars correspond to 5 μm.

Assembly of Lipid Tubules Depends on the Strength of Protein–Protein and Protein–Membrane Interactions.

The membrane tubules in Figure 2.1 appear to emerge from the protein-rich regions of the membrane surface, suggesting that they rely on self-association of membrane-bound his-FUS LC molecules. We would expect that the ability of these proteins to come together on membrane surfaces depends on both the extent of protein–membrane binding and the strength of protein–protein interactions. Therefore, the assembly of membrane tubules likely depends upon these parameters. To vary the extent of protein–membrane binding, we varied the concentration of Ni-NTA-DOGS lipids in the membrane vesicles. To vary the strength of interactions between his-FUS LC proteins, we varied the concentration of sodium chloride in the solution. This approach is based on published studies showing that the saturation concentration for liquid–liquid phase separation of FUS LC decreases as sodium chloride concentration increases, resulting in enhanced phase separation[121].

Holding the concentration of his-FUS LC constant at 1 μM, we mapped the prevalence of two-dimensional protein phase separation and lipid tubules as a function of both NaCl concentration (50 mM to 250 mM) and the concentration of Ni-NTA-DOGS lipids (2 to 15 mol%) (Figure 2.2a–d). We observed that increasing either parameter led to an increase in

both the fraction of vesicles exhibiting phase separation (Figure 2.2e and SI Appendix, Table 2.2) and the fraction of vesicles exhibiting lipid tubules (Figure 2.2f and SI Appendix, Table 2.3). Plotting the fraction of phase separated vesicles versus the fraction of vesicles with lipid tubules reveals a sharp transition to strong tubule formation when ~25% or more of the vesicles display phase separation (Figure 2.2g, Pearson's correlation coefficient, 0.8). Additionally, the brightness of the protein-rich phases and the tubules were each three to four times greater than the brightness of the protein-depleted phases (SI Appendix, Figure 2.9), further suggesting that tubules emerged from the protein-rich phase, though the accuracy may be limited by the errors associated with comparing the intensity of membrane surfaces with varying curvatures[126]. Some tubules clearly emerge from protein-rich regions (Figure 2.1g right, Figure 2.2b and d), while the majority appear to consume the protein-rich regions from which they formed (Figure 2.1e and g left), as summarized in SI Appendix, Figure 2.10. Importantly, most protein-rich phases appear to consist of a single layer of protein bound to the membrane surface, based on quantitative fluorescence analysis (SI Appendix, Figure 2.11) and poor recruitment of FUS LC proteins lacking a histidine tag to bare membranes and membranes covered by histidine-tagged FUS LC (SI Appendix, Figure 2.12 and 13). Notably, lipid phase boundaries have previously been observed to drive membrane budding[125]. However, we almost exclusively observe tubules, which have substantially higher curvature than a bud of equal surface area would have, suggesting that phase boundaries are not the primary driver of membrane curvature in the present study.

Collectively, these results demonstrate that formation of protein-lined lipid tubules is strongly correlated with phase separation of his-FUS LC on membrane surfaces. However, it remains unclear why phase separation on membrane surfaces drives the membrane to bend inward toward the lumen of the vesicle. In order to understand this phenomenon, we

developed a continuum mechanical model of membrane bending in the presence of protein phase separation.

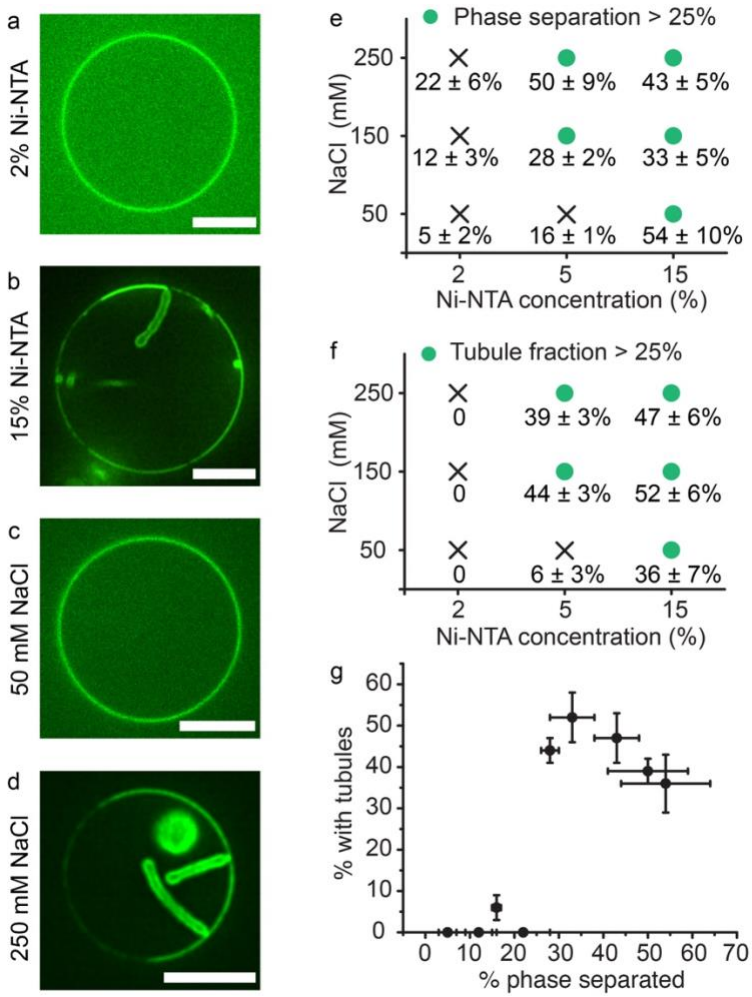

Figure 2. 2 Protein phase separation and tubule formation depend upon the concentration of membrane-bound proteins and the strength of protein-protein interactions. (a) Representative confocal images of FUS LC bound to GUVs (composition: 96 mol% POPC, 2 mol% Ni-NTA, 2 mol% DP-EG10-biotin, 0.1 mol% Texas Red-DHPE) containing 2 mol% Ni-NTA, and (b) GUVs (composition: 83 mol% POPC, 15 mol% Ni-NTA, 2 mol% DP-EG10-biotin, 0.1 mol% Texas Red-DHPE) containing 15% Ni-NTA. GUVs were incubated with 1μM Atto-488 labeled his-FUS LC in 25 mM HEPES, 150 mM NaCl pH 7.4 buffer. (c, d) Representative images of

GUVs (93 mol% POPC, 5 mol% Ni-NTA, 2 mol% DP-EG10 biotin and 0.1 mol% Texas Red-DHPE made in 560 mOsmo glucose solution) incubated with 1μM atto-488 labeled FUS LC in 25 mM HEPES pH 7.4 buffer containing (c) 50 mM and (d) 250 mM NaCl, respectively. Glucose was added to the buffers accordingly to maintain osmotic pressure balance. All scale bars represent 5 μm. (e, f) Percentage of GUVs displaying (e) protein phase separation and (f) inward lipid tubules as a function of Ni-NTA content, and NaCl concentration. Green dots indicate fractions exceeding 25%. (g) Percentage of GUVs with inward tubules as a function of percentage of GUVs with phase separation. Here the Pearson's correlation coefficient between phase separation and tubule formation was 0.8. Data are shown as mean value ± standard deviation. N > 100 GUVs were analyzed cumulatively from three independent replicates for each condition. Approximately 18 ± 1% for vesicles containing 15% Ni-NTA and exposed to 1μM FUS LC displayed both phase-separated regions and membrane tubules.

A Continuum Mechanics Model Predicts Tubule Shape and Dependence of Tubule Diameter on Membrane Bending Rigidity.

The morphologies of the tubules that we have observed can provide insights into the mechanism by which protein phase separation drives membrane bending. Some tubules consist of a well-defined "string of pearls" in which spherical shapes are separated by thin necks (Figure 2.1f). Other tubules have an undulating morphology in which the "pearls" are less well defined, with some tubules being nearly cylindrical (Figure 2.1e and 2.2b and 2d). This set of shapes—pearls, undulations, and cylinders—can be classified as Delaunay surfaces[127], which have a constant, nonzero mean curvature (Figure 2.3a). Unduloids are surfaces of revolution of an elliptic catenary[127,128]. With small changes in geometric parameters, a range of unduloid surfaces can be constructed[127] (Figure 2.3a). More importantly, Delaunay surfaces, particularly unduloids and their variants, are known to minimize the Helfrich energy for membrane bending[128]. The radius and shape of the unduloids depends on a single dimensionless parameter $\alpha = \sqrt{\frac{\lambda}{2\kappa C_0^2} + \frac{1}{4}}$, in which λ is the membrane tension, κ is the bending modulus, and C_0 is the spontaneous curvature. When $\alpha = 0.75$, the membrane resembles a cylinder and for $\alpha > 0.75$, the membrane

resembles an unduloid (Figure 2.3a).

Tubules with unduloid-like morphologies are known to arise when there is an area mismatch between the inner and outer leaflets of the lipid bilayer, such that the membrane has a finite spontaneous curvature[129]. For example, addition of lipids[74], polymers[73], and proteins[130] to the surfaces of membrane vesicles have each been shown to produce such tubules. However, in these cases, the tubules protruded outward from the membrane surfaces, as would be expected when the area of the outer leaflet exceeds that of the inner leaflet. In contrast, we observe tubules that protrude inward from the membrane surface, suggesting that protein phase separation reduces the area of the outer leaflet relative to that of the inner leaflet (Figure 2.3b).

We might expect such a reduction in area if attractive interactions between his-FUS LC peptides generates compressive forces at the membrane surface. How might these compressive forces arise? As an intrinsically disordered domain, FUS LC behaves more like a polymer than like a structured protein domain[120]. When polymers are tethered to surfaces, the density of polymer segments decreases substantially as the distance from the surface increases[36] (Figure 2.3b). If the membrane were to remain flat, this reduced density of segments would result in a reduction in interactions between the amino acids within FUS LC, as the distance from the membrane surface increased. These unsatisfied interactions create a driving force for membrane curvature. Specifically, if the membrane bends, such that protein-lined buds and tubules are formed, the density of protein segments will increase with increasing density from the membrane surface, such that some portion of the unsatisfied interactions can now be satisfied (i.e., $x > x'$ in Figure 2.3b). Another perspective on this potential mechanism comes from the work of Lipowsky[131] and Sung[132] who have examined the impact of adsorption of polymers on membrane surfaces. The assembly of FUS LC proteins at the membrane surface is analogous to adsorption of a

polymer because the network of protein–protein interactions creates a macromolecular condensate that adheres to the membrane at multiple points. Using thermodynamic arguments in combination with the principles of membrane mechanics, these authors showed that when a polymer adsorbs strongly at multiple points to the membrane surface, the membrane will bend in order to maximize contact with the polymer. This bending causes the membrane to form protein-lined structures that effectively engulf the polymer (SI Appendix, Figure 2.14). A detailed physical argument and derivation can be found in SI Appendix which shows how the adsorption of FUS LC condensates to the membrane surface could generate compressive stresses that act as an effective spontaneous curvature, driving membrane bending to form protein-lined membrane tubules with diameters that are consistent with our experimental results.

To examine the set of membrane shapes created by this mechanism, we used the Helfrich model with spontaneous curvature to simulate a compressive stress being applied to one leaflet of a lipid bilayer[75]. The area difference between the two leaflets was modeled using a locally specified spontaneous curvature for simplicity in simulations (Figure 2.3c). See SI Appendix for detailed model assumptions, derivations, and the relationship between the spontaneous curvature and the stresses in the bilayer (SI Appendix, Tables 2.5 and 2.6). The spontaneous curvature effectively represents the stresses due to the area difference between the two leaflets[133]. The governing equations were solved in an axisymmetric parametrization for ease of computation to demonstrate the principles underlying the formation of undulating and pearled tubules.

We first simulated a domain of fixed area and homogeneous bending rigidity that included the protein-enriched phase and the surrounding protein-depleted phase. Our results showed that increasing the spontaneous curvature in the protein-rich phase resulted in the formation of undulating tubules (Figure 2.3d) similar to those observed in

experiments (Figure 2.1). Furthermore, the simulations predicted that the tubule diameter would increase linearly in proportion to the square root of the bending modulus (Figure 2.3e). The bending energy corresponding to the formation of the undulating and pearled tubules is shown in SI Appendix, Figure 2.15. Notably, similar morphologies will arise anytime the membrane has a sufficient isotropic spontaneous curvature[73,74].

It is likely that the protein-enriched phase has an increased bending rigidity compared to the protein-depleted phase, owing to the higher density of protein contacts. Therefore, we next asked if the ratio of bending rigidities in the attached protein layer and the underlying membrane layer could impact the shapes of the tubules. We defined the ratio of bending rigidities, $\kappa_{ratio} = \frac{\kappa_{protein}}{\kappa_{membrane}}$, and varied the ratio in the range of 1 to 20, in which $\kappa_{ratio} = 1$ denotes uniform bending rigidity. With increasing κ_{ratio}, we observed that the tubules took on a more clearly defined pearled morphology (Figure 2.3f and 2.3g and SI Appendix, Figure 2.16) similar to those observed in some of our experiments (Figure 2.1f). We next sought to test these predictions.

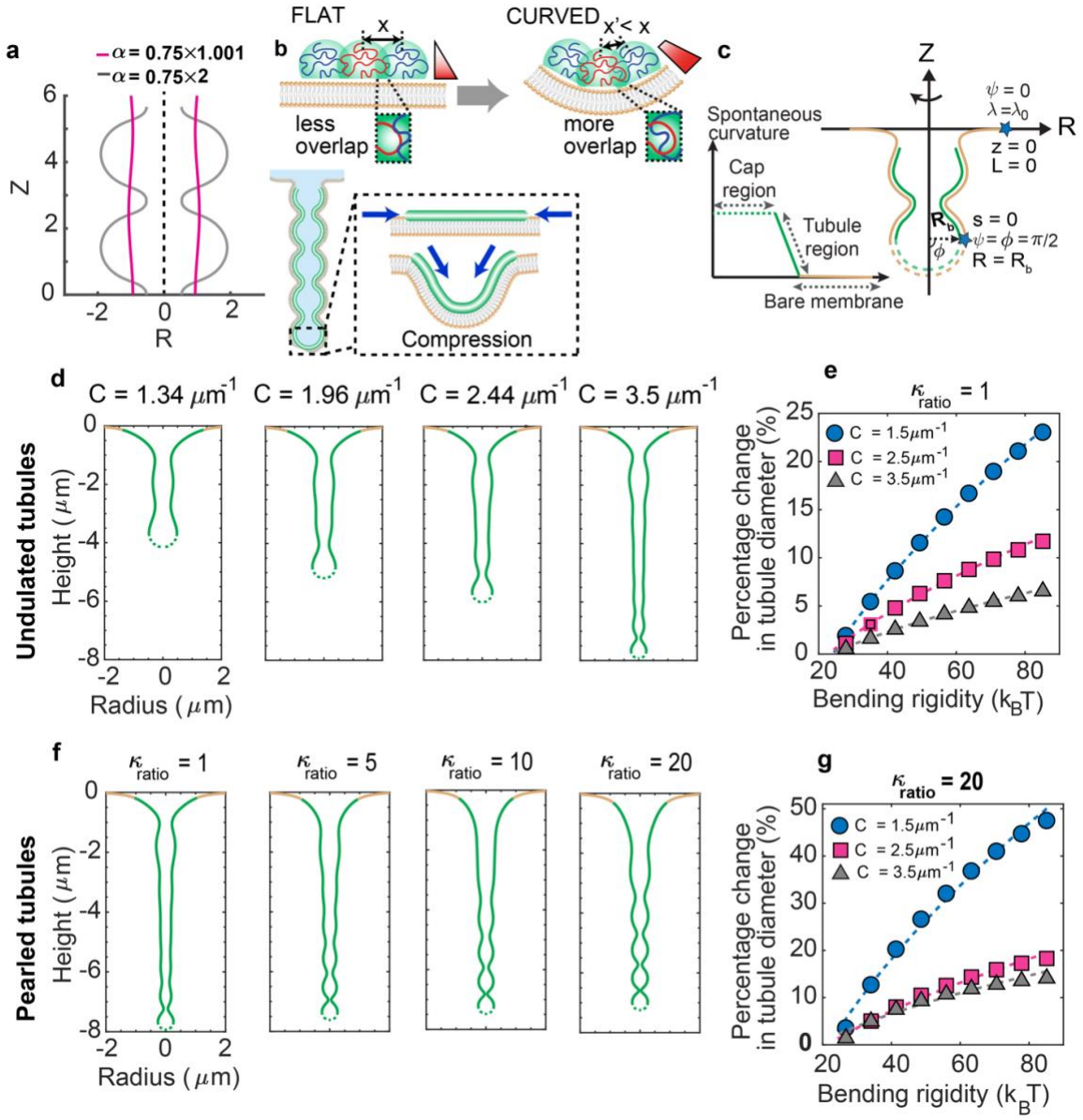

Figure 2. 3 Mechanical model of undulating and pearled tubule formation. (a) Unduloid-like shapes solution for Helfrich energy minimization at different values of non-dimensional parameter, α. For α~ 0.75, the membrane takes on a cylindrical shape (purple line); for α> 0.75, the unduloid becomes a sphere similar to a string of pearls (gray line). (b) Schematic depiction of membrane tubule formation due to the compressive stresses applied by liquid-liquid phase separation on the membrane. On a flat membrane, the density of protein segments decreases with increasing distance from the membrane surface, such that x is greater than x'. Therefore, if the membrane remains flat, there will be an increasing number of unsatisfied potential protein-protein

interactions as distance from the surface increases. These unsatisfied interactions create a driving force for membrane bending, which increases the density of protein segments at a distance from the membrane (x'<x), leading to more overlap among the proteins and stronger protein-protein interactions. (c) Schematic of the axisymmetric simulations depicting the simulation domain and the boundary conditions. The yellow region represents the bare membrane and the green region is the area coated by the proteins. The dashed lines indicate the cap of the tubule, assumed to have a constant curvature. The inset shows the spontaneous curvature distribution along the tubule region used to model the membrane shape. (d) Undulating tubules minimize the membrane bending energy as the spontaneous curvature increases for uniform bending rigidity of the membrane (κ = 80 k_BT). (e) Percentage of change in the tubule diameter ((D-$D_{\kappa = 25\ kBT}$)/$D_{\kappa = 25\ kBT}$) as a function of the bending rigidity for three different values of spontaneous curvature. The dashed lines show a square root dependence on the bending modulus by fitting to the curve () where for the gray line A=5.4, B=-26.44; for the pink line A= 2.71, B=-12.9; and for the blue line, A=1.53 and B=-7.4. (f) Pearled tubules minimize the bending energy of the membrane for heterogeneous membrane rigidity (κ_{ratio}= $\kappa_{protein\text{-}domain}/\kappa_{bare\ membrane}$), C_0 = 3.5 $\boldsymbol{\mu}m^{-1}$. (g) Percentage of change in the tubule diameter ((D-$D_{\kappa = 25\ kBT}$)/$D_{\kappa = 25\ kBT}$) as a function of the bending rigidity for three different values of spontaneous curvature for κ_{ratio}= 20 . The dashed lines are the fitted curve ($A\sqrt{\kappa} + B$) where for the gray line; A=10.98, B=-51.31, for the pink line; A= 4.22, B=-19.58, and for the blue line; A=3.1 and B=-13.

Tubule Diameter Varies with Membrane Bending Rigidity and Salt Concentration.

The continuum model predicted that the radii of the tubules should increase in proportion to the square root of the membrane bending rigidity. To examine this prediction, we measured the diameters of the resolvable lipid tubules formed by assembly of his-FUS LC on membrane surfaces as a function of membrane bending rigidity (Figure 2.4a–e and SI Appendix, Table 2.4). Here the bending rigidity of vesicles having each membrane composition was estimated based on published values for similar compositions, as noted in SI Appendix, Table 2.1. As membrane bending rigidity was increased from ~20 k_BT to ~76 k_BT, through variations in membrane lipid composition, we observed a substantial increase in membrane tubule diameter from 240 ± 100 nm (SD) to 400 ± 190 nm (SD)

(Figure 2.4e). For each lipid composition, tubules with both pearled and undulating morphologies were observed (Figure 2.4a–d). Notably, the exact lipid composition and membrane tension likely vary somewhat between vesicles within the same preparation. These differences likely contribute to the variability of tubule diameter, frequency, and morphology. Nonetheless, the data were reasonably well fit by a curve in which tubule diameter was proportional to the square root of bending rigidity, in agreement with the predictions of the simulation (compare Figure 2.4f and 2.3e and 3g). Here, optical reassignment during spinning disk confocal microscopy, followed by deconvolution, was used to increase the optical resolution to better than 150 nm[134].

A second prediction from our simulation is that the tubule diameter should increase as the rigidity of the protein-rich phase increases while the rigidity of the underlying membrane is held constant. To test this prediction, we examined the impact of sodium chloride concentration on tubule diameter. Increasing sodium chloride concentration has been previously shown to increase the strength of interactions between FUS LC molecules in condensed phases[120]. Therefore, we inferred that his-FUS LC might assemble into a more rigid protein layer at high salt concentration.

As the sodium chloride concentration increased from 50 mM to 250 mM, we observed an increase in tubule diameter of ~75%, from 240 ± 120 nm to 420 ± 280 nm (SD), in qualitative agreement with simulation results (compare Figure 2.4g with Figure 2.3g). Similarly, increasing either the concentration of histidine-binding lipids or the concentration of his-FUS LC in solution drove a significant increase in tubule diameter (SI Appendix, Figure 2.17). One interpretation is that these perturbations result in a greater density of proteins being recruited to the membrane surface, resulting in a more rigid protein layer, which is predicted by the model to increase tubule diameter (Figure 2.3g).

Further, the incidence of tightly pearled tubules increased significantly as NaCl concentration increased from 50 mM to 250 mM, in agreement with simulations (Figure 2.4h). A second means of increasing the ratio of protein to lipid rigidity is to decrease the rigidity of the lipids, which similarly resulted in an increase in the fraction of pearled tubules (SI Appendix, Figure 2.18). Notably, phase separation and formation of protein-lined tubules increased with increasing glutamine content of the FUS LC domain (SI Appendix, Figure 2.19) consistent with previous work on the importance of glutamine to phase separation of FUS LC into three-dimensional droplets[121]. Collectively, these data suggest that protein phase separation applies a compressive stress to the membrane surface, resulting in assembly of protein tubules directed inward from the membrane surface.

Notably, tubules formed by protein phase separation generally have larger diameters in comparison to tubules formed by rigid protein scaffolds such as BAR domains[135]. Additionally, the pearled and unduloid morphologies of tubules formed by phase separation are in contrast to those of tubules formed by rigid scaffolds, which generally have cylindrical morphologies of constant diameter[135]. Our simulation generates cylindrical morphologies only when we assume that the protein applies an anisotropic (deviatoric) curvature, as is the case for BAR domain scaffolds (SI Appendix, Figure 2.20). Therefore, the pearled and undulating morphologies of tubules observed in the current work suggest that protein phase separation drives membrane bending through a physical mechanism that is distinct from the mechanisms that rigid scaffolds use to deform membranes. However, we acknowledge that several unknowns, including the strength of protein–protein and protein–membrane interactions, the rigidity of the protein layer, and the magnitude of the compressive stresses produced by these interactions, limit our ability to describe this phenomenon in mechanistic detail at present.

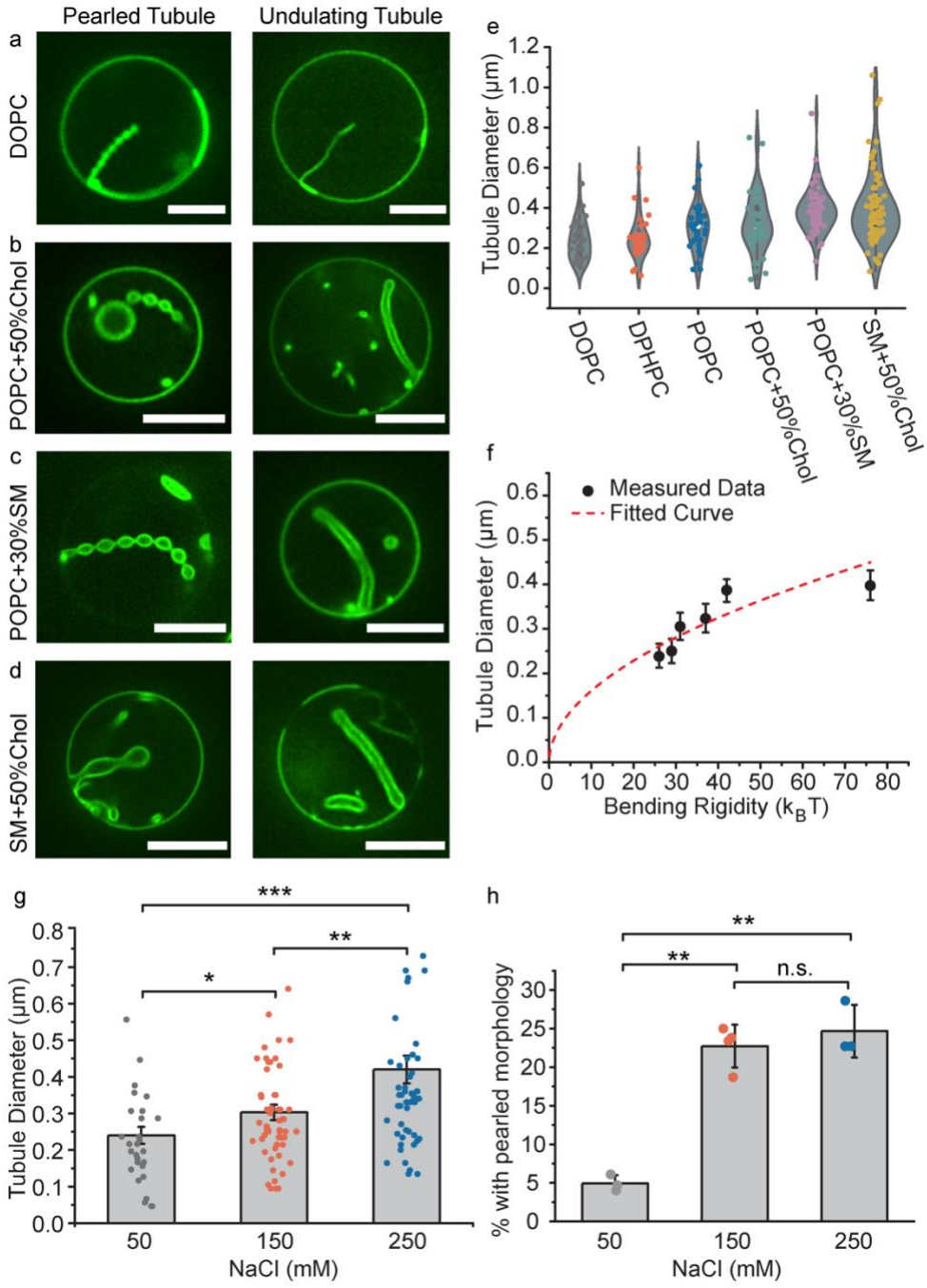

Figure 2. 4 Tubule diameter varies with membrane bending rigidity and salt concentration. (**a-f**) Six groups of GUVs with different compositions (listed in SI Appendix, Table S4 and SI Appendix, Materials and Methods) were used to vary membrane bending rigidity. GUVs were incubated with 1 μM atto-488–labeled his-FUS

LC in 25 mM HEPES, 150 mM NaCl, pH 7.4 buffer. (**a-d**) Representative super-resolution confocal images tubules with pearled (left) and undulating morphologies (right), from GUVs consisting primarily of (**a**) DOPC, (**b**) POPC + 50% Chol, (**c**) POPC + 30% SM, and (**d**) SM + 50% Chol. All scale bars are 5 μm. (**e)** Violin plot showing the measured tubule diameter distribution for tubules formed using each GUV composition. (**f)** GUV tubule diameter as a function of membrane bending rigidity. Data points from left to right represent DOPC, DPHPC, POPC, POPC + 50% Chol, POPC + 30% SM, and SM + 50% Chol, respectively. Data are displayed as mean ± standard error from at least 60 tubules per composition, gathered during 3 independent experiments. The measured tubule diameters increase roughly as the square root of membrane bending rigidity (red dash line, $R^2 = 0.64$). (**g**) Bar chart displaying average tubule diameter under different NaCl concentrations. GUVs (composition: 83 mol% POPC, 15 mol% Ni-NTA, 2 mol% DP-EG10-biotin and 0.1% Texas Red-DHPE) were incubated with 1μM atto-488 labeled his-FUS LC in 25 mM HEPES, pH 7.4 buffer with corresponding NaCl concentration under iso-osmotic conditions. Error bars correspond to standard error. Each point is a mean value of diameters measured at three positions along the same tubule. N > 100 GUVs were acquired cumulatively from three independent replicates for each condition. (**h**) Fraction of tubules that displayed a pearled morphology as a function of NaCl concentration Data are displayed as mean ± standard deviation from three independent experiments (n = 3) on separate preparations of vesicles, with cumulatively N > 100 vesicles categorized. Brackets show statistically significant comparisons using an unpaired, 2-tailed student's t test. * represents $p < 0.05$, ** represents $p < 0.01$, *** represents $p < 0.001$, and n.s. indicates a difference that was not statistically significant.

Membrane Bending by Protein Phase Separation Is a General Phenomenon that Can Be Driven by Diverse Protein Domains.

The model we have developed does not take into account the specific amino acid sequence of the FUS LC domain or the particular types of molecular interactions that drive the protein to phase separate. Instead, we have described tubule formation as a general process that could arise whenever protein phase separation occurs at the membrane surface. Therefore, we next asked whether the ability to drive lipid tubule formation is specific to FUS LC or whether it is a general property of membrane-bound domains that undergo liquid–liquid phase separation. To address this question, we evaluated two additional domains known to be involved in liquid–liquid phase separation, the low-complexity

domain of hnRNPA2 (hnRNPA2 LC), a protein involved in RNA processing and transport granule formation[122], and the RGG domain of LAF-1 (LAF-1 RGG), a DDX3 RNA helicase found in *Caenorhabditis elegans* P granules[123]. Both proteins contained N-terminal histidine tags, which we used to bring them to the membrane surface, as we did with FUS LC (Figure 2.5).

Similar to FUS LC, hnRNPA2 LC is a prion-like domain composed primarily of polar and aromatic residues. It contains relatively few aliphatic residues and is depleted in charged residues[122]. Both FUS LC and hnRNPA2 LC have an increased propensity to undergo liquid–liquid phase separation as the ionic strength of the surrounding medium increases[120,122]. Based on these similarities, we might expect hnRNAPA2 LC and FUS LC to have similar interactions at the membrane surface and therefore to behave similarly in our assays. As expected, when hnRNPA2 LC was added to giant vesicles at a concentration of 1 μM, inwardly directed lipid tubules with undulating and pearled morphologies were observed (Figure 2.5a). Further, the distribution of tubule diameters was similar between hnRNPA2 LC and FUS LC (Figure 2.5b and 5c).

In contrast to hnRNPA2 LC and FUS LC, LAF-1 RGG is dense in charged residues such as arginine and aspartic acid[123]. In this way, increasing the ionic strength of the surrounding medium opposes liquid–liquid phase separation of LAF-1 RGG[123], suggesting that the dominant driving force for liquid–liquid phase separation is electrostatic attraction between oppositely charged residues. To examine the impact of these differences on the formation of membrane tubules, we added 1 μM of LAF-1 RGG to giant vesicles. Interestingly, we observed inwardly directed lipid tubules, which were similar to those formed by FUS LC and hnRNPA2 LC (Figure 2.5d). The diameters of tubules formed by the three proteins covered approximately the same range, though tubules formed by LAF-1 RGG had a somewhat smaller average diameter (Figure 2.5e). Importantly, the fraction

of giant vesicles that displayed lipid tubules upon exposure to LAF-1 RGG decreased with increasing salt concentration. This trend, which is the opposite of what we observed for FUS LC (Figure 2.5f), is expected owing to the ability of high ionic strength solutions to screen the electrostatic interactions that support liquid–liquid phase separation of LAF-1 RGG[123]. Notably, changes in the salt concentration may also impact membrane bending rigidity[136]. However, the opposite impact of increased salt concentration in FUS LC and LAF-1 RGG experiments indicates that the dominant effect of salt concentration is on protein phase separation, not on membrane bending rigidity. Additionally, the diameter of lipid tubules formed by exposure to LAF-1 RGG increased with increasing membrane bending rigidity (SI Appendix, Figure 2.21) while the fraction of pearled tubules decreased (SI Appendix, Figure 2.18b), in agreement with our findings for tubules formed by exposure to FUS LC (Figure 2.4f and SI Appendix, Figure 2.18a).

Collectively, these results demonstrate that the ability of liquid–liquid phase separation at membrane surfaces to drive inward membrane protrusions is a general phenomenon that is not dependent on the specific molecular interactions that drive each protein to phase separate. Instead, liquid–liquid phase separation itself, rather than a particular pattern of electrostatic or hydrophobic interactions between proteins and lipids, appears to be responsible for generating the compressive stress that drives membrane deformation.

Notably, none of the proteins examined in this work are expected to insert into the membrane surface. Indeed, FUS LC did not bind measurably to membranes when its histidine tag was cleaved (SI Appendix, Figure 2.12), suggesting that insertion into the membrane is very weak, if it exists. However, proteins that insert into membranes are common and often result in outward membrane bending[137,138]. Such insertions, if coupled to domains that drive liquid–liquid phase separation, could work against the impact of

liquid–liquid phase separation on membrane curvature.

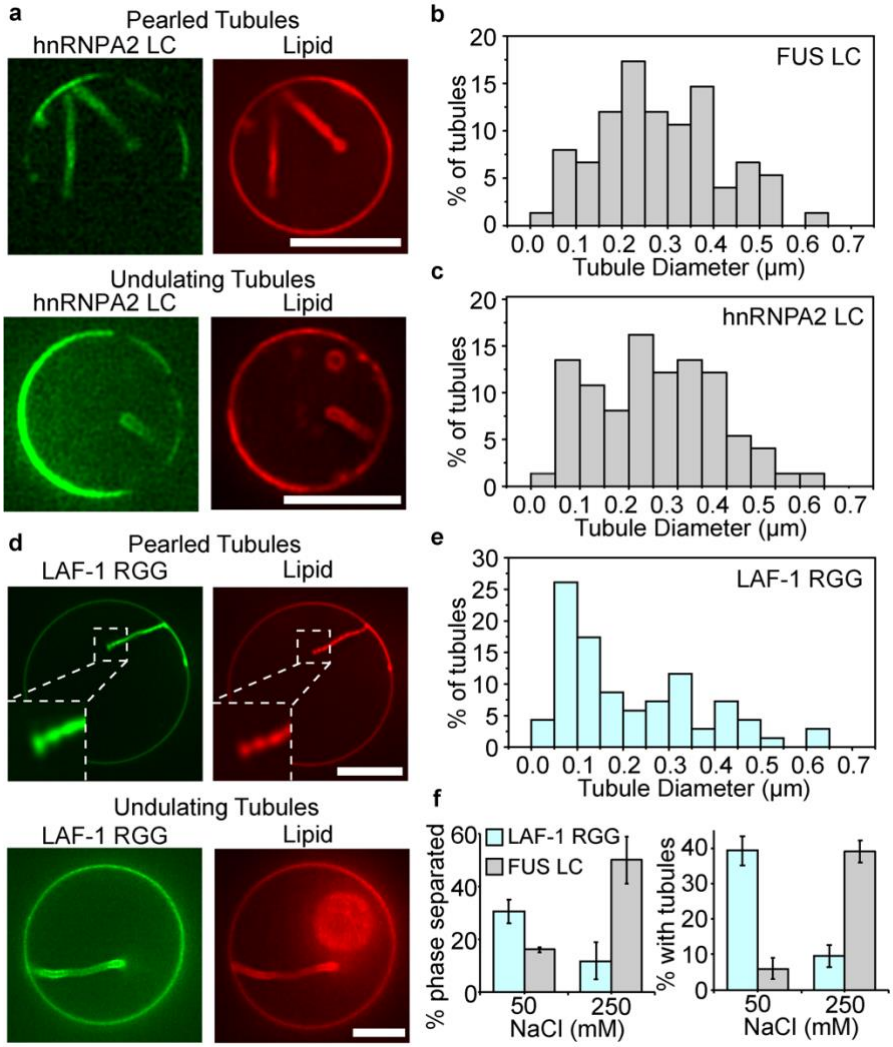

Figure 2. 5 hnRNPA2 LC and LAF-1 RGG domains drive formation of inwardly directed membrane tubules with similar morphologies to those formed by FUS LC. (**a**) his-hnRNPA2 LC at a concentration of 1 μM drove formation of inwardly directed tubules with pearled and undulating morphologies when introduced to GUVs consisting of 83 mol% POPC, 15 mol% Ni-NTA, 2 mol% DP-EG10 biotin and 0.1 mol% Texas Red-DHPE. (**b**) Distribution of tubule diameters formed upon exposure of GUVs to his-FUS LC, 75 total tubules. (**c**) Distribution of tubule diameters form upon exposure of GUVs to his-hnRNPA2 LC, 75 total tubules. (**d**) his-Laf-1 RGG at a concentration of 1 μM drove

formation of inwardly directed tubules with pearled and undulating morphologies when introduced to GUVs of the same composition as in a. (**e**) Distribution of tubule diameters formed upon exposure of GUVs to his-LAF-1 RGG, 70 total tubules. (**f**) The fraction of vesicles exhibiting two-dimensional protein phase separation and tubule formation by his-LAF-1 RGG decreased with increasing salt concentration. This is the opposite trend of that observed for vesicles exposed to his-FUS LC, data repeated from Figure 2e, f, for comparison. Error bars represent standard deviation of 3 trials, with cumulatively N > 300 GUVs analyzed. The scale bar in a, d is 5 μm.

Protein Phase Separation Drives Tubule Formation from Cell-Derived Membranes.

We next asked whether protein phase separation at membrane surfaces is sufficient to drive remodeling of cellular membranes. To address this question, we derived membrane vesicles from the plasma membranes of mammalian retinal pigmented epithelial (RPE) cells. To facilitate binding of FUS LC to the surfaces of these vesicles, we engineered the donor cells to express a chimeric transmembrane protein that consisted of the transmembrane domain of the transferrin receptor, fused to an extracellular blue fluorescing protein (BFP) domain for visualization. This chimera displayed a nanobody against GFP on the cell surface (Figure 2.6a and 6b). Membrane blebs extracted from these cells also displayed the nanobody on their surfaces, which facilitated the recruitment of GFP-tagged proteins (Figure 2.6a and 6b). Adding soluble GFP domains to the solution surrounding these blebs resulted in GFP being strongly concentrated at the bleb surfaces (Figure 2.6c). Notably, the GFP signal appeared to separate into brighter and dimmer regions on the surfaces of some of the blebs. This separation within blebs has been observed previously[139] and is thought to arise from lipid phase separation in which the transferrin receptor transmembrane domain is known to prefer the liquid disordered membrane phase[140].

When a GFP-tagged version of FUS LC, GFP-FUS LC[141], was introduced to blebs taken from the same donor cells, the GFP signal was similarly concentrated at the bleb surfaces (Figure 2.6d). However, the surfaces of blebs exposed to GFP-FUS LC did not remain flat. Instead, regions of the bleb surfaces with intense GFP signal bent inward, creating protein-lined membrane buds and tubules. Many of the tubules had pearl-like and undulating morphologies, similar to tubules formed by exposure of synthetic vesicles to his-FUS LC (compare Figure 2.1 and 2.6d). The diameter of the tubules ranged broadly from 150 nm to more than 1 μm (Figure 2.6e). Here, the average tubule diameter, 570 ± 260 nm (SD), was somewhat larger than that of tubules formed from synthetic membranes. This difference could arise from the enhanced bending rigidity of cell-derived membranes which contain a high density of transmembrane proteins. Alternatively, the GFP-FUS LC protein, which has been observed to form gel-like assemblies in solution[141,142], may increase the rigidity of the protein layer. Nonetheless, the range of curvatures observed in these cell-derived vesicles encompasses that of many cellular structures including filopodia, dendritic spines, phagosomes, and many organelles[43]. These results demonstrate that liquid–liquid phase separation of membrane-bound proteins is sufficient to deform complex, cell-derived membranes. Additionally, because these experiments use an antibody–antigen interaction to bring FUS LC to the membrane surface, rather than a histidine tag, these results show that histidine–lipid interactions are not required for membrane bending by liquid–liquid phase separation. Building on these findings, future work could examine the ability of protein phase separation to drive membrane remodeling in live cells, using either natural or engineered proteins.

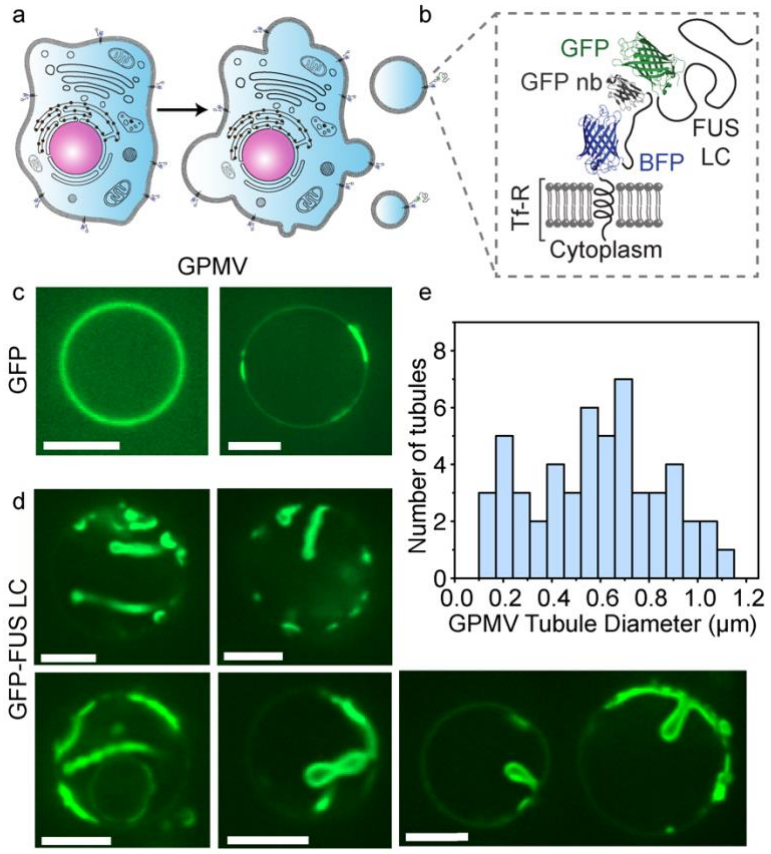

Figure 2. 6 Protein phase separation can drive tubule formation from cell-derived membranes. (**a**) Cartoon showing extraction of GPMVs from donor RPE cells. (**b**) Schematic of the architecture of the membrane receptor and ligand protein. GFP-FUS LC is recruited to the GPMV membrane by binding to a GFP nanobody displayed on the cell surface. (**c**) Confocal images of GPMVs incubated with 2 μM GFP and (D) GFP-FUS LC in buffer containing 10 mM HEPES, 2 mM $CaCl_2$, 150 mM NaCl, pH 7.4. (Scale bar, 5 μm.) (**e**) Distribution of diameters of tubules formed from GPMVs. n = 50 tubules measured.

DISCUSSION

Here, we demonstrate that protein phase separation at membrane surfaces can drive the assembly of protein-lined membrane tubules of physiologically relevant dimensions. This mechanism appears to be physically distinct from membrane bending by solid

scaffolds which include the rigid, tubular assemblies of BAR domains, dynamin, and shiga toxin as well as the cage-like geometries of protein coats formed by clathrin, COPII, and many viral capsids[52,143-145]. In contrast, we show that a family of model proteins that form liquid-like assemblies can drive the formation of membrane tubules with dynamic cylindrical and unduloid morphologies (Figure 2.1 and Movie 2.1). These results illustrate that increasing the spontaneous curvature of a membrane, which is the fundamental requirement for membrane bending[111,146-149], is not exclusive to structured scaffolds but can also arise from liquid-like protein interactions that generate stresses at membrane surfaces. Using this liquid scaffolding mechanism, cytosolic proteins that phase separate at membrane surfaces could contribute to outward membrane protrusions such as filopodia, dendritic spines, viral buds, and cilia. In contrast, proteins and receptors that assemble into liquid scaffolds on the outer cell surface could contribute to structures that bud into the cell, such as endocytic vesicles.

The inward tubule formation observed here in response to liquid–liquid phase separation is in direct contrast to the outwardly protruding tubules generated by repulsive interactions among self-avoiding disordered domains found in endocytic proteins[63,115]. These two sets of observations can be understood as two extremes of the same mechanism. Specifically, the membrane protein composite can be thought as two layers of a two-dimensional fluid, one layer consisting of lipids and the other consisting of proteins. Many studies have shown that lipid bilayers can only be stretched or compressed by a few percent[150,151]. In contrast, the protein layer is capable of dramatic changes in density. When self-avoiding domains become crowded on the membrane surface, they push each other apart. As the protein layer expands, the nearly inextensible lipid bilayer is forced to bend outward. In contrast, when self-interacting proteins undergo liquid–liquid phase separation on the membrane surface, the protein layer contracts, forcing the nearly incompressible

lipid bilayer to bend inward. Similar behavior has been observed in simplified models of biological tissues such as intestine[152] and brain[153], in which tissues fold owing to the differential compressibility of adjacent two-dimensional layers[154], suggesting a common mechanism in soft matter. While structured protein scaffolds are known to induce anisotropic spontaneous curvature, liquid-like scaffolds arising from assembly of disordered proteins are likely to induce isotropic spontaneous curvature. Notably, the formation of tubules and pearls due to anisotropic protein curvatures have been studied extensively using mechanical models[155-158].

What advantage might a liquid scaffold offer for membrane remodeling? We speculate that the lower energy barriers to assembly and disassembly associated with a liquid may allow the membrane greater freedom to deform into a variety of shapes and dimensions rather than the more narrowly defined set of geometries observed for most structured scaffolds. Indeed, many curved membrane structures, from cytoskeletal protrusions[159] to the endoplasmic reticulum[160], are known to have heterogenous and dynamic morphologies. In particular, the unduloid morphology reported here has been observed in the endosomal networks of plants[161]. In light of the ongoing discovery of liquid-like behavior in many membrane-bound protein networks[162], the ability of protein phase separation to shape membranes has the potential to impact membrane-associated processes throughout the cell.

ACKNOWLEDGMENTS

This research was supported by the NIH through Grants R01GM120549 and R35GM139531 (J.C.S.), R01GM132106 (P.R.), R01GM118530 (N.L.F.), R01NS116176 (N.L.F.), F32GM133138 (K.J.D.), NSF1845734 (N.L.F.), the Human Frontier Science

Program RGP0045/2018 (N.L.F.), and by the Welch Foundation F-2047 (J.C.S.). The plasmid DNA for GFP FUS LC was provided by the laboratory of S. McKnight, University of Texas Southwestern Medical Center.

MATERIALS AND METHODS

Reagents

1,2-dioleoyl-sn-glycero-3-phosphocholine (DOPC), 1,2-diphytanoyl-sn-glycero-3-phosphocholine (DPHPC), 1-palmitoyl-2-oleoyl-glycero-3-phosphocholine (POPC), Sphingomyelin (Brain, Porcine), cholesterol and 1,2-dioleoyl-sn-glycero-3-[(N-(5-amino-1-carboxypentyl)iminodiacetic acid)succinyl] (nickel salt) (DOGS-NTA-Ni), were purchased from Avanti Polar Lipids, Inc. NaCl, Tris hydrochloride (TrisHCl), 4-(2-hydroxyethyl)-1-piperazineethanesulfonic acid (HEPES), neutravidin, Texas Red-DHPE, isopropyl-β-D-thiogalactopyranoside (IPTG), β-mercaptoethanol (β-ME), BODIPY™ TR Ceramide and Triton X-100 were obtained from Thermo Fisher Scientific. 2-(N-Morpholino) ethanesulfonic acid hydrate, 4-Morpholineethanesulfonic acid (MES hydrate), 3-(Cyclohexylamino)-1-propanesulfonic acid (CAPS), Urea, NaH2PO4, Na2HPO4, Na3PO4, sodium tetraborate, Ethylenediaminetetraacetic acid (EDTA), phenylmethanesulfonyl fluoride (PMSF), EDTA-free protease inhibitor tablets, imidazole, poly-L-lysine (PLL), ATTO-594 NHS-ester, and ATTO-488 NHS-ester were purchased from Sigma-Aldrich. Dipalmitoyl-decaethylene glycol-biotin (DP-EG10-biotin) was kindly provided by Darryl Sasaki from Sandia National Laboratories[163]. Amine reactive PEG (mPEG-Succinimidyl Valerate MW 5000) and PEG-biotin (Biotin-PEG SVA, MW 5000) were purchased from Laysan Bio, Inc. Fetal bovine serum (FBS), trypsin, penicillin, streptomycin, L-glutamine, phosphate-buffered saline (PBS), Ham's F-12, Ham's F-12

without phenol red, Dulbecco's modified Eagle medium (DMEM) and DMEM without phenol red were purchased from GE Healthcare. N-ethylmalemide (NEM) was purchased from Bio Basic. All reagents were used without further purification.

Plasmids

The pRP1B FUS 1-163 plasmid for FUS LC (residues 1-163) protein incorporating a TEV cleavable N-terminal hexahistidine tag was a gift from Nicolas Fawzi Lab, Brown University[121]. This plasmid is available from AddGene (https://www.addgene.org/127192/). The plasmid for expression of GFP-FUS LC (residues 2-214) was generously provided by the lab of Steven McKnight at the University of Texas Southwestern Medical Center[141]. The pRSET vector coding for the nondimerizable hexa-his-tagged eGFP (hisGFP A206K) was kindly shared by Dr. Adam Arkin (University of California, Berkeley). The plasmids for QQ4xSS#1 and S12xQ are available from AddGene (https://www.addgene.org/127194/ , and https://www.addgene.org/127193/ , respectively). The plasmids for hnRNPA2 LC and LAF-1 RGG domain were also obtained from AddGene (https://www.addgene.org/98657/ (Fawzi laboratories) and http://www.addgene.org/124929/ (Good, Hammer, and Schuster laboratories), respectively). The plasmid for mammalian expression of TfR-Δecto-BFP-HA-GFPnb was generated by inserting a hemagglutinin (HA)-tag into the TfR-Δecto-BFP-GFPnb plasmid previously described[164]. First, the GFPnb sequence from this original plasmid was amplified by polymerase chain reaction (PCR) using primers that introduced the HA-tag sequence. The amplified HA-GFPnb sequence was then restriction cloned back into the original plasmid using NotI sites. All constructs were confirmed by DNA sequencing. Notably, the HA tag was included for screening purposes and did not play a functional role in the present study.

Production of stable cell line and cell culture

Human retinal pigmented epithelial (RPE) cells (ARPE-19) were purchased from American Type Culture Collection (Manassas, VA). RPE cells were stably transfected with the plasmid encoding TfR-Δecto-BFP-HA-GFPnb via lentiviral transfection. The TfR-Δecto-BFP-HA-GFPnb plasmid described above was subcloned onto the pLJM1 viral transfer vector (AddGene 19319). To generate lentiviruses, human embryonic kidney (HEK) 293T cells (ATCC) were co-transfected with the transfer plasmid, packaging plasmid Δ8.9, and the envelope plasmid VSVG using FuGENE transfection reagent (Promega). The transfected HEK 293T cells were incubated at 37ºC for 48 hours, after which the virus-containing media was collected and filtered through a 0.45 μm average pore sized filter. For transduction, the filtered virus was then added to RPE cells with 8 μg/mL Polybrene. The transduced RPE cells were selected with 2 μg/mL puromycin for 7 days, before cell sorting was performed by flow cytometry to select for cells containing BFP fluorescence. After selection, these cells were cultured in 1:1 F12:DMEM supplemented with 10% FBS, 20 mM HEPES, and 1% penicillin, 1% streptomycin, 1% L-glutamine (PSLG). Cells were incubated at 37 °C with 5% CO2 and passaged every 48−72 hours.

Protein expression and purification

Expression and purification of his-FUS LC was carried out according to previous report[120], with several modifications. In brief, his-FUS LC was overexpressed in E. Coli BL21(DE3) cells. Pellets of cells expressing his-FUS LC were harvested from 1 liter cultures induced with 1 mM IPTG after 4-hour incubation at 37°C and 220 RPM when OD 600 was around 0.8. The pellets were then lysed in a buffer containing 0.5 M TrisHCl pH 8, 5 mM EDTA, 5% glycerol, 10mM β-ME, 1mM PMSF, 1% Triton X-100 and one

EDTA-free protease inhibitor tablet (Sigma Aldrich) for 5 min on ice and then sonicated. The cell lysates were centrifuged at 40,000 RPM for 40 min and his-FUS LC resided in the insoluble fraction after centrifugation. Therefore, the insoluble fraction was resuspended in 8M urea, 20 mM NaPi pH 7.4, 300 mM NaCl and 10 mM imidazole. The resuspended sample was then centrifuged at 40,000 RPM for 40 min. In denaturing conditions, his-FUS LC is urea-soluble and so at this point resided in the supernatant. This supernatant was then mixed with Ni-NTA resin (G Biosciences, USA) for 1 hour at 4°C. The Ni-NTA resin was settled in a glass column and washed with the above solubilizing buffer. The bound proteins were eluted from the Ni-NTA resin with a buffer containing 8M urea, 20 mM NaPi pH 7.4, 300 mM NaCl and 500 mM imidazole. Unlike previous described applications, the TEV-cleavable his-tag of this protein was not removed, as it was needed for membrane binding. The purified proteins were then buffer-exchanged into 20 mM CAPS pH 11 storage buffer using 3K Amicon Ultra centrifugal filters (Millipore, USA). Small aliquots of the protein were frozen in liquid nitrogen at a protein concentration of approximately 1 mM. FUS LC mutants QQ4xSS#1 and S12xQ were purified following the same protocol as described above. For non-his FUS LC, purified his-FUS LC was cleaved by TEV protease and further purified to leave FUS LC with no remaining tags.

His-hnRNPA2 LC purification was performed as described previously[122]. When expressed in bacteria, his-hnRNPA2 LC is found in inclusion bodies. The expression and purification protocol for his-hnRNPA2 is the same as the protocol for purifying his-FUS LC, except that his-hnRNPA2 LC was finally exchanged into the storage buffer containing 20 mM MES, 8 M Urea pH 5.5.

Expression and purification of his-LAF-1 RGG was performed as described previously[165]. Briefly, his-LAF-1 RGG was overexpressed in E. Coli BL21(DE3) cells. Pellets of cells expressing his-FUS LC were harvested from 1 liter cultures induced with

0.5 mM IPTG after overnight incubation at 18°C and 220 RPM when OD 600 was around 0.8. The pellets were then lysed in a buffer containing 20 mM Tris, 500mM NaCl, 20 mM imidazole, and one EDTA-free protease inhibitor tablet (Sigma Aldrich) for 5 min on ice and then sonicated. The cell lysates were centrifuged at 40,000 RPM for 40 min and his-LAF-1 RGG was in the lysate after centrifugation. The lysate was then mixed with Ni-NTA resin (G Biosciences, USA) for 1 hour. The Ni-NTA resin was settled in a glass column and washed with a buffer containing 20mM Tris, 500 mM NaCl, 20 mM imidazole, at pH 7.5. The bound proteins were eluted from the Ni-NTA resin with a buffer containing 20 mM Tris, 500 mM NaCl, 500 mM imidazole, at pH 7.5. The purified proteins were then buffer-exchanged into a buffer containing 20mM Tris, 500mM NaCl, at pH 7.5. Small aliquots of the protein were frozen in liquid nitrogen at a protein concentration of approximately 120 μM and stored at -80 °C. To promote solubility of the protein, the entire purification process was performed at room temperature, except for the cell lysis process, which was done on ice.

Expression and purification of GFP-FUS LC was also conducted based on previously reported protocols[141]. Briefly, pellets of E. Coli BL21(DE3) cells expressing GFP-FUS LC were harvested from 1 liter cultures induced with 1 mM IPTG after overnight incubation at 16°C and 220 RPM. The cell pellets were then lysed in a buffer containing 50 mM Tris-HCl pH 7.5, 500 mM NaCl, 20 mM BME, 1mM PMSF, 1% Triton X-100 and one protease inhibitor tablet for 5 min on ice, and then sonicated. The cell lysates were centrifuged at 40,000 RPM for 40 min to separate the lysate from the insoluble fraction and GFP-FUS LC resided in the supernatant after centrifugation. Therefore, the supernatant was then mixed with Ni-NTA resin for 2 hours at 4°C. The Ni-NTA resin was then packed in a glass column and washed with a buffer containing 20 mM Na_3PO_4 and 150mM NaCl pH 7.4, 20 mM imidazole, 20 mM BME, and 0.1 mM PMSF. The bound protein was eluted from the

Ni-NTA resin with a buffer containing 20 mM Na_3PO_4 and 150mM NaCl pH 7.4, 500 mM imidazole, 20 mM BME, and 0.1 mM PMSF. The buffer was then exchanged into a storage buffer consisting of 20mM Na_3PO_4 pH 7.4 buffer using 10K Amicon Ultra centrifugal filters. The purified proteins were further concentrated and flash frozen in small aliquots at a concentration of approximately 120mM.

His-GFP was used as a controlled protein and its purification was performed according to a previously published protocol[166].

Protein labeling

His-FUS LC and non-his FUS LC were labeled with Atto-488 or Atto-594, an amine-reactive, NHS ester-functionalized green/red dye. Labeling occurred at or near the N-terminus because only the N-terminus and a lysine at residue position 5 in the leader sequence preceding the N-terminal region hexa-histidine tag were expected to react with the NHS-functionalized dye. The labeling reaction took place in a 50mM HEPES buffer at pH 7.4. Dye was added to the protein in 2-fold stoichiometric excess and allowed to react for 30 min at room temperature, empirically resulting in labelling ratio near 1:1 dye: protein. Labeled protein was then buffer-exchanged into 20mM CAPS pH 11 buffer and separated from unconjugated dye using 3K Amicon columns. His-hnRNPA2 LC and his-LAF-1 RGG were also labeled with Atto-488 following the same process in corresponding buffers. His-hnRNPA2 LC was buffer-exchanged into 20 mM MES, pH 5.5 buffer prior to reacting with the dye, and then buffer-exchanged back into 20 mM MES, 8 M Urea pH 5.5 for storage. His-LAF-1 RGG was labeled in its storage buffer (20 mM Tris, 500 mM NaCl, pH 7.5). Protein and dye concentrations were monitored using UV–Vis spectroscopy. Labeled proteins were dispensed into small aliquots, flash frozen in liquid nitrogen and

stored at -80°C. For all experiments involving labeled protein, a mix of 90% unlabeled / 10% labeled protein was used.

GUV preparation

For all GUV experiments except for experiments with different GUV membrane bending rigidity, GUVs were made of POPC, Ni-NTA, 2 mol% DP-EG10 biotin and an additional 0.1 mol% Texas Red DHPE lipids, with the contents of POPC and Ni-NTA adjusted accordingly.

For experiments with different GUV membrane bending rigidity, GUVs of six different compositions were prepared based on previous reports. The detailed compositions are shown in Table S4, above.

GUVs were prepared according to published protocols[167]. Briefly, lipid mixtures dissolved in chloroform were spread into a film on indium-tin-oxide (ITO) coated glass slides (resistance ~8-12W sq-1) and further dried in a vacuum desiccator for at least 2 h to remove all of the solvent. Electroformation was performed at 55°C in glucose solution. 360 milliosmole glucose solution was employed for making GUVs, except for GUVs used in different salt concentration experiments, where 560 milliosmole glucose solution was adopted to have more capacity to modulate osmolarity. The voltage was increased every 3 min from 50 to 1400 mVpp for the first 30 min at a frequency of 10 Hz. The voltage was then held at 1400 mVpp for 120 min and finally was increased to 2200 mVpp for the last 30 min during which the frequency was adjusted to 5 Hz. GUVs were stored in 4°C and used within 1d after electroformation.

GUV tethering

Prior to tethering, the osmolality of the GUV solution and experimental buffers were measured using a vapor pressure osmometer (Wescor). GUVs were tethered to glass coverslips as previously described[168]. Briefly, glass cover slips were passivated with a layer of biotinylated PLL-PEG, using 5 kDa PEG chains. GUVs doped with 2 mol% DP-EG10-biotin were then tethered to the passivated surface using neutravidin.

PLL-PEG was synthesized by combining amine reactive PEG and PEG-biotin in molar ratios of 98% and 2%, respectively. This PEG mixture was added to a 20 mg/mL mixture of PLL in a buffer consisting of 50mM sodium tetraborate (pH 8.5), such that the molar ratio of lysine subunits to PEG was 5:1. The mixture was continuously stirred at room temperature for 6 h and then buffer exchanged into 25mM HEPES, 150mM NaCl (pH 7.4) using ZebaTM Spin Desalting Column (ThermoFisher Scientific).

Buffer used for dilution and rinsing was 25mM HEPES, 150 mM NaCl pH 7.4 buffer unless specifically stated. For GUV experiments under different salt concentrations, 25mM HEPES pH 7.4 containing 50mM, 150mM, 250mM NaCl were used, respectively, to achieve salt gradient. Osmolarity balance was maintained by the addition of glucose to the buffer.

Imaging wells consisted of 5 mm diameter holes in 0.8 mm thick silicone gaskets (Grace Bio-Labs). Gaskets were placed directly onto no.1.5 glass coverslips (VWR International), creating a temporary water-proof seal. Prior to well assembly, gaskets and cover slips were cleaned in 2% v/v Hellmanex III (Hellma Analytics) solution, rinsed thoroughly with water, and dried under a nitrogen stream. In each dry imaging well, 20 μL of PLL-PEG was added. After 20 min of incubation, wells were serially rinsed with appropriate buffer by gently pipetting until a 15,000-fold dilution was achieved. Next, 4 μg of neutravidin dissolved in 25mM HEPES, 150mM NaCl (pH 7.4) was added to each sample well and allowed to incubate for 10 min. Wells were then rinsed with the

appropriate buffer to remove excess neutravidin. GUVs were diluted in appropriate buffer at ratio of 1:13 and then 20 μL of diluted GUVs was added to the well and allowed to incubate for 10 min. Excess GUVs were then rinsed from the well using the appropriate buffer and the sample was subsequently imaged using confocal fluorescence microscopy.

GUV fluorescence imaging

Imaging experiments were performed using a spinning disc confocal super resolution microscope (SpinSR10, Olympus, USA) equipped with a 1.49 NA/100X oil immersion objective. Laser wavelengths of 488 and 561 nm were used for excitation. Image stacks taken at fixed distances perpendicular to the membrane plane (0.5 μm steps) were acquired immediately after GUV tethering and again after protein addition. At least 30 fields of views were randomly selected for each sample for further analysis prior to and after the addition of protein, respectively.

Single molecule calibration

To measure the number of proteins in the protein-dense region on GUV surface, we followed a similar procedure as we have previously employed[115,130]. First, we determined the average brightness per single dye molecule on a sparsely covered coverslip. Next, we used the same imaging conditions to measure the average intensity of the rims of GUVs covered by the protein-rich and protein-poor phases. The number of protein molecules per diffraction-limited region can be estimated by dividing the value of intensity of the GUV rim by the average brightness of a single molecule and correcting for the average number of labels per protein. Then, if we assume that the laser illuminates an area on the side of the GUV that is equal to the product of the horizontal (300 nm) and vertical (500 nm) resolution of our microscope, we can divide the number of molecules per diffraction

limited by the illuminated area to arrive at an estimate of the number of membrane-bound proteins per membrane area.

Giant Plasma Membrane Vesicles (GPMVs)

GPMVs were derived from RPE cells that stably expressed TfR-Δecto-BFP-HA-GFPnb receptor, according to published protocols[169]. These donor cells were grown in 100 × 20 mm culture dishes. Prior to extraction of GPMVs, these cells were rinsed twice with 2 mL GPMV buffer (10 mM HEPES, 2 mM CaCl2, 150 mM NaCl, pH 7.4) and once with 2 mL active buffer (GPMV buffer containing 2mM N-ethylmalemide). The cells were then incubated in 4 mL active buffer at 37 °C for 10 h. During this time, GPMVs budded spontaneously from the plasma membrane of the cells. Following this incubation, the buffer containing GPMVs was collected and spun at 300 x g for 3 min at 4 °C to remove any detached cells. The supernatant was transferred to a fresh tube and centrifuged at 17,000 x g for 23 min at 4°C. The GPMV pellet was then resuspended in 200 μL fresh GPMV buffer and used immediately for imaging experiments.

GPMV imaging

Similar to imaging experiments with GUVs, 20 μL of GPMV-containing solution was added onto a glass coverslip. GPMVs were allowed to settle onto the coverslip surface at 4°C for 10 min. A spinning disc confocal microscope (Zeiss Axio Observer Z1 with Yokagawa CSU-X1M) was used to image GPMVs. GFP-FUS LC protein diluted in GPMV buffer was added to the sample at a 2 μM final concentration. GFP alone at the same concentration was adopted as a control protein that does not form condensates. Image stacks taken perpendicularly to the coverslips (0.5 μm steps) were acquired and at least 30

fields of views were randomly selected for each sample for further analysis prior to and after the addition of protein, respectively.

Statistical analysis

All GPMV and GUV experiments were repeated 3 times for each condition reported. ImageJ was employed to analyze confocal images. At least 100 GPMVs and GUVs were examined under each condition. The diameter of each tubule was determined by drawing a line perpendicular to the tubule at three different places along its length and calculating the average diameter. The distribution of tubule diameters for each condition was derived from measurements of at least 100 vesicles. To assess the significance of comparisons between conditions, an unpaired t-test was performed. Error bars in graphs represent either standard error or standard deviation as stated in figure captions.

Model development

The values of the parameters used in the simulations are listed in Supplementary Table S5. The definitions of the variables for this model are listed in Supplementary Table S6.

1. Assumptions

- We treat the lipid bilayer as an elastic shell assuming that the thickness of the bilayer is negligible compared to the radii of the membrane curvatures[170]. This assumption allows us to model the bending energy of the membrane using the Helfrich–Canham energy[75,171].
- We assume that the membrane is locally incompressible[172] using a Lagrange multiplier to implement this constraint[173,174].
- We ignore inertia and assume that the membrane is at mechanical equilibrium at all times[175-177].

- We model the net effect of the phase separation of the proteins on the membrane surface by spontaneous curvature (C). The magnitude of the spontaneous curvature represents the curvature-generating capability of the protein domain to bend the membrane[149,178] and the induced area difference between the leaflets[179-181].
- We assume that the protein phase separation induces a spherical membrane cap shape with a constant curvature (Figure 2. 3c)[182] for ease of computation.
- To keep the mathematics tractable, we assume that the geometry is rotationally symmetric (see Figure 2. 3c)[171,176,183]. This allows us to obtain solutions for different morphologies of the membrane tubules with a relatively simple numerical calculation.

2. Membrane mechanics

2.1 Helfrich energy and mechanical equilibrium

For the local energy density of a lipid bilayer membrane, we use the modified version of the Helfrich energy including the spatially varying spontaneous curvature and bending modulus as[178,183-185].

$$W = \kappa\left(\theta^{\xi}\right)\left(H - C\left(\theta^{\xi}\right)\right)^{2} + \kappa_G K \qquad \text{(S1)}$$

where W is the local energy density, H is the mean curvature, K is the Guassian curvature, C is the induced spontaneous curvature due to any asymmetry between the leaflets, κ is the bending modulus, κ_G is the Gaussian modulus, and θ^{ξ} is a representation of surface coordinates where $\xi \epsilon [1, 2]$. It should be noted that Eq. (S1) is different from the standard Helfrich energy by a factor of 2. We take this net effect into consideration by choosing the value of the bending modulus to be twice that of the standard value of bending modulus typically used for lipid bilayers[75]. The induced spontaneous curvature (C) in Eq. S1 can be related to the area difference between the bilayer leaflets given in the literature[179-181].

$$\Delta A - \Delta A_0 \equiv \frac{4d\kappa CA}{\pi\kappa_r} \tag{S2}$$

where d is the lipid bilayer with thickness, κ_r is the nonlocal membrane bending modulus, and A is the total surface area of the neutral plane. ΔA and ΔA_0 are the relaxed initial and bent area differences between the membrane leaflets, respectively. Thus, induced spontaneous and area difference are not independent parameters. Any stationary shape of membrane that is a result of area difference elasticity model (ADE) therefore can be also modeled by the spontaneous curvature given in Eq. S2.

As we showed previously, the normal variation of total energy of the membrane gives the so-called "shape equation,"[176,178,184]

$$\underbrace{\Delta[\kappa(H-C)] + 2\kappa(H-C)(2H^2-K) - 2\kappa H(H-C)^2}_{\text{Elastic effects}} = \underbrace{p + 2\lambda H}_{\text{Capillary effects}} \tag{S3}$$

Where Δ is the surface Laplacian, p is the pressure difference across the membrane, and λ can be interpreted to be the membrane tension[178].

A consequence of spatial variation of membrane properties and protein density is that λ is not homogeneous along the membrane[176,178,186]. Therefore, the balance of forces tangential to the membrane gives the spatial variation of membrane tension as,

$$\underbrace{\nabla\lambda}_{\substack{\text{Gradient of}\\ \text{surface tension}}} = \underbrace{2[\kappa(H-C)]\frac{\partial C}{\partial\theta^\xi}}_{\text{Protein density variation}} - \underbrace{\frac{\partial\kappa}{\partial\theta^\xi}(H-C)^2}_{\substack{\text{Bending modulus}-\text{induced}\\ \text{variation}}} \tag{S4}$$

where ∇ is the partial derivative with respect to the coordinate (θ^ξ).

2.2 Parametrization in axisymmetric coordinates

We define a surface of revolution (Figure 2. 3c) by

$$\boldsymbol{r}(s,\theta) = R(s)\boldsymbol{e_r}(\theta) + Z(s)\mathbf{k} \tag{S5}$$

where ($\boldsymbol{e_r}$, $\boldsymbol{e_\theta}$, $\mathbf{k}$) is the basis coordinate, s is the arc length along the curve, $R(s)$ is the radius from the axis of rotation and $Z(s)$ is the height from the base plane. We ψ as the angle made by the tangent with respect to the vertical such that $R' = \cos\psi$ and $Z' = \sin\psi$, which satisfies the identity $(R')^2 + (Z')^2 = 1$. Here, $()'$ is the partial derivative with respect to the arc length. We can define the normal and tangent vectors to the surface as

$$\boldsymbol{n} = -\sin\psi\,\boldsymbol{e_r}(\theta) + \cos\psi\,\boldsymbol{k}, \boldsymbol{a_s} = \cos\psi\,\boldsymbol{e_r}(\theta) + \sin\psi\;\boldsymbol{k} \tag{S6}$$

The tangential (κ_ν) and transverse (κ_τ) curvatures are given by

$$\kappa_\nu = \psi', \qquad \kappa_\tau = sin\,\psi/R \tag{S7}$$

and the mean curvature (H) and the Gaussian curvature (K) are defined as

$$H = \frac{1}{2}(\kappa_\nu + \kappa_\tau) = \frac{1}{2}(\psi' + sin\,\psi/R) \tag{S8}$$

To simplify the governing equations to first- order differential equations, we define $L = \frac{1}{2\kappa}R(W_H)'$ giving us [176,184,185],

$$\begin{aligned} &R' = \cos\psi,\ Z' = \sin\psi,\ R\psi' = 2RH - \sin\psi,\ RH' = L + RC' - \frac{R\kappa'}{\kappa}(H - C), \\ &\frac{L'}{R} = \frac{p}{\kappa} + 2H\left[(H-C)^2 + \frac{\lambda}{\kappa}\right] - 2(H-C)\left[H^2 + \left(H - \frac{\sin\psi}{R}\right)^2\right] - \frac{\kappa' L}{\kappa R}, \\ &\lambda' = 2[\kappa(H-C)]C' - \kappa'(H-C)^2. \end{aligned} \tag{S9}$$

In asymmetric coordinates, the total area of the manifold (A) can be expressed in term of arc length as,

$$A(s) = 2\pi \int_0^s R(\eta)d\eta \rightarrow \frac{dA}{ds} = 2\pi R \tag{S10}$$

Thus, Eq. (S10) allows us to convert the system of equations in Eq. (S9) that is in term of arc length to a system in terms of area given by

$$2\pi R\dot{R} = \cos\psi\,, 2\pi R\,\dot{Z} = \sin\psi\,, 2\pi R^2\dot{\psi} = 2RH - \sin\psi\,, 2\pi R^2\dot{H} = L + 2\pi R^2(\dot{C} - \frac{\dot{\kappa}}{\kappa}(H - C)),$$
$$2\pi\dot{L} = \frac{p}{\kappa} + 2H\left[(H - C)^2 + \frac{\lambda}{\kappa}\right] - 2(H - C)\left[H^2 + \left(H - \frac{\sin\psi}{R}\right)^2\right] - 2\pi\frac{\dot{\kappa}L}{\kappa}\,, \tag{S11}$$
$$2\pi R\dot{\lambda} = 4\pi R[\kappa(H - C)]\dot{C} - 2\pi R\dot{\kappa}(H - C)^2.$$

where ($\dot{}$) denotes the derivative with respect to the area.

To non-dimensionalize the system of equations (Eq. (S11)), we use two parameters, the radius of the GUV (R_0), and lipid bilayer bending modulus (κ_0). Using these constants, we can define

$$\zeta = \frac{A}{2\pi R_0^2},\ y = \frac{Z}{R_0},\ x = \frac{R}{R_0},\ h = HR_0,\ c = CR_0,\ l = LR_0,$$
$$\tilde{\lambda} = \frac{\lambda R_0^2}{\kappa_0},\ G = KR_0^2,\ \tilde{p} = \frac{pR_0^2}{\kappa_0},\ \widetilde{\kappa_G} = \frac{\kappa_G}{\kappa_0},\ \tilde{\kappa} = \frac{\kappa}{\kappa_0}. \tag{S12}$$

Rewriting Eq. (S11) in terms of the dimensionless variables in Eq. (S12), we get [176]

$$x\dot{x} = \cos\psi\,,\ x\dot{y} = \sin\psi\,,\ x^2\dot{\psi} = 2xh - \sin\psi\,,\ x^2\dot{h} = l + x^2(\dot{c} - \frac{\dot{\tilde{\kappa}}}{\tilde{\kappa}}(h - c)),$$
$$\dot{l} = \frac{\tilde{p}}{\tilde{\kappa}} + 2h\left[(h - c)^2 + \frac{\tilde{\lambda}}{\tilde{\kappa}}\right] - 2(h - c)\left[h^2 + \left(h - \frac{\sin\psi}{x}\right)^2\right] - \frac{\dot{\tilde{\kappa}}l}{\tilde{\kappa}} \tag{S13}$$
$$\dot{\tilde{\lambda}} = 2[\tilde{\kappa}(h - c)]\dot{c} - \dot{\kappa}(h - c)^2.$$

2.3 Boundary conditions

In order to solve the system of equations (Eq. S9), we need to provide six boundary conditions. We consider an axisymmetric circular patch of membrane. To impose the continuity at $s = 0$, we require to set $\psi = \pi/2$ and $R = R_b$ where we used the suggested length scale in Naito et al. [128] to relate the radius of undoloid to the physical properties of the membrane. At the other boundary far from the center of the patch ($s = s_{max}$), we set $Z = 0$ to be sure the membrane does not lift off. We also assume that the membrane at the far boundary remains flat, so we set $\psi = \psi' = 0$ and prescribe the tension as $\lambda = \lambda_0$. The boundary conditions can be summarized as

$$R(0) = R_b,\ \psi(0) = \frac{\pi}{2},\ Z(s_{max}) = 0, \psi(s_{max}) = 0,\ \psi'(s_{max}) = 0,\ \lambda(s_{max}) = \lambda_0. \quad \text{(S14)}$$

2.4. Delaunay shapes and other solution of Helfrich energy minimization in axisymmetric coordinates

The general shape equation (Eq. S3) is a nonlinear fourth order differential equation. Delaunay's surface including catenoids, unduloids, circular cylinder, and spheres are surfaces of revolution with constant mean curvature and they are found to be a solution of the Helfrich shape equation [187,188]. The general equation describing the Delaunay's shape is given by

$$sin\ \psi(R) = aR + \frac{e}{R}, \quad \text{(S15)}$$

where a and e are constants determining the type of surfaces. For example, if *(i)* $a = 0$, Eq. S15 gives the catenoid shapes, if *(ii)* $0 < ae < 1/4$, Eq. S15 gives the unduloid shapes, and if *(iii)* $ae < 0$, Eq. S15 corresponds to the nodoid surfaces[128,189]. It was shown[128,190] that the Delaunay shapes can be extended as

$$sin\,\psi(R) = aR + f + \frac{e}{R}\,, \tag{S16}$$

where f is a constant and for the special case of $f = 0$, Eq. S16 reduces to Delaunay surfaces in Eq.S15. By substituting Eq. S16 in the Helfrich shape equation (Eq. S3) we can find the constant a, f, and e as the function of the physical properties of the membrane as

$$2aC_0 = \frac{\lambda}{\kappa} + C_0^2,\ f = \pm\sqrt{2 + 4(\frac{a}{2C_0} - 1)}\,,\ e = \frac{1}{2C_0}. \tag{S17}$$

It should be mentioned that in our Helfrich equation (Eq.S1), bending rigidity (κ) is two times larger than the given bending rigidity in Naito et al. [128]. Also, in our Helfrich equation (Eq.S1), the spontaneous curvature is a representation of any induced asymmetry in the mean curvature (H) while in Naito et al., the spontaneous curvature refers to the total curvature. To convert the given equations in Naito et al. [128] to our parametrization, we multiplied the given spontaneous curvature in [128] by two and divide the bending rigidity by two.

Substituting Eq. S17 into Eq. S15 and using the length scale $R_m = \frac{1}{\sqrt{2aC_0}}$ we get [128]

$$sin\,\psi(r) = \alpha(r + r^{-1}) - \sqrt{4\alpha^2 - 2}, \quad \text{(S18)}$$

where $\alpha = (2R_m C_0)^{-1}$ and $r = \frac{R}{R_m}$. It should be mentioned that in Eq.S18, we just considered the negative branch of b due to the constraint of $|sin\,\psi| \leq 1$. Also, to satisfy the same constrain, $\alpha \leq 0.75$. In Figure 2.3a, we plotted the unduloid like shapes corresponding to Eq. S17 for two values of α. For $\alpha \to 0.75$, the unduloidlike shape becomes like a circular cylinder and with increasing α, multiple spheres form along the unduloid similar to a string of pearls. In addition to Delaunay shapes, there are multiple analytical studies that have shown how the curved proteins can bend the membrane into the pearled-shaped structures[191-194].

2.5. Helfrich energy for anisotropic spontaneous curvature

To model the effect of rigid protein scaffolds that may induce tubulation (such as BAR domain proteins), we used the modified version of Helfrich energy density including spatially varying deviatoric curvature as [149,156,195,196]

$$W = \kappa(\theta^{\xi})H^2 + \kappa(\theta^{\xi})(D - D_m(\theta^{\xi}))^2, \quad \text{(S19)}$$

Where D is the curvature deviator and D_m is the spontaneous (intrinsic) deviatoric curvature. In Eq. S19, we assumed that the induced spontaneous curvature C by BAR domain proteins is negligible compared to the deviatoric curvature D_m and we set $C = 0$.

Using Eq. S19, the membrane shape equation, the incompressibility condition, and the governing differential equations in axisymmetric coordinates have been developed [185,196,197].

3. Numerical calculation

We solved the system of first-order differential equations using 'bvp4c' solver in MATLAB. Here, we summarize the steps and assumptions that we used the simulation.

- All the simulations were performed for a fixed area of the membrane.
- The mesh size on the domain was chosen such that it was (initially) small around the s = 0 and then increased by moving toward the far away boundary ($s = s_{max}$)
- To ensure a smooth transition in the induced spontaneous curvature (C) along the tubular domain, we assumed that the spontaneous curvature decreases linearly[198] using a hyperbolic tangent function to define it as

$$C = \frac{C_0}{2}\left(\frac{A - A_0}{A_0}\right)\left[\tanh(g(A - A_0))\right], \quad \text{(S20)}$$

where A_0 represents the area of the phase-separated protein and g is a constant. You can find a more detailed analysis of the choice of the spontaneous curvature function and the parametric sensitivity of the shape equation in [199].

4. Estimating the magnitude of induced spontaneous curvature by FUS LC liquid-liquid phase separation using the polymer adsorption analogy

Strongly adsorbed polymers on the membrane surface (either flexible or semi flexible) can bend the membrane locally, resulting in the formation of polymer-lined buds or tubules [132,200]. This process is analogous to the surface stresses induced by multi-layer liquid phase separation of FUS LC on the lipid membrane surface. Thus, we can estimate the induced spontaneous curvature by FUS LC phase separation based on the scaling theory for surface adsorption of flexible polymers (Figure 2.14) [132,201].

Considering a system that consists of a membrane and an adsorbed flexible polymer, the total free energy is

$$E(H) = F(H) + 2\kappa A H^2, \tag{S21}$$

where $F(H)$ is the free energy of polymer adsorption and, for strong adsorption, is given by [132,201]. Here we assume the histidine-lipid interaction is strong, based on our finding that his-FUS LC is recruited by these interactions to the membrane under conditions for which interactions between FUS LC domains are too weak to drive protein adsorption on the membrane, as shown in Supplementary Figure 2.11-13, which are discussed in the main text.

$$F \sim -NT\epsilon \left(\frac{l}{b}\right)^2 \frac{b}{\xi}(1 - 2H\delta), \tag{S22}$$

where N $(N > 1)$ is a segmental number onto a planar surface, T is temperature, l is the persistence length of the polymer, b is the range of polymer attraction per segment, ξ is the polymer thickness of adsorption (reflecting the arrangement of the polymer segments perpendicular to the surface). In strong adsorption, the polymer thickness and the range of

polymer attraction are related by, $\xi = b(1+\delta)$, where, δ is a small positive number ($\delta \sim 0.1$). This is because most of the segments of the polymer lie within the polymer adsorption thickness region. ϵ is the adsorption strength that is given by [132,201]

Flexible polymers: $\epsilon \sim \frac{(\frac{b}{l})^2 U}{T} - 1$ (S23)

Semi flexible or stiff polymers: $\epsilon \sim (\frac{b}{l})^2 (\frac{U}{T} - 1)$,

where U is the interaction strength. Substituting Eq. S22 into Eq. S21 and minimizing the total free energy of system gives the induced spontaneous curvature in equilibrium as [132]

$C \sim -\frac{T\epsilon}{\kappa b}\delta$ (S24)

The negative sign in spontaneous curvature (Eq. S24) indicates that the membrane bends inward engulfing the polymer or FUS LC protein layer (Figure 2.14a).

Using Eq. S24, we can estimate the order of induced spontaneous curvature by FUS LC protein phase separation on the membrane surface. For the FUS LC phase separation, we know that $20k_BT < \kappa < 80k_BT$ (Figure 2. 4f), $b \sim 6-7\ nm$ (FUS LC radius $\sim 3.3\ nm$) [202], and $\epsilon \sim 10$ for the case of strong adsorption [132]. Substituting these numbers in Eqs. S23 and S.24 gives an estimate of $C \sim O\ (1\ \mu m^{-1})$. This is consistent with our experimental observation that the minimum radius of inward tubules is about $r = 50\ nm$ which is equivalent to the maximum spontaneous curvature of $C = 1/(2r) = 10\ \mu m^{-1}$. Also, in our simulation results, the applied spontaneous curvature is of order of $1\ \mu m^{-1}$ (see Figure 2. 3 in the main text).

5. Relationships between the stress profile in the bilayer and the spontaneous curvature

Spontaneous curvature is a macroscopic property in the continuum framework that represents the curvature-generating capability of any asymmetry between the two leaflets of lipid membranes. To understand how this macroscopic property is related to atomic and molecular interactions at the level of the bilayer, we use the stress profile through the thickness of the membrane (σ) defined as [203,204]

$$\sigma(z) = -(P_L(z) - P_N(z)), \tag{S25}$$

where $P_L(z)$ and $P_N(z)$ are the tangential and local pressures along the bilayer normal, z. The stress profile $\sigma(z)$ induces a bending moment (τ) along the cross-section of a planar bilayer given by [205,206]

$$\tau = \int_{-d/2}^{d/2} z\sigma(z)dz. \tag{S26}$$

On the other hand, for a relatively flat membrane, the asymmetry between leaflets induces a torque (T). Based on the Helfrich bending energy [75], this torque is proportional to the spontaneous curvature and the membrane bending rigidity given by [205,207]

$$T = -\kappa C, \tag{S27}$$

In mechanical equilibrium, $\tau = T$, which gives the relationship between the spontaneous curvature and the first moment of the stress profile as [205,208,209]

$$-\kappa C = \int_{-\frac{d}{2}}^{\frac{d}{2}} z\sigma(z)dz. \tag{S28}$$

Thus, the spontaneous curvature induced by the FUS-LC adsorption is going to induce a bending moment on the underlying bilayer by altering the stress profile across the thickness of the bilayer.

6. Relationship between the spontaneous curvature and the leaflet properties

In Eq. S28, we relate the induced spontaneous curvature to the molecular architecture of the lipids. It is also possible to express the spontaneous curvature in terms of the tensions and the thickness of bilayer leaflets [210,211] to further understand how the differences in leaflet stresses can give rise to bending. Let us consider a planar bilayer where the upper leaflet has a thickness of d_1, an interfacial area of A_1, and a tension of λ_1. The lower leaflet has a thickness of d_2, an interfacial area of A_2, and a tension of λ_2. Now, we bend the membrane assuming that the area of the neutral plane (A) is constant; this is a reasonable assumption since the membrane is incompressible. This allows us to relate the thickness of membrane leaflets after bending (d_1' and d_2') as a function of the mean curvature of the membrane (Figure 2.14b)

$$\mathrm{d}_1' \approx \mathrm{d}_1(1 - \mathrm{d}_1 H) \text{ and } \mathrm{d}_2' \approx \mathrm{d}_2(1 - \mathrm{d}_2 H) \quad \text{(S29)}$$

It should be mentioned that in Eq. S29, we have kept the terms up to the first order in curvature and ignored the higher order terms. Similarly, we can find the area of leaflets after bending (A_1' and A_2') (Figure 2.14b)

$$\mathrm{A}_1' \approx \mathrm{A}_1(1 + 2\mathrm{d}_1 H) \text{ and } \mathrm{A}_2' \approx \mathrm{A}_2(1 - 2\mathrm{d}_2 H) \quad \text{(S30)}$$

Having leaflets with tensions λ_1 and λ_2, we calculate the interfacial energy (E_{inter}) due to change in the area of leaflets as

$$\mathrm{E}_{inter} = \lambda_1(\mathrm{A}_1' - \mathrm{A}_1) + \lambda_2(\mathrm{A}_2' - \mathrm{A}_2) \rightarrow \mathrm{E}_{inter} \approx 2(\mathrm{d}_1\lambda_1 - \mathrm{d}_2\lambda_2)HA, \quad \text{(S31)}$$

This interfacial energy is balanced by the membrane bending energy of the neutral plane given by the Helfrich energy as

$$\mathrm{E}_{ben} = \kappa(\mathrm{H} - \mathrm{C})^2 A \xrightarrow{first\ order\ approximation} \mathrm{E}_{ben} \approx (\kappa\mathrm{C}^2 - 2\kappa\mathrm{HC})A. \quad \text{(S32)}$$

In mechanical equilibrium and for a nearly flat membrane, we have

$$\frac{\partial \mathrm{E}_{ben}}{\partial \mathrm{H}}\Big|_{H=0} = \frac{\partial \mathrm{E}_{inter}}{\partial \mathrm{H}}\Big|_{H=0}, \quad \text{(S33)}$$

which yields to [211]

$$\kappa\mathrm{C} = \mathrm{d}_2\lambda_2 - \mathrm{d}_1\lambda_1. \quad \text{(S34)}$$

Eq. S34 shows how the magnitude of induced spontaneous curvature depends on the mechanical tensions and thickness of bilayer leaflets. Indeed, both mechanical tension and the thickness of bilayer leaflets can be defined using the stress profile ($\sigma(z)$) [211] such that Eq. S28 and Eq. S34 becomes identical. These ideas give us insights into how the spontaneous curvature induced by FUS LC causes differential stresses in the bilayer, resulting in compression leaflet nearest to the protein layer and expansion in the leaflet farthest from the protein layer.

SI APPENDIX

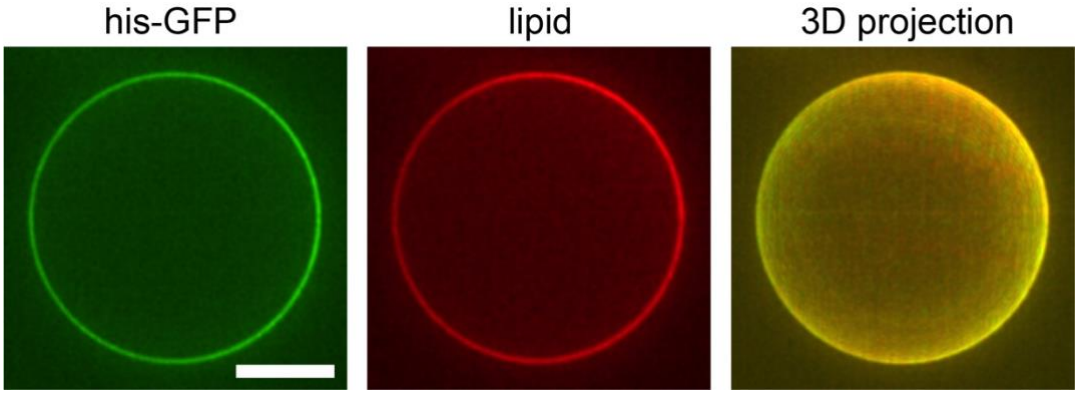

Figure 2. 7 Representative super-resolution images of GUVs incubated with 1μM of his-GFP in 25 mM HEPES, 150 mM NaCl pH 7.4 buffer. GUV consists of 93 mol% POPC, 5 mol% Ni-NTA, 2 mol% DP-EG10-biotin and 0.1 mol% Texas Red-DHPE. Scale bar = 5 μm.

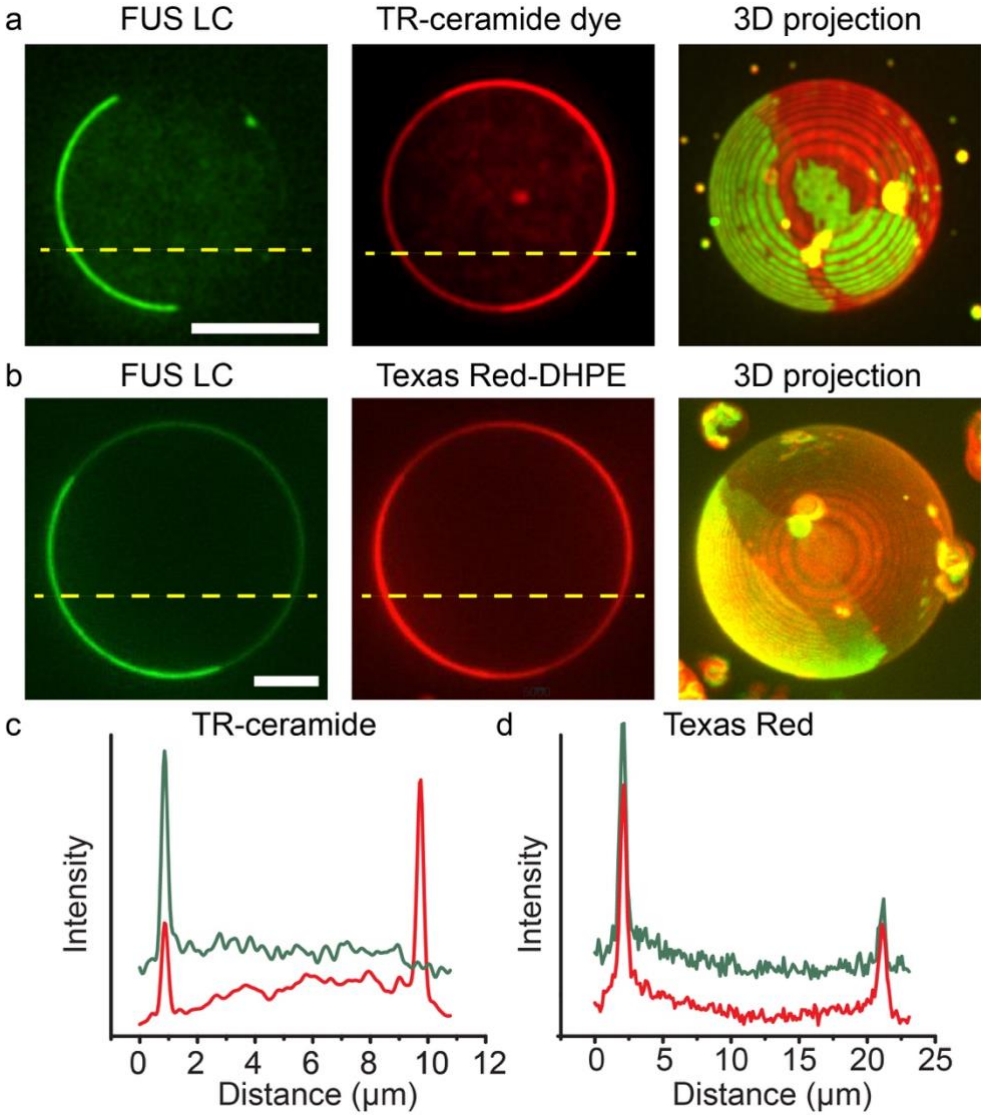

Figure 2. 8 Fewer labeled lipids enriched in the protein-rich region when TR-ceramide, rather than Texas Red-DHPE, was used as the labeled lipid. **a, b** Representative super-resolution images of GUVs labeled with TR-ceramide (**a**) and Texas Red-DHPE (**b**) incubated with 1μM of his-FUS LC in 25 mM HEPES, 150 mM NaCl pH 7.4 buffer. GUVs in panel **a** consist of 83 mol% POPC, 15 mol% Ni-NTA, 2 mol% DP-EG10-biotin and 1 mol% TR-ceramide. GUVs in panel **b** consist of 93 mol% POPC, 5 mol% Ni-NTA, 2 mol% DP-EG10-biotin and 0.1 mol% Texas Red-DHPE. Scale bar = 5 μm. **c, d** Intensity distribution along the dashed line across a TR-ceramide labeled GUV (**c**) and a Texas Red-DHPE labeled GUV (**d**) as shown in panel **a** and **b**. Green line represents the protein signal and the red line represents the lipid signal.

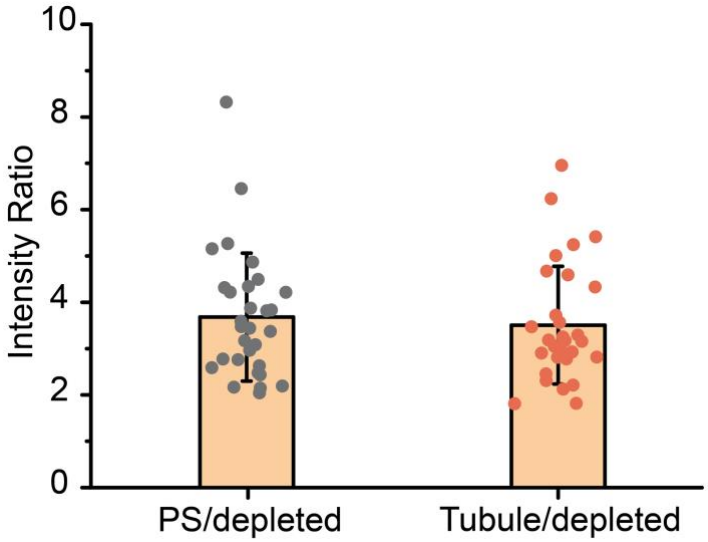

Figure 2. 9 Comparison of intensity ratio between the protein-dense phase and the protein-depleted phase; and membrane tubules and the protein-depleted phase. Each point represents a measured ratio of intensities within the same confocal image. Bar chart displays the mean intensity ratio (N = 30). Error bars correspond to standard deviation. GUVs (composition: 83 mol% POPC, 15 mol% Ni-NTA, 2 mol% DP-EG10-biotin and 0.1% Texas Red-DHPE) were incubated with 1μM atto-488 labeled his-FUS LC in 25 mM HEPES, 150 mM NaCl, pH 7.4 buffer.

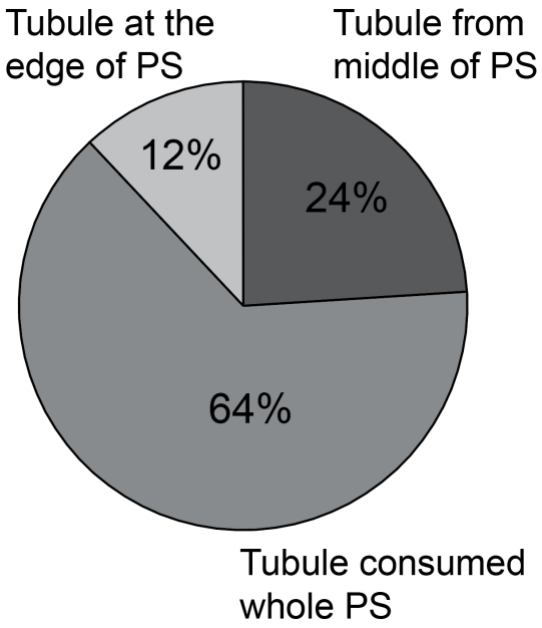

Figure 2. 10 Pie chart displaying the fraction of tubules formed at the edge of the protein-rich phase (PS), in the middle of the protein-rich phase, and tubules consuming the entire protein-rich phase. In total 100 (N = 100) tubules formed on the surfaces of GUVs (composition: 83 mol% POPC, 15 mol% Ni-NTA, 2 mol% DP-EG10-biotin and 0.1% Texas Red-DHPE) incubated with 1μM his-FUS LC in 25 mM HEPES, 150 mM NaCl, pH 7.4 buffer were categorized.

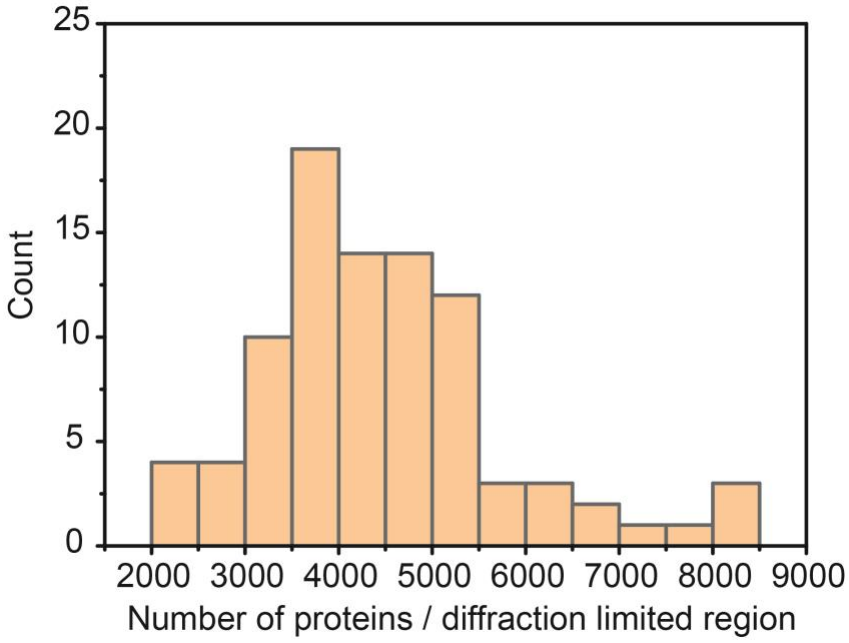

Figure 2. 11 Distribution of the number of proteins per diffraction limited area in the protein-rich region on GUV membranes. Number of proteins was estimated by dividing the intensity of the GUV rim in confocal images by the measured intensity of proteins labeled with single molecules of the fluorophore. N = 90 protein-rich regions analyzed. GUVs (composition: 83 mol% POPC, 15 mol% Ni-NTA, 2 mol% DP-EG10-biotin and 0.1% Texas Red-DHPE) were incubated with 1μM his-FUS LC (10% atto-488 labeled, 90% unlabeled) in 25 mM HEPES, 150 mM NaCl, pH 7.4 buffer.

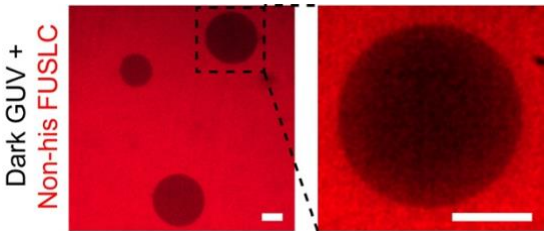

Figure 2. 12 FUS LC without histidine tag cannot bind to the GUV membrane surface. No measurable protein binding was detected when GUVs were incubated with 1μM atto 594 labeled FUSLC proteins that lacked histidine tags. GUVs composition: 83 mol% POPC, 15 mol% Ni-NTA, 2 mol% DP-EG10-biotin. Buffer: 25 mM HEPES, 150 mM NaCl, pH 7.4.

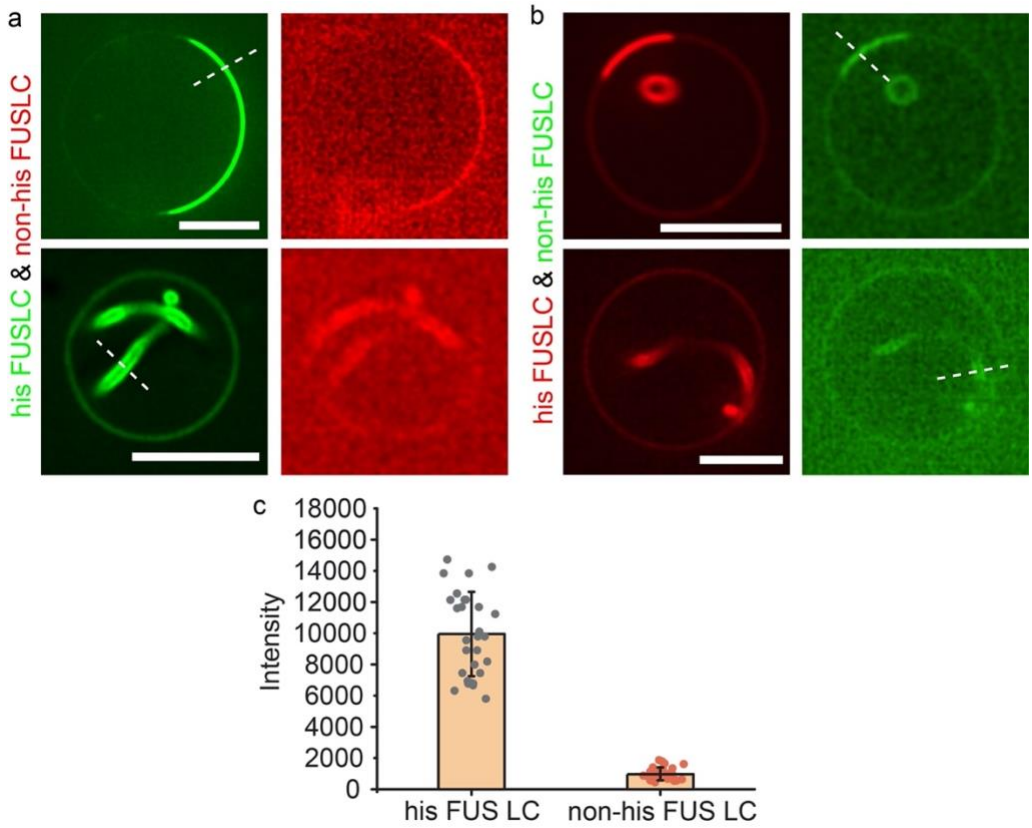

Figure 2. 13 The recruitment of FUS LC to the GUV membrane surface through FUS-FUS interactions is much weaker compared to recruitment through histidine-nickel interactions. (**a**) Protein-rich phase (upper panel) and protein-lined tubule (bottom panel) when 1μM atto-488 labeled his-FUS LC (10% labeled) and 1μM atto-594 labeled non-his FUS LC (10% labeled) were added together to unlabeled GUVs. (**b**) Protein-rich phase (upper panel) and protein-lined tubule (bottom panel) when 1μM atto-594 labeled his-FUS LC (10% labeled) and 1μM atto-488 labeled non-his FUS LC (10% labeled) were added together to unlabeled GUVs. (**c**) Intensity analysis of atto-488 labeled his-FUS LC and atto-488 labeled non-his FUS LC in protein rich regions (indicated by white dashed lines). Bar chart shows the average intensity. Error bars represent standard deviation. N = 30 regions were analyzed for both his-FUS LC and non-his FUS LC.

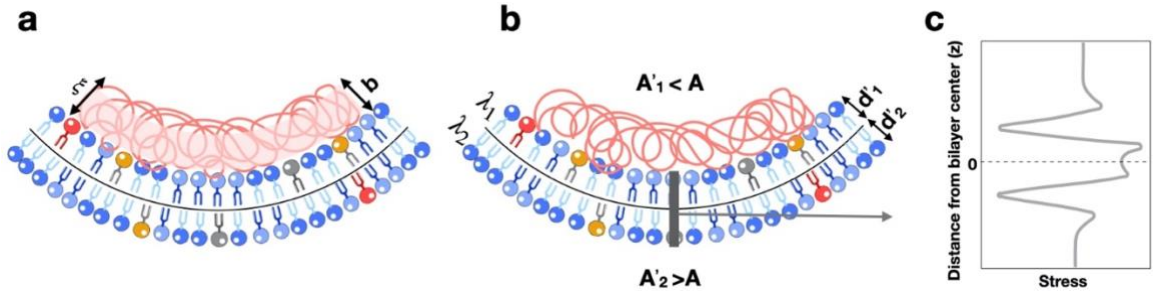

Figure 2. 14 (a) Schematic picture of induced spontaneous curvature by the layer of condensed FUS LC on the membrane surface. Here, we used the strong polymer adsorption analogy where b is the adsorption thickness and ξ thickness of the protein layer. (b) Schematic depiction of a curved bilayer due to asymmetry between the leaflets. In the shown schematic, the upper leaflet has thickness d_1', tension λ_1, and interfacial area $\mathrm{A}_1' < A$ while the lower leaflet has thickness d_2', tension λ_2, and interfacial area $\mathrm{A}_2' < A$. (c) Stress profile through membrane thickness (z).

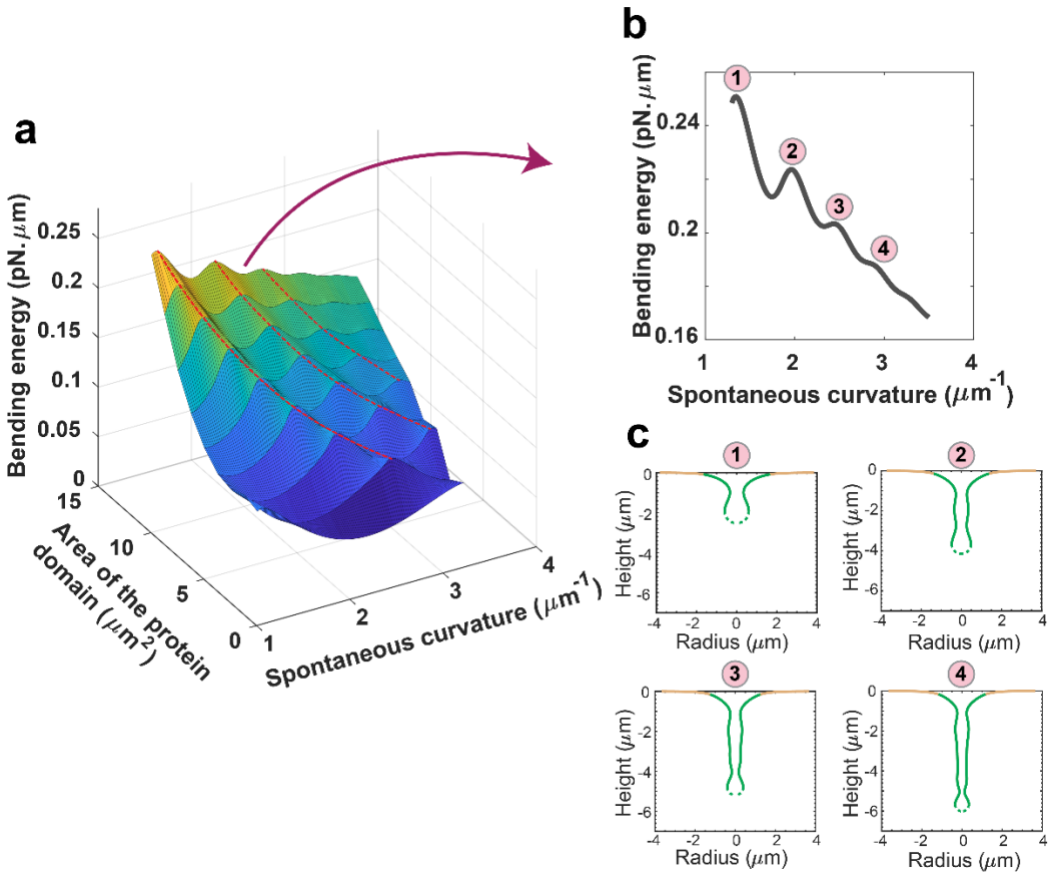

Figure 2. 15 Spontaneous curvature and the area of the protein domain regulate the morphology of the undulated tubules. (**a**) Bending energy of the protein domain as the function of the spontaneous curvature and area of the protein domain. For a small area of the protein domain, there is just a local maximum with increasing the magnitude of the spontaneous curvature. However, for the larger area of the protein domain, the bending energy has an oscillation behavior with multiple local maxima as a function the spontaneous curvature. With decreasing the area of the protein domain, the bending energy decreases and also local maximum shifts toward the larger values of the spontaneous curvature (red dotted lines). (**b**) The bending energy as the function of spontaneous curvature for $A_0 = 4\pi\ \mu m^2$. With increasing the magnitude of spontaneous curvature, there are multiple local maxima. Here, we labeled the four local maxima with numbers one to four. (**c**) The morphology of the membrane at the local maximum bending energy points in panel b.

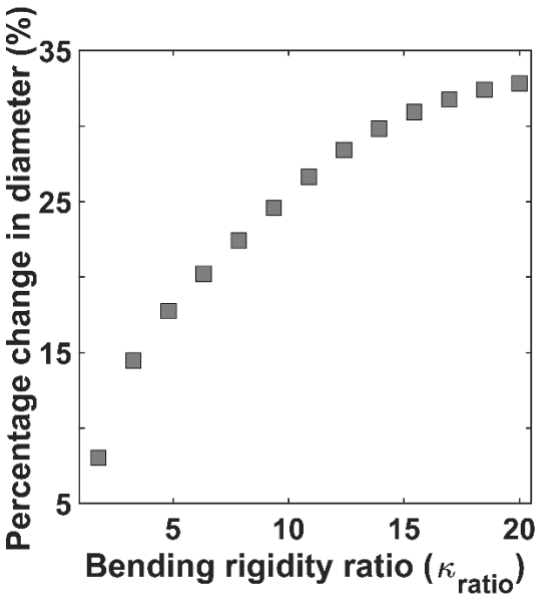

Figure 2. 16 The tubule diameter increases with increasing the bending rigidity of the protein domain compared to the bare membrane. We defined the percentage of change in the tubule diameter as $(D - D_{\kappa_{ratio}=1})/D_{\kappa_{ratio}=1})$ and $\kappa_{\text{ratio}} = \kappa_{\text{proetin}}/\kappa_{\text{membrane}}$. Here, we set $C_0 = 3.5\,\mu m^{-1}$, $\lambda_0 = 0.9\,pN/\mu m$, $A_0 = 4\pi\,\mu m^2$, and increased the bending rigidity ratio from $\kappa_{ratio} = 1$ (uniform rigidity) to $\kappa_{ratio} = 20$. Based on our results, with increasing the bending rigidity of the protein domain to $\kappa_{\text{ratio}} = 20$, the tubule diameter increases about 35% compared to the uniform bending rigidity. This increase in the tubule diameter with increasing the bending rigidity of the protein domain is qualitatively consistent with the experimental results shown in Figure 2. 4g.

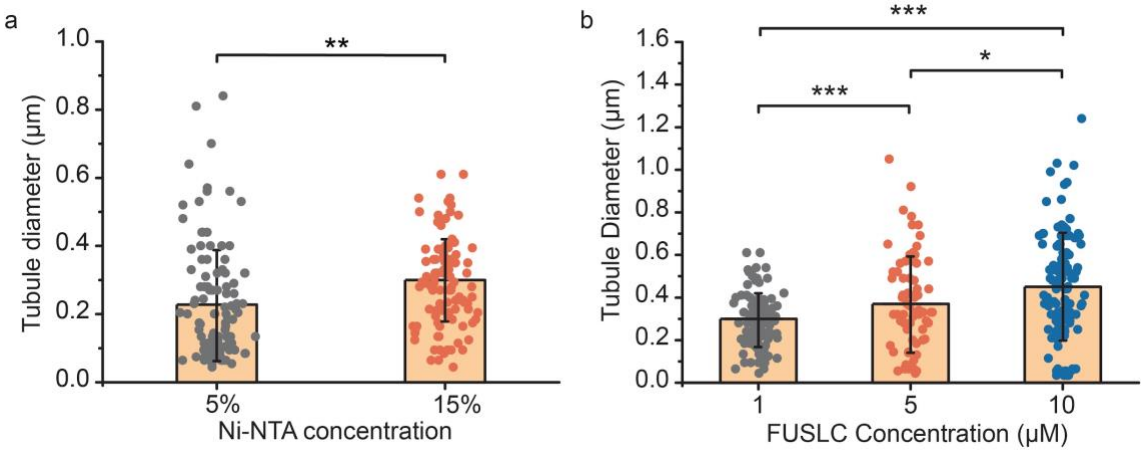

Figure 2. 17 Tubule diameter varies with Ni-NTA and protein concentration. Bar chart displaying average tubule diameter for GUVs with different Ni-NTA concentration (**a**) and FUS LC concentration (**b**). (**a**) GUVs with corresponding Ni-NTA content were incubated with 1μM FUS LC in 25 mM HEPES, 150mM NaCl pH 7.4 buffer. (**b**) GUVs (composition: 83 mol% POPC, 15 mol% Ni-NTA, 2 mol% DP-EG10-biotin and 0.1% Texas Red-DHPE) were incubated with corresponding concentration of FUS LC in 25 mM HEPES, 150mM NaCl pH 7.4 buffer. Error bars correspond to standard deviation. Each point is a mean value of diameters measured at three positions along the same tubule. N > 100 tubules were analyzed for each group. Brackets show statistically significant comparisons using an unpaired, 2-tailed student's t test. * represents $p < 0.05$, ** represents $p < 0.01$, *** represents $p < 0.001$.

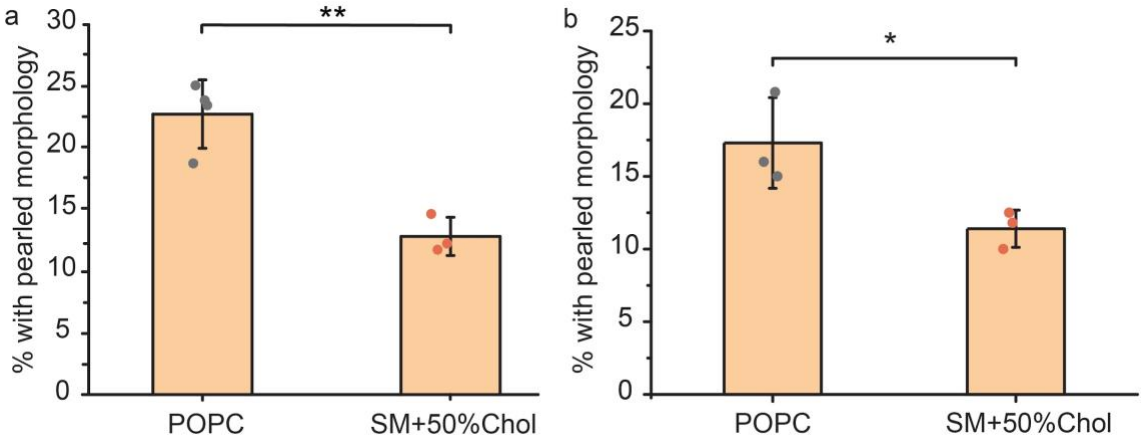

Figure 2. 18 Impact of membrane bending rigidity on the fraction of tubules induced by FUS LC (a) and LAF-1 RGG (b) that displayed a pearled morphology. Data are displayed as mean ± standard deviation from three independent experiments (n = 3) on separate preparations of vesicles, with cumulatively N > 100 vesicles categorized. Brackets show statistically significant comparisons using an unpaired, 2-tailed student's t test. * represents $p < 0.05$, ** represents $p < 0.01$.

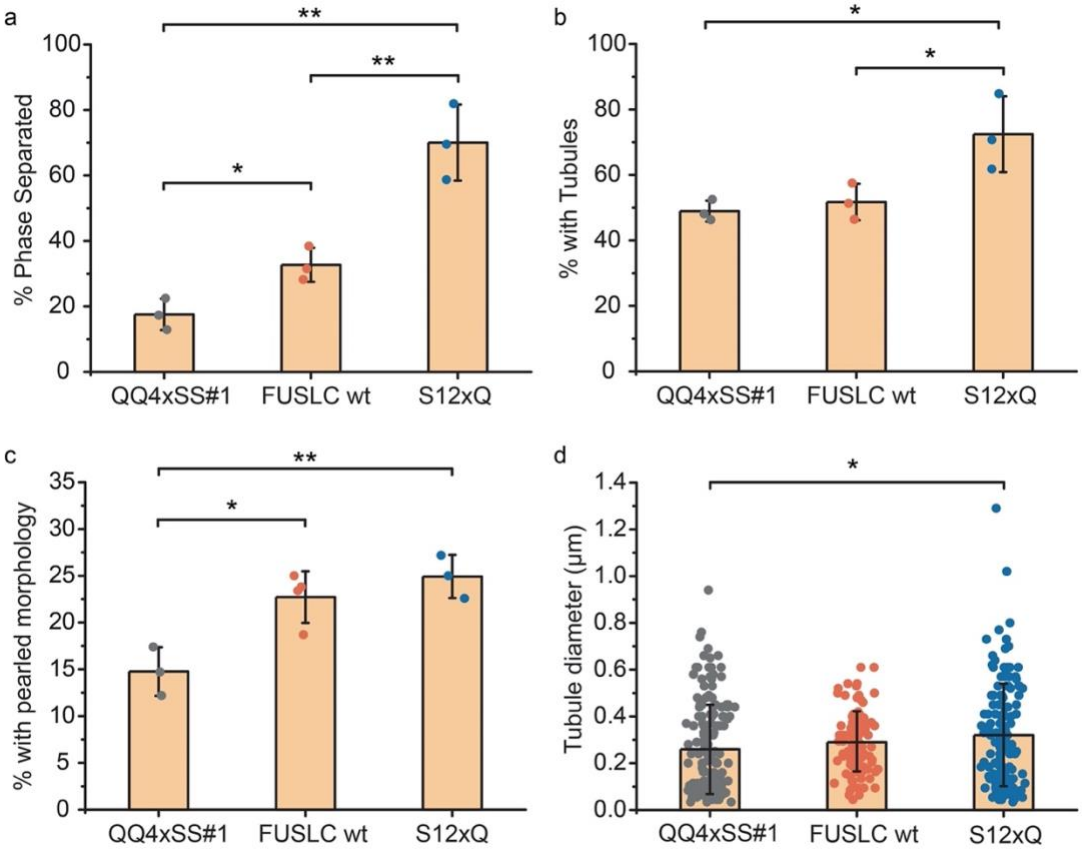

Figure 2. 19 Impact of Glutamine content on phase separation, tubule formation, pearled tubule fraction and tubule diameter for GUVs exposed by FUS LC. QQ4xSS#1, which replaces 8 glutamine residues (4 pairs Q, in QQ motifs) in wt FUS LC with serines, drives weaker phase separation on GUV surfaces when compared to wild type FUSLC, while S12xQ, which adds 12 glutamine residues to wild type FUS LC by replacing serines, drives enhanced phase separation. (**a**) Phase separation, (**b**) formation of protein-lined tubules, (**c**) frequency of pearled tubule and (**d**) average tubule diameter increases with increasing glutamine content of the FUS LC domain. Bar chart displays average value, and error bars correspond to standard deviation. Points in (**a-c**) are results from three independent experiments. Each point in (**d**) is a mean value of diameters measured at three positions along the same tubule. N > 100 tubules were analyzed for each variant. GUVs (composition: 83 mol% POPC, 15 mol% Ni-NTA, 2 mol% DP-EG10-biotin and 0.1% Texas Red-DHPE) were incubated with 1μM FUS LC variants in 25 mM HEPES, 150 mM NaCl pH 7.4 buffer. Brackets show statistically significant comparisons using an unpaired, 2-tailed student's t test. * represents $p < 0.05$, ** represents $p < 0.01$

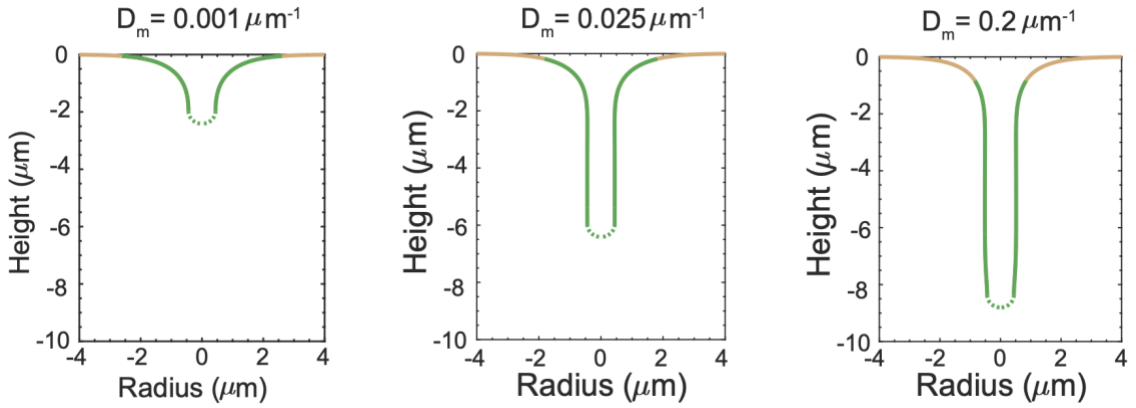

Figure 2. 20 Deviatoric curvature (D_m) induced by rigid protein scaffolds results in cylindrical tubules rather than pearled tubules. The green domain is the area covered by rigid protein scaffolds and the yellow domain is the bare lipid membrane. Here, we set $\kappa_{ratio} = 1$ (uniform rigidity), $C_0 = 0$, $\lambda_0 = 0.9\,pN/\mu m$, and $A_0 = 8\pi\,\mu m^2$. Based on our results, the membrane tubule becomes longer with increasing magnitude of the deviatoric curvature.

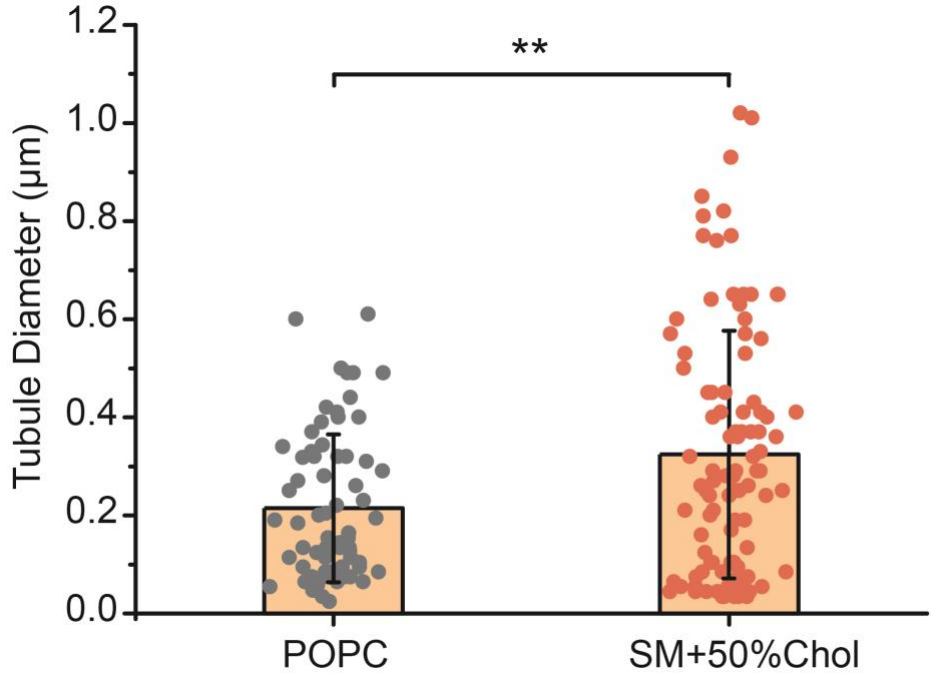

Figure 2. 21 The diameter of tubules induced by LAF-1 RGG phase separation increases as membrane bending rigidity increases. Bar chart shows the average tubule diameter of all measured tubules (N = 96). Error bars correspond to standard deviation. Data were collected from POPC and SM + 50%Chol GUVs incubated with 1μM atto-488 labeled his-LAF-1 RGG in 25 mM HEPES, 150 mM NaCl, pH 7.4 buffer. Brackets show

statistically significant comparisons using an unpaired, 2-tailed student's t test. ** represents $p < 0.01$.

Table 2. 1 Tubule frequency as a function of FUS LC concentration. GUVs consist of 93 mol% POPC, 5 mol% Ni-NTA, 2 mol% DP-EG10-biotin and 0.1 mol% Texas Red-DHPE. Data were collected from three independent replicates. Each replicate used a different batch of GUVs.

Protein Conc.(μM)	Experiment 1			Experiment 2			Experiment 3			Sum	
	w/ tubule	total	Tubule frequency (%)	w/ tubule	total	Tubule frequency (%)	w/ tubule	total	Tubule frequency (%)	Avg. tubule freq. (%)	Std. dev.
0.1	1	71	1.4	3	94	3.2	5	100	5	1.7	1.4
0.5	25	114	21.9	26	100	26	20	115	17.4	21.8	4.3
1	96	219	43.8	51	124	41.1	47	100	47	44	3.0
5	50	109	45.9	42	99	42.4	53	123	43.1	43.8	1.9
10	52	146	35.6	41	106	38.7	35	108	32.4	35.6	3.2
15	71	199	35.7	40	107	37.4	35	101	34.6	35.9	1.4
25	50	144	34.7	37	99	37.4	34	110	30.9	34.3	3.3

Table 2. 2 Percentage of GUVs displaying protein-rich phase separation (PS) domains as a function of Ni-NTA contents and NaCl concentration. GUVs primarily consist of POPC with varying Ni-NTA, 2 mol% DP-EG10-biotin and 0.1 mol% Texas Red-DHPE. N > 100 GUVs were analyzed cumulatively from three independent replicates for each condition. Each replicate used a different batch of GUVs.

Ni-NTA conc. (%)	NaCl Conc. (μM)	Experiment 1			Experiment 2			Experiment 3			Sum	
		PS	total	PS freq. (%)	PS	total	PS freq. (%)	PS	total	PS freq. (%)	Avg. PS freq. (%)	Std. dev.
2	50	1	26	3.8	2	27	7.4	2	44	4.5	5.3	1.9
	150	4	42	9.5	6	43	14.0	4	29	13.8	12.4	2.5
	250	12	44	27.3	11	70	15.7	14	63	22.2	21.7	5.8
5	50	7	48	14.6	11	66	16.7	6	35	17.1	16.1	1.4
	150	26	100	26	34	124	27.4	66	219	30.1	27.9	2.1
	250	47	96	49.0	15	36	41.7	40	67	59.7	50.1	9.0
15	50	23	36	63.9	17	39	43.6	34	63	54.0	53.8	10.1
	150	23	73	31.5	11	39	28.2	43	112	38.4	32.7	5.2

	250	41	95	43.2	39	81	48.1	10	26	38.5	43.3	4.8

Table 2. 3 Percentage of GUVs displaying inward tubules as a function of Ni-NTA contents and NaCl concentration. GUVs primarily consist of POPC with varying Ni-NTA, 2 mol% DP-EG10-biotin and 0.1 mol% Texas Red-DHPE. N > 100 GUVs were analyzed cumulatively from three independent replicates for each condition. Each replicate used a different batch of GUVs.

Ni-NTA conc. (%)	NaCl Conc. (μM)	Experiment 1			Experiment 2			Experiment 3			Sum	
		Tubule	total	Tubule freq. （%）	Tubule	total	Tubule freq. (%)	Tubule	total	Tubule freq. (%)	Avg. tubule freq. (%)	Std. Dev.
	50	0	26	0	0	27	0	0	44	0	0	0
2	150	0	42	0	0	43	0	0	29	0	0	0
	250	0	44	0	0	70	0	0	63	0	0	0
	50	4	48	8.3	5	66	7.6	1	35	2.9	6.3	3.0
5	150	47	100	47.0	51	124	41.1	96	219	43.8	44.0	2.9
	250	40	96	41.7	14	36	38.9	24	67	35.8	38.8	2.9
	50	15	36	41.7	11	39	28.2	24	63	38.1	36.0	7.0
15	150	42	73	57.5	20	39	51.3	52	112	46.4	51.7	5.6
	250	42	95	44.2	43	81	53.1	11	26	42.3	46.5	5.8

Table 2. 4 Summary of GUV compositions for different membrane bending rigidity experiments

Group	Membrane composition	Approximate Bending Rigidity from major components (k_BT)
DOPC	83 mol% DOPC, 15 mol% Ni-NTA, 2 mol% DP-EG10 biotin, 0.1% Texas Red DHPE	26 [77]
DPHPC	83 mol% DPHPC, 15 mol% Ni-NTA, 2 mol% DP-EG10 biotin, 0.1% Texas Red DHPE	29 [212]
POPC	83 mol% POPC, 15 mol% Ni-NTA, 2 mol% DP-EG10 biotin, 0.1% Texas Red DHPE	31 [213]

1:1 POPC: Cholesterol "POPC+50% Chol"	41.5 mol% POPC, 41.5 mol% Cholesterol, 15 mol% Ni-NTA, 2 mol% DP-EG10 biotin, 0.1% Texas Red DHPE	37 [214]
POPC+30% Sphingomyelin	58.1 mol% POPC, 24.9 mol% Sphingomyelin, 15 mol% Ni-NTA, 2 mol% DP-EG10 biotin, 0.1% Texas Red DHPE	42 [215]
1:1 Sphingomyelin: Cholesterol "SM+50% Chol"	41.5 mol% Sphingomyelin, 41.5 mol% Cholesterol, 15 mol% Ni-NTA, 2 mol% DP-EG10 biotin, 0.1% Texas Red DHPE	76 [216]

In addition, a batch of GUVs labeled with TR-Ceramide was made as a comparison. The composition was 83 mol% POPC, 15 mol% Ni-NTA, 2 mol% DP-EG10-biotin and 1 mol% TR-Ceramide.

Table 2. 5 Value of parameters in simulation

Figures	Parameters and values
Figure 2.3d	$C_0 = 1.34 - 3.5 \quad \mu m^{-1}$ $\kappa = 22 - 85\ k_B T$ $\lambda_0 = 0.9\ pN/\mu m$ $\kappa_{\text{ratio}} = 1$ $A_0 = 4\pi\ \mu m^2$
Figure 2.3f	$C_0 = 3.5 \quad \mu m^{-1}$ $\kappa = 22 - 85\ k_B T$ $\lambda_0 = 0.9\ pN/\mu m$ $\kappa_{\text{ratio}} = 20$ $A_0 = 4\pi\ \mu m^2$

Table 2. 6 Notation used in the model

Notation	Description	Units
W	Local energy per unit area	$pN/\mu m$
H	Mean curvature of surface	μm^{-1}
D	Curvature deviator	μm^{-1}
K	Gaussian curvature of surface	μm^{-1}
C	Spontaneous curvature	μm^{-1}
D_m	spontaneous deviatoric curvature	μm^{-1}

κ	Bending modulus	k_BT
κ_r	Nonlocal bending modulus	k_BT
κ_G	Gaussian modulus	k_BT
d	Bilayer thickness	nm
l	Persistence length	nm
b	Adsorption thickness	nm
ξ	protein multi-layer thickness	nm
θ^{ξ}	Surface coordinate	
$\boldsymbol{\kappa_\tau}$	Transverse curvature	μm^{-1}
$\boldsymbol{\kappa_v}$	Tangential curvature	μm^{-1}
λ	Membrane tension	$pN/\mu m$
ψ	Angle between radial and tangential vectors	
$\boldsymbol{n}$	Normal vector to membrane surface	Unit vector
$\boldsymbol{a_s}$	Tangential vector to membrane surface	Unit vector
R	Radial distance	μm
Z	Elevation from base plane	μm
s	Arc length	μm
A	Membrane area	μm^2
A_0	Area of the protein domain	μm^2
U	Interaction strength	k_BT
p	Pressure difference across the membrane	$pN/\mu m^2$
L	Shape equation variable	μm^{-1}
$\boldsymbol{k}$	Altitudinal basis vector	Unit vector
$\boldsymbol{e}(\theta)$	Azimuthal basis vector	Unit vector
$\boldsymbol{e_r}(\theta)$	Radial basis vector	Unit vector
x	Dimensionless radial distance	
y	Dimensionless height	
h	Dimensionless mean curvature	
c	Dimensionless spontaneous curvature	
I	Dimensionless L	
$\tilde{\lambda}$	Dimensionless membrane tension	
$\tilde{\kappa}$	Dimensionless bending modulus	

Supplementary Movie 2.1 Confocal image series of a GUV containing protein-lined tubules formed upon exposure to his-FUS LC (1 μM). Tubules are flexible and display dynamic changes in morphology. The images were taken along an axis perpendicular to the imaging plane. The images are 0.5 μm apart. The composition of the GUV was 83 mol% POPC, 15 mol% DOGS Ni-NTA, 2 mol% DP-EG10-biotin, and 0.1 mol% Texas Red-DHPE. The buffer composition was 25 mM HEPES, 150 mM NaCl, pH 7.4. The scale bar is 5 μm long. [Link]

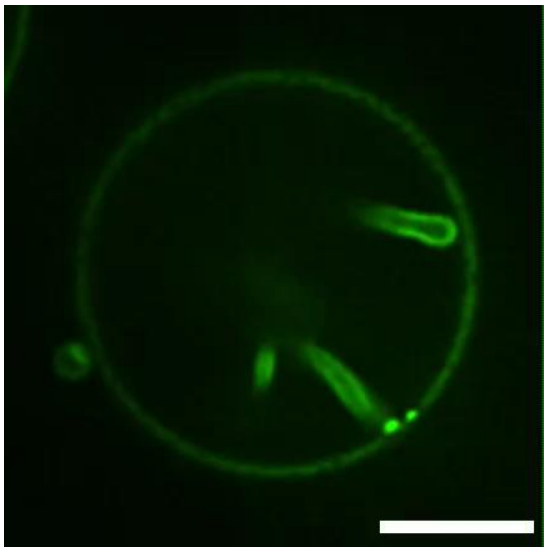

Supplementary Movie 2.2 On the top surface of a giant unilamellar vesicle (GUV), domains of the protein-depleted phase (dark), move randomly within the protein-enriched phase (bright), confocal image series. The ability of the depleted phase regions to move rapidly within the enriched phase, as well as fluctuations in the boundaries of the depleted phase, suggest that the enriched phase is liquid-like, rather than a rigid solid. The his-FUS LC protein was labeled with Atto-488. The protein concentration was 5 μM. The composition of the GUVs was 83 mol% POPC, 15 mol% DOPG-Ni-NTA, 2 mol% DP EG10-Biotin, 0.1% Texas Red DHPE and the experiment was performed in 25 mM HEPES, 150 mM NaCl, pH 7.4 buffer. The scale bar is 5 μm long. [Link]

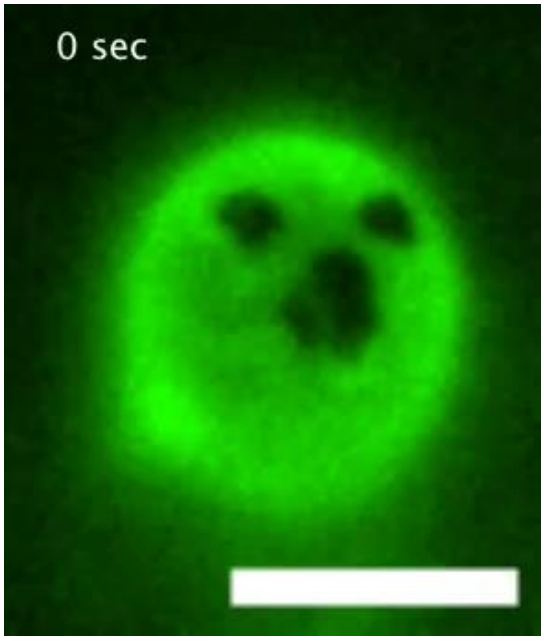

REFERENCES

36. DiMarzio, E. A. & McCrackin, F. L. One‐Dimensional Model of Polymer Adsorption. *The Journal of Chemical Physics* **43**, 539-547 (1965).

43. Hurley, J. H., Boura, E., Carlson, L.-A. & Różycki, B. Membrane budding. *Cell* **143**, 875-887 (2010).

52. Daumke, O., Roux, A. & Haucke, V. BAR domain scaffolds in dynamin-mediated membrane fission. *Cell* **156**, 882-892 (2014).

63. Snead, W. T. *et al.* BAR scaffolds drive membrane fission by crowding disordered domains. *J Cell Biol* **218**, 664-682 (2019).

73. Tsafrir, I. *et al.* Pearling instabilities of membrane tubes with anchored polymers. *Phys Rev Lett* **86**, 1138-1141 (2001).
74. Sanborn, J., Oglęcka, K., Kraut, R. S. & Parikh, A. N. Transient pearling and vesiculation of membrane tubes under osmotic gradients. *Faraday discussions* **161**, 167-176 (2013).
75. Helfrich, W. Elastic properties of lipid bilayers: theory and possible experiments. *Zeitschrift für Naturforschung C* **28**, 693-703 (1973).
77. Gracia, R. S., Bezlyepkina, N., Knorr, R. L., Lipowsky, R. & Dimova, R. Effect of cholesterol on the rigidity of saturated and unsaturated membranes: fluctuation and electrodeformation analysis of giant vesicles. *Soft Matter* **6**, 1472-1482 (2010).
109. Kirchhausen, T., Owen, D. & Harrison, S. C. Molecular structure, function, and dynamics of clathrin-mediated membrane traffic. *Cold Spring Harb Perspect Biol* **6**, a016725 (2014).
110. Mattila, P. K. & Lappalainen, P. Filopodia: molecular architecture and cellular functions. *Nature reviews Molecular cell biology* **9**, 446-454 (2008).
111. Zimmerberg, J. & Kozlov, M. M. How proteins produce cellular membrane curvature. *Nat Rev Mol Cell Biol* **7**, 9-19 (2006).
112. Stachowiak, J. C., Brodsky, F. M. & Miller, E. A. A cost-benefit analysis of the physical mechanisms of membrane curvature. *Nat Cell Biol* **15**, 1019-1027 (2013).
113. Drin, G. & Antonny, B. Amphipathic helices and membrane curvature. *FEBS letters* **584**, 1840-1847 (2010).
114. Christ, L., Raiborg, C., Wenzel, E. M., Campsteijn, C. & Stenmark, H. Cellular functions and molecular mechanisms of the ESCRT membrane-scission machinery. *Trends in biochemical sciences* **42**, 42-56 (2017).
115. Busch, D. J. *et al.* Intrinsically disordered proteins drive membrane curvature. *Nat Commun* **6**, 7875 (2015).
116. Brangwynne, Clifford P., Tompa, P. & Pappu, Rohit V. Polymer physics of intracellular phase transitions. *Nature Physics* **11**, 899-904 (2015).
117. Banjade, S. & Rosen, M. K. Phase transitions of multivalent proteins can promote clustering of membrane receptors. *Elife* **3** (2014).
118. Huang, W. Y. *et al.* A molecular assembly phase transition and kinetic proofreading modulate Ras activation by SOS. *Science* **363**, 1098-1103 (2019).
119. Alenquer, M. *et al.* Influenza A virus ribonucleoproteins form liquid organelles at endoplasmic reticulum exit sites. *Nature communications* **10**, 1-19 (2019).

120. Burke, K. A., Janke, A. M., Rhine, C. L. & Fawzi, N. L. Residue-by-Residue View of In Vitro FUS Granules that Bind the C-Terminal Domain of RNA Polymerase II. *Mol Cell* **60**, 231-241 (2015).
121. Murthy, A. C. *et al.* Molecular interactions underlying liquid− liquid phase separation of the FUS low-complexity domain. *Nature structural & molecular biology* **26**, 637-648 (2019).
122. Ryan, V. H. *et al.* Mechanistic view of hnRNPA2 low-complexity domain structure, interactions, and phase separation altered by mutation and arginine methylation. *Molecular cell* **69**, 465-479. e467 (2018).
123. Elbaum-Garfinkle, S. *et al.* The disordered P granule protein LAF-1 drives phase separation into droplets with tunable viscosity and dynamics. *Proceedings of the National Academy of Sciences* **112**, 7189-7194 (2015).
124. Veatch, S. L. & Keller, S. L. Separation of liquid phases in giant vesicles of ternary mixtures of phospholipids and cholesterol. *Biophysical journal* **85**, 3074-3083 (2003).
125. Baumgart, T., Hess, S. T. & Webb, W. W. Imaging coexisting fluid domains in biomembrane models coupling curvature and line tension. *Nature* **425**, 821-824 (2003).
126. Domanov, Y. A. *et al.* Mobility in geometrically confined membranes. *Proceedings of the National Academy of Sciences* **108**, 12605-12610 (2011).
127. Walker, A. E. Kreyszig, Differential Geometry (Mathematical Expositions No. 11, Toronto, and Oxford University Press, 1959), pp. xiv+ 352, 48s. *Proceedings of the Edinburgh Mathematical Society* **12**, 164-165 (1961).
128. Naito, H., Okuda, M. & Zhong-Can, O.-Y. New solutions to the Helfrich variation problem for the shapes of lipid bilayer vesicles: beyond Delaunay's surfaces. *Physical review letters* **74**, 4345 (1995).
129. Bar-Ziv, R. & Moses, E. Instability and" pearling" states produced in tubular membranes by competition of curvature and tension. *Physical review letters* **73**, 1392 (1994).
130. Snead, W. T. *et al.* Membrane fission by protein crowding. *Proc Natl Acad Sci U S A* **114**, E3258-E3267 (2017).
131. Indrani, C. H. V. & Lipowsky, R. Membranes with anchored polymers at the adsorption transition. *Europhysics Letters* **36**, 491 (1996).
132. Kim, Y. W. & Sung, W. Membrane curvature induced by polymer adsorption. *Physical Review E* **63**, 041910 (2001).

133. Wiese, W., Harbich, W. & Helfrich, W. Budding of lipid bilayer vesicles and flat membranes. *Journal of physics: Condensed matter* **4**, 1647 (1992).
134. Hayashi, S. Resolution doubling using confocal microscopy via analogy with structured illumination microscopy. *Japanese Journal of Applied Physics* **55**, 082501 (2016).
135. Frost, A., Unger, V. M. & De Camilli, P. The BAR domain superfamily: membrane-molding macromolecules. *Cell* **137**, 191-196 (2009).
136. Helfrich, W. & Prost, J. Intrinsic bending force in anisotropic membranes made of chiral molecules. *Physical Review A* **38**, 3065 (1988).
137. Janosi, L., Li, Z., Hancock, J. F. & Gorfe, A. A. Organization, dynamics, and segregation of Ras nanoclusters in membrane domains. *Proceedings of the National Academy of Sciences* **109**, 8097-8102 (2012).
138. Ford, M. G. *et al.* Curvature of clathrin-coated pits driven by epsin. *Nature* **419**, 361 (2002).
139. Lorent, J. H. *et al.* Structural determinants and functional consequences of protein affinity for membrane rafts. *Nature communications* **8**, 1219 (2017).
140. Harder, T., Scheiffele, P., Verkade, P. & Simons, K. Lipid domain structure of the plasma membrane revealed by patching of membrane components. *The Journal of cell biology* **141**, 929-942 (1998).
141. Kato, M. *et al.* Cell-free formation of RNA granules: low complexity sequence domains form dynamic fibers within hydrogels. *Cell* **149**, 753-767 (2012).
142. Murray, D. T. *et al.* Structure of FUS protein fibrils and its relevance to self-assembly and phase separation of low-complexity domains. *Cell* **171**, 615-627. e616 (2017).
143. Faini, M., Beck, R., Wieland, F. T. & Briggs, J. A. Vesicle coats: structure, function, and general principles of assembly. *Trends in cell biology* **23**, 279-288 (2013).
144. Luque, D. & Castón, J. R. Cryo-electron microscopy for the study of virus assembly. *Nature chemical biology* **16**, 231-239 (2020).
145. Römer, W. *et al.* Shiga toxin induces tubular membrane invaginations for its uptake into cells. *Nature* **450**, 670-675 (2007).
146. Campelo, F. & Hernández-Machado, A. Model for curvature-driven pearling instability in membranes. *Physical review letters* **99**, 088101 (2007).
147. Callan-Jones, A. & Bassereau, P. Curvature-driven membrane lipid and protein distribution. *Current Opinion in Solid State and Materials Science* **17**, 143-150 (2013).

148. Fošnarič, M. *et al.* Theoretical study of vesicle shapes driven by coupling curved proteins and active cytoskeletal forces. *Soft Matter* **15**, 5319-5330 (2019).
149. Alimohamadi, H. & Rangamani, P. Modeling membrane curvature generation due to membrane–protein interactions. *Biomolecules* **8**, 120 (2018).
150. Evans, E. A., Waugh, R. & Melnik, L. Elastic area compressibility modulus of red cell membrane. *Biophysical Journal* **16**, 585-595 (1976).
151. Rawicz, W., Olbrich, K., McIntosh, T., Needham, D. & Evans, E. Effect of chain length and unsaturation on elasticity of lipid bilayers. *Biophysical journal* **79**, 328-339 (2000).
152. Wang, S., Walton, K. D. & Gumucio, D. L. Signals and forces shaping organogenesis of the small intestine. *Current Topics in Developmental Biology* **132**, 31-65 (2019).
153. Tallinen, T. *et al.* On the growth and form of cortical convolutions. *Nature Physics* **12**, 588-593 (2016).
154. Hughes, A. J. *et al.* Engineered tissue folding by mechanical compaction of the mesenchyme. *Developmental cell* **44**, 165-178. e166 (2018).
155. Kralj-Iglič, V. *et al.* Amphiphile-induced tubular budding of the bilayer membrane. *European Biophysics Journal* **34**, 1066-1070 (2005).
156. Iglič, A., Babnik, B., Gimsa, U. & Kralj-Iglič, V. On the role of membrane anisotropy in the beading transition of undulated tubular membrane structures. *Journal of Physics A: Mathematical and General* **38**, 8527 (2005).
157. Iglič, A., Kralj-Iglič, V. & Majhenc, J. Cylindrical shapes of closed lipid bilayer structures correspond to an extreme area difference between the two monolayers of the bilayer. *Journal of biomechanics* **32**, 1343-1347 (1999).
158. Sens, P. & Turner, M. S. Theoretical model for the formation of caveolae and similar membrane invaginations. *Biophysical journal* **86**, 2049-2057 (2004).
159. Ridley, A. J. Life at the leading edge. *Cell* **145**, 1012-1022 (2011).
160. Pendin, D., McNew, J. A. & Daga, A. Balancing ER dynamics: shaping, bending, severing, and mending membranes. *Current opinion in cell biology* **23**, 435-442 (2011).
161. Buono, R. A. *et al.* ESCRT-mediated vesicle concatenation in plant endosomes. *Journal of Cell Biology* **216**, 2167-2177 (2017).
162. Snead, W. T. & Gladfelter, A. S. The control centers of biomolecular phase separation: how membrane surfaces, PTMs, and active processes regulate condensation. *Molecular cell* **76**, 295-305 (2019).

163. Momin, N. *et al.* Designing lipids for selective partitioning into liquid ordered membrane domains. *Soft Matter* **11**, 3241-3250 (2015).
164. DeGroot, A. C. *et al.* Entropic control of receptor recycling using engineered ligands. *Biophysical journal* **114**, 1377-1388 (2018).
165. Schuster, B. S. *et al.* Controllable protein phase separation and modular recruitment to form responsive membraneless organelles. *Nature communications* **9**, 1-12 (2018).
166. Stachowiak, J. C. *et al.* Membrane bending by protein-protein crowding. *Nat Cell Biol* **14**, 944-949 (2012).
167. Angelova, M. I. & Dimitrov, D. S. Liposome electroformation. *Faraday discussions of the Chemical Society* **81**, 303-311 (1986).
168. Zeno, W. F. *et al.* Synergy between intrinsically disordered domains and structured proteins amplifies membrane curvature sensing. *Nat Commun* **9**, 4152 (2018).
169. Sezgin, E. *et al.* Elucidating membrane structure and protein behavior using giant plasma membrane vesicles. *Nature protocols* **7**, 1042-1051 (2012).
170. Deuling, H. & Helfrich, W. Red blood cell shapes as explained on the basis of curvature elasticity. *Biophys. J.* **16**, 861-868 (1976).
171. Canham, P. B. The minimum energy of bending as a possible explanation of the biconcave shape of the human red blood cell. *Journal of theoretical biology* **26**, 61-81 (1970).
172. Rawicz, W., Olbrich, K. C., McIntosh, T., Needham, D. & Evans, E. Effect of chain length and unsaturation on elasticity of lipid bilayers. *Biophysical journal* **79**, 328-339 (2000).
173. Steigmann, D. Fluid films with curvature elasticity. (1999).
174. Rangamani, P., Agrawal, A., Mandadapu, K. K., Oster, G. & Steigmann, D. J. Interaction between surface shape and intra-surface viscous flow on lipid membranes. *Biomechanics and modeling in mechanobiology* **12**, 833-845 (2013).
175. Jenkins, J. T. Static equilibrium configurations of a model red blood cell. *Journal of mathematical biology* **4**, 149-169 (1977).
176. Hassinger, J. E., Oster, G., Drubin, D. G. & Rangamani, P. Design principles for robust vesiculation in clathrin-mediated endocytosis. *Proceedings of the national academy of sciences* **114**, E1118-E1127 (2017).
177. Alimohamadi, H., Ovryn, B. & Rangamani, P. Modeling membrane nanotube morphology: the role of heterogeneity in composition and material properties. *Scientific reports* **10**, 1-15 (2020).

178. Rangamani, P., Mandadap, K. K. & Oster, G. Protein-induced membrane curvature alters local membrane tension. *Biophys. J.* **107**, 751-762 (2014).
179. Miao, L., Seifert, U., Wortis, M. & Dobereiner, H. G. Budding transitions of fluid-bilayer vesicles: The effect of area-difference elasticity. *Phys Rev E Stat Phys Plasmas Fluids Relat Interdiscip Topics* **49**, 5389-5407 (1994).
180. Mukhopadhyay, R., Lim, H. W. G. & Wortis, M. Echinocyte shapes: bending, stretching, and shear determine spicule shape and spacing. *Biophys J* **82**, 1756-1772 (2002).
181. Dobereiner, H. G., Evans, E., Kraus, M., Seifert, U. & Wortis, M. Mapping vesicle shapes into the phase diagram: A comparison of experiment and theory. *Physical Review E* **55**, 4458-4474 (1997).
182. Foret, L. Shape and energy of a membrane bud induced by protein coats or viral protein assembly. *The European Physical Journal E* **37**, 42 (2014).
183. Walani, N., Torres, J. & Agrawal, A. Endocytic proteins drive vesicle growth via instability in high membrane tension environment. *Proceedings of the national academy of sciences* **112**, E1423-E1432 (2015).
184. Agrawal, A. & Steigmann, D. J. Modeling protein-mediated morphology in biomembranes. *Biomechanics and modeling in mechanobiology* **8**, 371 (2009).
185. Alimohamadi, H., Vasan, R., Hassinger, J. E., Stachowiak, J. C. & Rangamani, P. The role of traction in membrane curvature generation. *Molecular biology of the cell* **29**, 2024-2035 (2018).
186. Agrawal, A. & Steigmann, D. J. Boundary-value problems in the theory of lipid membranes. *Continuum Mechanics and Thermodynamics* **21**, 57-82 (2009).
187. Delaunay, C. Sur la surface de révolution dont la courbure moyenne est constante. *Journal de mathématiques pures et appliquées*, 309-314 (1841).
188. Mladenov, I. New solutions of the shape equation. *The European Physical Journal B-Condensed Matter and Complex Systems* **29**, 327-330 (2002).
189. Zhanchun, T., Jixing, L. & Yuzhang, X. *Geometric Methods in Elastic Theory of Membranes in Liquid Crystal Phases*. Vol. 2 (World Scientific, 2017).
190. Djondjorov, P., Hadzhilazova, M., Mladenov, I. M. & Vassilev, V. in *Proceedings of the Eleventh International Conference on Geometry, Integrability and Quantization.* 108-117 (Institute of Biophysics and Biomedical Engineering, Bulgarian Academy of …).
191. Fosnaric, M. *et al.* Theoretical study of vesicle shapes driven by coupling curved proteins and active cytoskeletal forces. *Soft Matter* **15**, 5319-5330 (2019).

192. Callan-Jones, A. & Bassereau, P. Curvature-driven membrane lipid and protein distribution. *Curr Opin Solid St M* **17**, 143-150 (2013).
193. Bobrovska, N., Gozdz, W., Kralj-Iglic, V. & Iglic, A. On the Role of Anisotropy of Membrane Components in Formation and Stabilization of Tubular Structures in Multicomponent Membranes. *Plos One* **8** (2013).
194. Iglic, A., Slivnika, T. & Kralj-Iglic, V. Elastic properties of biological membranes influenced by attached proteins. *J Biomech* **40**, 2492-2500 (2007).
195. Kralj-Iglič, V., Heinrich, V., Svetina, S. & Žekš, B. Free energy of closed membrane with anisotropic inclusions. *The European Physical Journal B-Condensed Matter and Complex Systems* **10**, 5-8 (1999).
196. Walani, N., Torres, J. & Agrawal, A. Anisotropic spontaneous curvatures in lipid membranes. *Physical Review E* **89**, 062715 (2014).
197. Alimohamadi, H., Bell, M., Halpain, S. & Rangamani, P. Mechanical principles governing the shapes of dendritic spines. *bioRxiv* (2020).
198. Campelo, F. & Hernández–Machado, A. Polymer-induced tubulation in lipid vesicles. *Physical review letters* **100**, 158103 (2008).
199. Rangamani, P., Behzadan, A. & Holst, M. Local sensitivity analysis of the 'membrane shape equation' derived from the Helfrich energy. *arxiv* **https://arxiv.org/pdf/2005.12550.pdf** (2020).
200. Indrani, C. H. V. & Lipowsky, R. Membranes with anchored polymers at the adsorption transition. *EPL (Europhysics Letters)* **36**, 491 (1996).
201. Kim, Y. W. & Sung, W. Vesicular budding induced by a long and flexible polymer. *EPL (Europhysics Letters)* **47**, 292 (1999).
202. Ryan, V. H. *et al.* Mechanistic View of hnRNPA2 Low-Complexity Domain Structure, Interactions, and Phase Separation Altered by Mutation and Arginine Methylation. *Mol Cell* **69**, 465-+ (2018).
203. Goetz, R. & Lipowsky, R. Computer simulations of bilayer membranes: self-assembly and interfacial tension. *The Journal of chemical physics* **108**, 7397-7409 (1998).
204. Grafmüller, A., Shillcock, J. & Lipowsky, R. The fusion of membranes and vesicles: pathway and energy barriers from dissipative particle dynamics. *Biophysical journal* **96**, 2658-2675 (2009).
205. Helfrich, W. Amphiphilic mesophases made of defects. *Physics of defects*, 715-755 (1981).

206. Marsh, D. Lateral pressure profile, spontaneous curvature frustration, and the incorporation and conformation of proteins in membranes. *Biophysical journal* **93**, 3884-3899 (2007).
207. Fournier, J.-B. On the stress and torque tensors in fluid membranes. *Soft Matter* **3**, 883-888 (2007).
208. Szleifer, I., Kramer, D., Ben‐Shaul, A., Gelbart, W. M. & Safran, S. A. Molecular theory of curvature elasticity in surfactant films. *The Journal of chemical physics* **92**, 6800-6817 (1990).
209. Gompper, G. & Klein, S. Ginzburg-Landau theory of aqueous surfactant solutions. *Journal de Physique II* **2**, 1725-1744 (1992).
210. Lipowsky, R. & Döbereiner, H.-G. Vesicles in contact with nanoparticles and colloids. *EPL (Europhysics Letters)* **43**, 219 (1998).
211. Lipowsky, R. Spontaneous tubulation of membranes and vesicles reveals membrane tension generated by spontaneous curvature. *Faraday discussions* **161**, 305-331 (2013).
212. Vitkova, V., Meleard, P., Pott, T. & Bivas, I. Alamethicin influence on the membrane bending elasticity. *Eur Biophys J* **35**, 281-286 (2006).
213. Bouvrais, H., Pott, T., Bagatolli, L. A., Ipsen, J. H. & Meleard, P. Impact of membrane-anchored fluorescent probes on the mechanical properties of lipid bilayers. *Biochim Biophys Acta* **1798**, 1333-1337 (2010).
214. Arriaga, L. R. *et al.* Stiffening Effect of Cholesterol on Disordered Lipid Phases: A Combined Neutron Spin Echo plus Dynamic Light Scattering Analysis of the Bending Elasticity of Large Unilamellar Vesicles. *Biophys. J.* **96**, 3629-3637 (2009).
215. Doktorova, M., Harries, D. & Khelashvili, G. Determination of bending rigidity and tilt modulus of lipid membranes from real-space fluctuation analysis of molecular dynamics simulations. *Physical Chemistry Chemical Physics* **19**, 16806-16818 (2017).
216. Roux, A. *et al.* Role of curvature and phase transition in lipid sorting and fission of membrane tubules. *Embo Journal* **24**, 1537-1545 (2005).

Chapter 3: The ins and outs of membrane bending by intrinsically disordered proteins [3]

ABSTRACT

The ability of proteins to generate curved membrane structures is essential to diverse cellular functions, from membrane traffic to nuclear transport. Established mechanisms of membrane bending require protein domains with specific structural features such as curved scaffolds and wedge-like amphipathic helices. However, recent work has shown that intrinsically disordered proteins, which lack a well-defined secondary structure, can also be potent drivers of membrane curvature. Specifically, steric pressure among membrane-bound disordered domains that repel one another can drive convex bending. In contrast, disordered domains that attract one another, forming liquid-like condensates, can drive concave bending by compressing membrane surfaces. How might disordered domains that contain both repulsive and attractive domains impact membrane curvature? Here we examine a series of recombinant chimeras that link attractive and repulsive domains within the same, membrane-bound protein. When the attractive domain was closer to the membrane, condensation of these domains helped to concentrate the repulsive domains, amplifying steric pressure, leading to convex curvature. In contrast, when the order of the attractive and repulsive domains was reversed, such that the repulsive domain was closer to the membrane surface, attractive interactions dominated, resulting in concave curvature. Further, a transition from convex to concave curvature was observed when an increase in ionic strength was used to simultaneously reduce steric clashes among the repulsive domains while increasing condensation of the attractive domains. In agreement with a

[3] This chapter is published as: Yuan F, Lee CT, Sangani A, Houser JR, Wang L, Lafer EM, Rangamani P, Stachowiak JC. The ins and outs of membrane bending by intrinsically disordered proteins. *Science Advances* **9**, eadg3485 (2023).

simple mechanical model, these results illustrate a set of design rules that can be used to control membrane curvature by adjusting the balance between attractive and repulsive interactions among disordered proteins.

INTRODUCTION

Highly curved membrane surfaces are found throughout the cell and play a role in a myriad of cellular processes, from endocytosis and exocytosis, to budding of enveloped viruses, protein recycling during autophagy, and the structure and maintenance of all organelles[43,217,218]. Protein-lipid interactions are known to drive membrane curvature through several established and emerging mechanisms. The first mechanisms of curvature generation to be characterized relied upon proteins with specific structural features. For example, insertion of a wedge-like amphipathic helix into the membrane surface increases the area of one membrane leaflet relative to the other, causing the membrane to bend toward the protein layer, such that convex membrane buds and tubules "coated" by proteins are created[113]. In a second mechanism, proteins that bind to membrane surfaces using inherently curved surfaces, such as BAR (Bin/Amphiphysin/RVS) domains, can drive the membrane to conform to their curvature. Interestingly, these scaffolds can have either convex or concave surfaces, enabling them to produce either protein-coated or protein-lined membrane buds and tubules, respectively[52].

More recent work has demonstrated that specific structural motifs, such as amphipathic helices and BAR domains, are not the only means of generating membrane

curvature. In particular, several reports have demonstrated that proteins without a well-defined secondary structure - intrinsically disordered proteins - are also capable of shaping membrane surfaces[115,219]. Several proteins involved in endocytosis, including AP180 and Epsin1, contain intrinsically disordered domains with substantial molecular weight (400-500 amino acids) and high net charge. When these domains become crowded on membrane surfaces, steric and electrostatic repulsion between them drives the membrane to bend toward the protein layer, such that the area available per protein domain is increased. This process leads to convex, protein-coated membrane buds and tubules[63,115]. Similarly, crowding among glycosylated proteins on the plasma membrane surface is thought to drive assembly of tube-like cellular protrusions[220].

In contrast, many disordered domains have recently been found to attract one another through a network of weak interactions, leading to condensation of a protein liquid phase[116,221]. When disordered domains with these attractive interactions encounter one another on membrane surfaces, they seek to maximize contact with one another, generating a compressive stress at the membrane surface[71]. This stress bends the membrane away from the protein layer such that the area per protein on the membrane surfaces is decreased, resulting in concave, protein-lined membrane buds and tubules.

These observations collectively suggest that the differential stresses induced by a layer of disordered proteins on the membrane surface can be tuned to control the directionality and magnitude of membrane bending. Importantly, disordered domains that are repulsive or non-interacting and disordered domains that attract one another, often exist within the

same protein, and have been characterized as “stickers” and “spacers”, respectively, by computational modeling efforts[88]. Therefore, to predict the overall impact of an intrinsically disordered protein on membrane curvature, we must understand how repulsive and attractive domains work together to apply bending stresses to the membrane surface.

Toward this goal, here we examine a series of disordered protein chimeras, which combine protein domains previously shown to drive either convex or concave membrane curvature. Using these chimeras, we demonstrate that disordered protein layers with opposite curvature preferences can either work together to amplify curvature or can oppose one another to create context-dependent control of membrane shape. In agreement with a simple mechanical model, this work outlines a set of design rules that can be used to understand the impact of disordered proteins on membrane curvature.

RESULTS

Attractive domains cluster repulsive domains at membrane surfaces, amplifying convex membrane bending.

Here we examine a series of recombinant protein chimeras which link disordered protein domains that predominantly repel one another with disordered domains that predominantly attract one another. For the repulsive domain, we have chosen the C-terminal domain of the endocytic adaptor protein, AP180. Previous work has demonstrated that this domain generates repulsive interactions at membrane surfaces through a combination of steric and electrostatic effects[222]. We used amino acids 328-518 of AP180, approximately the first third of the C-terminal domain, which has a net negative charge of

-21[222]. We will refer to this domain henceforth as the "short" version of AP180, or AP180S. For the attractive domain, we chose the low complexity domain of fused in sarcoma (FUSLC), residues 1-163. FUSLC is known to undergo liquid-liquid phase separation (LLPS) both in solution[120] and when recruited to membrane surfaces[71]. FUSLC domains attract one another through a combination of pi-pi and dipole-dipole interactions among amino acid side chains[116].

The first chimera we examined consisted of an N-terminal histidine tag, for attachment to DGS-NTA-Ni lipids, followed by the FUSLC and AP180S domains, FUSLC-AP180S (Figure 3.1a left panel). When this protein attaches to the membrane surface using its histidine tag, the FUSLC domain is closer to the membrane relative to AP180S (Figure 3.1a right panel). The individual domains, his-AP180S and his-FUSLC were used in control studies. Each protein was fluorescently labeled at amine groups using an N-hydroxysuccinimide (NHS)-reactive dye, Atto 488 for visualization, as described under Materials and Methods. The protein to Atto 488 ratio was less than 1:1. We observed the impact of each of the three proteins on membrane shape by incubating the proteins with giant unilamellar vesicles (GUVs) containing DOGS-Ni-NTA lipids. GUVs consisted of 83 mol% POPC, 15 mol% DGS-NTA-Ni, 2 mol% DP-EG10 biotin for coverslip tethering and 0.1 mol% Texas Red-DHPE for visualization.

When GUVs were exposed to 1 μM of his-AP180S, we observed protein recruitment to GUV surfaces within minutes, followed by emergence and extension of lipid tubules directed outward from the surfaces of GUVs (Figure 3.1b). Consistent with our previous

reports, these tubules were diffraction limited in width and had lengths that often approached or exceeded the initial diameter of the GUVs[115,166,223]. The tubules were visible in both the protein (Atto 488) and lipid (Texas Red) fluorescent channels. Because the protein was added to the outside of the GUVs and was excluded from the GUV lumens (Figure 3.7), we inferred that the protein must coat the outer surfaces of these convex tubules, as we have reported previously[115]. Approximately 33% of GUVs exposed to his-AP180S displayed outwardly directed membrane tubules, while inwardly directed tubules were observed very rarely (Figure 3.1e).

In contrast, when GUVs were exposed to 1 μM of his-FUCLC, the protein was recruited to GUV surfaces within minutes, followed by emergence of inwardly directed membrane tubules. As we have reported previously[71], these tubules often displayed undulating morphologies, with diameters ranging from a few hundred nanometers to micrometers, such that the lumens of the tubules could often be resolved by fluorescence microscopy with deconvolution, Figure 3.1c. As with tubules formed upon addition of his-AP180S, tubules formed upon addition of his-FUSLC colocalized in the membrane and protein fluorescent channels. Owing to exclusion of protein from the GUV lumen, and the inward direction of the tubules, we inferred that the his-FUSLC protein lined these concave tubules[71]. Approximately 52% of GUVs exposed to his-FUSLC displayed inwardly directed membrane tubules, while outwardly directed tubules were observed very rarely (Figure 3.1e). Notably, outwardly directed tubules were generally narrower than inwardly directed tubules, likely because the attractive interactions between proteins that drive

inward tubules tend to simultaneously increase the membrane rigidity[71], making it more difficult to curve the membrane.

When GUVs were exposed to 1 μM of the chimera, his-FUSLC-AP180S, it bound rapidly to the membrane surface, similar to the control proteins. Shortly after binding to the membrane surface, outwardly directed, protein-coated tubules were observed on GUV surfaces (Figure 3.1d), similar in morphology to those created by binding of his-AP180S (Figure 3.1b). Quantification of the frequency with which outwardly-directed tubules were observed revealed that the chimera, his-FUSLC-AP180S, was more likely to generate tubules when applied at a given solution concentration, in comparison to his-AP180S (Figure 3.1f). Increasing the concentration of sodium chloride (NaCl) in the buffer slightly decreased the formation of outwardly directed membrane tubules by his-AP180S, presumably by screening electrostatic repulsion, as described previously[222]. In contrast, the same increase in NaCl concentration somewhat increased formation of outwardly directed tubules by the chimera, his-FUSLC-AP180S, Figure 3.1g. This trend suggests that clustering of FUSLC domains, which increases with increasing NaCl concentration[120], promotes outward tubule formation by the chimera. Notably, changes in pH might also be capable of shifting the balance between attractive and repulsive interactions among the chimeras. However, the significant shifts in pH that would be required to change the net charge of the chimeras are likely to also change the mechanical properties of the membranes[224], making the results difficult to interpret. Collectively, these results suggest that the presence of the FUSLC domain enhanced formation of outward tubules by the AP180S domain, perhaps by forming local clusters of the protein, which would be expected

to enhance membrane binding, helping to generate local steric pressure (Figure 3.1h), which is then relaxed by membrane bending. In particular, when FUSLC domains bind to one another, their associated AP180S domains are brought into close contact with one another, resulting in a local increase in the density of AP180 domains on the membrane surface. Because steric pressure is expected to increase non-linearly with increasing density of AP180 domains[115], the close contact created by association between the FUSLC domains is likely responsible for the increased capacity of his-FUSLC-AP180S to generate protein-coated membrane tubules in comparison to his-AP180S[63].

These results suggest that the preference of the AP180S domain for convex curvature dominate over the preference of FUSLC for concave curvature. This dominance could result simply from the magnitude of the repulsive interactions generated by AP180S exceeding the magnitude of attractive interactions generated by FUSLC. Alternatively, the dominance of AP180S could arise from its position further from the neutral surface of the curved membrane, such that repulsive interactions among AP180S domains generate a larger bending moment in comparison to attractive interactions among FUSLC domains, as depicted in Figure 3.1h. Based on these results alone, it is unclear to what extent the order of the protein domains relative to the membrane surface plays a role in curvature generation.

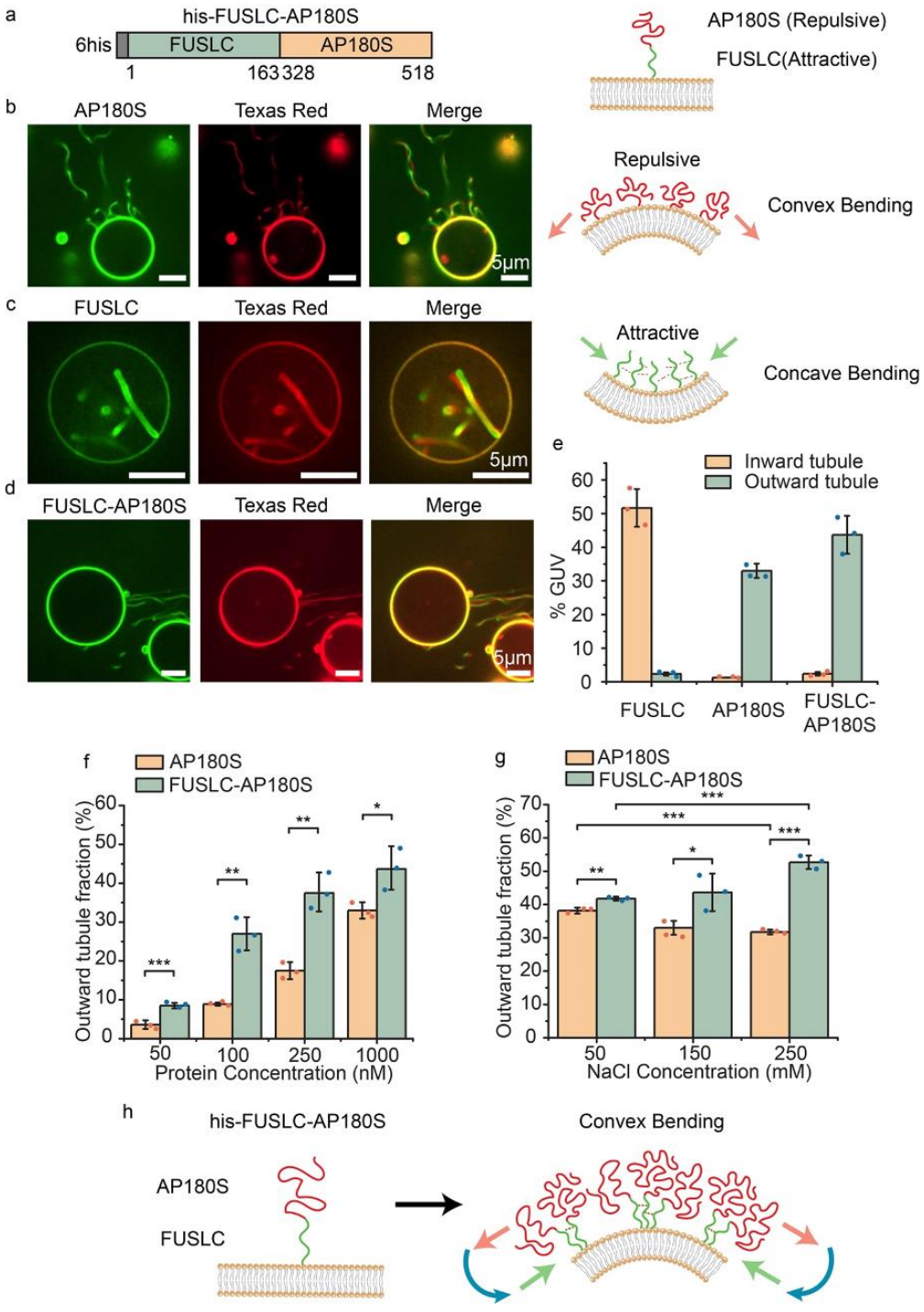

Figure 3. 1 Attractive domains cluster repulsive domains at membrane surfaces, amplifying convex membrane bending. (a) Schematic of the recombinant chimera his-

FUSLC-AP180S (left panel) and the expected orientation of the two domains relative to the membrane surface, when the histidine tag binds to Ni-NTA lipids (right panel). (b) Representative images of protein-coated tubules emanating from GUV surfaces (protein and lipid channels) when incubated with 1μM his-AP180S (left panel), and the cartoon of membrane convex bending by intrinsically disordered proteins (IDPs) that repel one another (right panel). (c) Representative super-resolution images of protein-lined tubules emanating from GUV surface when incubated with 1 μM his-FUSLC (left panel) and the corresponding cartoon of concave membrane bending by IDPs that attract one another (right panel). (d) Representative images of outward tubule formation when 1 μM his-FUSLC-AP180S was applied to GUVs. All scale bars are 5 μm. (e) The fraction of GUVs displaying inward and outward tubules when incubated with 1 μM his-FUSLC, his-AP180S, or his-FUSLC-AP180S. (f, g) The fraction of GUVs displaying outward tubules as a function of protein concentration (f), and under different NaCl concentrations when incubated with 1 μM protein (g). Error bars represent the standard deviation of three independent trials (displayed by the dots). Significance was evaluated using an unpaired, two-tailed student's t test. *: $P < 0.05$, **: $P < 0.01$, ***: $P < 0.001$. Significance comparison between inward and outward tubule fraction for FUSLC, AP180S, and FUSLC-AP180S in panel (e) all have p value smaller than 0.001. GUV membrane composition was 83 mol% POPC, 15 mol% DGS-NTA-Ni, 2 mol% DP-EG10 biotin, and 0.1 mol% Texas Red-DHPE. All experiments were conducted in 25 mM HEPES, 150 mM NaCl buffer, pH 7.4 unless the NaCl concentration was specifically adjusted as shown in individual panels. (f) Schematic of attractive interactions among FUSLC domains amplifying crowding and repulsion among AP180S domains, leading to convex membrane bending.

Reversing the order of the domains relative to the membrane surface reverses the direction of membrane curvature.

Based on our findings in Figure 3.1, we next asked what might happen if we reversed the order of the domains, creating a chimera that combined repulsive interactions at the membrane surface with attractive interactions farther away. To answer this question, we created the chimera his-AP180S-FUSLC, Figure 3.2a. When this chimera, labeled with Atto488 dye, bound to the surfaces of GUVs, we observed phase separation of the protein on the membrane surface, resulting in rounded, spherical cap-like structures on the membrane surface, which were enriched in the chimeric protein, Figure 3.2b. These structures were similar to those that we observed previously with his-FUSLC[71], suggesting

that the his-AP180S-FUSLC chimera underwent coacervation on membrane surfaces. Within minutes after protein binding, many of the protein-rich regions spontaneously curved inward, creating protein-lined membrane tubules with similar morphologies to those observed upon exposure of vesicles to his-FUSLC, Figure 3.2c. The fraction of GUVs displaying protein phase separation and protein-lined tubules increased significantly as salt concentration increased (Figure 3.2d), suggesting that the attractive interaction became stronger at higher salt concentration, which is consistent with the behavior of FUSLC alone[71,120]. Similarly, the diameters of the tubules formed by the his-AP180S-FUSLC chimera were typically resolvable using deconvoluted confocal fluorescence microscopy. Interestingly, the distribution of tubule diameter shifted toward larger values as the concentration of NaCl increased, Figure 3.2e. This shift may be due to increased attraction among FUSLC domains with increasing salt concentration[120], which may increase the rigidity of the protein layer on the membrane surface, making it more difficult for the membrane to take on high curvature[71]. Notably, the fraction of vesicles displaying phase separation, the fraction of vesicles displaying inward tubules, and the average diameter of the tubules were all significantly lower than the corresponding values for vesicles exposed to FUSLC alone (Figure 3.8)[71]. These results suggest that AP180S may weaken the attractive interactions among FUSLC domains, such that phase separation is less effective, leaving the membrane more flexible, such that tubules of higher curvature can be formed.

Collectively, these results suggest that attractive interactions among FUSLC domains at a distance from the membrane surface drive the membrane to bend inward, generating protein-lined tubules. The observation that the two chimeras, his-FUSLC-AP180S and his-AP180S-FUSLC generate tubules of opposite curvature suggests that the two chimers create stresses with opposite signs on the membrane surface. In particular, the observation

of convex, outwardly directed tubules, suggests that his-FUSLC-AP180S stretches the outer membrane leaflet while compressing the inward leaflet, generating a bending moment orientated as shown in Figure 3.1h. This orientation is consistent with attractive forces closer to the membrane surface and repulsive forces farther away, as depicted in the figure. In contrast, the observation of concave, inwardly directed tubules, suggests that his-AP180S-FUSLC compresses the outer membrane leaflet while stretching the inward leaflet, generating a bending moment that is oriented as shown in Figure 3.2f, opposite to that in Figure 3.1h. This orientation is consistent with repulsive forces adjacent to the membrane surface and attractive forces farther away, as indicated in the figure. Both results suggest that AP180S and FUSLC form somewhat separate layers on the membrane surface, which is consistent with the relative exclusion of AP180S from droplets consisting of FUSLC (Figure 3.9). Collectively, these results demonstrate that the orientation of disordered protein domains relative to the membrane surface can be used to control the magnitude and direction of the bending moment they exert, ultimately providing control over membrane shape.

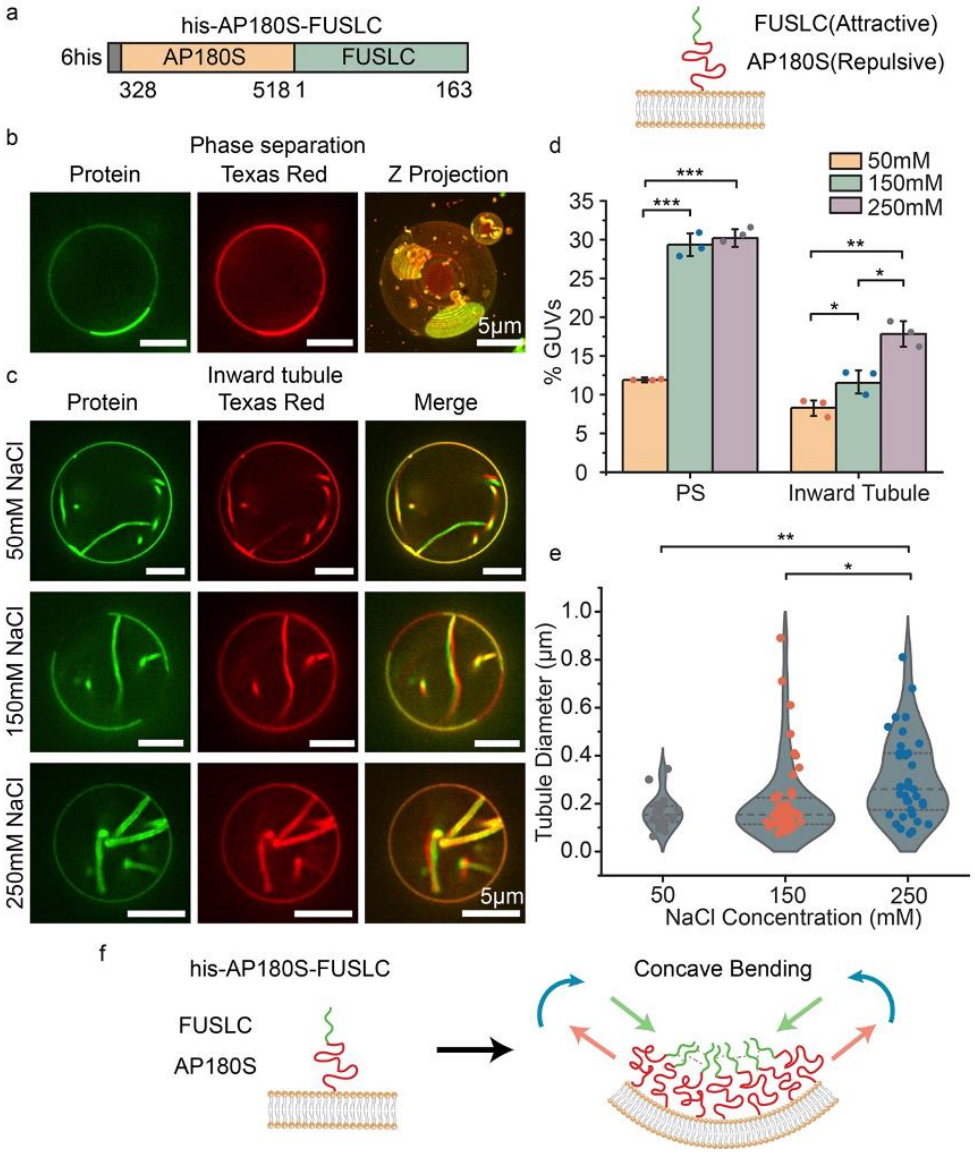

Figure 3. 2 Using a repulsive domain to link an attractive domain to the membrane surface generates protein-lined, concave membrane tubules. (a) Schematic of the recombinant chimera his-AP180S-FUSLC (left panel) and the orientation of his-AP180S-FUSLC on the membrane surface when it binds to DGS-NTA-Ni lipids (right panel). (b) Representative super-resolution images (protein and lipid channel) of protein liquid-liquid phase separation when GUVs were exposed to 1 μM his-AP180S-FUSLC in 25 mM HEPES, 150 mM NaCl buffer, pH 7.4. (c) Representative protein and lipid channel confocal images of tubules emanating inward from GUV surfaces when incubated with 1 μM his-AP180S-FUSLC in 25 mM HEPES, pH 7.4 buffer containing 50 mM, 150 mM,

and 250 mM NaCl, respectively. Scale bar is 5 μm. (d) Fraction of GUVs showing protein phase separation (PS) and inward tubules in the presence of different NaCl concentrations. (e) Violin plot displaying inward tubule diameter distribution in the presence of different NaCl concentrations. Error bars represent the standard deviation from three independent trials (shown by the dots). In total, n >100 GUVs were imaged for each NaCl concentration. Statistical significance was tested using an unpaired, two-tailed student's t test. *: $P < 0.05$, **: $P < 0.01$, ***: $P < 0.001$. GUV composition was 83 mol% POPC, 15 mol% DGS-NTA-Ni, 2 mol% DP-EG10 biotin, and 0.1 mol% Texas Red-DHPE. (f) Schematic of concave membrane bending when attractive domains are further from the membrane surface, relative to repulsive domains.

Combining chimeras with opposite impacts on membrane curvature provides control over membrane shape.

If his-FUSLC-AP180S and his-AP180S-FUSLC apply opposite bending stresses on the membrane surface, then it should be possible to control the direction of membrane bending by exposing vesicles to varying ratios of the two chimeras (Figure 3.3a). To evaluate this prediction, we exposed giant vesicles (unlabeled) to his-AP180S-FUSLC, labeled with Atto488 (green), and his-FUSLC-AP180S, labeled with Atto594 (red) (Figure 3.3a, 3b). his-FUSLC-AP180S and his-AP180S-FUSLC were combined in ratios ranging from 0.1: 1 to 1:1. At the lowest ratios, where his-AP180S-FUSLC dominated, vesicles with inwardly-directed tubules were most common (Figure 3.3c top panel). In contrast, for the highest ratios, where the two chimeras had equal concentrations, outwardly directed tubules dominated (Figure 3.3c bottom panel). For the intermediate ratio of 0.25:1, inward and outward tubules each existed in about 5% of vesicles separately, with the remaining 90% of membranes lacking tubules (Figure 3.3c middle panel and Figure 3.3d). In all cases, it was very rare to observe vesicles with both inward and outward tubules present simultaneously. Instead, nearly all vesicles exhibited tubules of a single orientation, (Figure 3.3d). These results suggest that the bending moments generated by the two chimeras can be balanced out when they are combined, stabilizing a relatively flat membrane

morphology. This balance is likely enabled by the ability of the two chimeras to mix with one another when they bind to membrane surfaces. At all ratios, we observed colocalization between the fluorescence signals associated with the two proteins, suggesting that they were not segregated on the membrane surface. This mixing behavior is expected, as both chimeras contain the FUSLC domain. Nonetheless, inward tubules appeared somewhat enriched in the chimera that prefers concave curvature, his-AP180S-FUSLC (Figure 3.3c, 0.1:1, 3.10), while outward tubules appeared somewhat enriched in the chimera that prefers convex curvature, his-FUSLC-AP180S (Figure 3.3c, 0.5:1). Taken together, these results illustrate that protein domains with opposite curvature preferences can work together to maintain flat membrane surfaces.

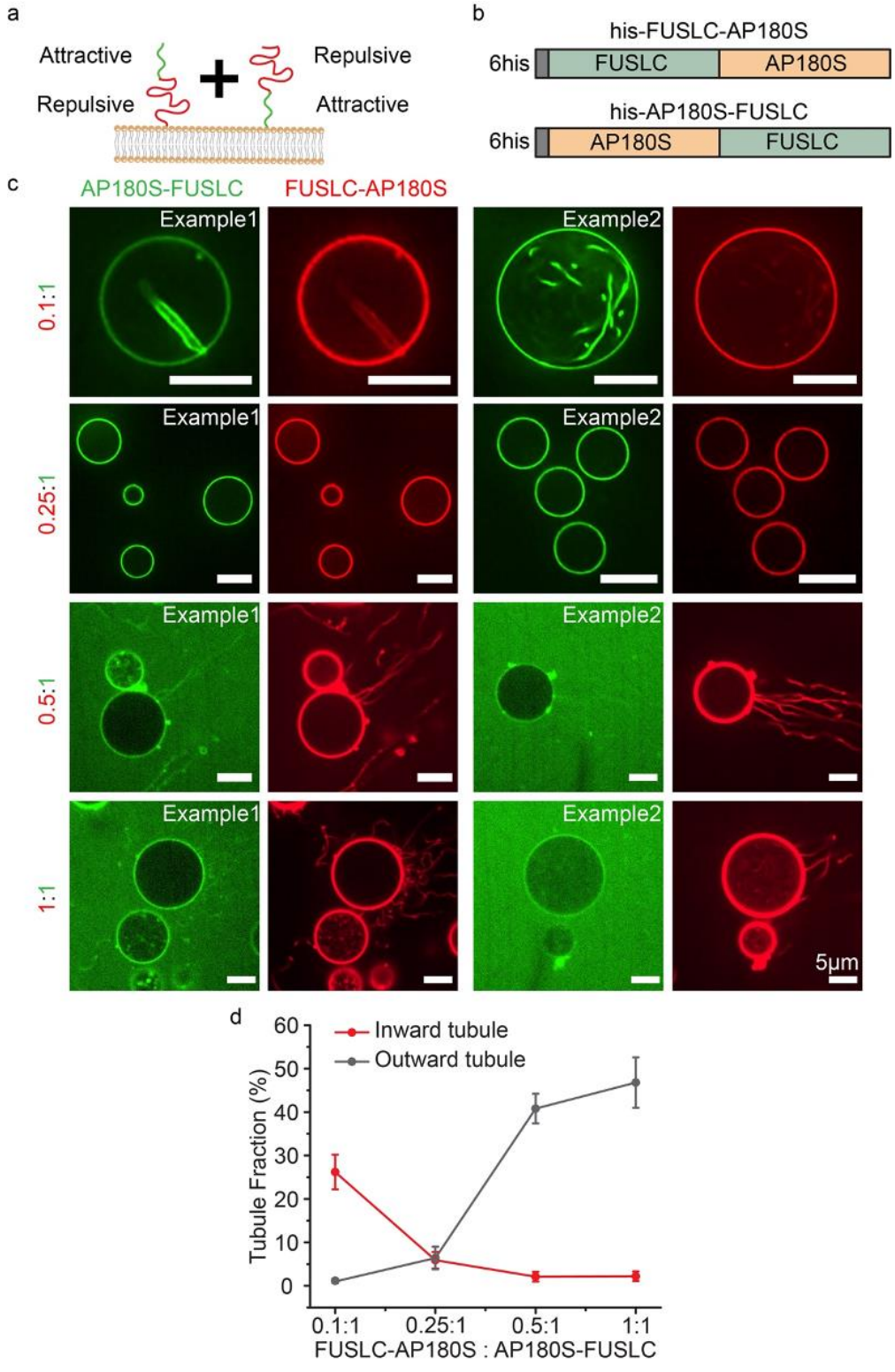
a
Attractive
Repulsive
Repulsive
Attractive
b
his-FUSLC-AP180S
6his
FUSLC
AP180S
his-AP180S-FUSLC
6his
AP180S
FUSLC
c
AP180S-FUSLC
FUSLC-AP180S
Example1
Example2
0.1:1
0.25:1
0.5:1
1:1
5μm
d
Inward tubule
Outward tubule
Tubule Fraction (%)
60
50
40
30
20
10
0
0.1:1
0.25:1
0.5:1
1:1
FUSLC-AP180S : AP180S-FUSLC

Figure 3. 3 Combining chimeras with opposite impacts on membrane curvature provides control over membrane shape. (a) Cartoon of adding his-FUSLC-AP180S and his-AP180S-FUSLC simultaneously to the membrane and the relative position of the attractive and repulsive domains relative to the membrane surface. (b) Schematic of the two recombinant chimera his-FUSLC-AP180S and his-AP180S-FUSLC. (c) Representative confocal images of GUVs incubated with his-FUSLC-AP180S and his-AP180S-FUSLC, mixed at different ratios (from 0.1:1 to 1:1). His-AP180S-FUSLC was maintained at 1 μM in all conditions. Experiments were done in 25 mM HEPES, 150 mM NaCl buffer, pH 7.4. GUV composition was 83 mol% POPC, 15 mol% DGS-NTA-Ni, 2 mol% DP-EG10 biotin, and 0.1 mol% Texas Red-DHPE. All scale bars are 5 μm. (d) The frequency of GUVs displaying outward tubules and inward tubules as a function of his-FUSLC-AP180S to his-AP180S-FUSLC ratio. Error bars represent the standard deviation from three independent trials. In total n >200 GUVs were imaged for each ratio.

Ionic strength can shift the balance between attractive and repulsive interactions, reversing the direction of membrane curvature.

If membrane curvature results from the balance between attractive and repulsive interactions among disordered domains, then it should be possible to modulate curvature by perturbing this balance. We tested this principle by using changes in ionic strength to vary the relative magnitude of attractive and repulsive interactions. Specifically, to achieve a greater dynamic range in the magnitude of the repulsive interactions, we created a new chimera, which linked FUSLC to the full C-terminal domain of AP180 (residues 328-898), which has a net negative charge of -32[222]. We will refer to this domain as the "long version" of AP180, or AP180L, yielding the chimera, his-AP180L-FUSLC, Figure 3.4a, 4b. By incorporating a larger portion of AP180, with a larger hydrodynamic radius[222], this chimera should generate a larger steric pressure, which may be capable of overcoming the attractive interactions among the FUSLC domains, depending on the ionic strength. It is worth noting that the effect of his-FUSLC-AP180L was not tested, since, on the basis of our findings with his-FUSLC-AP180S, we would simply expect more outward tubules if we were to make the repulsive domain larger.

Giant vesicles were exposed to 1 μM of his-AP180L-FUSLC at a range of NaCl concentrations: 50 mM, 150 mM, and 250 mM, Figure 3.4c, d. At 50 mM NaCl, exposure to the chimera drove formation of protein-coated, outwardly directed membrane tubules. This result suggests that electrostatic repulsion among the AP180L domains, which is maximized at low NaCl concentration, dominated over attractive interactions between FUSLC domains, setting up an outwardly directed bending moment, as shown in Figure 3.4e, top. In contrast, at the higher salt concentrations, 150 mM and 250 mM, exposure to the chimera drove formation of protein-lined, inwardly directed tubules, suggesting that repulsive interactions among the AP180L domains, which are reduced at higher salt concentrations, were overcome by attractive interactions among FUSLC domains, setting up an inwardly directed bending moment, as shown in Figure 3.4e, bottom. Further, we were able to observe the transition from outward to inward tubules *in-situ* as we gradually changed the NaCl concentration from 50 mM to 150 mM (Figure 3.4f). Collectively these results demonstrate that it is possible to control the direction of membrane bending by changing environmental conditions, such as ionic strength, which alter the balance between attractive and repulsive interactions among disordered protein domains. Depending on the domains used, other environmental variables such as pH, temperature, and the presence of multivalent ligands could also be used to tune interaction strength.

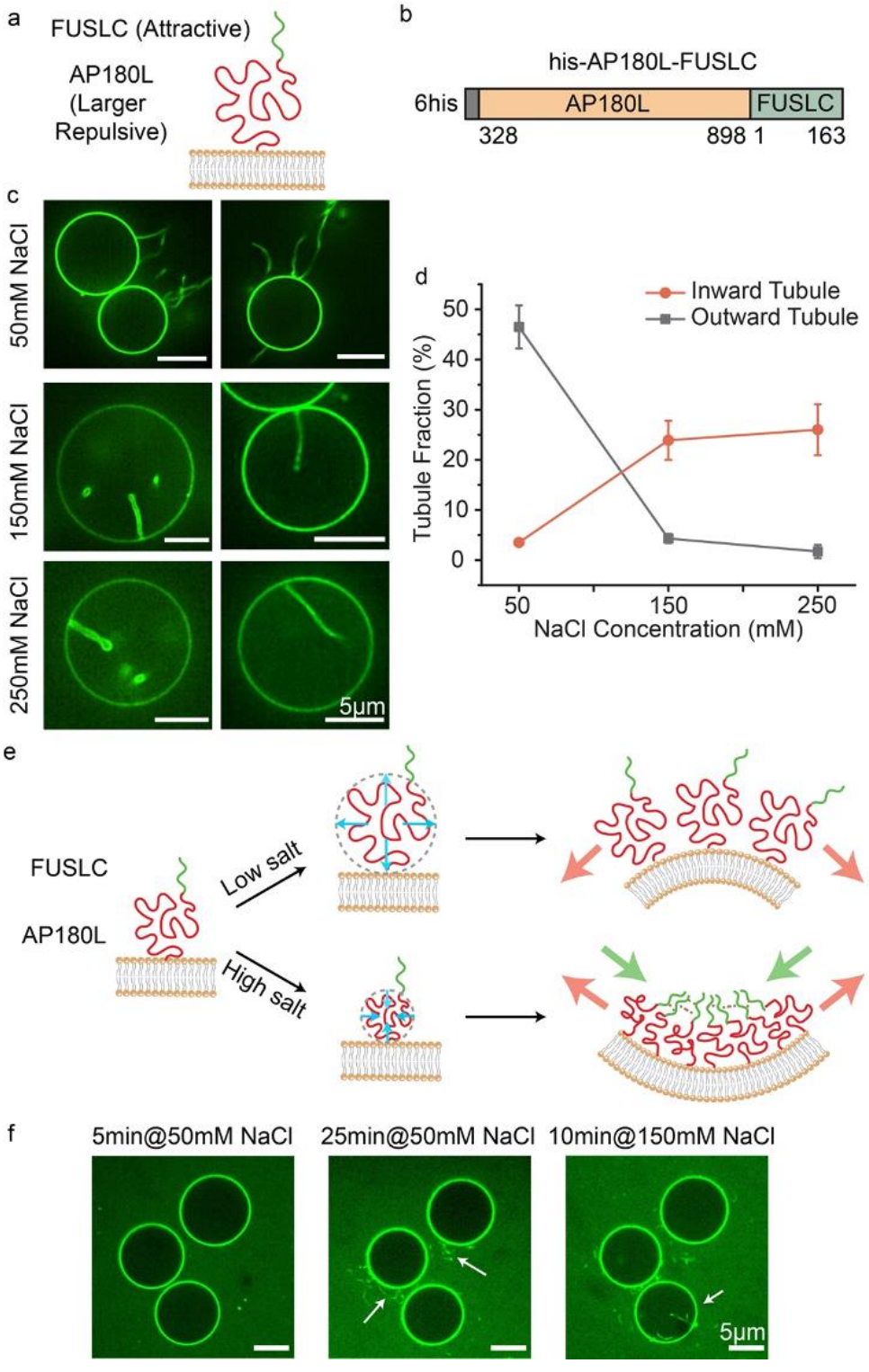
a
FUSLC (Attractive)
AP180L
(Larger
Repulsive)
b
his-AP180L-FUSLC
6his
AP180L
FUSLC
328
898 1
163
c
50mM NaCl
150mM NaCl
250mM NaCl
5μm
d
Inward Tubule
Outward Tubule
Tubule Fraction (%)
0
10
20
30
40
50
50
150
250
NaCl Concentration (mM)
e
FUSLC
AP180L
Low salt
High salt
f
5min@50mM NaCl
25min@50mM NaCl
10min@150mM NaCl
5μm

Figure 3. 4 Ionic strength can shift the balance between attractive and repulsive interactions, reversing the direction of membrane curvature. (a,b) Schematic of the orientation of his-AP180L-FUSLC when binding to the membrane (a), and the diagram of the domains (b). (c) Representative deconvoluted images of GUVs when incubated with 1 μM his-AP180L-FUSLC in 25 mM HEPES, pH 7.4 buffer containing 50 mM, 150 mM, and 250 mM NaCl, respectively. Scale bar is 5 μm. (d) The frequency of GUVs displaying outward tubules and inward tubules as a function of NaCl concentration. Error bars represent the standard deviation of three trials. n > 90 GUVs were imaged in each trial. GUV composition was 83 mol% POPC, 15 mol% DGS-NTA-Ni, 2 mol% DP-EG10 biotin, and 0.1 mol% Texas Red-DHPE. (e) Schematic depicting dependence of membrane curvature on ionic strength. (f) *In-situ* observation of outward and inward tubule formation as salt concentration increases.

Reversing the response of the attractive domain to ionic strength reverses the direction of membrane tubules.

Having demonstrated the ability to control the direction of membrane curvature by varying ionic strength, we next sought to test the generality of the principle by altering the response of the attractive domain to NaCl concentration. Specifically, we replaced FUSLC with the RGG domain (1-168) of the Laf-1 protein[123,165], another disordered domain that is known to undergo liquid-liquid phase separation. RGG is rich in positively charged arginine residues and negatively charged aspartic acid residues, such that electrostatic attraction plays a major role in the coacervation of RGG domains[116]. For this reason, attraction between RGG domains is expected to decrease with increasing NaCl concentration, opposite to the response of FUSLC.

To test the impact of replacing FUSLC with RGG, we constructed a chimera between AP180L and RGG, his-AP180L-RGG (Figure 3.5a). We exposed giant unilamellar vesicles to these chimeras at a concentration of 1 μM, while gradually increasing the NaCl concentration. At the lowest concentrations of NaCl, inwardly directed tubules were much more probable in comparison to outwardly directed tubules, which were rarely observed

(Figure 3.5b). This result suggests that electrostatic interactions among RGG domains, which are strongest at low salt concentration, dominated over repulsive interactions among AP180L domains, leading to an inwardly directed bending moment, similar to what was observed for the his-AP180L-FUSLC chimera at high salt concentration.

As the NaCl concentration increased, the frequency of inwardly directed tubules fell as the frequency of outwardly directed tubules increased. Only at 1 M NaCl did outwardly directed tubules become more frequent than inwardly directed tubules (Figure 3.5c). As predicted, this trend is opposite to that observed for his-AP180L-FUSLC, where outwardly directed tubules dominated at low salt concentrations. Interestingly, when we added urea (at 250 mM NaCl) to attenuate all protein-protein interactions, we mainly observed outward tubules, as would be expected when non-specific, steric interactions are dominant. This result is the opposite of what we observed at the same NaCl concentration in the absence of urea (Figure 3.5d, e), further confirming that specific, attractive interactions among RGG domains provided the driving force for inward bending of the membrane. Collectively these results demonstrate that by reversing the response of the attractive domain to changes in ionic strength, it is possible to reverse the sign of the bending moment that the protein layer applies to the membrane, resulting in a reversal of the direction of membrane curvature.

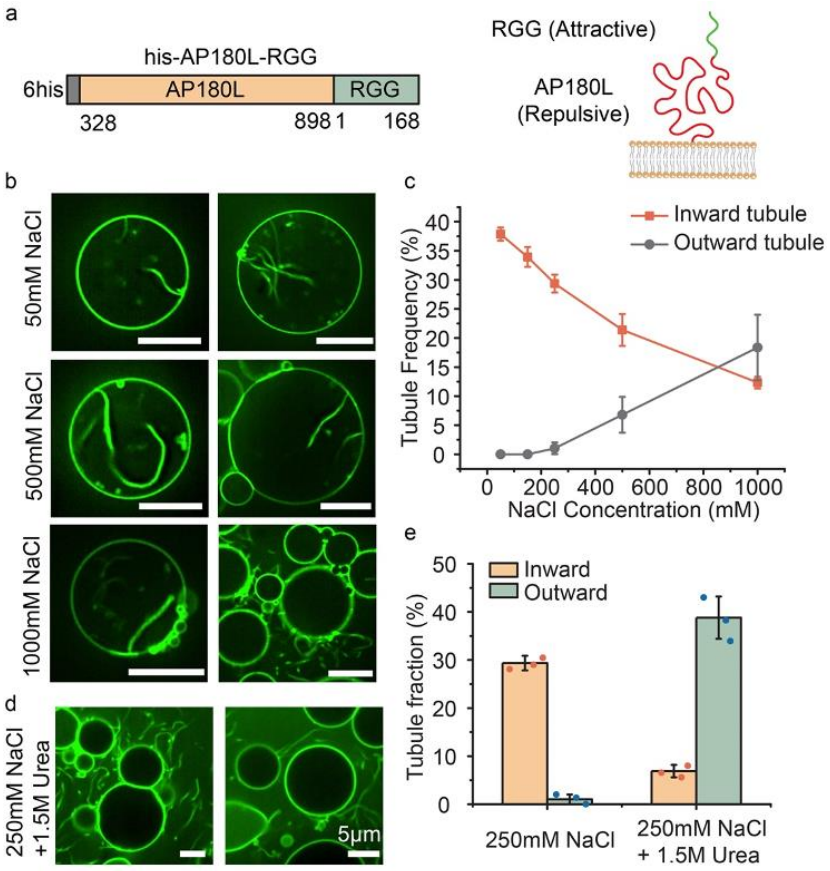

Figure 3. 5 Reversing the response of the attractive domain to ionic strength reverses the direction of membrane tubules. (a) Schematic of his-AP180L-RGG domains (left panel) and their orientation relative to the membrane (right panel). (b) Representative confocal images of tubules emanating from GUVs incubated with 1 μM his-AP180L-RGG in 25 mM HEPES, pH 7.4 buffers containing 50 mM, 500 mM, or 1000 mM NaCl, respectively. (c) The fraction of GUVs displaying inward and outward tubules as a function of NaCl concentration. Data represent mean ± standard deviation, n = 3 independent experiments. (d) Representative confocal images of tubules emanating from GUVs incubated with 1 μM his-AP180L-RGG in 25 mM HEPES, 250 mM NaCl, pH 7.4 buffer with 1.5 M urea. (e) The fraction of GUVs exhibiting inward and outward tubules after exposure to 1 μM his-AP180L-RGG in 25 mM HEPES, 250 mM NaCl pH 7.4 buffer and 25 mM HEPES, 250 mM NaCl pH 7.4 buffer with 1.5 M urea. Error bars represent the standard deviation of three independent trials (indicated by the dots). Statistical significance between inward and outward tubule frequency was tested by an unpaired, two-tailed student's t test. In panel (e) both have p values were smaller than 0.001. n > 100 GUVs were imaged in each trial. GUV composition was 83 mol% POPC, 15 mol% DGS-NTA-Ni, 2 mol% DP-EG10 biotin, and 0.1 mol% Texas Red-DHPE. (Scale bars in b and d are 5 μm.)

A simple mechanical model reproduces the ability of disordered protein chimeras to drive inward and outward curvature.

In Figure 3.6a, we summarize our experimental results in the form of an empirical phase diagram, in which the curvature driving abilities of the chimeras are represented as a function of salt concentration and relative separation between the attractive, LLPS-inducing domain (FUSLC or RGG), and the membrane surface. Here we see that the domain that is farthest from the membrane surface generally determines whether the net interaction between chimeras is attractive or repulsive. For example, the his-FUSLC-AP180S chimera, which places the FUSLC domain in closest proximity to the membrane surface, resulted in outward membrane tubules at all salt concentrations, suggesting that repulsion among AP180S domains dominated. In contrast, the his-AP180S-FUSLC chimera, which places the FUSLC domain farther from the membrane, resulted only in inward tubules, suggesting that attraction among the FUSLC domains dominated. Mixtures of these two chimeras effectively neutralized membrane curvature (blue circle). The his-AP180L-FUSLC chimera moves the FUSLC domain even farther from the membrane surface, but also increases the potential for steric and electrostatic repulsion, by increasing the size of the AP180-derived domain. As a result, the impact of this chimera on membrane curvature was conditional, with electrostatic repulsion among AP180L domains dominating at low salt concentration, resulting in outward tubules, and attraction among FUSLC domains dominating at higher salt concentrations, resulting in inward tubules. As described in the previous section, the his-AP180L-RGG chimera (not shown on the phase diagram) reversed this trend, owing to the opposite response of RGG-RGG interactions to changes in salt concentrations, when compared to FUSLC-FUSLC interactions[116].

Taken together, these data suggest that when the net interaction between the domains that make up a chimera is attractive, the chimera will drive inward membrane bending. In

contrast, if the net interaction is repulsive, the chimera will drive outward bending. To illustrate this concept, we developed a simple mechanical model, which treats the layer of membrane-bound protein chimeras as a layer of polymers chains grafted onto a flexible surface (Figure 3.6b-d, 3.11), see Supplementary Information. Briefly, following recently published theoretical work on membrane-bound polymer brushes[220,225-228] we wrote an expression for the free energy of the protein-membrane composite system (Equations S1, S2). The free energy of the brush-like IDP layer includes contributions from chain stretching, attractive or repulsive interactions between chains, and the loss of entropy upon ion partitioning into the brush. The membrane energy is the conventional Helfrich-Canham-Evans Hamiltonian[171,229,230]. Minimizing the free energy with respect to membrane curvature, Figure 3.6b plots the equilibrium membrane bending moment (vertical axis), which is proportional to spontaneous curvature, as a function of the density of protein monomers at the membrane surface, and the second virial coefficient associated with chain-chain interactions, *A* (horizontal axes). *A* is positive when the chains have net repulsive interactions and negative when their net interactions are attractive. In agreement with our experimental results, this simple model predicts that membrane curvature will increase with the monomer density and will be positive (outward curvature) when the chains repel one another and negative (inward curvature) when they attract one another. With the range of spontaneous curvatures obtained in Figure 3.6b, we next minimized the free energy of a cylindrical tube and found the corresponding tube radii as a function of monomer concentration and *A*, Figure 3.6c.

For a proof of principle of inward and outward tube formation, we used Mem3DG[231] to build a model of the membrane surface in three dimensions. Mem3DG is a framework and simulation engine that enables us to solve the governing equations of membrane bending using principles of discrete differential geometry. For this demonstration, we

started from a spherical vesicle and applied a weak Gaussian point force, decaying in time, to induce initial tube formation. Proteins which impart spontaneous curvature matching the direction of the tube bind and support the extrusion of the tubule. The resulting configurations, shown in Figure 3.6d, exhibit pearled tubules similar to those observed in experiments, (Figure 3.2c, 3.4c) suggesting that our simple physical model captures the main features of our experimental system.

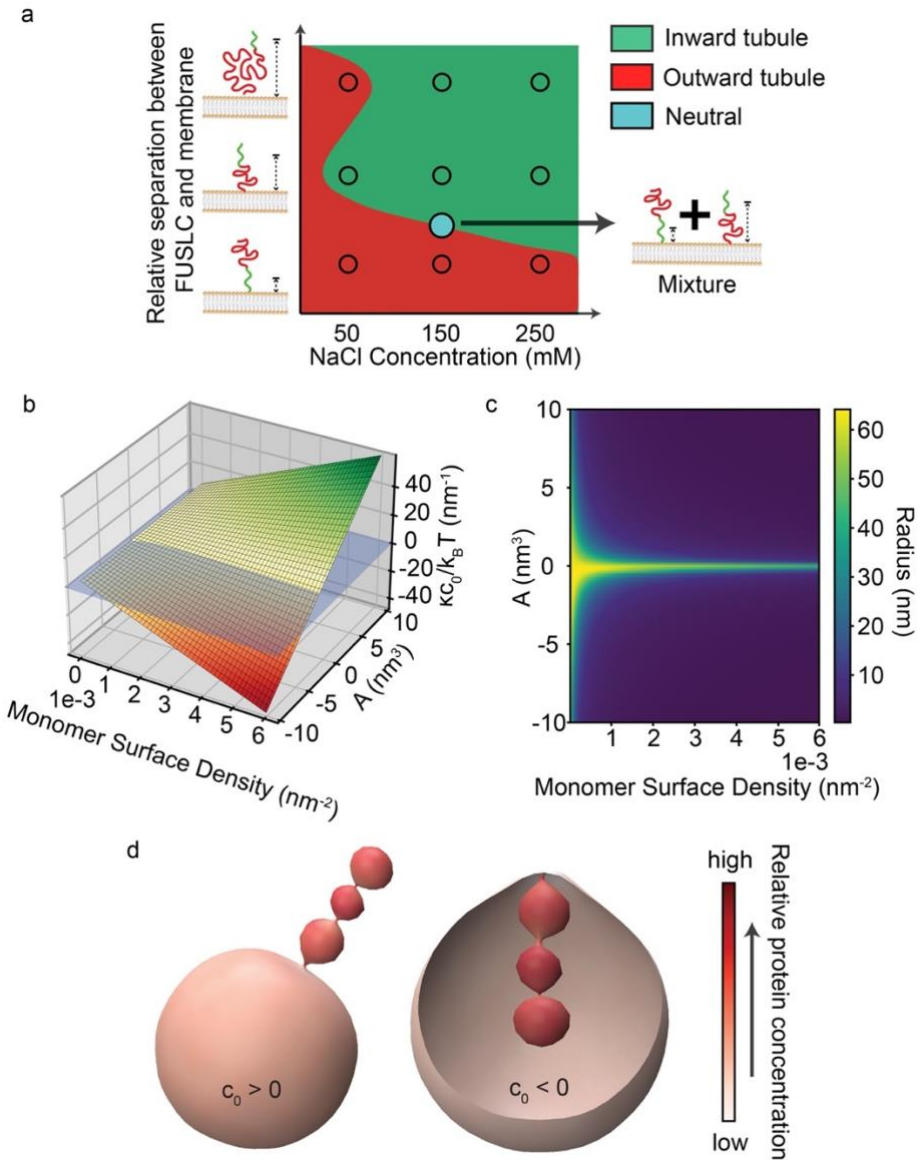

Figure 3. 6 A simple mechanical model reproduces the ability of disordered protein chimeras to drive inward and outward curvature. (a) Empirical phase diagram displaying the membrane curvature preferences of disordered protein chimeras as a function of salt concentration and distance of the attractive domain (FUSLC) from the membrane surface. (b) Modeling the membrane attached chimeras as a polymer brush demonstrates that the bending moment induced by the proteins (vertical axis) increases with increasing concentration of monomers at the membrane surface and second virial coefficient, *A*. (c) Predicted tube radius as a function of monomer surface density and *A*. (d) Simulation of inward and outward tubulation using Mem3DG. Color indicates local

protein concentration, demonstrating how proteins accumulate and reinforce the curvature of the tubule.

DISCUSSION

In this study, we have shown that the balance between attractive and repulsive interactions determines the extent and direction of membrane curvature by intrinsically disordered proteins. Specifically, while disordered domains that repel one another generate steric pressure that drives outward, convex membrane bending[7], attractive interactions among disordered domains do the opposite, generating compressive stress that results in inward, concave membrane bending[71]. By generating chimeras that combined these two types of interactions within the same protein, we have illustrated a set of design principles that can be used to control membrane shape in response to external stimuli.

The first principle is that the orientation of a chimera with respect to the membrane surface can be used to control the direction of membrane bending. Specifically, the domain farthest from the membrane surface tends to dominate the membrane curvature, likely because the farther domain has the advantage of a larger moment arm, and can therefore apply a larger bending stress. In this way, putting the repulsive domain farther from the membrane surface led to convex, outward bending, while placing the attractive domain farther from the membrane surface led to concave, inward bending (Figure 3.1d, 3.2c).

The second principle we identified is that chimeras with opposite curvature preferences can be used to counteract one another, leading to a relatively flat, stable membrane even in the presence of these proteins. In particular, we mixed the convex curvature preferring chimera (his-FUSLC-AP180S) with the concave preferring chimera (his-AP180S-FUSLC) at a range of ratios, and identified an intermediate regime in which the membrane preferred to remain flat, whereas tubules, of either convex or concave

curvature, dominated at other ratios (Figure 3.3c). Flat, protein-decorated, membranes are found throughout the cell, from regions of the plasma membrane to the sheets of the endoplasmic reticulum and the cisternae of the Golgi apparatus[111,217,218,232], suggesting the importance of stabilizing flat, as well as curved, membrane shapes in the presence of membrane-bound proteins.

The final design principle we identified is that membrane curvature can be tuned and even reversed when the balance between attractive and repulsive protein interactions is altered by environmental changes. Specifically, we used a decrease in ionic strength to simultaneously strengthen electrostatic repulsion between AP180L domains, while weakening attractive interactions among FUSLC domains. These collective effects ultimately reversed the direction of membrane bending. Specifically, the chimeric protein his-AP180L-FUSLC formed concave tubules at high ionic strength and convex tubules at low ionic strength (Figure 3.4c). This result illustrates that the dominance of the domain farthest from the membrane surface – identified in the first principle – can ultimately be overcome if there is a sufficient imbalance between attractive and repulsive interactions. Sensitivity of membrane-protein interactions to changes in the local environment is likely an important factor in cellular and organellar membranes where curvatures of both directions are observed, such as the endoplasmic reticulum and the inner membrane of mitochondria.

Collectively, these principles illustrate that the diverse and dynamic curvatures found in cellular membranes can be achieved by disordered proteins, entirely in the absence of structured domains. As 30-50% of all proteins are now thought to contain significant regions of intrinsic disorder[233,234], these observations have the potential to substantially expand our understanding of the proteome responsible for membrane curvature. More broadly, many proteins that are known to play a role in defining membrane shape contain

both structured and intrinsically disordered domains[235]. On the basis of our current and previous findings[63], it appears increasingly likely that structured and disordered curvature drivers collaborate to define the shape of cellular membranes. As one example, recent work has illustrated that BAR domains, structured curvature-inducing scaffolds, are often found within proteins that also contain substantial disordered domains, such that steric pressure among the disordered domains amplifies the inherent curvature preference of the BAR domains, resulting in convex membrane curvature[63]. Another example is the influenza matrix protein M1, which provides the major driving force in virus budding[236]. A recent *in vitro* study showed that the structured N terminal domain of M1 binds to the membrane, but requires the disordered C terminal domain to achieve polymerization, ultimately driving concave membrane invagination[237]. Coordination between structured and disordered domains may also play a role in maintaining the curvature of the nuclear pore complex, which is lined by nucleoporins that contain disordered domains rich in phenylalanine-glycine (FG) repeats[238-240]. Recent work suggests that the FG-rich domains form a flexible network that has the properties of a protein condensate[241]. Based on our findings, interactions between these domains could help to stabilize the complex architecture of the nuclear pore, which contains both convex and concave curvatures. Inspired by these examples and the growing recognition of the role that disordered proteins play in curving membranes, the design rules identified in the present study have broad implications for our understanding of the diverse mechanisms by which protein networks shape biological membranes.

ACKNOWLEDGEMENT

This research was supported by the NIH through grants R35GM139531 (J.C.S), R01GM132106 (P.R), the NSF DMS through grant 1934411 (P.R and J.C.S), ONR N00014-20-1-2469 to (P.R), the Welch Foundation through grant F-2047 (J.C.S.), Kavli Institute for Brain and Mind Postdoctoral Award (C.T.L) and the University of Texas at Austin, Graduate School Continuing Fellowship 2022-2023 (F.Y). The authors would like to thank Cuncheng Zhu and Arijit Mahapatra for helpful discussions.

MATERIALS AND METHODS

Reagents

POPC (1-palmitoyl-2-oleoyl-glycero-3-phosphocholine) and DGS-NTA-Ni (1,2-dioleoyl-sn-glycero-3-[(N-(5-amino-1-carboxypentyl) iminodiacetic acid)-succinyl] (nickel salt)) were purchased from Avanti Polar Lipids, Inc. Texas Red-DHPE (Texas Red 1,2-dihexadecanoyl-sn-glycero-3-phosphoethanolamine triethylammonium salt), NeutrAvidin, TrisHCl (Tris hydrochloride), HEPES (4-(2-hydroxyethyl)-1-piperazineethanesulfonic acid), IPTG (isopropyl-β-D-thiogalactopyranoside), b-ME (b-mercaptoethanol), TCEP (tris(2-carboxyethyl)phosphine) and Triton X-100 were purchased from Thermo Fisher Scientific. Tryptone, Yeast Extract, NaCl, NaH_2PO_4, Na_2HPO_4, Urea, sodium tetraborate, EDTA (Ethylenediaminetetraacetic acid), $CaCl_2$, glycerol, EDTA-free protease inhibitor tablets, imidazole, PMSF (phenylmethanesulfonylfluoride), PLL (poly-L-lysine), ATTO-594 NHS-ester, and ATTO-488 NHS-ester were purchased from Sigma-Aldrich. DP-EG10-biotin (dipalmitoyl-decaethylene glycol-biotin) was generously provided by Darryl Sasaki from Sandia National Laboratories, Livermore, CA[163]. Amine reactive polyethylene glycol

(mPEG-Succinimidyl Valerate MW 5000) and PEG-biotin (Biotin-PEG SVA, MW 5000) were purchased from Laysan Bio, Inc. All reagents were used without further purification.

Plasmids

The DNA plasmids for AP180CTD (rat AP180, amino acids 328-898) in a pET32c vector was kindly provided by Ernst Ungewickell, Hannover Medical School, Germany. DNA coding for histidine-tagged AP180CTD (his-AP180CTD, denoted as his-AP180L) was cloned into a pGex4T2 vector as previously described[115] to incorporate a GST-tag at the N terminus of his-AP180CTD to stabilize AP180CTD during purification. The AP180CTD (1/3) construct (denoted as his-AP180S) was generated by introducing a stop codon in place of the codon for alanine at position 213. The plasmids for his-FUSLC (residue 1 to 163) and LAF-1 RGG (residue 1 to 168) were acquired from Addgene (https://www.addgene.org/127192/ (Fawzi laboratories) and www.addgene.org/124929/ (Hammer laboratories), respectively). The plasmid for his-FUSLC-AP180S was generated by restriction cloning the FUSLC domain into the Sal1 restriction site between the histidine tag and AP180S. The plasmid for his-AP180S-FUSLC was generated by replacing his-AP180L in the pGex4T2 vector with FUSLC-AP180S-his. First, the FUSLC-AP180S sequence from the his-FUSLC-AP180S plasmid was amplified by PCR using primers that introduced an EcoR1 cutting site to the N terminus of FUSLC-AP180S and a histidine tag, stop codon and Xho1 cutting site to the C terminus (FUSLC-AP180S-his). The his-AP180L sequence was cut out using EcoR1 and Xho1 and then EcoR1 and Xho1 digested FUSLC-AP180S-his was ligated with the remaining backbone, yielding the pGex4T2 GST-FUSLC-AP180S-his plasmid for his-AP180S-FUSLC purification. The plasmids for his-AP180L-FUSLC and his-AP180L-RGG were generated by inserting FUSLC and RGG

into the C terminus of his-AP180L in a pGex4T2 vector, using restriction cloning. All constructs were confirmed by DNA sequencing.

Protein expression and purification

His-AP180S, his-FUSLC-AP180S, his-AP180S-FUSLC, his-AP180L-FUSLC, and his-AP180L-RGG constructs were each expressed as fusion proteins with an N-terminal GST tag for increased stability. GST was subsequently removed by thrombin cleavage. All the above proteins were purified based on the following protocol. Plasmids were transformed into *E. coli* BL21Star (DE3) pLysS competent cells (NEB Cat # C2530), which were grown at 30°C to an OD 600 of 0.8. Protein expression was induced with 1 mM IPTG for 24h at 12°C, shaken at 200 rpm. The whole purification process was performed at 4ºC. The cells were pelleted from 2L cultures by centrifugation at 4,785 x g (5,000 rpm in Beckman JLA-8.1000) for 20 min. Pellets were resuspended in 100mL lysis buffer (0.5 M TrisHCl pH 8.0, 5 v/v % glycerol, 5 mM EDTA, 5 mM TCEP, 1 mM PMSF) plus EDTA free protease inhibitor tablets (1 tablet/50ml), 1.0% Triton-X100, followed by homogenization with a dounce homogenizer and sonication (5 x 2,000J) on ice. The lysate was clarified by centrifugation at 26,581 x g (18K rpm in Beckman JA-25.50) for 25 min. The clarified lysate was then applied to a 10mL bed volume Glutathione Sepharose 4B (Cytiva Cat # 17075605) column, washed with 100mL lysis buffer plus 0.2% Triton X-100, EDTA free protease inhibitor tablets (1 tablet/50ml), followed by 50mL lysis buffer. The protein was eluted with lysis buffer plus 15 mM reduced glutathione and buffer-exchanged into 50 mM TrisHCl pH 8.0, 10 mM $CaCl_2$, 150 mM NaCl, 5 mM EDTA using a Zeba desalting column (Thermo Scientific cat # 89891). GST was cleaved using the Thrombin CleanCleave kit (Sigma-Aldrich cat # RECOMT) for 14 hours at 4 °C with gentle rocking. The GST-tag and any uncut protein were removed by a second Glutathione

Sepharose 4B column. The resulting purified protein was concentrated using an Amicon Ultra-15 centrifugal filter (MilliporeSigma cat # UFC903024) and stored as liquid nitrogen pellets at −80 °C.

Expression and purification of his-FUSLC was carried out according to a previous report[71]. In brief, his-FUSLC was overexpressed in *E. Coli* BL21(DE3) cells. Pellets of cells expressing his-FUSLC were harvested from 1L cultures induced with 1 mM IPTG after 4-hour incubation at 37°C and 220 RPM when OD 600 was around 0.8. The pellets were then lysed in a buffer containing 0.5 M TrisHCl pH 8, 5 mM EDTA, 5% glycerol, 10mM β-ME, 1mM PMSF, 1% Triton X-100 plus EDTA-free protease inhibitor tablet (1 tablet/50mL) for 5 min on ice and then sonicated. The cell lysates were centrifuged at 40,000 RPM for 40 min and his-FUSLC resided in the insoluble fraction after centrifugation. Therefore, the insoluble fraction was resuspended in 8M urea, 20 mM NaPi pH 7.4, 300 mM NaCl and 10 mM imidazole. The resuspended sample was then centrifuged at 40,000 RPM for 40 min. In denaturing conditions, his-FUSLC is Urea-soluble and so at this point resided in the supernatant. This supernatant was then mixed with Ni-NTA resin (G Biosciences, USA) for 1 hour at 4°C. The Ni-NTA resin was settled in a chromatography column and washed with the above solubilizing buffer. The bound proteins were eluted from the Ni-NTA resin with a buffer containing 8M urea, 20 mM NaPi pH 7.4, 300 mM NaCl and 500 mM imidazole. The purified proteins were then buffer-exchanged into 20 mM CAPS pH 11 storage buffer using 3K Amicon Ultra centrifugal filters (Millipore, USA). Small aliquots of the protein were frozen in liquid nitrogen at a protein concentration of approximately 1 mM and stored at -80 °C.

Protein labeling

All proteins used in this study were labeled with Atto-488 or Atto-594, amine-reactive, NHS ester-functionalized fluorescent dyes. The labeling reaction took place in a 50 mM HEPES buffer at pH 7.4 for his-FUSLC and in 25 mM HEPES, 150 mM NaCl, 5 mM TCEP at pH 7.4 for AP180CTD-derived proteins. Dye was added to the protein in 2-fold stoichiometric excess and allowed to react for 30 minutes at room temperature, empirically resulting in labelling ratio from 0.8 to 1.5 dyes per protein. Labeled protein was then buffer-exchanged into 20 mM CAPS pH 11 buffer for his-FUSLC and 50 mM TrisHCl pH 8.0, 10 mM $CaCl_2$, 150 mM NaCl, 5 mM EDTA, 5mM TCEP for AP180CTD-derived proteins and separated from unconjugated dye as well using 3K Amicon columns. Protein and dye concentrations were monitored using UV–Vis spectroscopy. Labeled proteins were dispensed into small aliquots, flash frozen in liquid nitrogen and stored at -80°C. For all experiments involving labeled protein, a mix of 90% unlabeled / 10% labeled protein was used.

GUV preparation

GUVs were made of 83% POPC, 15% Ni-NTA, 2 mol% DP-EG10 biotin. An additional 0.1 mol% Texas Red DHPE lipids were added for visualization if needed. GUVs were prepared by electroformation according to published protocols[167]. Briefly, lipid mixtures dissolved in chloroform were spread into a film on indium-tin-oxide (ITO) coated glass slides (resistance ~8-12 W sq-1) and further dried in a vacuum desiccator for at least 2 hours to remove all of the solvent. Electroformation was performed at 55°C in glucose solution. Glucose solutions with different osmolarity were used to match the osmolarity of buffers with different NaCl concentrations. To be specific, 560 milliosmole glucose solution was employed for making GUVs used in 250 mM and lower NaCl buffers. 940 milliosmole glucose solution was used for GUVs in 500 mM NaCl buffer. For GUVs used

under 1 M NaCl buffer and 250 mM NaCl plus 1.5 M Urea, 1800 milliosmole glucose solution was adopted to adapt to the high osmotic pressure. The voltage was increased every 3 min from 50 to 1400 mV peak to peak for the first 30 min at a frequency of 10 Hz. The voltage was then held at 1400 mV peak to peak for 120 min and finally was increased to 2200 mV peak to peak for the last 30 min during which the frequency was adjusted to 5 Hz. GUVs were stored in 4°C and used within 3 days after electroformation.

GUV tethering and sample preparation

GUVs were tethered to glass coverslips for imaging as previously described[168]. Briefly, glass cover slips were passivated with a layer of biotinylated PLL-PEG, using 5 kDa PEG chains. GUVs doped with 2 mol% DP-EG10-biotin were then tethered to the passivated surface using neutravidin.

PLL-PEG was synthesized by combining amine reactive PEG and PEG-biotin in molar ratios of 98% and 2%, respectively. This PEG mixture was added to a 20 mg/mL mixture of PLL in a buffer consisting of 50 mM sodium tetraborate (pH 8.5), such that the molar ratio of lysine subunits to PEG was 5:1. The mixture was continuously stirred at room temperature for 6 h and then buffer exchanged into 25 mM HEPES, 150 mM NaCl (pH 7.4) using ZebaTM Spin Desalting Column (ThermoFisher Scientific).

Prior to tethering, the osmolality of the GUV solution and experimental buffers were measured using a vapor pressure osmometer (Wescor). Buffer used for dilution and rinsing was 25 mM HEPES pH 7.4 with corresponding NaCl concentrations. Osmolarity balance was maintained by the addition of glucose to the buffer.

Imaging wells consisted of 5 mm diameter holes in 0.8 mm thick silicone gaskets (Grace Bio-Labs). Gaskets were placed directly onto no.1.5 glass coverslips (VWR International), creating a temporary water-proof seal. Prior to well assembly, gaskets and

cover slips were cleaned in 2% v/v Hellmanex III (Hellma Analytics) solution, rinsed thoroughly with water, and dried under a nitrogen stream. In each dry imaging well, 20 μL of PLL-PEG was added. After 20 min of incubation, wells were serially rinsed with appropriate buffer by gently pipetting until a 15,000-fold dilution was achieved. Next, 4 μg of neutravidin dissolved in 25 mM HEPES, 150 mM NaCl (pH 7.4) was added to each sample well and allowed to incubate for 10 minutes. Wells were then rinsed with the appropriate buffer to remove excess neutravidin. GUVs were diluted in appropriate buffer at ratio of 1:13 and then 20 μL of diluted GUVs was added to the well and allowed to incubate for 10 minutes. Excess GUVs were then rinsed from the well using the appropriate buffer and the sample was subsequently imaged using confocal fluorescence microscopy.

GUV fluorescence imaging

Imaging experiments were performed using a spinning disc confocal super resolution microscope (SpinSR10, Olympus, USA) equipped with a 1.49 NA/100X oil immersion objective. Laser wavelengths of 488 and 561 nm were used for excitation. Image stacks taken at fixed distances perpendicular to the membrane plane (0.5 μm steps) were acquired immediately after GUV tethering and again after protein addition. Images taken under deconvolution mode were processed by the built-in deconvolution function in Olympus CellSens software (Dimension 3.2, Build 23706). At least 30 fields of views were randomly selected for each sample for further analysis prior to and after the addition of protein, respectively. Imaging was proceeded 5 min after adding proteins to achieve protein binding and reaching a relatively equilibrium state.

Statistical Analysis

All GUV experiments were repeated 3 times for each condition reported. ImageJ was employed to analyze confocal images. At least 100 GUVs were examined under each condition. The diameter of each inward tubule was determined by drawing a line perpendicular to the tubule at three different places along its length and calculating the average diameter. To assess the significance of comparisons between conditions, an unpaired t-test was performed. Error bars in graphs represent either standard error or standard deviation as stated in figure captions.

SUPPLEMENTARY MATERIALS

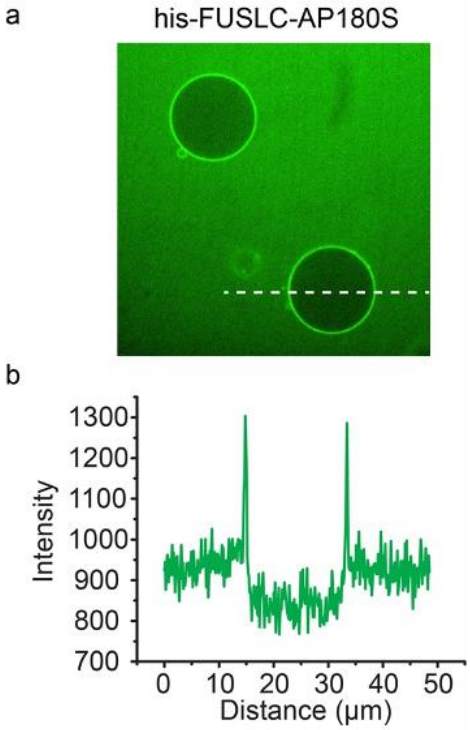

Figure 3. 7 (a) Representative confocal images showing protein exclusion from the inner lumen of GUVs. (b) Intensity distribution of protein channel along the dashed line shown in the image.

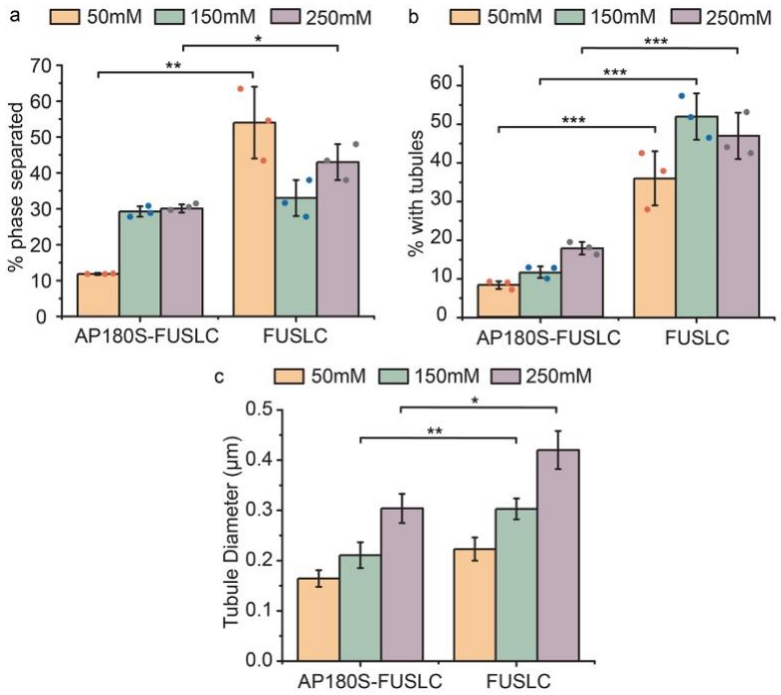

Figure 3. 8 Bar chart comparison of percentage of GUVs displaying protein phase separation (a), inward tubules (b) and average inward tubule diameter (c) when incubated with his-AP180S-FUSLC and his-FUSLC under different salt concentrations. The data for his-FUSLC are cited from our previous report[12]. Error bars in (a) and (b) represent the standard deviation of three independent trials (indicated by the dots). Error bars in (c) correspond to standard error of all data points measured under each condition. Statistical significance was tested using an unpaired, two-tailed student's t test. *: $P < 0.05$, **: $P < 0.01$, ***: $P < 0.001$. GUV composition is 83 mol% POPC, 15 mol% DGS-NTA-Ni, 2 mol% DP-EG10 biotin, and 0.1 mol% Texas Red-DHPE.

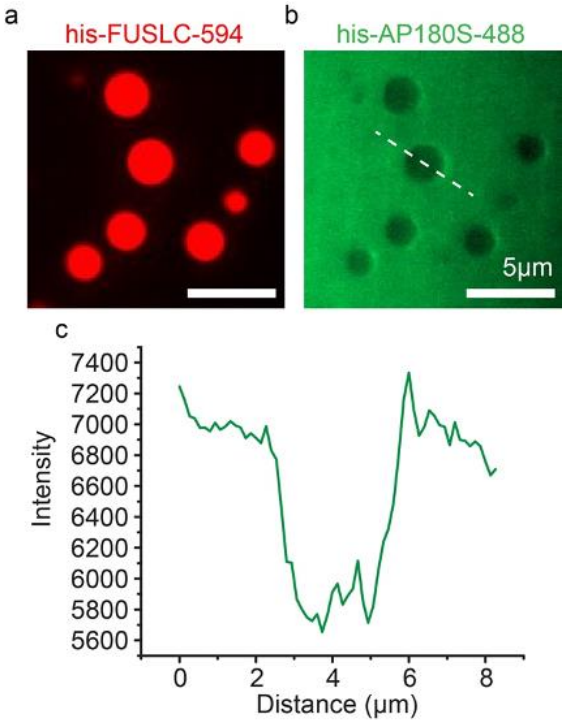

Figure 3. 9 (a, b) Representative image of AP180S exclusion from his-FUSLC droplets in solution. (c) Intensity distribution of his-AP180S along the white dashed line across the his-FUSLC droplet in panel b. his-FUSLC concentration is 25 μM and his-AP180S is 5 μM. Experiment was done in 25mM HEPES, 150mM NaCl, pH 7.4 buffer.

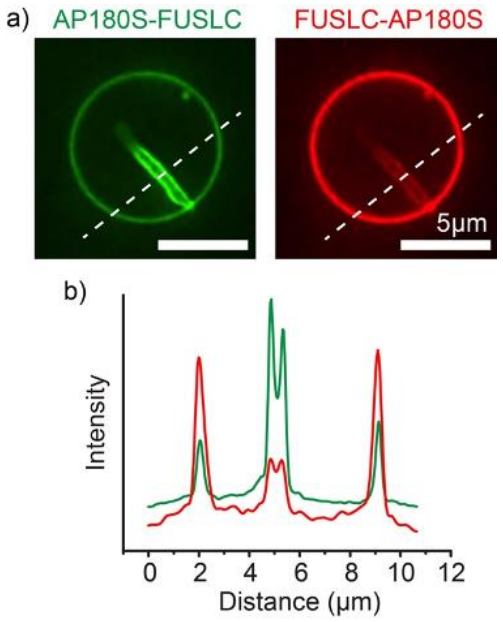

Figure 3. 10 AP180S-FUSLC is more enriched in the inward protein-lined tubules than FUSLC-AP180S. (a) Representative super-resolution images of protein-lined tubules when GUVs were incubated with 1 μM of his-AP180S-FUSLC and 0.1 μM of his-FUSLC-AP180S at the same time. (b) Intensity distribution along the dashed line across the GUV.

Supplementary Information about Simulations

To the first order, the total system energy can be written as:

$$W_{total} = W_{protein} + W_{membrane} = F_{brush}H + \kappa(H - c_0)^2 \qquad \text{Equation S1}$$

where F_{brush} is the protein energy density, H is the mean curvature of the membrane, κ is the bending modulus, and c_0 the spontaneous curvature. The first term, the product of protein energy density and mean curvature, captures the moment arm generated by the protein steric interactions which are offset from the membrane surface. The second term is the conventional Helfrich-Canham-Evans hamiltonian which captures the membrane's bending elasticity.[171,229,230]

The physics of interacting polymers grafted on surfaces has been explored in detail and the brush polymer theory has been developed to model the contributions to the polymer energy density [225-228]. Following the theory, the protein energy density, F brush, is defined as,

$$F_{brush} = F_{elastic\ stretching} + F_{interactions} + F_{ion} = k_B T s[\frac{3}{2a^2 s^2 c} + Ac^2 + \frac{\alpha^2 c^2}{2\Phi}]$$

Equation S2

where s is the local area per protein, a is the Kuhn length, c the protein monomer concentration (considered to be an amino acid residue for the IDPs of interest), A the second virial coefficient, Φ the bulk ionic concentration, $k_B T$ is the Boltzmann constant and temperature, and α the degree of ionization. While a freely jointed polymer chain is expected to form a glob like structure which maximizes its configurational entropy[242], high density packing conveyed by the area occupancy and protein concentration, can lead to stretching and subsequent entropy loss which is captured by the first term. The free energy density of the short-ranged interactions which can drive phenomena such as steric pressure and condensation is modeled by the virial expansion truncated to second order, the second term of Eq. S2. Here we note that A, the second virial coefficient, is a complex function of the specific protein chemistry/identity[243,244] and can take a positive or negative value corresponding to repulsive or attractive behavior respectively. Conventional biochemistry and statistical mechanics further imply that A is a function of the local chemical environment which can screen the strength of interactions. In lieu of detailed experimental

characterization of A given the combinatorial conditions, we will instead systematically vary the value of A across a range of values corresponding to net protein attraction/aggregation and repulsion. The third term of Eq. S2, captures the loss of entropy of ions partitioning into the brush layer as a result of Donnan's equilibrium. From the brush polymer theories, this term corresponds to the so-called quenched or strongly dissociating condition which assumes that the polymer has a fixed ionization extent given by α.

To interrogate how the IDP layer and membrane couple to drive spontaneous curvature we can study how the energy of the system changes with respect to changing mean curvature, $\partial W/\partial H$. The stationary point where $\frac{\partial W}{\partial H} = 0$, corresponds to the minima and is given by

$$\frac{\partial W}{\partial H} = F_{brush} + 2\kappa c_0 = 0 \qquad \text{Equation S3}$$

Rearranging, we obtain the classic relationship linking the moment of the protein interactions with the spontaneous curvature and bending rigidity, $-2\kappa c_0 = F_{brush}$.

For a quantitative evaluation of this relationship, we further assume and prescribe values for the parameters. The Kuhn length, a, is twice the persistence length of a polymer. For an IDP we approximate this as twice the length of a residue, ~1 nm.[245] To relate the end-to-end stretch distance of the grafted IDP (i.e., thickness of the brush layer), d, to polymer area occupancy we write a conservation equation,

$$s = \frac{N}{d c_p} \qquad \text{Equation S4}$$

where N is the number of amino acids, and c_p is the protein monomer concentration. We further assume that the degree of ionization for each protein is around 10%, $\alpha = 0.1$, the

brush layer is 20 nm thick, and prescribe 150 mM ion concentration. Under these conditions we vary the second virial coefficient, A, from -10 – 10 nm^3 corresponding to net attractive (e.g., FUSLC) and repulsive (e.g., AP180S) conditions respectively. We find that the extent of spontaneous curvature induced is a function of protein concentration in line with the experimental observations, Figure 3.6b.

To evaluate how the spontaneous curvature influences the geometry of a membrane tube, we followed the approach outlined by Shurer, Derenyi and colleagues[220,246]. Considering the special case of a cylindrical membrane tube experiencing a pulling force at zero osmotic pressure, the Helfrich-Canham-Evans free energy is given by,

$$W_{cyl} = [\frac{\kappa}{2}(\frac{1}{R} - c_0)^2 + \sigma]2\pi RL - fL \qquad \text{Equation S5}$$

where κ is the bending modulus, R is the radius of the cylinder, c_0 is the spontaneous curvature, σ is the tension, f is the pulling force acting over length L. At equilibrium, where $\frac{\partial W_{cyl}}{\partial R} = 0$ and $\partial W_{cyl}/\partial L = 0$, the tube radius is

$$R = \frac{1}{\sqrt{{c_0}^2 + 2\sigma/\kappa}} \qquad \text{Equation S6}$$

and the pulling force,

$$f = 2\pi\kappa(\sqrt{{c_0}^2 + 2\sigma\kappa} - c_0) \qquad \text{Equation S7}$$

Assuming a canonical bending rigidity value of 20 k_BT and membrane tension 0.01 mNm^{-1}, and substituting the predicted values from Figure 3.6b, we obtain the radius and force predictions in Figure 3.6c and Figure 3.11.

For a proof of principle of inward and outward tube formation with pearling, we use Mem3DG[231] to build a model in three dimensions without assumptions of axisymmetry.

Mem3DG is a framework and simulation engine that enables us to solve the governing equations of membrane bending. Using principles from discrete differential geometry, we compute the energy of a geometric configuration and vertexwise forces in a consistent manner with traditional physics approaches; coupled with an energy minimization or time integration scheme, we get from the model a trajectory of the evolving domain subject to the bending and other prescribed physics. For the demonstration, we start from a spherical vesicle and apply a weak Gaussian point force, decaying in time, in an inward or outward direction to induce initial tube formation. Proteins which impart spontaneous curvature matching the direction of the tube bind and support the extrusion of pearls. Driven by the membrane tension and protein spontaneous curvature, the resulting configurations, shown in Figure 3.6d, exhibit pearled tubules similar to those observed in experiments, (Figure 3.2c, 3.4c) suggesting that our simple physical model captures the main features of our experimental system.

All parameters for the Mem3DG and simple mechanical models are archived on GitHub: https://github.com/RangamaniLabUCSD/2023-IDP-bending. Mem3DG source code corresponding to commit 361affa9423d44f3cf239585ac350340a212b1f8 used to run the model can also be obtained from GitHub https://github.com/RangamaniLabUCSD/Mem3DG/.

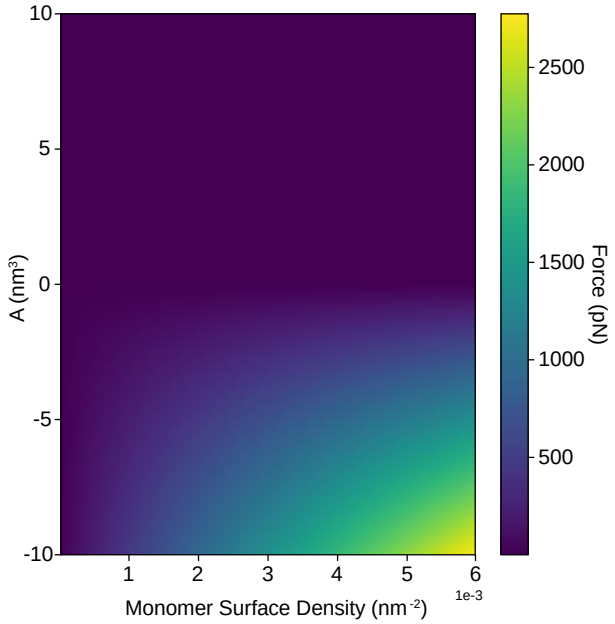

Figure 3. 11 The equilibrium pulling force required to sustain a tube coated by differing surface concentrations of protein. The vertical axis is the second virial coefficient, A, which represents the net attraction—repulsion of the protein.

REFERENCES

43. Hurley, J. H., Boura, E., Carlson, L.-A. & Różycki, B. Membrane budding. *Cell* **143**, 875-887 (2010).

52. Daumke, O., Roux, A. & Haucke, V. BAR domain scaffolds in dynamin-mediated membrane fission. *Cell* **156**, 882-892 (2014).

63. Snead, W. T. *et al.* BAR scaffolds drive membrane fission by crowding disordered domains. *J Cell Biol* **218**, 664-682 (2019).
71. Yuan, F. *et al.* Membrane bending by protein phase separation. *Proceedings of the National Academy of Sciences* **118** (2021).
88. Martin, E. W. *et al.* Valence and patterning of aromatic residues determine the phase behavior of prion-like domains. *Science* **367**, 694-699 (2020).
111. Zimmerberg, J. & Kozlov, M. M. How proteins produce cellular membrane curvature. *Nat Rev Mol Cell Biol* **7**, 9-19 (2006).
113. Drin, G. & Antonny, B. Amphipathic helices and membrane curvature. *FEBS letters* **584**, 1840-1847 (2010).
115. Busch, D. J. *et al.* Intrinsically disordered proteins drive membrane curvature. *Nat Commun* **6**, 7875 (2015).
116. Brangwynne, Clifford P., Tompa, P. & Pappu, Rohit V. Polymer physics of intracellular phase transitions. *Nature Physics* **11**, 899-904 (2015).
120. Burke, K. A., Janke, A. M., Rhine, C. L. & Fawzi, N. L. Residue-by-Residue View of In Vitro FUS Granules that Bind the C-Terminal Domain of RNA Polymerase II. *Mol Cell* **60**, 231-241 (2015).
123. Elbaum-Garfinkle, S. *et al.* The disordered P granule protein LAF-1 drives phase separation into droplets with tunable viscosity and dynamics. *Proceedings of the National Academy of Sciences* **112**, 7189-7194 (2015).
163. Momin, N. *et al.* Designing lipids for selective partitioning into liquid ordered membrane domains. *Soft Matter* **11**, 3241-3250 (2015).
165. Schuster, B. S. *et al.* Controllable protein phase separation and modular recruitment to form responsive membraneless organelles. *Nature communications* **9**, 1-12 (2018).
166. Stachowiak, J. C. *et al.* Membrane bending by protein-protein crowding. *Nat Cell Biol* **14**, 944-949 (2012).
167. Angelova, M. I. & Dimitrov, D. S. Liposome electroformation. *Faraday discussions of the Chemical Society* **81**, 303-311 (1986).
168. Zeno, W. F. *et al.* Synergy between intrinsically disordered domains and structured proteins amplifies membrane curvature sensing. *Nat Commun* **9**, 4152 (2018).
171. Canham, P. B. The minimum energy of bending as a possible explanation of the biconcave shape of the human red blood cell. *Journal of theoretical biology* **26**, 61-81 (1970).

217. McMahon, H. T. & Boucrot, E. Membrane curvature at a glance. *J Cell Sci* **128**, 1065-1070 (2015).
218. Jarsch, I. K., Daste, F. & Gallop, J. L. Membrane curvature in cell biology: An integration of molecular mechanisms. *J Cell Biol* **214**, 375-387 (2016).
219. Snead, W. T. & Stachowiak, J. C. Structure Versus Stochasticity-The Role of Molecular Crowding and Intrinsic Disorder in Membrane Fission. *J Mol Biol* **430**, 2293-2308 (2018).
220. Shurer, C. R. *et al.* Physical principles of membrane shape regulation by the glycocalyx. *Cell* **177**, 1757-1770. e1721 (2019).
221. Boeynaems, S. *et al.* Protein Phase Separation: A New Phase in Cell Biology. *Trends Cell Biol* **28**, 420-435 (2018).
222. Zeno, W. F. *et al.* Molecular mechanisms of membrane curvature sensing by a disordered protein. *Journal of the American Chemical Society* **141**, 10361-10371 (2019).
223. Stachowiak, J. C., Hayden, C. C. & Sasaki, D. Y. Steric confinement of proteins on lipid membranes can drive curvature and tubulation. *Proceedings of the National Academy of Sciences* **107**, 7781-7786 (2010).
224. Angelova, M. I. *et al.* pH sensing by lipids in membranes: The fundamentals of pH-driven migration, polarization and deformations of lipid bilayer assemblies. *Biochimica et Biophysica Acta (BBA)-Biomembranes* **1860**, 2042-2063 (2018).
225. Zhulina, E., Birshtein, T. & Borisov, O. Curved polymer and polyelectrolyte brushes beyond the Daoud-Cotton model. *The European Physical Journal E* **20**, 243-256 (2006).
226. Israels, R., Leermakers, F., Fleer, G. J. & Zhulina, E. B. Charged polymeric brushes: Structure and scaling relations. *Macromolecules* **27**, 3249-3261 (1994).
227. Borisov, O. & Zhulina, E. Effect of salt on self-assembly in charged block copolymer micelles. *Macromolecules* **35**, 4472-4480 (2002).
228. Zhulina, E. & Borisov, O. Polyelectrolytes grafted to curved surfaces. *Macromolecules* **29**, 2618-2626 (1996).
229. Evans, E. MECHANICS AND THERMODYNAMICS OF BIOMEMBRANES. II. (1979).
230. Evans, E. A. Bending resistance and chemically induced moments in membrane bilayers. *Biophysical journal* **14**, 923-931 (1974).
231. Zhu, C., Lee, C. T. & Rangamani, P. Mem3DG: modeling membrane mechanochemical dynamics in 3D using discrete differential geometry. *Biophysical reports* **2**, 100062 (2022).

232. McMahon, H. T. & Gallop, J. L. Membrane curvature and mechanisms of dynamic cell membrane remodelling. *Nature* **438**, 590-596 (2005).
233. Uversky, V. N. Intrinsically Disordered Proteins and Their "Mysterious" (Meta)Physics. *Frontiers in Physics* **7** (2019).
234. Xue, B., Dunker, A. K. & Uversky, V. N. Orderly order in protein intrinsic disorder distribution: disorder in 3500 proteomes from viruses and the three domains of life. *Journal of Biomolecular Structure and Dynamics* **30**, 137-149 (2012).
235. Owen, D. J., Collins, B. M. & Evans, P. R. Adaptors for clathrin coats: structure and function. *Annual review of cell and developmental biology* **20**, 153 (2004).
236. Gómez-Puertas, P., Albo, C., Pérez-Pastrana, E., Vivo, A. & Portela, A. Influenza virus matrix protein is the major driving force in virus budding. *Journal of virology* **74**, 11538 (2000).
237. Saletti, D. *et al.* The Matrix protein M1 from influenza C virus induces tubular membrane invaginations in an in vitro cell membrane model. *Scientific reports* **7**, 1-14 (2017).
238. Strambio-De-Castillia, C., Niepel, M. & Rout, M. P. The nuclear pore complex: bridging nuclear transport and gene regulation. *Nature reviews Molecular cell biology* **11**, 490-501 (2010).
239. Rout, M. P. *et al.* The yeast nuclear pore complex: composition, architecture, and transport mechanism. *The Journal of cell biology* **148**, 635-652 (2000).
240. Denning, D. P., Patel, S. S., Uversky, V., Fink, A. L. & Rexach, M. Disorder in the nuclear pore complex: the FG repeat regions of nucleoporins are natively unfolded. *Proceedings of the National Academy of Sciences* **100**, 2450-2455 (2003).
241. Nag, N., Sasidharan, S., Uversky, V. N., Saudagar, P. & Tripathi, T. Phase separation of FG-nucleoporins in nuclear pore complexes. *Biochimica et Biophysica Acta (BBA)-Molecular Cell Research* **1869**, 119205 (2022).
242. Kratky, O. & Porod, G. Röntgenuntersuchung gelöster fadenmoleküle. *Recueil des Travaux Chimiques des Pays‐Bas* **68**, 1106-1122 (1949).
243. Neal, B., Asthagiri, D. & Lenhoff, A. Molecular origins of osmotic second virial coefficients of proteins. *Biophysical Journal* **75**, 2469-2477 (1998).
244. Quigley, A. & Williams, D. The second virial coefficient as a predictor of protein aggregation propensity: a self-interaction chromatography study. *European Journal of Pharmaceutics and Biopharmaceutics* **96**, 282-290 (2015).

245. Choi, U. B., McCann, J. J., Weninger, K. R. & Bowen, M. E. Beyond the random coil: stochastic conformational switching in intrinsically disordered proteins. *Structure* **19**, 566-576 (2011).
246. Derényi, I., Jülicher, F. & Prost, J. Formation and interaction of membrane tubes. *Physical review letters* **88**, 238101 (2002).

Chapter 4: Ubiquitin-driven protein condensation promotes clathrin-mediated endocytosis[4]

ABSTRACT

Clathrin-mediated endocytosis is an essential cellular pathway that enables signaling and recycling of transmembrane proteins and lipids. During endocytosis, dozens of cytosolic proteins come together at the plasma membrane, assembling into a highly interconnected network that drives endocytic vesicle biogenesis. Recently, multiple labs have reported that early endocytic proteins form liquid-like condensates, which provide a flexible platform for the efficient assembly of endocytic vesicles. Given the importance of this network in the dynamics of endocytosis, how might cells regulate its stability? Many receptors and endocytic proteins are ubiquitylated, while early endocytic proteins such as Eps15 contain ubiquitin-interacting motifs. Therefore, we examined the influence of ubiquitin on the stability of the early endocytic protein network. In vitro, we found that recruitment of small amounts of polyubiquitin dramatically increased the stability of Eps15 condensates, suggesting that ubiquitylation could nucleate endocytic sites. In live cell imaging experiments, a version of Eps15 that lacked the ubiquitin-interacting motif failed to rescue defects in endocytic initiation created by Eps15 knockout. Furthermore, fusion of Eps15 to a deubiquitinase enzyme destabilized nascent endocytic sites within minutes. These results suggest that ubiquitylation drives assembly of the flexible protein network responsible for catalyzing endocytic events. More broadly, this work illustrates a biophysical mechanism by which ubiquitylated transmembrane proteins at the plasma membrane could regulate the efficiency of endocytic recycling.

[4] This chapter is available on preprint website bioRxiv as: Yuan F, Gollapudi S, Day K, Ashby G, Sangani A, Malady BT, Wang L, Lafer EM, Huibregtse JM, Stachowiak JC. Ubiquitin-driven protein condensation promotes clathrin-mediated endocytosis. *bioRxiv* (2023).

INTRODUCTION

Endocytosis, which is responsible for internalizing proteins and lipids from the plasma membrane, is essential for a myriad of cellular functions including signaling, nutrient import, and recycling[247]. Clathrin-mediated endocytosis is the best understood pathway of cellular internalization[248]. In the earliest moments of clathrin-mediated endocytosis, initiator proteins including Eps15, Fcho, and Intersectin assemble together to create a nascent endocytic site[248,249]. The resulting network of initiators recruits adaptor proteins, such as AP2, CALM/AP180, and Epsin, among many others, which in turn recruit clathrin triskelia[248,250]. Assembly of triskelia into an icosahedral lattice works in concert with adaptor proteins to induce membrane curvature and vesicle budding[248,250]. As clathrin coated structures grow, transmembrane cargo proteins are recruited into them. Many cargo proteins contain biochemical motifs that mediate binding to endocytic adaptor proteins[251], while post-translational modifications, such as ubiquitylation, drive uptake of transmembrane proteins destined for degradation or recycling[252-255]. Once the clathrin coat is fully assembled and loaded with cargo proteins, scission occurs, resulting in the formation of clathrin-coated vesicles that bud off from the plasma membrane, followed by uncoating[248,249].

Interestingly, the early initiator proteins of clathrin-mediated endocytosis are not incorporated into endocytic vesicles[256,257]. Instead, they function like catalysts, remaining at the plasma membrane to initiate multiple rounds of endocytosis. To promote growth of a clathrin-coated vesicle, the initiator network must remain flexible, allowing clathrin and its adaptors to accumulate and rearrange. Similarly, as the vesicle matures, the network of initiators must ultimately dissociate from it, allowing the final coated vesicle to depart into the cytosol. In line with these requirements, recent work has shown that initiator proteins, which contain substantial regions of intrinsic disorder, form liquid-like assemblies that

undergo rapid exchange[97,258-260]. Specifically, Day and colleagues showed that Eps15 and Fcho1/2 form a liquid-like network, which exhibits optimal catalytic activity when its level of assembly is maintained within an intermediate range[258]. When the network assembly was too weak, the fraction of endocytic events that were short-lived, likely aborting without creating a vesicle, increased. Conversely, an excessively strong initiator network led to the accumulation of overly stable, stalled endocytic structures. Work by Wilfling and colleagues suggests that such structures may mature into autophagic sites, rather than resulting in endocytosis[259,260]. More broadly, Kozak and colleagues found that Ede1, the yeast homolog of Eps15, mediates assembly of liquid-like condensates that incorporate many endocytic components, suggesting that the requirement for a flexible network of endocytic initiator proteins may be broadly conserved[97].

Motivated by these findings, we set out to understand how cells regulate the stability of the early endocytic network. As noted above, Eps15/Ede1 is a key component of this network. Interestingly, several studies have suggested that ubiquitylation can play an important role in mediating interactions between Eps15, cargo proteins, and endocytic adaptor proteins[255,261-264]. Specifically, Hicke and collaborators identified a ubiquitin association domain near the C terminus of Ede1, which enabled interactions between Ede1 and ubiquitinated proteins[255,261]. Similarly, Paolo di Fiore and colleagues reported that the two ubiquitin interacting motifs (UIMs) at the C terminus of Eps15 are essential for its interactions with ubiquitinated proteins[263]. Further, studies by Drubin and colleagues suggested that the ubiquitylation state of Ede1 plays an important role in endocytic dynamics in budding yeast[265].

These findings led us to ask whether ubiquitylation might impact the assembly of liquid-like networks of early endocytic proteins. Using purified proteins *in vitro*, we found that recruitment of small amounts of polyubiquitin significantly enhanced the stability of

liquid-like Eps15 droplets, suggesting a potential role for ubiquitylation in nucleating endocytic sites. Through live cell imaging, we observed that expression of UIM-deficient Eps15 in cells lacking endogenous Eps15 failed to rescue the defect in clathrin-mediated endocytosis caused by Eps15 knockout. Similarly, removing ubiquitin from Eps15 and its close interactors by recruitment of an Eps15 variant containing a broad-spectrum deubiquitinase domain resulted in a significant destabilization of nascent endocytic sites. Finally, using an optogenetic approach, we found that this destabilization occurred within minutes following recruitment of deubiquitinases to endocytic sites. Collectively, these results suggest that ubiquitylation plays a critical role in stabilizing the flexible protein network responsible for catalyzing clathrin-mediated endocytosis.

RESULTS

Polyubiquitin partitions strongly to liquid-like droplets of Eps15

We first asked to what extent monoubiquitin and polyubiquitin interact with liquid-like networks of Eps15. To address this question, we compared the partitioning of monoubiquitin (MonoUb) and lysine-63-linked tetra-ubiquitin (K63 TetraUb) into Eps15 droplets *in vitro*. Notably, K63-linked polyubiquitin chains are thought to play an important role in recycling of receptors from the cell surface[266-269]. Eps15 is composed of three major domains: the N-terminal region, which consists of three Eps15 Homology (EH) domains; a central coiled-coil domain, which is responsible for dimerization of Eps15; and an intrinsically disordered C-terminal domain[270]. The C-terminal domain contains a binding site for the α-subunit of the clathrin adaptor-protein complex AP2, two ubiquitin-interacting motifs (UIMs) (Figure 4.1a, top), and 15 tripeptide Asp-Pro-Phe (DPF) motifs[270-272]. The DPF motifs mediate oligomerization of Eps15 by binding to its N-

terminal EH domains[270-272]. As previously reported, full-length Eps15 assembles into liquid-like droplets through these multivalent interaction when added to a solution of 3% w/v PEG8000 in a buffer consisting of 20 mM Tris-HCl, 150 mM NaCl, 5 mM TCEP, 1 mM EDTA and 1 mM EGTA at pH 7.5[258] (Figure 4.1a, bottom, where ten percent of Eps15 molecules were labeled with the N-hydroxysuccinimide (NHS)-reactive dye, Atto 488 for visualization).

To examine the impact of ubiquitin of phase separation of Eps15, MonoUb and TetraUb, labeled with Atto 647, were added to Eps15 droplets at a final concentration of 1 μM and 0.25 μM, respectively, maintaining an equivalent mass per volume of ubiquitin. Images of the Eps15 droplets were collected after a 5-minute incubation. As shown in Figure 4.1b, 1c, both MonoUb and TetraUb partitioned uniformly into Eps15 droplets. However, the partition coefficient of TetraUb into Eps15 droplets, indicated by the ratio between the intensity of ubiquitin in the droplet (I_D) and the surrounding solution (I_S), was about twice that of MonoUb (4.1 ± 0.8 vs. 1.8 ± 0.2, Figure 4.1d), suggesting that Eps15 interacted more strongly with TetraUb, compared to MonoUb. Importantly, Eps15 droplets incubated with either MonoUb or TetraUb remained liquid-like, readily fusing and re-rounding upon contact (Figure 4.1e, 1f and Supplementary Information movie 4.1 and 4.2).

Further, MonoUb and TetraUb partitioned much more weakly into droplets consisting of a version of Eps15 that lacked its UIMs, Eps15ΔUIM (Δaa 851-896), (1.4 ± 0.1 and 1.5 ± 0.1 respectively, with no significant difference, Figure 4.1g, 1h and 1i). These results confirm that Eps15's UIMs play a key role in the partitioning of ubiquitin into Eps15 droplets, where both (i) Eps15-Eps15 interactions and (ii) Eps15-ubiquitin interactions are expected to exist within droplets (Figure 4.1j, 1k).

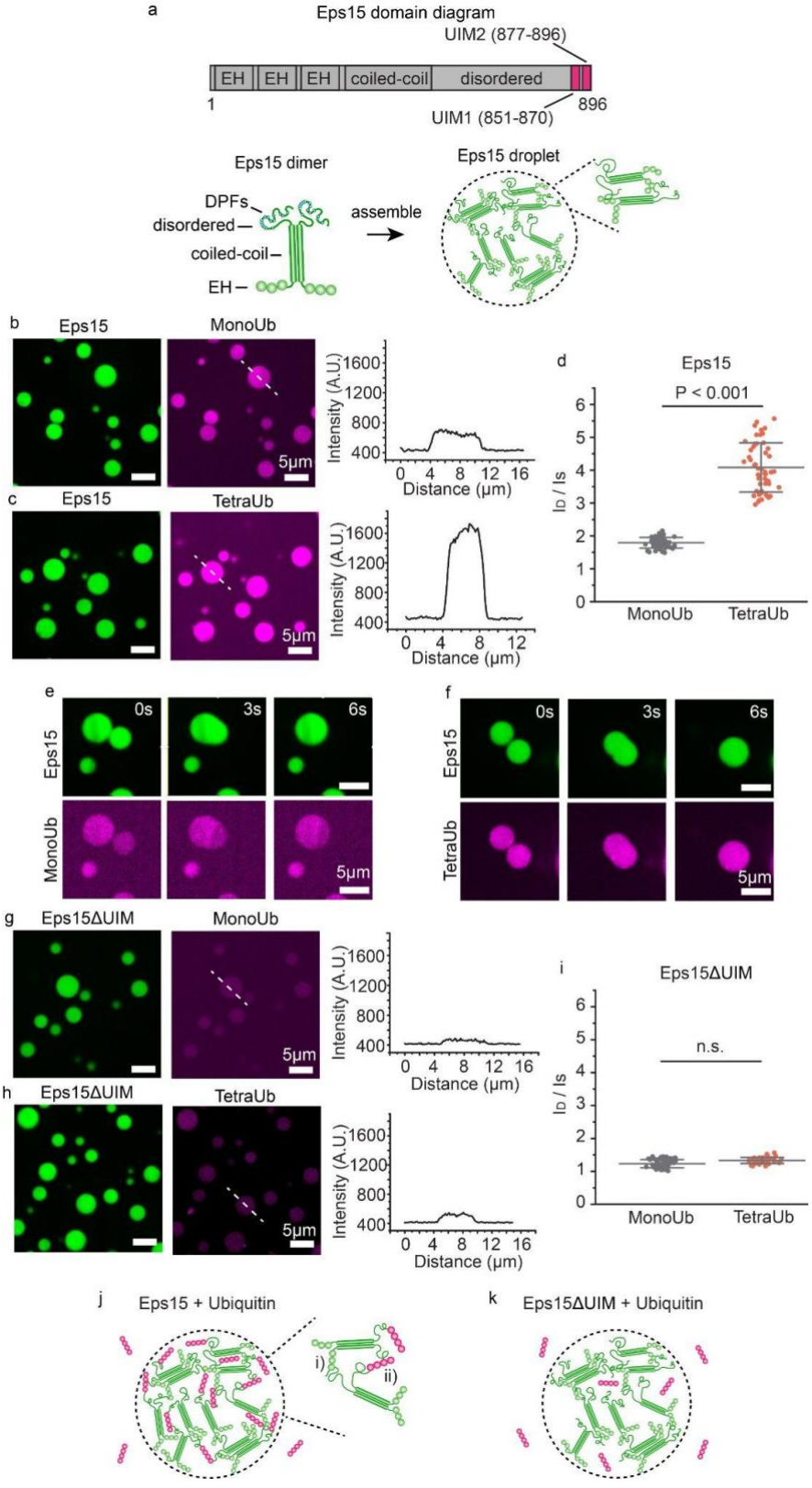
a
Eps15 domain diagram
UIM2 (877-896)
EH
EH
EH
coiled-coil
disordered
1
896
UIM1 (851-870)
Eps15 dimer
DPFs
disordered
coiled-coil
EH
assemble
Eps15 droplet
b
Eps15
MonoUb
5μm
Intensity (A.U.)
Distance (μm)
c
Eps15
TetraUb
5μm
d
Eps15
P < 0.001
ID / IS
MonoUb
TetraUb
e
Eps15
MonoUb
0s
3s
6s
5μm
f
Eps15
TetraUb
0s
3s
6s
5μm
g
Eps15ΔUIM
MonoUb
5μm
h
Eps15ΔUIM
TetraUb
5μm
i
Eps15ΔUIM
n.s.
MonoUb
TetraUb
j
Eps15 + Ubiquitin
i)
ii)
k
Eps15ΔUIM + Ubiquitin

Figure 4. 1 Polyubiquitin partitions strongly into liquid-like droplets of Eps15. a, top: Schematic of Eps15 functional domains. Eps15 consists of three EH domains at its N terminus followed by a coiled-coil domain and a long-disordered region containing two ubiquitin interacting motifs (UIMs) at the C terminal end. Bottom: cartoons depict domain organization of Eps15 in dimeric form. 15 tripeptide Asp-Pro-Phe (DPF) motifs are interspersed throughout the disordered region, which can bind the EH domains and allow itself to assemble into liquid-like droplets. **b, c,** Eps15 (7μM) droplets (green) incubated with 1μM MonoUb and 0.25μM K63 linkage TetraUb (magenta), respectively. Plots on the right depict intensity profile of ubiquitin channel along the white dashed line shown in the corresponding images. **d,** The distribution of the ubiquitin intensity ratio between the intensity inside the droplets (ID) and the solution (IS). In total 50 droplets were analyzed under each condition. **e, f,** Representative time course of fusion events between droplets containing Eps15 and MonoUb (**e**) and droplets containing Eps15 and TetraUb (**f**). **g-i**, Same with b-d except that droplets were formed with Eps15 mutant, Eps15ΔUIM, with the depletion of the two UIMs (aa 851-896). **j, k**, Pictorial representation of ubiquitin binding and partitioning into Eps15 droplets through interaction with UIMs at the C terminus of Eps15 (**j**) and deletion of UIMs impairs ubiquitin partitioning into Eps15 droplets (**k**). Inset in **j** shows the two types of interactions in Eps15-polyubiquitin network: i) DPF motif interacting with EH domain, and ii) polyubiquitin interacting with UIM domains. All droplet experiments were performed in 20 mM Tris-HCl, 150 mM NaCl, 5 mM TCEP, 1 mM EDTA and 1 mM EGTA at pH 7.5 with 3% w/v PEG8000. Error bars are standard deviation. Statistical significance was tested using an unpaired, two-tailed student's t test. All scale bars equal 5 μm.

Polyubiquitin promotes phase separation of Eps15 on membrane surfaces.

We next asked how the interaction between ubiquitin and Eps15 might impact assembly of Eps15 condensates on the surfaces of lipid membranes. To address this question, we purified Eps15 fused with an N-terminal 6 histidine tag (his-Eps15) and incubated it at a concentration of 0.5 μM with giant unilamellar vesicles (GUVs) consisting of 93 mol% POPC, 5 mol% DGS-NTA-Ni, and 2 mol% DP-EG10 biotin for coverslip tethering. Here, his-Eps15 was recruited to the surfaces of GUVs through binding between the histidine tag and Ni-NTA lipid headgroups (Figure 4.2a, left). His-Eps15 bound uniformly to the surfaces of GUVs (Figure 4.2a, left, and 2b), indicating that it alone does not phase separate on membrane surfaces, consistent with a previous report[258]. Similarly,

when 0.5 μM his-Eps15 and 0.5 μM MonoUb were added simultaneously to GUVs, MonoUb was recruited to the membrane surface through its interaction with Eps15, and both proteins decorated the surfaces of GUVs uniformly (Figure 4.2c). However, when 0.5 μM his-Eps15 and 0.2 μM TetraUb were added simultaneously to GUVs, the two proteins co-partitioned into protein-rich (bright) and protein-depleted (dim) phases on GUV surfaces (Figure 4.2d and 4.2a, right), similar to previous observations of protein phase separation on GUVs[71,258]. Three-dimensional reconstruction of image stacks revealed that the bright regions formed hemispherical domains on GUVs, which were surrounded by dimmer regions, indicating phase separation (Figure 4.7), as quantified in Figure 4.2g. In contrast, when UIMs were removed from his-Eps15 (his-Eps15ΔUIM), neither MonoUb nor TetraUb could be strongly recruited to GUV surfaces, and his-Eps15ΔUIM bound uniformly to the membrane surface, rather than phase separating (Figure 4.2e, 2f and 2g). These results illustrate that TetraUb promotes phase separation of Eps15 on membrane surfaces in a manner that depends upon Eps15's UIMs, suggesting that TetraUb strengthens the Eps15 network, likely by creating cross-links between Eps15 molecules (Figure 4.2a, right).

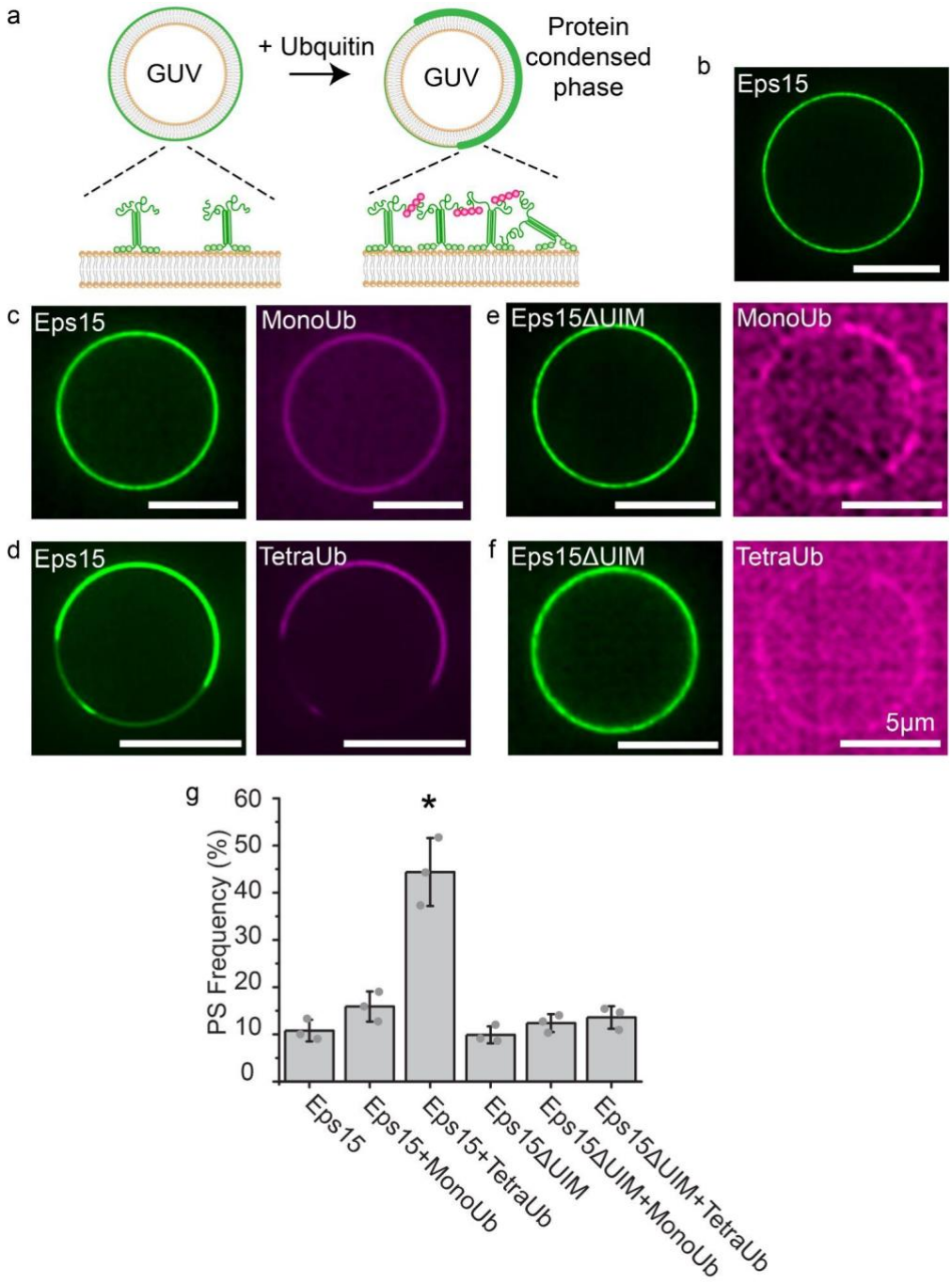

Figure 4. 2 Polyubiquitin promotes phase separation of Eps15 on membrane surfaces. **a,** Cartoon depicting his-Eps15 binding to GUV membrane (left) and polyubiquitin driving Eps15 phase separation on GUV membrane by linking Eps15 through interaction with the UIMs (right). **b-f**, Representative images of GUVs incubated with indicated proteins: 0.5 μM his-Eps15 alone (**b**), 0.5 μM his-Eps15 with 0.5 μM MonoUb (**c**), 0.5 μM his-Eps15 with 0.2 μM TetraUb (**d**), 0.5 μM his-Eps15ΔUIM with 0.5 μM MonoUb (**e**), and 0.5 μM

his-Eps15ΔUIM with 0.2 μM TetraUb (**f**). All scale bars are 5 μm. **g**, Frequency of GUVs displaying protein-rich domains for each set of proteins. GUVs were counted as displaying protein-rich domains if they contained distinct regions in which protein signal intensity differed by at least two-fold and the bright region covered at least 10% of the GUV surface in any z-slice. For each bar, n = 3 biologically independent experiments (each individual dot) with at least 44 total GUVs for each condition. Data are mean ± SD. *: $P < 0.001$ compared to all other groups using unpaired, two-tailed student's t test. GUVs contain 93 mol% POPC, 5 mol% DGS-NTA-Ni, and 2 mol% DP-EG10-biotin. All experiments were conducted in 20 mM Tris-HCl, 150 mM NaCl, 5 mM TCEP at pH 7.5 buffer.

Eps15 knockout creates a significant defect in coated pit dynamics that cannot be rescued by a version of Eps15 that lacks the ubiquitin interacting motif.

Having demonstrated that polyubiquitin can promote phase separation of Eps15 *in vitro*, we next sought to evaluate the impact of interactions between Eps15 and ubiquitin during the dynamic growth and maturation of endocytic structures at the plasma membrane of living cells. Previous work has demonstrated that Eps15 plays an important role in stabilizing complexes of early endocytic proteins[273]. Importantly, the dynamic assembly of endocytic structures at the plasma membrane is a highly heterogeneous process. While most assemblies of endocytic proteins ultimately result in productive endocytic events, a minority of these assemblies have aberrant stability, resulting in their failure to develop into endocytic vesicles. In particular, endocytic assemblies that persist at the plasma membrane for less than 20 seconds are generally regarded as "short-lived" structures[274]. These unstable assemblies, which typically consist of a small number of proteins, often stochastically disassemble before forming a productive vesicle. Productive assemblies typically form vesicles and depart from the plasma membranes over timescales of 20 seconds to several minutes. In contrast, structures that persist at the plasma membrane for longer periods are typically characterized as "long-lived" structures[275]. These overly stable assemblies, which are often larger than productive endocytic structures, may fail to develop into endocytic vesicles.

While it is difficult to determine whether individual assemblies of endocytic proteins form productive vesicles, shifts in the lifetime of endocytic structures provide insight into the overall efficiency of endocytosis. Specifically, an increase in short-lived structures indicates a reduction in stability, while an increase in productive or long-lived structures indicates an increase in stability. Within this framework, Eps15 knockout has recently been shown to decrease the productivity of endocytosis by increasing the fraction of endocytic structures that are short-lived[258]. Building on this result, we assessed the impact of interactions between Eps15 and ubiquitin on the dynamics of endocytosis.

We evaluated endocytic dynamics in a human breast cancer-derived epithelial cell line, SUM159, which was gene edited to (i) knockout Eps15, and (ii) add a C-terminal halo-tag to the sigma2 subunit of AP2. As AP2 is the major adaptor protein of the clathrin-mediated endocytic pathway[276,277], the halo tag, bound to JF646 dye, was used to visualize and track endocytic structures in real-time during live cell imaging[278]. Imaging experiments were performed using total internal reflection fluorescence (TIRF) microscopy to isolate the plasma membrane of adherent cells. In TIRF images, endocytic structures appear as diffraction-limited fluorescent puncta in the JF646 channel, Figure 4.3a. Eps15, and its variants, described below, were tagged at their C-termini with mCherry for visualization, and appeared co-localized with puncta of AP2 (JF646), Figure 4.3a. Based on the literature cited above, we loosely classified endocytic structures that persisted at the plasma membrane for less than 20s as “short-lived”, structures that persisted from 20 - 180 seconds as “productive”, and structures that persisted for longer than 180 seconds as “long-lived”. Endocytic structures within each of these categories were observed in our experiments (Figure 4.3a) and the distribution of lifetimes for the full population of endocytic structures is shown in Figure 4.3b. In agreement with a recent report[258], Eps15KO cells had a significantly higher frequency of short-lived structures compared to wildtype cells with

endogenous expression of Eps15 (15.4 ± 3.3% vs. 4.4 ± 1.3%, Figure 4.3b, 3c). This defect was effectively rescued by transient expression of wildtype Eps15 in Eps15KO cells (5.2 ± 1.6% vs. 4.4 ± 1.3% short-lived structures, Figure 4.3b, 3c).

We also analyzed the impact of Eps15 knockout on the intensity of endocytic structures in the AP2 channel, which, owing to the near 1:1 stochiometric ratio between AP2 and clathrin[279], serves as a proxy for the maturity and size of endocytic structures. This analysis revealed that Eps15 knockout resulted in significantly reduced AP2 intensity, suggesting less developed endocytic structures, compared to wildtype cells and knockout cells transiently expressing wildtype Eps15, Figure 4.3d and Figure 4.8. Specifically, histograms of AP2 intensity showed a shift towards smaller values when Eps15 was knocked out (850 ± 12, green dotted line, vs. 660 ± 5, red dotted line, in wildtype cells, Figure 4.3e), a defect which was rescued by transient expression of wildtype Eps15 in knockout cells (840 ± 9, black dotted line, vs. green dotted line, Figure 4.3e). Collectively, these results demonstrate that Eps15 knockout destabilizes endocytic structures, limiting their maturation.

Having established these controls, we next examined the impact of Eps15's UIMs on its ability to promote efficient endocytosis. Specifically, we measured the extent to which a version of Eps15 lacking the UIMs (Eps15ΔUIM, as described above) could rescue the defect in endocytic dynamics created by knockout of the wildtype protein. Interestingly, we found that the elevated number of short-lived endocytic structures observed upon Eps15 knockout was not substantially reduced by expression of Eps15ΔUIM at equivalent levels to the level of Eps15wt required for full rescue, (15.1 ± 1.9% vs. 15.4 ± 3.3%, Figure 4.3b, 3c). Similarly, expression of Eps15ΔUIM failed to elevate the average AP2 intensity at endocytic sites significantly above levels measured in knockout cells (Figure 4.3d, no significant difference between Eps15ΔUIM and Eps15KO in AP2 intensity, and AP2

distribution peaked at 710 ± 9, black dotted line, vs. red dotted line, Figure 4.3e), indicating an inability to stabilize endocytic structures. These results suggest that Eps15's UIMs are essential to its ability to promote assembly and maturation of endocytic structures.

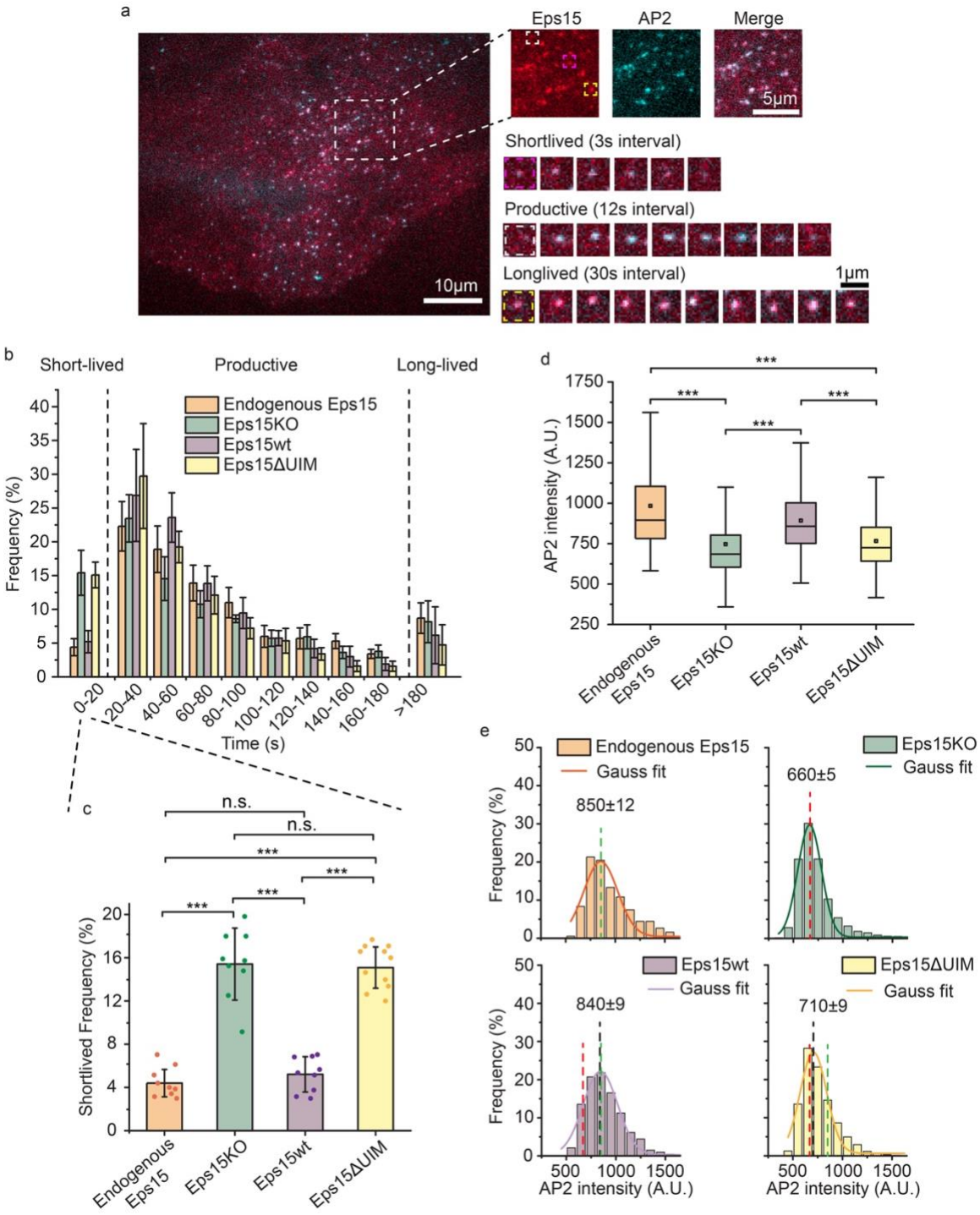

Figure 4. 3 Eps15 knockout creates a significant defect in coated pit dynamics that cannot be rescued by a version of Eps15 that lacks the ubiquitin interacting motif. a, Representative image of a SUM cell expressing gene-edited AP-2 σ2-HaloTag: JF646 (cyan) and Eps15-mCherry (red). Large inset highlights three representative clathrin-

coated structures shown in smaller insets: short- lived (pink), productive (white) and long-lived (yellow) structures lasting 18 s, 96 s and > 5 min, respectively. Scale bars are labeled in the images. **b**, Histograms of lifetime distributions of clathrin-coated structures under different experimental groups. Endogenous Eps15 represents SUM cells that have endogenous Eps15 expression. Lifetime shorter than 20 s is considered short-lived, lifetime between 20 and 180 s is labeled as productive and structures lasted longer than 180 s are long-lived. Eps15KO represents SUM cells that were CRISPR modified to knockout alleles of endogenous Eps15. Eps15wt and Eps15ΔUIM represent Eps15KO cells transfected with wildtype Eps15 and Eps15 with the depletion of both UIM domains, respectively. mCherry was fused to the C terminus of Eps15 and Eps15ΔUIM for visualization. **c,** bar chat of the short-lived fraction for each group from **b,** error bars are standard deviation, dots represent the results from different samples. **d**, Box plot of endocytic pits AP2 intensity in all four groups. **e**, Histograms and the Gauss fit of the AP2 intensity distribution tracked in endocytic pits under different experimental groups. Green dotted line indicates the peak distribution in Endogenous Eps15 cells, and red dotted line indicates the peak distribution in Eps15KO cells. For Endogenous Eps15 group, n = 9 biologically independent cell samples were collected and in total 2002 pits were analyzed. For Eps15KO, n = 9 and 2475 pits. Eps15wt, n = 9 and 2554 pits and Eps15ΔUIM, n = 11, 3952 pits. An unpaired, two-tailed student's t test was used for statistical significance. n.s. means no significant difference. ***: $P < 0.001$. All cell images were collected at 37°C.

Polyubiquitin elevates the melting temperature of liquid-like Eps15 networks.

The shorter lifetime of endocytic structures formed when Eps15ΔUIM replaces wild-type Eps15 suggests that loss of the UIMs destabilizes the network of early endocytic proteins. To test this idea, we sought to assess the impact of ubiquitin on the thermodynamic stability of liquid-like condensates of Eps15. For this purpose, we returned to the *in vitro* condensate system in Figure 4.1 and measured the temperature above which Eps15 condensates dissolve or melt, which is a key indicator of their stability[258]. Specifically, when we heated solutions of Eps15, liquid-like Eps15 droplets gradually dissolved, eventually melting such that the solution became homogenous (fully dissolved, Figure 4.4). The higher the melting temperature, the more energy is needed to prevent proteins from forming condensates, suggesting a more stable protein network.

To determine the melting temperature, images of Eps15 droplets were taken at each temperature as we heated the sample, starting from room temperature. As shown in Figure 4a, Eps15 droplets formed from a 7 μM protein solution, which gradually dissolved with increasing temperature and melted at approximately 32°C (Figure 4.4a), in agreement with a previous report[258]. We next examined the impact of ubiquitin on the melting temperature. Keeping Eps15 concentration at 7 μM, addition of 500 nM MonoUb slightly increased the melting temperature to 34°C (Figure 4.4b). In contrast, addition of 100 nM TetraUb raised the melting temperature more substantially from 32°C to 42°C (Figure 4.4c), suggesting that TetraUb is substantially more effective in stabilizing Eps15 condensates, in comparison to MonoUb. Using these data, we mapped a temperature-concentration phase diagram for Eps15 condensates (Figure 4.4d). Specifically, the relative fluorescence intensity of the droplets compared with the surrounding solution provided an estimate of the relative protein concentration in the two phases, C_D and C_S, respectively. These concentrations represent the ends of a tie-line on a temperature-concentration phase diagram at each temperature. As the temperature increased, the intensity of the Eps15 droplets decreased (Figure 4.4a-c) and the tie-lines became shorter as C_D and C_S became more similar, Figure 4.4d. The two concentrations ultimately became equivalent above the melting temperature, owing to dissolution of the droplets, Figure 4.4d. These results are in line with a recent report showing that poly-ubiquitin can enhance phase separation of proteins involved in protein degradation and autophagy[280].

To assess the impact of Eps15's UIM domains, we mapped the phase diagram of Eps15ΔUIM droplets in the presence of either MonoUb or TetraUb (Figure 4.4f, 4g and Figure 4.9), keeping protein concentrations the same as those used in experiments with wild-type Eps15. The phase diagram indicated that neither MonoUb nor TetraUb had a significant impact on the melting temperature of condensates composed of Eps15ΔUIM,

demonstrating that the stabilization effect observed with wildtype Eps15 arises from specific interactions between Eps15 and ubiquitin. Collectively, these results demonstrate that polyubiquitin not only partitions preferentially into Eps15 condensates (Figure 4.1) but can also help to crosslink and reinforce the protein network in a manner that is UIM-dependent (Figure 4.4e).

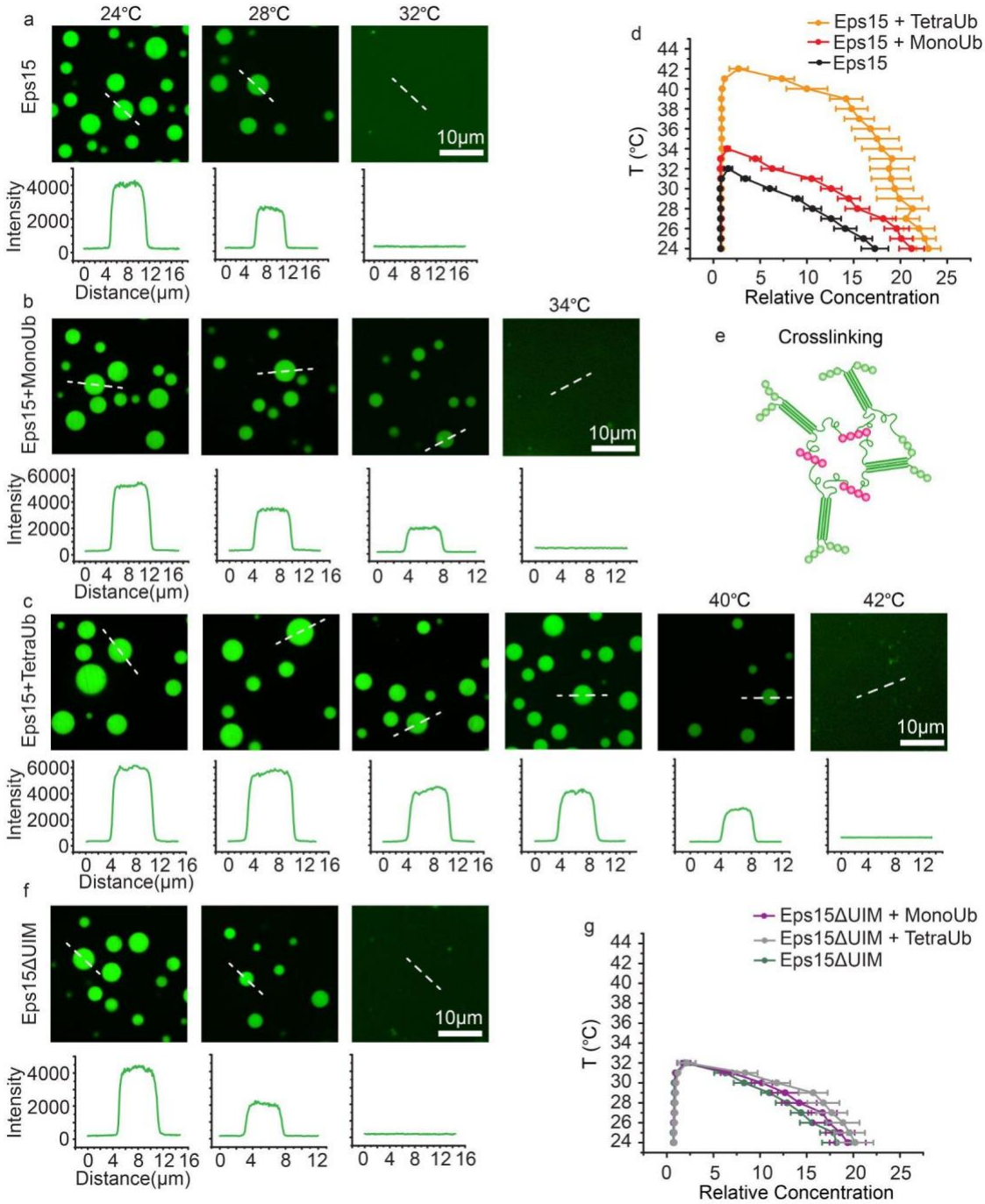

Figure 4. 4 Polyubiquitin elevates the melting temperature of liquid-like Eps15 networks. a-c, f, Representative images of protein droplets at increasing temperatures. Plots show fluorescence intensity of Eps15 measured along dotted lines in each image. Droplets are formed from (**a**) 7 μM Eps15, (**b**) 0.5 μM MonoUb, 7 μM Eps15, (**c**) 0.1 μM TetraUb, 7 μM Eps15 and (**f**) 7 μM Eps15ΔUIM in 20 mM Tris-HCl, 150 mM NaCl, 5 mM TCEP, 1 mM EDTA and 1 mM EGTA at pH 7.5 buffer with 3% PEG8000. **d, g**, Phase

diagram of Eps15/MonoUb/TetraUb (**d**) and Eps15ΔUIM/MonoUb/TetraUb (**g**) droplets mapped by Atto488-labelled Eps15/Eps15ΔUIM fluorescence intensity. Intensity was normalized based on the intensity of the solution. Dots on the right side are protein concentrations in droplets and dots on the left side are concentrations in solution. At least 20 droplets are analyzed under each temperature. Data are mean ± SD. Scale bars equal 10 μm. **e,** Schematic of polyubiquitin crosslinking and stabilizing Eps15 network.

Fusion of a deubiquitinating enzyme to Eps15 results in about twice as many short-lived endocytic events than deletion of Eps15.

If polyubiquitin stabilizes endocytic protein networks, then stripping ubiquitin from the proteins that make up an endocytic site should disrupt the dynamics of endocytosis. To test this concept, we added a deubiquitinating enzyme (DUB) to Eps15 to remove ubiquitin modifications from Eps15 as well as its close interactors, which likely include other endocytic proteins and the intracellular domains of receptors that enter endocytic sites[281-283]. Using this approach, we sought to probe the broader sensitivity of endocytic assemblies to loss of ubiquitination. Here a "broad-spectrum" deubiquitinase, UL36, was adopted. UL36, which consists of the N-terminal domain (residues 15-260) of the type I Herpes virus VP1/2 tegument protein[281,284], cleaves both K63 and K48-linked polyubiquitin chains[282,284,285]. K63-linked chains are more traditionally associated with endocytic recycling[268,286], while K48-linked chains, which are mainly involved in targeting proteins for proteasomal degradation[286], have a less understood relationship with endocytosis. UL36 was inserted at the C-terminus of Eps15, prior to the mCherry tag, to create the fusion protein Eps15-DUB (Figure 4.5a). As a control for the potential non-specific impact of the DUB fusion on endocytic function, a catalytically inactive UL36, which contains a mutation of its core catalytic residues (Cys65 to Ala)[282,285], was inserted at the same position as the catalytically active UL36 to create the chimera, Eps15-DUB-dead (Figure 4.5a). We then expressed both Eps15-DUB and Eps15-DUB-dead in Eps15 knockout cells

and tracked endocytic dynamics with TIRF microscopy, as described in Figure 4.3. TIRF images revealed clear colocalization of Eps15-DUB and Eps15-DUB-dead (mCherry) with endocytic sites, represented by fluorescent puncta in the AP2 (JF646) channel, Figure 4.5b. However, expression of Eps15-DUB in Eps15KO cells led to a further decrease in AP2 intensity (Figure 4.5b and Figure 4.5c, top, 570 ± 11) at endocytic sites compared to Eps15 knockout cells alone (Figure 4.5c, red dotted line), suggesting smaller, less mature endocytic sites. In contrast, expression of Eps15-DUB-dead restored AP2 intensity to a level more similar to wildtype cells (Figure 4.5b, and Figure 4.5c, bottom, 810 ± 12, vs. the green dotted line). Furthermore, the fraction of unstable, short-lived endocytic sites increased by more than 60% in cells expressing Eps15-DUB, compared to cells lacking Eps15 (27.5 ± 5.8% vs. 15.4 ± 3.3% Figure 4.5d). These results suggest that Eps15-DUB not only failed to rescue the defect caused by Eps15 knockout, but made the defect substantially larger, such that there is a strong bias toward unproductive, short-lived endocytic events when ubiquitin is removed from endocytic sites (Figure 4.5e). In contrast, Eps15-DUB-dead provided a partial rescue of endocytic dynamics, reducing the fraction of short-lived structures to 10.7 ± 1.8%, Figure 4.5d. These results suggest that the importance of ubiquitylation to endocytosis likely extends beyond Eps15. In particular, if Eps15 were the only endocytic protein that relied on ubiquitin for its assembly, we would have expected Eps15-DUB to create no greater effect on endocytic dynamics than Eps15ΔUIM. These results could be explained by the presence of other UIMs within endocytic proteins, such as Epsin[261,263,287], which could interact with ubiquitin modifications on virtually any endocytic protein or transmembrane cargo protein.

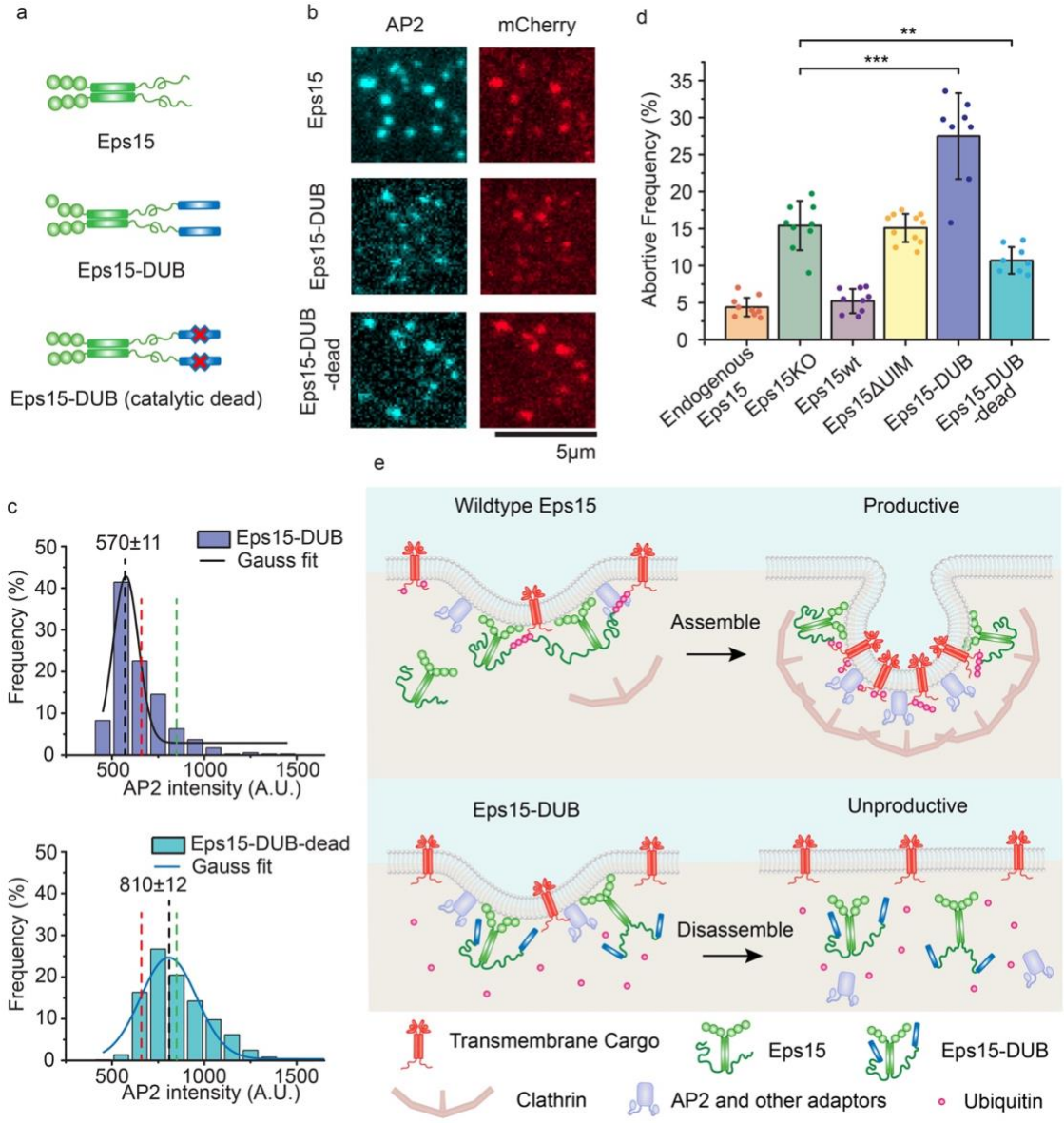

Figure 4. 5 Fusion of a deubiquitinating enzyme to Eps15 results in even more short-lived endocytic events than deletion of Eps15. a, Schematic of Eps15 dimeric form, Eps15-DUB (deubiquitinase fused to C terminal end of Eps15), and Eps15-DUB-dead (same with DUB but with a mutation that makes DUB catalytically dead). mCherry is not shown in the cartoon but all three constructs have mCherry at their C terminus for visualization. **b**, Representative images showing Eps15, Eps15-DUB and Eps15-DUB-dead colocalization with AP2 in endocytic sites when Eps15KO SUM cells were transfected to express corresponding proteins. Scale bar = 5 μm. **c**, Histograms and the Gauss fit of the AP2 intensity distribution tracked in endocytic pits when expressing Eps15-DUB (top) and Eps15-DUB-dead (bottom), respectively. The green dotted line and red

dotted line are corresponding to Eps15KO group and endogenous Eps15 group in Figure 3. **d**, Frequency of short-lived structures under each condition. Endogenous Eps15, Eps15KO, Eps15wt and Eps15ΔUIM are adopted from the same data in shown in Figure 3. For Eps15-DUB, n = 8 biologically independent cell samples were collected and in total 1053 pits were analyzed. For Eps15-DUB-dead, n = 8 and 1464 pits were analyzed. Dots represent the frequency from each sample. An unpaired, two-tailed student's t test was used for statistical significance. **: $P < 0.01$, ***: $P < 0.001$. Error bars represent standard deviation. Cells were imaged at 37°C for all conditions. **e**, Schematic showing how polyubiquitin stabilizes the endocytic protein network by interacting with and cross-linking UIMs on endocytic proteins, resulting in productive clathrin-mediated endocytosis (Top). Removal of ubiquitin from the endocytic protein network using DUB decreases the network multivalency thus making the network less stable, resulting in less efficient clathrin-mediated endocytosis (bottom).

Light-activated recruitment of DUBs demonstrates that loss of ubiquitination destabilizes endocytic sites within minutes.

While the results in the previous section suggest the importance of ubiquitylation to endocytic dynamics, it is not clear whether the observed shifts result from an acute impact on endocytosis versus broader physiological changes resulting from expression of deubiquitinases. Therefore, we sought to develop a system that would allow us to measure endocytic dynamics immediately after recruitment of deubiquitinases to endocytic sites. For this purpose, we made use of our previous observation that monomeric Eps15, which is created by deletion of Eps15's coiled-coil domain, is not stably recruited to endocytic sites, likely owing to reduced affinity for the endocytic protein network[258]. Therefore, we created a chimeric protein in which Eps15's coiled-coil domain was replaced by a domain that forms dimers and oligomers upon blue light exposure, the photolyase homology region (PHR) of CRY2[288] (Figure 4.6a). As reported previously, the resulting chimera, Eps15-CRY2 assembles upon blue light exposure, resulting in its stable recruitment to endocytic sites[258].

Similarly, we found that when Eps15-CRY2 was transiently expressed in Eps15 knockout cells, it colocalized weakly with endocytic sites prior to blue light exposure (Figure 4.6b, top). The fraction of short-lived endocytic sites in these cells remained similar to the level in knockout cells (17.7 ± 4.4%, Figure 4.6h), consistent with previous findings that a monomeric version of Eps15 cannot rescue Eps15 knockout[258]. However, upon exposure to blue light, Eps15-CRY2 was recruited to endocytic sites (Figure 4.6b, bottom, and Figure 4.10, fraction of pits showing Eps15 colocalization increased from 35.5 ± 5.5% to 74.1 ± 6%). Simultaneously with the increase in Eps15 recruitment, more AP2 was recruited to endocytic sites (mean AP2 intensity shifted from 740 ± 12 to 910 ± 16, Figure 4.6b, 6c, Supplementary Information Movie 4.3), suggesting increased stability and maturation of endocytic sites. Similarly, the fraction of short-lived endocytic structures was reduced to near wild type levels, 7.3 ± 3.2% (Figure 4.6h), confirming that light-induced assembly of Eps15 stabilized endocytic sites, rescuing the defects associated with Eps15 knockout[258]. Importantly, in these experiments, endocytic dynamics were consecutively measured before and after blue light exposure in each cell, such that changes associated with light-activated protein assembly were directly observed for individual cells (see Materials and Methods).

We next repeated these experiments in Eps15 knockout cells that transiently expressed a blue light activated Eps15 chimera fused to the UL36 deubiquitinase enzyme, Eps15-CRY2-DUB. Similar to Eps15-CRY2, in the absence of blue light, this protein colocalized weakly with endocytic sites (Figure 4.6d, top, Figure 4.10) and failed to substantially reduce the fraction of short-lived endocytic sites (16.5 ± 3.5%, Figure 4.6h). However, upon exposure to blue light, increased recruitment of this DUB-containing chimera to endocytic sites resulted in an 69% increase in the fraction of short-lived endocytic sites (27.9 ± 6.0%, Figure 4.6h), which correlated with a substantial reduction in recruitment of

AP2 to endocytic sites (710 ± 8 to 550 ± 6, Figure 4.6e, Supplementary Information Movie 4.3). In contrast, expression of an Eps15-CRY2 chimera that contained the catalytically inactive DUB, Eps15-CRY2-DUB-dead, reduced the fraction of short-lived endocytic structures to near wild type levels (8.0 ± 3.0% vs. 7.3 ± 3.2%, Figure 4.6h) upon blue light exposure. Similarly, recruitment of AP2 to endocytic sites in cells expressing Eps15-CRY2-DUB-dead was similar to that in cells expressing Eps15-CRY2 (Figure 4.6f, Figure 4.6g, 740 ± 12 to 910 ± 16, and Supplementary Information Movie 4.3), suggesting that the DUB fusion did not sterically inhibit endocytic dynamics. Importantly, the fraction of short-lived endocytic events in cells expressing each of the CRY2 chimeras was similar to that in Eps15 knockout cells, suggesting that expression of Eps15-CRY2-DUB did not significantly impact endocytic dynamics prior to its light-activated recruitment to endocytic sites. Taken together, these results suggest that loss of ubiquitylation acutely destabilizes endocytic sites within minutes.

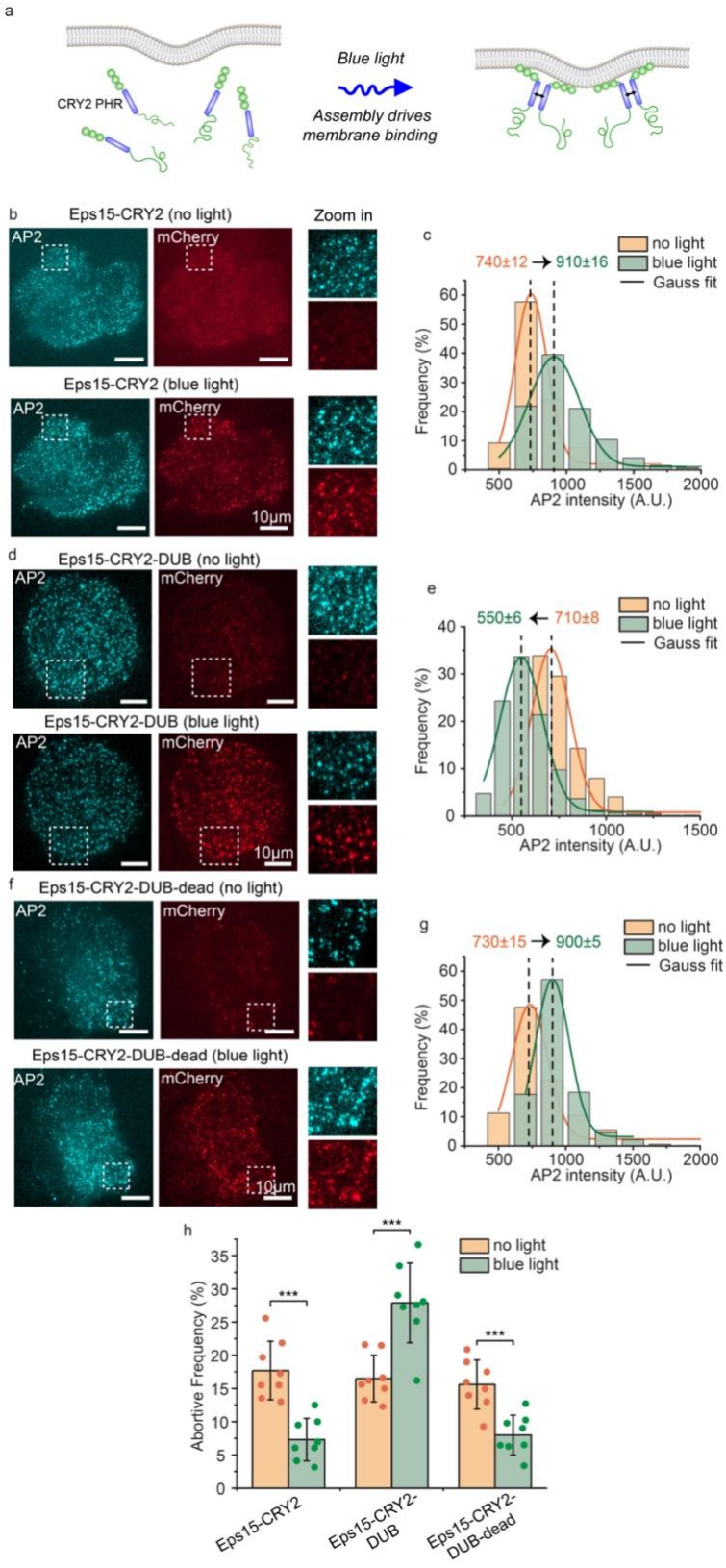
a
CRY2 PHR
Blue light
Assembly drives membrane binding
b
Eps15-CRY2 (no light)
Zoom in
AP2
mCherry
Eps15-CRY2 (blue light)
10μm
c
740±12 → 910±16
no light
blue light
Gauss fit
Frequency (%)
AP2 intensity (A.U.)
d
Eps15-CRY2-DUB (no light)
Eps15-CRY2-DUB (blue light)
e
550±6 ← 710±8
f
Eps15-CRY2-DUB-dead (no light)
Eps15-CRY2-DUB-dead (blue light)
g
730±15 → 900±5
h
Abortive Frequency (%)
***
Eps15-CRY2
Eps15-CRY2-DUB
Eps15-CRY2-DUB-dead

Figure 4. 6 Light-activated recruitment of DUBs demonstrates that loss of ubiquitination destabilizes endocytic sites within minutes. a, Schematic of blue light driving assembly and membrane binding of Eps15-CRY2 chimera in which the Eps15 coiled-coil domain is replaced with the light-activation CRY2 PHR domain. **b, d, f**, Representative images of Eps15KO SUM cells expressing Eps15-CRY2 (**b**), Eps15-CRY2-DUB (**d**) and Eps15-CRY2-DUB-dead (**f**) before and after applying blue light. AP-2 σ2-HaloTag was labeled with JF646 (cyan). Insets show the zoom-in area of the white dashed box. mCherry was fused to all three constructs at their C terminus for visualization. Scale bar = 10 μm. **c, e, g**, Histograms and the Gauss fit of the AP2 intensity distribution tracked in endocytic pits when expressing Eps15-CRY2 (**c**), Eps15-CRY2-DUB (**e**) and Eps15-CRY2-DUB-dead (**g**) before and after exposed to blue light, respectively. **h**, Frequency of short-lived structures comparison before and after blue light was applied to the cells under each condition. For Eps15-CYR2, n = 8 biologically independent cell samples were collected and in total 1060 pits (before light) and 1068 pits (blue light) were analyzed. For Eps15-CRY2-DUB, n = 8 and 1099 pits (before light) and 1371 pits (blue light) were analyzed. For Eps15-CRY2-DUB-dead, n = 8 and total pits = 1044 (before light) and 918 (blue light). Dots represent frequency from each sample. An unpaired, two-tailed student's t test was used for statistical significance. ***: $P < 0.001$. Error bars represent standard deviation. Cells were imaged at 37°C for all conditions.

DISCUSSION

Here we demonstrate that ubiquitylation plays an important role in stabilizing the flexible network of early initiator proteins during clathrin-mediated endocytosis. *In vitro* experiments with protein droplets and giant unilamellar vesicles collectively demonstrated that polyubiquitin, but not monoubiquitin, is strongly recruited to liquid-like networks of the initiator protein, Eps15. Importantly, these effects required Eps15's ubiquitin interacting motif (UIM). Similarly, in live cell imaging experiments, a version of Eps15 lacking the UIM domain failed to rescue the increase in short-lived endocytic structures resulting from Eps15 knockout. These results suggest that interactions between Eps15 and ubiquitylated proteins, either transmembrane cargo or other endocytic proteins, can stabilize the early endocytic network. Testing this idea *in vitro*, we found that the melting temperature of the Eps15 network increased substantially in the presence of polyubiquitin, but not monoubiquitin, an effect which required Eps15's UIM domain. To test the impact

of ubiquitin on the stability of endocytic sites more broadly, we next evaluated the impact of deubiquitinase (DUB) enzymes on coated vesicle dynamics. Here we found that expressing a version of Eps15 fused to a broad-spectrum DUB approximately doubled the number of unstable, short-lived endocytic sites, rather than rescuing the defect created by Eps15 knockout. Further, by using a light activated recruitment system for Eps15-DUB, we demonstrated that loss of ubiquitin can acutely destabilize endocytic sites within minutes, a result which likely represents the cumulative effect of removing ubiquitin from multiple endocytic proteins and transmembrane protein cargos.

Our finding that polyubiquitin can stabilize early endocytic networks is supported by earlier work suggesting the importance of ubiquitylation in endocytosis. Specifically, the early initiator protein, Eps15, and the adaptor protein, Epsin, are both known to contain UIM motifs[263,289]. Epsin, in particular, is thought to act as a cargo adaptor for ubiquitinated transmembrane proteins[255,289,290]. Interestingly, Eps15 and Epsin interact through binding between Eps15's EH domains and Epsin's NPF (asparagine, proline, phenylalanine) domain, suggesting that they may be key components within a ubiquitin-stabilized protein network that facilities efficient endocytosis[291,292].

Similarly, prior work in budding yeast cells suggests that mono- and poly-ubiquitylated transmembrane proteins contribute to the stability of endocytic sites. Specifically, attachment of K63-linked polyubiquitin chains to permeases at the plasma membrane significantly accelerated their internalization by the clathrin pathway[266]. Further, conjugation of cargo proteins with polyubiquitin chains promoted more efficient endocytosis than conjugation with monoubiquitin[293]. Additionally, endogenous deubiquitinases (DUBs) were found to play a critical role in the turnover of endocytic sites, avoiding overly stable, long-lived sites that become stalled[268]. While the role of ubiquitination in mammalian cell endocytosis has been less explored, ubiquitination of

receptors is known to be important for Epsin-mediated uptake of influenza virus by the clathrin pathway[287].

In the context of this literature, our work suggests that a key role of ubiquitylation is to stabilize the early endocytic network, such that endocytic sites mature efficiently into productive coated vesicles (Figure 4.5e). Specifically, an increase or decrease in ubiquitination at endocytic sites, which cells could achieve by modulating ubiquitylation of endocytic proteins or transmembrane cargos, could effectively modulate endocytic dynamics. Prior work on endocytic dynamics has suggested that nascent endocytic sites mature into productive endocytic structures by passing through a series of biochemical "checkpoints" or criteria, the precise identity of which remains unknown[247]. In this context, our results suggest that the ubiquitin content of endocytic sites, which stabilizes the flexible network of early endocytic proteins, may constitute such a checkpoint.

MATERIALS AND METHODS

Reagents

Tris-HCl (Tris hydrochloride), HEPES (4-(2-hydroxyethyl)-1-piperazineethanesulfonic acid), IPTG (isopropyl-β-D-thiogalactopyranoside), NaCl, β-mercaptoethanol, Triton X-100, neutravidin, and Texas Red-DHPE (Texas Red 1,2-dihexadecanoyl-sn-glycero-3-phosphoethanolamine triethylammonium salt) were purchased from Thermo Fisher Scientific. Sodium bicarbonate, sodium tetraborate, EDTA (Ethylene diamine tetraacetic acid), EGTA (Ethylene glycol tetraacetic acid), glycerol, TCEP (tris(2-carboxyethyl) phosphine), DTT (Dithiothreitol), PMSF (phenylmethanesulfonylfluoride), EDTA-free protease inhibitor tablets, thrombin, imidazole, sodium bicarbonate, PLL (poly-l-lysine), Atto640 NHS ester and Atto488 NHS

ester were purchased from Sigma-Aldrich. Monoubiquitin and K63 linked Tetraubiquitin were purchased from Boston Biochem (Catalog #: U-100H and UC-310). PEG 8000 (Polyethylene glycol 8000) was purchased from Promega (Catalog #: V3011). Amine-reactive PEG (mPEG-succinimidyl valerate MW 5000) and PEG-biotin (Biotin-PEG SVA, MW 5000) were purchased from Laysan Bio. DP-EG10-biotin (dipalmitoyl-decaethylene glycol-biotin) was provided by D. Sasaki (Sandia National Laboratories). POPC (1-palmitoyl-2-oleoyl-glycero-3-phosphocholine) and DGS-NTA-Ni (1,2-dioleoyl-sn-glycero-3-[(N-(5-amino-1-carboxypentyl) iminodiacetic acid)-succinyl] (nickel salt)) were purchased from Avanti Polar Lipids. All reagents were used without further purification.

Plasmids

Plasmids used for purifying Eps15 and Eps15ΔUIM from bacteria are pET28a-6×His-Eps15 (FL) and pET28a-6×His-Eps15ΔUIM. pET28a-6×His-Eps15 (FL) encoding H. sapiens Eps15 was kindly provided by T. Kirchhausen[270], Harvard Medical School, USA. pET28a-6×His-Eps15ΔUIM was generated by using site-directed mutagenesis to introduce a stop codon after residue 850 of Eps15 to generate a truncated version lacking residues 851-896 corresponding to the UIM domains at the C terminus. The forward primer 5'-GTGCTTATCCCTGAGAAGAAGATATGATCG-3' and reverse primer 5'-CATATCTTCTTCTCAGGGATAAGCACTGAAG-3' were used.

Plasmids used for mammalian cell expression of Eps15 variants were derived from Eps15-pmCherryN1 (Addgene plasmid #27696, a gift from C. Merrifield[294]), which encodes Eps15-mCherry (denoted as Eps15wt). All of the following Eps15 variants contain mCherry at their C terminal end for visualization even though mCherry is not mentioned in their names. The Eps15ΔUIM plasmid was generated by PCR-mediated deletion of the UIM domains (residues 851-896). The 138 base pairs corresponding to the two UIM

domains were deleted using the 5’ phosphorylated forward primer 5’-CGGATGGGTTCGACCTC-3’ and the reverse primer 5’-GGGATAAGCACTGAAGTTGG-3’. After PCR amplification and purification, the PCR product was recircularized to generate the Eps15ΔUIM. Plasmids encoding the broad-spectrum deubiquitinase (DUB), UL36, and the catalytically inert mutant (C56S, DUB-dead), were generously provided by J. A. MacGurn[282]. Plasmids encoding the Eps15-DUB and Eps15-DUB-dead were generated by restriction cloning. Amplification of the DUB and DUB-dead was achieved using the forward primer 5’-CATGAGGATCCAATGGACTACAAAGACCATGACG-3’ and the reverse primer 5’-CATGAGGATCCGGGTATGGGTAAAAGATGCGG-3’. The amplicon was then inserted into the Eps15-pmCherryN1 at the BamH1 restriction sites between Eps15 and mCherry. The plasmid encoding Eps15-CRY2 was generated by using the crytochrome 2 photolyase homology region (CRY2 PHR) domain of *Arabidopsis thaliana* to replace the coiled-coil domain in Eps15 based on our previous report[258]. Specifically, the CRY2 PHR domain was PCR amplified from pCRY2PHR-mCherryN1 (Addgene plasmid #26866, a gift from C. Tucker[295]) using primers 5′-TAGGATCAAGTCCTGTTGCAGCCACCATGAAGATGGACAAAAAGAC-3′ and 5′-ATCAGTTTCATTTGCATTGAGGCTGCTGCTCCGATCAT-3′. This fragment was inserted by Gibson assembly (New England Biolabs) into Eps15-pmCherryN1 (Addgene plasmid#27696, a gift from C. Merrifield[294]), which were PCR amplified to exclude Eps15 coiled-coil domain (residues 328–490) using primers 5′-TCATGATCGGAGCAGCAGCCTCAATGCAAATGAAACTGATGGAAATGAAAG ATTTGGAAAATCATAATAG-3′ and 5′-TTGTCCATCTTCATGGTGGCTGCAACAGGACTTGATCCTATGAT-3′. Plasmids encoding Eps15-CRY2-DUB and Eps15-CRY2-DUB-dead were generated by inserting

DUB and DUB-dead in between Eps15-CRY2 and mCherry through Gibson assembly. The primers 5'-GTCAGCTGGCCCGGGATCCAATGGACTACAAA-3' and 5'-CTCACCATGGTGGCGACCGGTGGATCCGGGTA-3' were used for amplifying DUB and DUB-dead and primers 5'-TTTACCCATACCCGGATCCACCGGTCGCCACCA-3' and 5'- TCATGGTCTTTGTAGTCCATTGGATCCCGGGCCAG-3' were used for amplifying the vector Eps15-CRY2.

All constructs were confirmed by DNA sequencing.

Protein purification

Eps15 and Eps15ΔUIM were purified based on a previously reported protocol[258]. Briefly, full-length Eps15 and Eps15ΔUIM were expressed as N-terminal 6×His-tagged constructs in BL21 (DE3) Escherichia coli cells. Cells were grown in 2×YT medium for 3-4 h at 30 °C to an optical density at 600 nm of 0.6-0.9, then protein expression was induced with 1 mM IPTG at 30 °C for 6-8 hours. Cells were collected, and bacteria were lysed in lysis buffer using homogenization and probe sonication on ice. Lysis buffer consisted of 20 mM Tris-HCl, pH 8.0, 300 mM NaCl, 5% glycerol, 10 mM imidazole, 1 mM TCEP, 1 mM PMSF, 0.5% Triton X-100 and 1 EDTA-free protease inhibitor cocktail tablet (Roche: Cat#05056489001) per 50 mL buffer. Proteins were incubated with Ni-NTA Agarose (Qiagen, Cat#30230) resin for 30 min at 4 °C in a beaker with stirring, followed by extensive washing with 10 column volumes of lysis buffer with 20 mM imidazole and 0.2% Triton X-100 and 5 column volumes of buffer without Triton X-100. Then proteins were eluted from the resin in 20 mM Tris-HCl, pH 8.0, 300 mM NaCl, 5% glycerol, 250 mM imidazole, 0.5 mM TCEP, 1 mM PMSF, and EDTA-free protease inhibitor cocktail tablet. Eluted proteins were further purified by gel filtration chromatography using a Superose 6 column run in 20 mM Tris-HCl, pH 8.0, 150 mM NaCl, 1 mM EDTA, and 5 mM DTT.

For droplet experiments, prior to running the gel filtration column, the 6×His tag on the proteins was further cleaved with Thrombin CleanCleave kit (Sigma-Aldrich, Cat# RECMT) overnight at 4 °C on the rocking table after desaltig in 50 mM Tris-HCl, pH 8.0, 10 mM $CaCl_2$, 150 mM NaCl and 1 mM EDTA using a Zeba Spin desalting column (Thermo Scientific, Cat#89894). The purified proteins were dispensed into small aliquots, flash frozen in liquid ntitrogen and stored at -80 °C.

Protein labeling

Eps15 and Eps15ΔUIM were labeled with amine-reactive NHS ester dyes Atto488 in phosphate-buffered saline (PBS, Hyclone) containing 10 mM sodium bicarbonate, pH 8.3. Monoubiquitin and tetraubiquitin were labeled with Atto640 in PBS, pH 7.4. The concentration of dye was adjusted experimentally to obtain a labeling ratio of 0.5–1 dye molecule per protein, typically using 2-fold molar excess of dye. Reactions were performed for 30 min on ice. Then labeled Eps15 and Eps15ΔUIM was buffer exchanged into 20 mM Tris-HCl pH 7.5, 150 mM NaCl, 5 mM TCEP, 1 mM EDTA, 1 mM EGTA and separated from unconjugated dye using Princeton CentriSpin-20 size-exclusion spin columns (Princeton Separations). The labeled monoubiquitin and tetraubiquitin were buffer exchanged to 20 mM Tris-HCl, 150 mM NaCl, pH 7.5 and separated from unconjugated dye as well using 3K Amicon columns. Labeled proteins were dispensed into small aliquots, flash frozen in liquid nitrogen and stored at -80°C. For all experiments involving labeled Eps15 and Eps15ΔUIM, a mix of 90% unlabelled/10% labeled protein was used. 100% labeled monoubiquitin and tetraubiquitin were directly used due to their small fraction compared to Eps15 variants.

PLL-PEG preparation

PLL-PEG and biotinylated PLL-PEG were prepared as described previously with minor alterations[168]. Briefly, for PLL-PEG, amine-reactive mPEG-succinimidyl valerate was mixed with poly-L-lysine (15–30 kD) at a molar ratio of 1:5 PEG to poly-L-lysine. For biotinylated PLL-PEG, amine reactive PEG and PEG-biotin was first mixed at a molar ratio of 98% to 2%, respectively, and then mixed with PLL at 1:5 PEG to PLL molar ratio. The conjugation reaction was performed in 50 mM sodium tetraborate pH 8.5 solution and allowed to react overnight at room temperature with continued stirring. The products were buffer exchanged into 5 mM HEPES, 150 mM NaCl pH 7.4 using Zeba spin desalting columns (7K MWCO, ThermoFisher) and stored at 4 °C.

Protein droplets

Eps15 or Eps15ΔUIM droplets were formed by mixing proteins with 3% w/v PEG8000 in 20 mM Tris-HCl pH 7.5, 150 mM NaCl, 5 mM TCEP 1 mM EDTA, 1 mM EGTA. 7 μM Eps15 or Eps15ΔUIM was used to form the droplets, with addition of ubiquitins accordingly. For imaging droplets, 2% PLL-PEG were used to passivate coverslips (incubated for 20 min) before adding protein-containing solutions. Imaging wells consisted of 5 mm diameter holes in 0.8 mm thick silicone gaskets (Grace Bio-Labs). Gaskets were placed directly onto no.1.5 glass coverslips (VWR International), creating a temporary water-proof seal. Prior to well assembly, gaskets and cover slips were cleaned in 2% v/v Hellmanex III (Hellma Analytics) solution, rinsed thoroughly with water, and dried under a nitrogen stream. The imaging well was washed 6-8 times with 20 mM Tris-HCl, 150 mM NaCl and 5 mM TCEP buffer before adding solutions that contained proteins.

GUV preparation

GUVs consisted of 93 mol% POPC, 5 mol% Ni-NTA, and 2 mol% DP-EG10 biotin. GUVs were prepared by electroformation according to published protocols[167]. Briefly, lipid mixtures dissolved in chloroform were spread into a film on indium-tin-oxide (ITO) coated glass slides (resistance ~8-12 W per square) and further dried in a vacuum desiccator for at least 2 hours to remove all of the solvent. Electroformation was performed at 55°C in glucose solution with an osmolarity that matched the buffer to be used in the experiments. The voltage was increased every 3 min from 50 to 1400 mV peak to peak for the first 30 min at a frequency of 10 Hz. The voltage was then held at 1400 mV peak to peak, 10 Hz, for 120 min and finally was increased to 2200 mV peak to peak, for the last 30 min during which the frequency was adjusted to 5 Hz. GUVs were stored in 4°C and used within 3 days after electroformation.

GUV tethering

GUVs were tethered to glass coverslips for imaging as previously described[71]. Briefly, glass cover slips were passivated with a layer of biotinylated PLL-PEG, using 5 kDa PEG chains. GUVs doped with 2 mol% DP-EG10-biotin were then tethered to the passivated surface using neutravidin. Imaging wells consisted of 5 mm diameter holes in 0.8 mm thick silicone gaskets were prepared by placing silicone gaskets onto Hellmanex III cleaned coverslips. In each imaging well, 20 μL of biotinylated PLL-PEG was added. After 20 min of incubation, wells were serially rinsed with appropriate buffer by gently pipetting until a 15,000-fold dilution was achieved. Next, 4 μg of neutravidin dissolved in 25 mM HEPES, 150 mM NaCl (pH 7.4) was added to each sample well and allowed to incubate for 10 minutes. Wells were then rinsed with the appropriate buffer to remove excess neutravidin. GUVs were diluted in 20 mM Tris-HCl, 150 mM NaCl, 5 mM TCEP, pH 7.5 at ratio of 1:13 and then 20 μL of diluted GUVs was added to the well and allowed to incubate for 10

minutes. Excess GUVs were then rinsed from the well using the same buffer and the sample was subsequently imaged using confocal fluorescence microscopy.

Cell culture

Human-derived SUM159 cells gene-edited to add a HaloTag to both alleles of AP-2 σ2 were a gift from T. Kirchhausen[296]. Cells were further gene-edited to knock out both alleles of endogenous Eps15 using CRISPR-associated protein 9 (Cas9) to produce the Eps15 knockout cells developed previously by our group[258].

Cells were grown in 1:1 DMEM high glucose: Ham's F-12 (Hyclone, GE Healthcare) supplemented with 5% fetal bovine serum (Hyclone), Penicillin/Streptomycin/l-glutamine (Hyclone), 1 μg ml^{-1} hydrocortisone (H4001; Sigma-Aldrich), 5 μg ml^{-1} insulin (I6634; Sigma-Aldrich) and 10 mM HEPES, pH 7.4 and incubated at 37 °C with 5% CO_2. Cells were seeded onto acid-washed coverslips at a density of 3×10^4 cells per coverslip for 24 h before transfection with 1μg of plasmid DNA using 3 μl Fugene HD transfection reagent (Promega). HaloTagged AP-2 σ2 was visualized by adding Janelia Fluor 646-HaloTag ligand (Promega). Ligand (100 nM) was added to cells and incubated at 37 °C for 15 min. Cells were washed with fresh medium and imaged immediately.

Fluorescence microscopy

Images of protein droplets and GUVs were collected on a spinning disc confocal super resolution microscope (SpinSR10, Olympus, USA) equipped with a 1.49 NA/100X oil immersion objective. For GUV imaging, image stacks taken at fixed distances perpendicular to the membrane plane (0.5 μm steps) were acquired immediately after GUV tethering and again after protein addition. Images taken under deconvolution mode were processed by the built-in deconvolution function in Olympus CellSens software (Dimension 3.2, Build 23706). At least 30 fields of views were randomly selected for each

sample for further analysis. Imaging was performed 5 min after adding proteins, providing sufficient time to achieve protein binding and reach a steady state level of binding. For experiments used to construct phase diagrams, temperature was monitored by a thermistor placed in the protein solution in a sealed chamber to prevent evaporation. Samples were heated from room temperature through an aluminum plate fixed to the top of the chamber. Temperature was increased in steps of 1 °C until the critical temperature was reached. Images of at least 20 droplets were taken at each temperature, once the temperature stabilized.

Live-cell images were collected on a TIRF microscope consisting of an Olympus IX73 microscope body, a Photometrics Evolve Delta EMCCD camera, and an Olympus 1.4 NA ×100 Plan-Apo oil objective, using MicroManager version 1.4.23. The coverslip was heated to produce a sample temperature of 37 °C using an aluminum plate fixed to the back of the sample. All live-cell imaging was conducted in TIRF mode at the plasma membrane 48 h after transfection. Transfection media used for imaging lacked pH indicator (phenol red) and was supplemented with 1 μL OxyFluor (Oxyrase, Mansfield, OH) per 33 μL media to decrease photobleaching during live-cell fluorescence imaging. 532 nm and 640 nm lasers were used for excitation of mCherry and Janelia Fluor 646-HaloTag ligand of AP2, respectively. Cell movies were collected over 10 min at 2 s intervals between frames. For blue-light assays, samples were exposed to 25 μW 473 nm light as measured out of the objective when in wide-field mode. Blue light was applied for 500 ms every 3 s for cell samples. Cell movies were collected over 11 min at 3 s intervals between frames, and analysis of movies began after 1 min of imaging to allow for blue light to take effect.

Image analysis

Fluorescence images analyzed in ImageJ (http://rsbweb.nih.gov/ij/). Intensity values along line scans were measured in unprocessed images using ImageJ. For phase diagrams, fluorescence intensity was measured in the center square of a 3 × 3 grid for each image where illumination was even. Two images were analyzed at each temperature for each condition. The intensity was normalized to the mean intensity value of the solution (200 A.U.).

Clathrin-coated structures were detected and tracked using cmeAnalysis in MATLAB[297]. The point spread function of the data was used to determine the standard deviation of the Gaussian function. AP-2 σ2 signal was used as the master channel to track clathrin-coated structures. Detected structures were analyzed if they persisted in at least three consecutive frames. The lifetimes of clathrin-coated that met these criteria were recorded for lifetime distribution analysis under different conditions.

Statistical analysis

For all experiments yielding micrographs, each experiment was repeated independently on different days at least three times, with similar results. Phase diagram experiments were repeated independently twice with similar results. Collection of cell image data for clathrin-mediated endocytosis analysis was performed independently on at least two different days for each cell type or experimental condition. Statistical analysis was carried out using a two-tailed student's t-test (unpaired, unequal variance) to probe for statistical significance ($P < 0.05$).

ACKNOWLEDGEMENTS

We thank T. Kirchhausen for the gift of SUM159/AP2-σ2-Halo Tag cells and J. MacGurn for the gift of plasmids encoding deubiquitinase UL36 and its catalytically

inactive mutant. This research was supported by the National Institutes of Health through grants R35GM139531 to J.C.S., the Welch Foundation through grant F-2047 to J.C.S., and the University of Texas at Austin, Graduate School Continuing Fellowship 2022-2023 to F.Y.

SUPPLEMENTARY INFORMATION

Movie S1: Eps15 droplets fusion with addition of MonoUb. Eps15 (7μM) droplets (green) were incubated with 1μM MonoUb (magenta) in 20 mM Tris-HCl, 150 mM NaCl, 5 mM TCEP, 1 mM EDTA and 1 mM EGTA at pH 7.5 with 3% w/v PEG8000. **[Link]**

Movie S2: Eps15 droplets fusion with addition of TetraUb. Eps15 (7μM) droplets (green) were incubated with 0.25μM K63 linkage TetraUb (magenta) in 20 mM Tris-HCl, 150 mM NaCl, 5 mM TCEP, 1 mM EDTA and 1 mM EGTA at pH 7.5 with 3% w/v PEG8000. [Link]

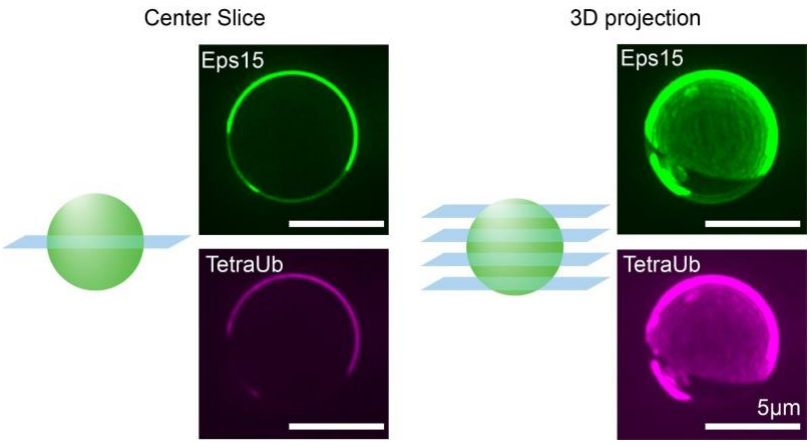

Figure 4. 7 Centre slices (left) and corresponding z-projections (right) of representative images of Eps15 (green) assembled into protein condensed region together with TetraUb

(magenta) on GUV membrane. GUVs were incubated with 0.5 μM Eps15 and 0.2 μM TetraUb in 20 mM Tris-HCl pH 7.5, 150 mM NaCl, 5 mM TCEP buffer. Scale bar = 5 μm.

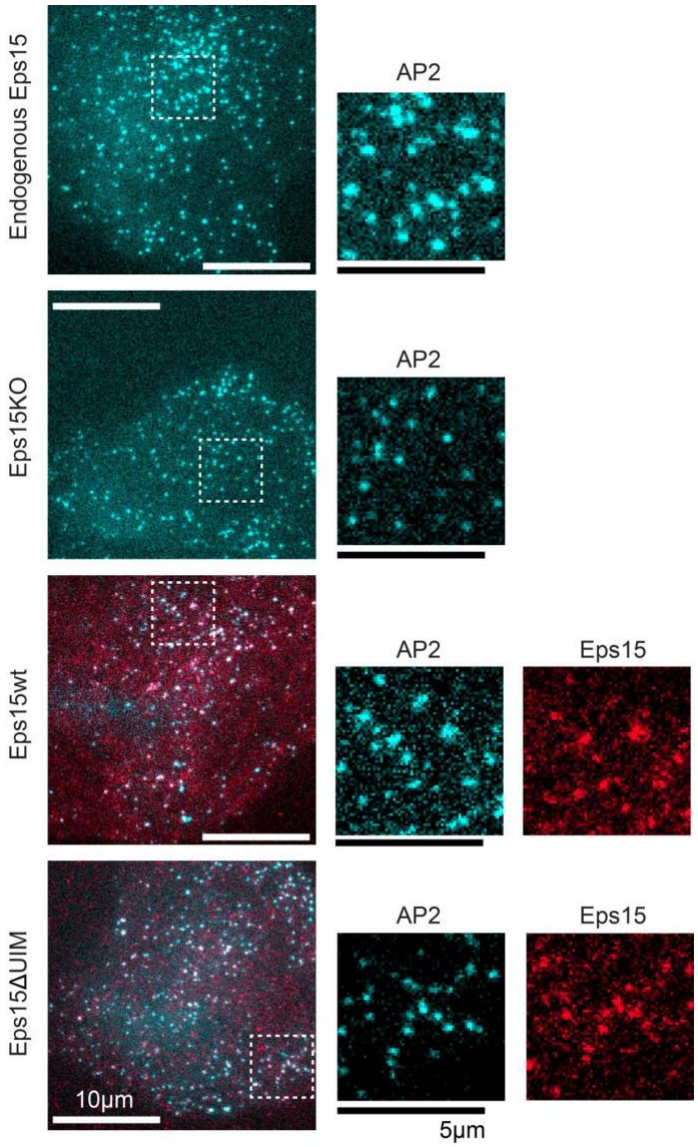

Figure 4. 8 Representative image of endocytic pits in live SUM cells expressing gene-edited AP2 σ2-HaloTag: JF646 (cyan) and Eps15 variants (red). Endogenous Eps15 represents SUM cells expressing gene-edited AP2 σ2-HaloTag. Eps15KO represents SUM cells that were further CRISPR modified to knockout alleles of endogenous Eps15. Eps15wt and Eps15ΔUIM represent Eps15KO cells transfected with wildtype Eps15 and Eps15 with the depletion of both UIM domains, respectively. mCherry was fused to the C terminus of Eps15 and Eps15ΔUIM for visualization. Insets are the zoom-in area of the

white dashed box. Scale bars are labeled in images. Cells were imaged at 37°C for all conditions.

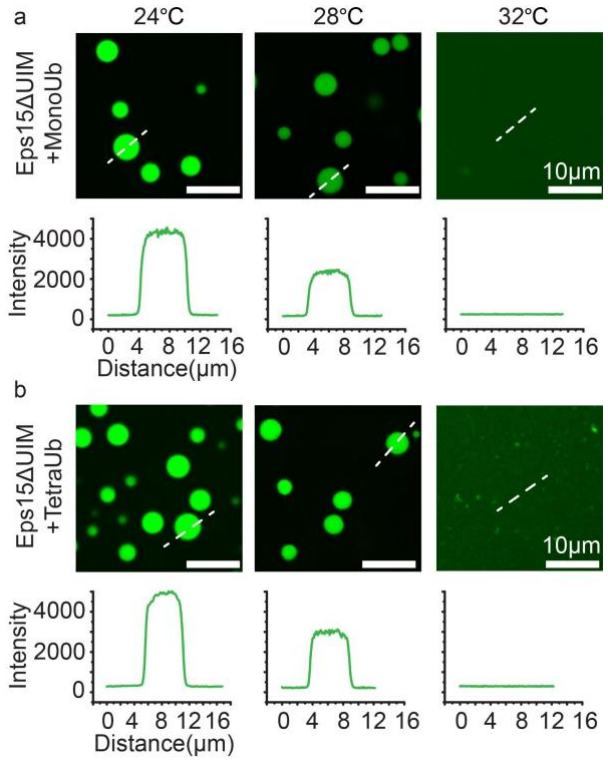

Figure 4. 9 Representative images of protein droplets at increasing temperatures. Plots show fluorescence intensity of Eps15ΔUIM measured along dotted lines in each image. Droplets are formed from (**a**) 0.5 μM MonoUb, 7 μM Eps15ΔUIM and (**b**) 0.1 μM TetraUb, 7 μM Eps15ΔUIM in 20 mM Tris-HCl, 150 mM NaCl, 5 mM TCEP, 1 mM EDTA and 1 mM EGTA at pH 7.5 buffer with 3% PEG8000. Scale bars equal 10 μm.

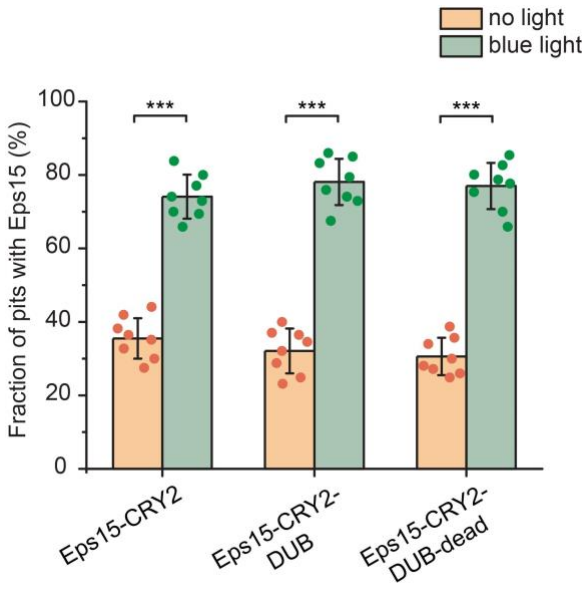

Figure 4. 10 Fraction of endocytic pits showing Eps15 colocalization before and after exposure to blue light when expressing Eps15-CRY2, Eps15-CRY2-DUB, or Eps15-CRY2-DUB-dead. For Eps15-CYR2, n = 8 biologically independent cell samples were collected and in total 1060 pits (before light) and 1068 pits (blue light) were analyzed. For Eps15-CRY2-DUB, n = 8 and 1099 pits (before light) and 1371 pits (blue light) were analyzed. For Eps15-CRY2-DUB-dead, n = 8 and total pits = 1044 (before light) and 918 (blue light). Dots represent frequency from each sample. An unpaired, two-tailed student's t test was used for statistical significance. ***: $P < 0.001$. Error bars represent standard deviation. Cells were imaged at 37°C for all conditions.

Movie S3: Change of Eps15 and AP2 channel upon light activation in cells expressing Eps15-CRY2, Eps15-CRY2-DUB and Eps15-CRY2-DUB-dead, respectively. **[Link]**

REFERENCES

71. Yuan, F. *et al.* Membrane bending by protein phase separation. *Proceedings of the National Academy of Sciences* **118** (2021).

97. Kozak, M. & Kaksonen, M. Condensation of Ede1 promotes the initiation of endocytosis. *Elife* **11**, e72865 (2022).
167. Angelova, M. I. & Dimitrov, D. S. Liposome electroformation. *Faraday discussions of the Chemical Society* **81**, 303-311 (1986).
168. Zeno, W. F. *et al.* Synergy between intrinsically disordered domains and structured proteins amplifies membrane curvature sensing. *Nat Commun* **9**, 4152 (2018).
247. Mettlen, M., Chen, P.-H., Srinivasan, S., Danuser, G. & Schmid, S. L. Regulation of clathrin-mediated endocytosis. *Annual review of biochemistry* **87**, 871-896 (2018).
248. McMahon, H. T. & Boucrot, E. Molecular mechanism and physiological functions of clathrin-mediated endocytosis. *Nature reviews Molecular cell biology* **12**, 517-533 (2011).
249. Kaksonen, M. & Roux, A. Mechanisms of clathrin-mediated endocytosis. *Nature reviews Molecular cell biology* **19**, 313-326 (2018).
250. Chen, Z. & Schmid, S. L. Evolving models for assembling and shaping clathrin-coated pits. *Journal of Cell Biology* **219**, e202005126 (2020).
251. Traub, L. M. Tickets to ride: selecting cargo for clathrin-regulated internalization. *Nature reviews Molecular cell biology* **10**, 583-596 (2009).
252. Hicke, L. & Riezman, H. Ubiquitination of a yeast plasma membrane receptor signals its ligand-stimulated endocytosis. *Cell* **84**, 277-287 (1996).
253. Galan, J. M., Moreau, V., Andre, B., Volland, C. & Haguenauer-Tsapis, R. Ubiquitination Mediated by the Npi1p/Rsp5p Ubiquitin-protein Ligase Is Required for Endocytosis of the Yeast Uracil Permease (∗). *Journal of Biological Chemistry* **271**, 10946-10952 (1996).
254. Lin, C. H., MacGurn, J. A., Chu, T., Stefan, C. J. & Emr, S. D. Arrestin-related ubiquitin-ligase adaptors regulate endocytosis and protein turnover at the cell surface. *Cell* **135**, 714-725 (2008).
255. Dores, M. R., Schnell, J. D., Maldonado‐Baez, L., Wendland, B. & Hicke, L. The function of yeast epsin and Ede1 ubiquitin‐binding domains during receptor internalization. *Traffic* **11**, 151-160 (2010).
256. Tebar, F., Sorkina, T., Sorkin, A., Ericsson, M. & Kirchhausen, T. Eps15 is a component of clathrin-coated pits and vesicles and is located at the rim of coated pits. *Journal of Biological Chemistry* **271**, 28727-28730 (1996).
257. Sochacki, K. A., Dickey, A. M., Strub, M.-P. & Taraska, J. W. Endocytic proteins are partitioned at the edge of the clathrin lattice in mammalian cells. *Nature cell biology* **19**, 352-361 (2017).

258. Day, K. J. *et al.* Liquid-like protein interactions catalyse assembly of endocytic vesicles. *Nature Cell Biology* **23**, 366-376 (2021).
259. Wilfling, F. *et al.* A selective autophagy pathway for phase-separated endocytic protein deposits. *Molecular Cell* **80**, 764-778. e767 (2020).
260. Wilfling, F., Lee, C.-W., Erdmann, P. S. & Baumeister, W. Autophagy ENDing unproductive phase-separated endocytic protein deposits. *Autophagy* **17**, 3264-3265 (2021).
261. Shih, S. C. *et al.* Epsins and Vps27p/Hrs contain ubiquitin-binding domains that function in receptor endocytosis. *Nature cell biology* **4**, 389-393 (2002).
262. Hicke, L. & Dunn, R. Regulation of membrane protein transport by ubiquitin and ubiquitin-binding proteins. *Annual review of cell and developmental biology* **19**, 141-172 (2003).
263. Polo, S. *et al.* A single motif responsible for ubiquitin recognition and monoubiquitination in endocytic proteins. *Nature* **416**, 451-455 (2002).
264. Riezman, H. The ubiquitin connection. *Nature* **416**, 381-383 (2002).
265. Weinberg, J. S. & Drubin, D. G. Regulation of clathrin-mediated endocytosis by dynamic ubiquitination and deubiquitination. *Current Biology* **24**, 951-959 (2014).
266. Galan, J.-M. & Haguenauer-Tsapis, R. Ubiquitin lys63 is involved in ubiquitination of a yeast plasma membrane protein. *The EMBO journal* **16**, 5847-5854 (1997).
267. Huang, F. *et al.* Lysine 63-linked polyubiquitination is required for EGF receptor degradation. *Proceedings of the National Academy of Sciences* **110**, 15722-15727 (2013).
268. Erpapazoglou, Z., Walker, O. & Haguenauer-Tsapis, R. Versatile roles of k63-linked ubiquitin chains in trafficking. *Cells* **3**, 1027-1088 (2014).
269. Piper, R. C., Dikic, I. & Lukacs, G. L. Ubiquitin-dependent sorting in endocytosis. *Cold Spring Harbor perspectives in biology* **6**, a016808 (2014).
270. Cupers, P., ter Haar, E., Boll, W. & Kirchhausen, T. Parallel dimers and anti-parallel tetramers formed by epidermal growth factor receptor pathway substrate clone 15 (EPS15). *Journal of Biological Chemistry* **272**, 33430-33434 (1997).
271. Benmerah, A., Poupon, V., Cerf-Bensussan, N. & Dautry-Varsat, A. Mapping of Eps15 domains involved in its targeting to clathrin-coated pits. *Journal of Biological Chemistry* **275**, 3288-3295 (2000).

272. Santonico, E., Panni, S., Falconi, M., Castagnoli, L. & Cesareni, G. Binding to DPF-motif by the POB1 EH domain is responsible for POB1-Eps15 interaction. *BMC biochemistry* **8**, 1-14 (2007).
273. Lu, R. & Drubin, D. G. Selection and stabilization of endocytic sites by Ede1, a yeast functional homologue of human Eps15. *Molecular biology of the cell* **28**, 567-575 (2017).
274. Ehrlich, M. *et al.* Endocytosis by random initiation and stabilization of clathrin-coated pits. *Cell* **118**, 591-605 (2004).
275. Boulant, S., Kural, C., Zeeh, J.-C., Ubelmann, F. & Kirchhausen, T. Actin dynamics counteract membrane tension during clathrin-mediated endocytosis. *Nature cell biology* **13**, 1124-1131 (2011).
276. Collins, B. M., McCoy, A. J., Kent, H. M., Evans, P. R. & Owen, D. J. Molecular architecture and functional model of the endocytic AP2 complex. *Cell* **109**, 523-535 (2002).
277. Owen, D. J., Collins, B. M. & Evans, P. R. Adaptors for clathrin coats: structure and function. *Annu. Rev. Cell Dev. Biol.* **20**, 153-191 (2004).
278. Grimm, J. B. *et al.* A general method to improve fluorophores for live-cell and single-molecule microscopy. *Nature methods* **12**, 244-250 (2015).
279. Blondeau, F. *et al.* Tandem MS analysis of brain clathrin-coated vesicles reveals their critical involvement in synaptic vesicle recycling. *Proceedings of the National Academy of Sciences* **101**, 3833-3838 (2004).
280. Dao, T. P. *et al.* Mechanistic insights into enhancement or inhibition of phase separation by different polyubiquitin chains. *EMBO reports* **23**, e55056 (2022).
281. Stringer, D. K. & Piper, R. C. A single ubiquitin is sufficient for cargo protein entry into MVBs in the absence of ESCRT ubiquitination. *Journal of Cell Biology* **192**, 229-242 (2011).
282. Xu, P. *et al.* COPI mediates recycling of an exocytic SNARE by recognition of a ubiquitin sorting signal. *Elife* **6**, e28342 (2017).
283. Nielsen, C. P., Jernigan, K. K., Diggins, N. L., Webb, D. J. & MacGurn, J. A. USP9X deubiquitylates DVL2 to regulate WNT pathway specification. *Cell reports* **28**, 1074-1089. e1075 (2019).
284. Kattenhorn, L. M., Korbel, G. A., Kessler, B. M., Spooner, E. & Ploegh, H. L. A deubiquitinating enzyme encoded by HSV-1 belongs to a family of cysteine proteases that is conserved across the family Herpesviridae. *Molecular cell* **19**, 547-557 (2005).

285. Bolstad, M., Abaitua, F., Crump, C. & O'Hare, P. Autocatalytic activity of the ubiquitin-specific protease domain of herpes simplex virus 1 VP1-2. *Journal of virology* **85**, 8738-8751 (2011).
286. Komander, D. & Rape, M. The ubiquitin code. *Annual review of biochemistry* **81**, 203-229 (2012).
287. Chen, C. & Zhuang, X. Epsin 1 is a cargo-specific adaptor for the clathrin-mediated endocytosis of the influenza virus. *Proceedings of the National Academy of Sciences* **105**, 11790-11795 (2008).
288. Bugaj, L. J., Choksi, A. T., Mesuda, C. K., Kane, R. S. & Schaffer, D. V. Optogenetic protein clustering and signaling activation in mammalian cells. *Nature methods* **10**, 249-252 (2013).
289. Wendland, B. Epsins: adaptors in endocytosis? *Nature reviews Molecular cell biology* **3**, 971-977 (2002).
290. Hawryluk, M. J. *et al.* Epsin 1 is a polyubiquitin‐selective clathrin‐associated sorting protein. *Traffic* **7**, 262-281 (2006).
291. Chen, H. *et al.* Epsin is an EH-domain-binding protein implicated in clathrin-mediated endocytosis. *Nature* **394**, 793-797 (1998).
292. Aguilar, R. C., Watson, H. A. & Wendland, B. The yeast Epsin Ent1 is recruited to membranes through multiple independent interactions. *Journal of Biological Chemistry* **278**, 10737-10743 (2003).
293. Dupre, S., Urban-Grimal, D. & Haguenauer-Tsapis, R. Ubiquitin and endocytic internalization in yeast and animal cells. *Biochimica et Biophysica Acta (BBA)-Molecular Cell Research* **1695**, 89-111 (2004).
294. Taylor, M. J., Perrais, D. & Merrifield, C. J. A high precision survey of the molecular dynamics of mammalian clathrin-mediated endocytosis. *PLoS biology* **9**, e1000604 (2011).
295. Kennedy, M. J. *et al.* Rapid blue-light–mediated induction of protein interactions in living cells. *Nature methods* **7**, 973-975 (2010).
296. Aguet, F. *et al.* Membrane dynamics of dividing cells imaged by lattice light-sheet microscopy. *Molecular biology of the cell* **27**, 3418-3435 (2016).
297. Aguet, F., Antonescu, C. N., Mettlen, M., Schmid, S. L. & Danuser, G. Advances in analysis of low signal-to-noise images link dynamin and AP2 to the functions of an endocytic checkpoint. *Developmental cell* **26**, 279-291 (2013).

Bibliography

1. Elkin, S. R., Lakoduk, A. M. & Schmid, S. L. Endocytic pathways and endosomal trafficking: a primer. *Wiener Medizinische Wochenschrift* **166**, 196-204 (2016).
2. Stachowiak, J. C., Brodsky, F. M. & Miller, E. A. A cost–benefit analysis of the physical mechanisms of membrane curvature. *Nature cell biology* **15**, 1019-1027 (2013).
3. Di Fiore, P. P. & De Camilli, P. Endocytosis and signaling: an inseparable partnership. *Cell* **106**, 1-4 (2001).
4. McMahon, H. T. & Boucrot, E. Molecular mechanism and physiological functions of clathrin-mediated endocytosis. *Nat Rev Mol Cell Biol* **12**, 517-533 (2011).
5. Robinson, M. S. Forty Years of Clathrin-coated Vesicles. *Traffic* **16**, 1210-1238 (2015).
6. Ford, M. *et al.* Curvature of clathrin-coated pits driven by epsin. *Nature* **419**, 361-366 (2002).
7. Fotin, A. *et al.* Molecular model for a complete clathrin lattice from electron cryomicroscopy. *Nature* **432**, 573-579 (2004).
8. Fath, S., Mancias, J. D., Bi, X. & Goldberg, J. Structure and organization of coat proteins in the COPII cage. *Cell* **129**, 1325-1336 (2007).
9. Frost, A., Unger, V. M. & De Camilli, P. The BAR domain superfamily: membrane-molding macromolecules. *Cell* **137**, 191-196 (2009).
10. Johannes, L., Wunder, C. & Bassereau, P. Bending "On the Rocks"-A Cocktail of Biophysical Modules to Build Endocytic Pathways. *Cold Spring Harbor Perspectives in Biology* **6** (2014).
11. Ford, M. G., Jenni, S. & Nunnari, J. The crystal structure of dynamin. *Nature* **477**, 561-566 (2011).
12. Faelber, K. *et al.* Crystal structure of nucleotide-free dynamin. *Nature* **477**, 556-560 (2011).
13. Dafforn, T. R. & Smith, C. J. Natively unfolded domains in endocytosis: hooks, lines and linkers. *EMBO reports* **5**, 1046-1052 (2004).
14. Owen, D. J., Collins, B. M. & Evans, P. R. Adaptors for clathrin coats: structure and function. *Annual review of cell and developmental biology* **20**, 153-191 (2004).

15. Zhuo, Y. *et al.* Dynamic interactions between clathrin and locally structured elements in a disordered protein mediate clathrin lattice assembly. *Journal of Molecular Biology* **404**, 274-290 (2010).
16. Pietrosemoli, N., Pancsa, R. & Tompa, P. Structural disorder provides increased adaptability for vesicle trafficking pathways. *PLoS computational biology* **9**, e1003144 (2013).
17. Schmid, E. M. *et al.* Role of the AP2 beta-appendage hub in recruiting partners for clathrin-coated vesicle assembly. *PLoS Biol* **4**, e262 (2006).
18. Schmid, E. M. & McMahon, H. T. Integrating molecular and network biology to decode endocytosis. *Nature* **448**, 883-888 (2007).
19. Dafforn, T. R. & Smith, C. J. Natively unfolded domains in endocytosis: hooks, lines and linkers. *EMBO Reports* **5**, 1046-1052 (2004).
20. Zeno, W. F. *et al.* Synergy between intrinsically disordered domains and structured proteins amplifies membrane curvature sensing. *Nature Communications* **9**, 4152 (2018).
21. Zeno, W. F. *et al.* Molecular Mechanisms of Membrane Curvature Sensing by a Disordered Protein. *Journal of the American Chemical Society* (2019).
22. Hatzakis, N. S. *et al.* How curved membranes recruit amphipathic helices and protein anchoring motifs. *Nat Chem Biol* **5**, 835-841 (2009).
23. Bhatia, V. K. *et al.* Amphipathic motifs in BAR domains are essential for membrane curvature sensing. *EMBO J* **28**, 3303-3314 (2009).
24. Theillet, F. X. *et al.* The alphabet of intrinsic disorder: I. Act like a Pro: On the abundance and roles of proline residues in intrinsically disordered proteins. *Intrinsically Disord Proteins* **1**, e24360 (2013).
25. Kalthoff, C., Alves, J., Urbanke, C., Knorr, R. & Ungewickell, E. J. Unusual structural organization of the endocytic proteins AP180 and epsin 1. *Journal of Biological Chemistry* **277**, 8209-8216 (2002).
26. Srinivasan, N., Bhagawati, M., Ananthanarayanan, B. & Kumar, S. Stimuli-sensitive intrinsically disordered protein brushes. *Nature communications* **5**, 5145 (2014).
27. Mao, A. H., Crick, S. L., Vitalis, A., Chicoine, C. L. & Pappu, R. V. Net charge per residue modulates conformational ensembles of intrinsically disordered proteins. *Proceedings of the National Academy of Sciences of the United States of America* **107**, 8183-8188 (2010).
28. Uversky, V. N., Gillespie, J. R. & Fink, A. L. Why are "natively unfolded" proteins unstructured under physiologic conditions? *Proteins* **41**, 415-427 (2000).

29. Bernado, P. & Svergun, D. I. Structural analysis of intrinsically disordered proteins by small-angle X-ray scattering. *Molecular biosystems* **8**, 151-167 (2012).
30. Jensen, M. R., Zweckstetter, M., Huang, J.-r. & Blackledge, M. Exploring free-energy landscapes of intrinsically disordered proteins at atomic resolution using NMR spectroscopy. *Chemical reviews* **114**, 6632-6660 (2014).
31. Nettels, D., Hoffmann, A. & Schuler, B. Unfolded protein and peptide dynamics investigated with single-molecule FRET and correlation spectroscopy from picoseconds to seconds. *The Journal of Physical Chemistry B* **112**, 6137-6146 (2008).
32. Hofmann, H. *et al.* Polymer scaling laws of unfolded and intrinsically disordered proteins quantified with single-molecule spectroscopy. *Proceedings of the National Academy of Sciences* **109**, 16155-16160 (2012).
33. Flory, P. J. The configuration of real polymer chains. *The Journal of Chemical Physics* **17**, 303-310 (1949).
34. Phillips, R., Kondev, J., Theriot, J. & Garcia, H. *Physical biology of the cell*. (Garland Science, 2012).
35. DiMarzio, E. A. Proper accounting of conformations of a polymer near a surface. *The Journal of Chemical Physics* **42**, 2101-2106 (1965).
36. DiMarzio, E. A. & McCrackin, F. L. One‐Dimensional Model of Polymer Adsorption. *The Journal of Chemical Physics* **43**, 539-547 (1965).
37. Lipowsky, R. Bending of membranes by anchored polymers. *EPL (Europhysics Letters)* **30**, 197 (1995).
38. Capraro, B. R., Yoon, Y., Cho, W. & Baumgart, T. Curvature sensing by the epsin N-terminal homology domain measured on cylindrical lipid membrane tethers. *J Am Chem Soc* **132**, 1200-1201 (2010).
39. Joseph, J. G., Osorio, C., Yee, V., Agrawal, A. & Liu, A. P. Complimentary action of structured and unstructured domains of epsin supports clathrin-mediated endocytosis at high tension. *Communications biology* **3**, 1-16 (2020).
40. Tillu, V. A. *et al.* Cavin1 intrinsically disordered domains are essential for fuzzy electrostatic interactions and caveola formation. *Nature communications* **12**, 1-18 (2021).
41. Su, M. *et al.* Comparative Study of Curvature Sensing Mediated by F-BAR and an Intrinsically Disordered Region of FBP17. *Iscience* **23**, 101712 (2020).
42. McMahon, H. T. & Boucrot, E. Molecular mechanism and physiological functions of clathrin-mediated endocytosis. *Nature reviews. Molecular cell biology* **12**, 517-533 (2011).

43. Hurley, J. H., Boura, E., Carlson, L.-A. & Różycki, B. Membrane budding. *Cell* **143**, 875-887 (2010).
44. Stachowiak, J. C., Brodsky, F. M. & Miller, E. A. A cost-benefit analysis of the physical mechanisms of membrane curvature. *Nature Cell Biology* **15**, 1019-1027 (2013).
45. Baumgart, T., Capraro, B. R., Zhu, C. & Das, S. L. Thermodynamics and mechanics of membrane curvature generation and sensing by proteins and lipids. *Annu Rev Phys Chem* **62**, 483-506 (2011).
46. Sheetz, M. P. & Singer, S. J. Biological membranes as bilayer couples, A molecular mechanism of drug-erythrocyte interactions. *Proceedings of the National Academy of the Sciences of the United States of America* **71**, 4457-4461 (1974).
47. Campelo, F., McMahon, H. & Kozlov, M. The hydrophobic insertion mechanism of membrane curvature generation by proteins. *Biophysical Journal* **95**, 2325-2339 (2008).
48. Lee, M. *et al.* Sar1p N-terminal helix initiates membrane curvature and completes the fission of a COPII vesicle. *Cell* **122**, 605-617 (2005).
49. Miller, S. E. *et al.* The molecular basis for the endocytosis of small R-SNAREs by the clathrin adaptor CALM. *Cell* **147**, 1118-1131 (2011).
50. Kirchhausen, T. Bending membranes. *Nature Cell Biology* **14**, 906-908 (2012).
51. Mim, C. & Unger, V. M. Membrane curvature and its generation by BAR proteins. *Trends Biochem Sci* **37**, 526-533 (2012).
52. Daumke, O., Roux, A. & Haucke, V. BAR domain scaffolds in dynamin-mediated membrane fission. *Cell* **156**, 882-892 (2014).
53. Stachowiak, J., Hayden, C. & Sasaki, D. Steric confinement of proteins on lipid membranes can drive curvature and tubulation. *Proceedings of the National Academy of Sciences of the United States of America* **107**, 7781-7786 (2010).
54. Stachowiak, J. *et al.* Membrane bending by protein-protein crowding. *Nature Cell Biology* **14**, 944-+ (2012).
55. Shi, Z. & Baumgart, T. Membrane tension and peripheral protein density mediate membrane shape transitions. *Nature Communications* **6**, 5974 (2015).
56. Snead, W. T. *et al.* Membrane fission by protein crowding. *Proceedings of the National Academy of Sciences of the United States of America* **114**, E3258-E3267 (2017).

57. Houser, J. R., Hayden, C. C., Thirumalai, D. & Stachowiak, J. C. A Forster Resonance Energy Transfer-Based Sensor of Steric Pressure on Membrane Surfaces. *J Am Chem Soc* **142**, 20796-20805 (2020).
58. Kory, N., Thiam, A., Farese, R. & Walther, T. Protein Crowding Is a Determinant of Lipid Droplet Protein Composition. *Developmental Cell* **34**, 351-363 (2015).
59. Carignano, M. A. & Szleifer, I. On the Structure and Pressure of Tethered Polymer Layers in Good Solvent. *Macromolecules* **28**, 3197-3204 (1995).
60. Lipowsky, R. Bending of Membranes by Anchored Polymers. *Eurphysics Letters* **30**, 197-202 (1995).
61. Gennes, P. G. d. *Scaling concepts in polymer physics*. (Cornell University Press, 1979).
62. Busch, D. J. *et al.* Intrinsically disordered proteins drive membrane curvature. *Nature Communications* **6**, 7875 (2015).
63. Snead, W. T. *et al.* BAR scaffolds drive membrane fission by crowding disordered domains. *J Cell Biol* **218**, 664-682 (2019).
64. Jiang, Z., de Messieres, M. & Lee, J. C. Membrane remodeling by alpha-synuclein and effects on amyloid formation. *Journal of the American Chemical Society* **135**, 15970-15973 (2013).
65. Shurer, C. R. *et al.* Physical Principles of Membrane Shape Regulation by the Glycocalyx. *Cell* **177**, 1757-1770 e1721 (2019).
66. Banani, S. F., Lee, H. O., Hyman, A. A. & Rosen, M. K. Biomolecular condensates: organizers of cellular biochemistry. *Nat Rev Mol Cell Biol* **18**, 285-298 (2017).
67. Brangwynne, Clifford P., Tompa, P. & Pappu, Rohit V. Polymer physics of intracellular phase transitions. *Nature Physics* **11**, 899 (2015).
68. Li, P. *et al.* Phase transitions in the assembly of multivalent signalling proteins. *Nature* **483**, 336-340 (2012).
69. Banani, S. F. *et al.* Compositional Control of Phase-Separated Cellular Bodies. *Cell* **166**, 651-663 (2016).
70. Lin, Y., Protter, D. S., Rosen, M. K. & Parker, R. Formation and Maturation of Phase-Separated Liquid Droplets by RNA-Binding Proteins. *Mol Cell* **60**, 208-219 (2015).
71. Yuan, F. *et al.* Membrane bending by protein phase separation. *Proceedings of the National Academy of Sciences* **118** (2021).
72. Day, K. J. *et al.* Liquid-like protein interactions catalyse assembly of endocytic vesicles. *Nat Cell Biol* **23**, 366-376 (2021).

73. Tsafrir, I. *et al.* Pearling instabilities of membrane tubes with anchored polymers. *Phys Rev Lett* **86**, 1138-1141 (2001).
74. Sanborn, J., Oglęcka, K., Kraut, R. S. & Parikh, A. N. Transient pearling and vesiculation of membrane tubes under osmotic gradients. *Faraday discussions* **161**, 167-176 (2013).
75. Helfrich, W. Elastic properties of lipid bilayers: theory and possible experiments. *Zeitschrift für Naturforschung C* **28**, 693-703 (1973).
76. Kusumaatmaja, H., May, A. I. & Knorr, R. L. Intracellular wetting mediates contacts between liquid compartments and membrane-bound organelles. *Journal of Cell Biology* **220**, e202103175 (2021).
77. Gracia, R. S., Bezlyepkina, N., Knorr, R. L., Lipowsky, R. & Dimova, R. Effect of cholesterol on the rigidity of saturated and unsaturated membranes: fluctuation and electrodeformation analysis of giant vesicles. *Soft Matter* **6**, 1472-1482 (2010).
78. Aumiller Jr, W. M. & Keating, C. D. Experimental models for dynamic compartmentalization of biomolecules in liquid organelles: Reversible formation and partitioning in aqueous biphasic systems. *Advances in colloid and interface science* **239**, 75-87 (2017).
79. Jawerth, L. M. *et al.* Salt-dependent rheology and surface tension of protein condensates using optical traps. *Physical review letters* **121**, 258101 (2018).
80. Kusumaatmaja, H. *et al.* Wetting of phase-separated droplets on plant vacuole membranes leads to a competition between tonoplast budding and nanotube formation. *Proceedings of the National Academy of Sciences* **118** (2021).
81. Zheng, H. & Staehelin, L. A. Protein storage vacuoles are transformed into lytic vacuoles in root meristematic cells of germinating seedlings by multiple, cell type-specific mechanisms. *Plant Physiology* **155**, 2023-2035 (2011).
82. Agudo-Canalejo, J. *et al.* Wetting regulates autophagy of phase-separated compartments and the cytosol. *Nature* **591**, 142-146 (2021).
83. Schultz, S. W. *et al.* Should I bend or should I grow: the mechanisms of droplet-mediated autophagosome formation. *Autophagy* **17**, 1046-1048 (2021).
84. Kageyama, S. *et al.* p62/SQSTM1-droplet serves as a platform for autophagosome formation and anti-oxidative stress response. *Nature communications* **12**, 1-16 (2021).
85. Milovanovic, D., Wu, Y., Bian, X. & De Camilli, P. A liquid phase of synapsin and lipid vesicles. *Science* **361**, 604-607 (2018).
86. Pechstein, A. *et al.* Vesicle clustering in a living synapse depends on a synapsin region that mediates phase separation. *Cell reports* **30**, 2594-2602. e2593 (2020).

87. Park, D. *et al.* Cooperative function of synaptophysin and synapsin in the generation of synaptic vesicle-like clusters in non-neuronal cells. *Nature communications* **12**, 1-10 (2021).
88. Martin, E. W. *et al.* Valence and patterning of aromatic residues determine the phase behavior of prion-like domains. *Science* **367**, 694-699 (2020).
89. Kumari, S., Curado, S., Mayya, V. & Dustin, M. L. T cell antigen receptor activation and actin cytoskeleton remodeling. *Biochim Biophys Acta* **1838**, 546-556 (2014).
90. Hwang, J. R., Byeon, Y., Kim, D. & Park, S. G. Recent insights of T cell receptor-mediated signaling pathways for T cell activation and development. *Exp Mol Med* **52**, 750-761 (2020).
91. Su, X. *et al.* Phase separation of signaling molecules promotes T cell receptor signal transduction. *Science* **352**, 595-599 (2016).
92. Salvi, N. *Intrinsically Disordered Proteins: Dynamics, Binding, and Function*. (Academic Press, 2019).
93. Huang, W. Y. *et al.* Phosphotyrosine-mediated LAT assembly on membranes drives kinetic bifurcation in recruitment dynamics of the Ras activator SOS. *Proceedings of the National Academy of Sciences of the United States of America* **113**, 8218-8223 (2016).
94. Huang, W. Y. C. *et al.* A molecular assembly phase transition and kinetic proofreading modulate Ras activation by SOS. *Science* **363**, 1098-1103 (2019).
95. Chung, J. K. *et al.* Coupled membrane lipid miscibility and phosphotyrosine-driven protein condensation phase transitions. *Biophys J* **120**, 1257-1265 (2021).
96. Smith, S. M., Baker, M., Halebian, M. & Smith, C. J. Weak Molecular Interactions in Clathrin-Mediated Endocytosis. *Front Mol Biosci* **4**, 72 (2017).
97. Kozak, M. & Kaksonen, M. Condensation of Ede1 promotes the initiation of endocytosis. *Elife* **11**, e72865 (2022).
98. Sun, Y. *et al.* Switch-like Arp2/3 activation upon WASP and WIP recruitment to an apparent threshold level by multivalent linker proteins in vivo. *Elife* **6** (2017).
99. Wilfling, F. *et al.* A Selective Autophagy Pathway for Phase-Separated Endocytic Protein Deposits. *Mol Cell* **80**, 764-778 e767 (2020).
100. Parton, R. G. & del Pozo, M. A. Caveolae as plasma membrane sensors, protectors and organizers. *Nat Rev Mol Cell Biol* **14**, 98-112 (2013).
101. Parton, R. G. Caveolae: Structure, Function, and Relationship to Disease. *Annu Rev Cell Dev Biol* **34**, 111-136 (2018).

102. Parton, R. G., Tillu, V., McMahon, K. A. & Collins, B. M. Key phases in the formation of caveolae. *Curr Opin Cell Biol* **71**, 7-14 (2021).
103. Tillu, V. A. *et al.* Cavin1 intrinsically disordered domains are essential for fuzzy electrostatic interactions and caveola formation. *Nat Commun* **12**, 931 (2021).
104. Zamparo, M. *et al.* Optimality in Self-Organized Molecular Sorting. *Phys Rev Lett* **126**, 088101 (2021).
105. Farre, J. C. & Subramani, S. Mechanistic insights into selective autophagy pathways: lessons from yeast. *Nat Rev Mol Cell Biol* **17**, 537-552 (2016).
106. Yamamoto, H. *et al.* The Intrinsically Disordered Protein Atg13 Mediates Supramolecular Assembly of Autophagy Initiation Complexes. *Dev Cell* **38**, 86-99 (2016).
107. Fujioka, Y. *et al.* Phase separation organizes the site of autophagosome formation. *Nature* **578**, 301-305 (2020).
108. Wu, X. *et al.* RIM and RIM-BP Form Presynaptic Active-Zone-like Condensates via Phase Separation. *Mol Cell* **73**, 971-984 e975 (2019).
109. Kirchhausen, T., Owen, D. & Harrison, S. C. Molecular structure, function, and dynamics of clathrin-mediated membrane traffic. *Cold Spring Harb Perspect Biol* **6**, a016725 (2014).
110. Mattila, P. K. & Lappalainen, P. Filopodia: molecular architecture and cellular functions. *Nature reviews Molecular cell biology* **9**, 446-454 (2008).
111. Zimmerberg, J. & Kozlov, M. M. How proteins produce cellular membrane curvature. *Nat Rev Mol Cell Biol* **7**, 9-19 (2006).
112. Stachowiak, J. C., Brodsky, F. M. & Miller, E. A. A cost-benefit analysis of the physical mechanisms of membrane curvature. *Nat Cell Biol* **15**, 1019-1027 (2013).
113. Drin, G. & Antonny, B. Amphipathic helices and membrane curvature. *FEBS letters* **584**, 1840-1847 (2010).
114. Christ, L., Raiborg, C., Wenzel, E. M., Campsteijn, C. & Stenmark, H. Cellular functions and molecular mechanisms of the ESCRT membrane-scission machinery. *Trends in biochemical sciences* **42**, 42-56 (2017).
115. Busch, D. J. *et al.* Intrinsically disordered proteins drive membrane curvature. *Nat Commun* **6**, 7875 (2015).
116. Brangwynne, Clifford P., Tompa, P. & Pappu, Rohit V. Polymer physics of intracellular phase transitions. *Nature Physics* **11**, 899-904 (2015).
117. Banjade, S. & Rosen, M. K. Phase transitions of multivalent proteins can promote clustering of membrane receptors. *Elife* **3** (2014).

118. Huang, W. Y. *et al.* A molecular assembly phase transition and kinetic proofreading modulate Ras activation by SOS. *Science* **363**, 1098-1103 (2019).
119. Alenquer, M. *et al.* Influenza A virus ribonucleoproteins form liquid organelles at endoplasmic reticulum exit sites. *Nature communications* **10**, 1-19 (2019).
120. Burke, K. A., Janke, A. M., Rhine, C. L. & Fawzi, N. L. Residue-by-Residue View of In Vitro FUS Granules that Bind the C-Terminal Domain of RNA Polymerase II. *Mol Cell* **60**, 231-241 (2015).
121. Murthy, A. C. *et al.* Molecular interactions underlying liquid− liquid phase separation of the FUS low-complexity domain. *Nature structural & molecular biology* **26**, 637-648 (2019).
122. Ryan, V. H. *et al.* Mechanistic view of hnRNPA2 low-complexity domain structure, interactions, and phase separation altered by mutation and arginine methylation. *Molecular cell* **69**, 465-479. e467 (2018).
123. Elbaum-Garfinkle, S. *et al.* The disordered P granule protein LAF-1 drives phase separation into droplets with tunable viscosity and dynamics. *Proceedings of the National Academy of Sciences* **112**, 7189-7194 (2015).
124. Veatch, S. L. & Keller, S. L. Separation of liquid phases in giant vesicles of ternary mixtures of phospholipids and cholesterol. *Biophysical journal* **85**, 3074-3083 (2003).
125. Baumgart, T., Hess, S. T. & Webb, W. W. Imaging coexisting fluid domains in biomembrane models coupling curvature and line tension. *Nature* **425**, 821-824 (2003).
126. Domanov, Y. A. *et al.* Mobility in geometrically confined membranes. *Proceedings of the National Academy of Sciences* **108**, 12605-12610 (2011).
127. Walker, A. E. Kreyszig, Differential Geometry (Mathematical Expositions No. 11, Toronto, and Oxford University Press, 1959), pp. xiv+ 352, 48s. *Proceedings of the Edinburgh Mathematical Society* **12**, 164-165 (1961).
128. Naito, H., Okuda, M. & Zhong-Can, O.-Y. New solutions to the Helfrich variation problem for the shapes of lipid bilayer vesicles: beyond Delaunay's surfaces. *Physical review letters* **74**, 4345 (1995).
129. Bar-Ziv, R. & Moses, E. Instability and" pearling" states produced in tubular membranes by competition of curvature and tension. *Physical review letters* **73**, 1392 (1994).
130. Snead, W. T. *et al.* Membrane fission by protein crowding. *Proc Natl Acad Sci U S A* **114**, E3258-E3267 (2017).
131. Indrani, C. H. V. & Lipowsky, R. Membranes with anchored polymers at the adsorption transition. *Europhysics Letters* **36**, 491 (1996).

132. Kim, Y. W. & Sung, W. Membrane curvature induced by polymer adsorption. *Physical Review E* **63**, 041910 (2001).
133. Wiese, W., Harbich, W. & Helfrich, W. Budding of lipid bilayer vesicles and flat membranes. *Journal of physics: Condensed matter* **4**, 1647 (1992).
134. Hayashi, S. Resolution doubling using confocal microscopy via analogy with structured illumination microscopy. *Japanese Journal of Applied Physics* **55**, 082501 (2016).
135. Frost, A., Unger, V. M. & De Camilli, P. The BAR domain superfamily: membrane-molding macromolecules. *Cell* **137**, 191-196 (2009).
136. Helfrich, W. & Prost, J. Intrinsic bending force in anisotropic membranes made of chiral molecules. *Physical Review A* **38**, 3065 (1988).
137. Janosi, L., Li, Z., Hancock, J. F. & Gorfe, A. A. Organization, dynamics, and segregation of Ras nanoclusters in membrane domains. *Proceedings of the National Academy of Sciences* **109**, 8097-8102 (2012).
138. Ford, M. G. *et al.* Curvature of clathrin-coated pits driven by epsin. *Nature* **419**, 361 (2002).
139. Lorent, J. H. *et al.* Structural determinants and functional consequences of protein affinity for membrane rafts. *Nature communications* **8**, 1219 (2017).
140. Harder, T., Scheiffele, P., Verkade, P. & Simons, K. Lipid domain structure of the plasma membrane revealed by patching of membrane components. *The Journal of cell biology* **141**, 929-942 (1998).
141. Kato, M. *et al.* Cell-free formation of RNA granules: low complexity sequence domains form dynamic fibers within hydrogels. *Cell* **149**, 753-767 (2012).
142. Murray, D. T. *et al.* Structure of FUS protein fibrils and its relevance to self-assembly and phase separation of low-complexity domains. *Cell* **171**, 615-627. e616 (2017).
143. Faini, M., Beck, R., Wieland, F. T. & Briggs, J. A. Vesicle coats: structure, function, and general principles of assembly. *Trends in cell biology* **23**, 279-288 (2013).
144. Luque, D. & Castón, J. R. Cryo-electron microscopy for the study of virus assembly. *Nature chemical biology* **16**, 231-239 (2020).
145. Römer, W. *et al.* Shiga toxin induces tubular membrane invaginations for its uptake into cells. *Nature* **450**, 670-675 (2007).
146. Campelo, F. & Hernández-Machado, A. Model for curvature-driven pearling instability in membranes. *Physical review letters* **99**, 088101 (2007).

147. Callan-Jones, A. & Bassereau, P. Curvature-driven membrane lipid and protein distribution. *Current Opinion in Solid State and Materials Science* **17**, 143-150 (2013).
148. Fošnarič, M. *et al.* Theoretical study of vesicle shapes driven by coupling curved proteins and active cytoskeletal forces. *Soft Matter* **15**, 5319-5330 (2019).
149. Alimohamadi, H. & Rangamani, P. Modeling membrane curvature generation due to membrane–protein interactions. *Biomolecules* **8**, 120 (2018).
150. Evans, E. A., Waugh, R. & Melnik, L. Elastic area compressibility modulus of red cell membrane. *Biophysical Journal* **16**, 585-595 (1976).
151. Rawicz, W., Olbrich, K., McIntosh, T., Needham, D. & Evans, E. Effect of chain length and unsaturation on elasticity of lipid bilayers. *Biophysical journal* **79**, 328-339 (2000).
152. Wang, S., Walton, K. D. & Gumucio, D. L. Signals and forces shaping organogenesis of the small intestine. *Current Topics in Developmental Biology* **132**, 31-65 (2019).
153. Tallinen, T. *et al.* On the growth and form of cortical convolutions. *Nature Physics* **12**, 588-593 (2016).
154. Hughes, A. J. *et al.* Engineered tissue folding by mechanical compaction of the mesenchyme. *Developmental cell* **44**, 165-178. e166 (2018).
155. Kralj-Iglič, V. *et al.* Amphiphile-induced tubular budding of the bilayer membrane. *European Biophysics Journal* **34**, 1066-1070 (2005).
156. Iglič, A., Babnik, B., Gimsa, U. & Kralj-Iglič, V. On the role of membrane anisotropy in the beading transition of undulated tubular membrane structures. *Journal of Physics A: Mathematical and General* **38**, 8527 (2005).
157. Iglič, A., Kralj-Iglič, V. & Majhenc, J. Cylindrical shapes of closed lipid bilayer structures correspond to an extreme area difference between the two monolayers of the bilayer. *Journal of biomechanics* **32**, 1343-1347 (1999).
158. Sens, P. & Turner, M. S. Theoretical model for the formation of caveolae and similar membrane invaginations. *Biophysical journal* **86**, 2049-2057 (2004).
159. Ridley, A. J. Life at the leading edge. *Cell* **145**, 1012-1022 (2011).
160. Pendin, D., McNew, J. A. & Daga, A. Balancing ER dynamics: shaping, bending, severing, and mending membranes. *Current opinion in cell biology* **23**, 435-442 (2011).
161. Buono, R. A. *et al.* ESCRT-mediated vesicle concatenation in plant endosomes. *Journal of Cell Biology* **216**, 2167-2177 (2017).

162. Snead, W. T. & Gladfelter, A. S. The control centers of biomolecular phase separation: how membrane surfaces, PTMs, and active processes regulate condensation. *Molecular cell* **76**, 295-305 (2019).
163. Momin, N. *et al.* Designing lipids for selective partitioning into liquid ordered membrane domains. *Soft Matter* **11**, 3241-3250 (2015).
164. DeGroot, A. C. *et al.* Entropic control of receptor recycling using engineered ligands. *Biophysical journal* **114**, 1377-1388 (2018).
165. Schuster, B. S. *et al.* Controllable protein phase separation and modular recruitment to form responsive membraneless organelles. *Nature communications* **9**, 1-12 (2018).
166. Stachowiak, J. C. *et al.* Membrane bending by protein-protein crowding. *Nat Cell Biol* **14**, 944-949 (2012).
167. Angelova, M. I. & Dimitrov, D. S. Liposome electroformation. *Faraday discussions of the Chemical Society* **81**, 303-311 (1986).
168. Zeno, W. F. *et al.* Synergy between intrinsically disordered domains and structured proteins amplifies membrane curvature sensing. *Nat Commun* **9**, 4152 (2018).
169. Sezgin, E. *et al.* Elucidating membrane structure and protein behavior using giant plasma membrane vesicles. *Nature protocols* **7**, 1042-1051 (2012).
170. Deuling, H. & Helfrich, W. Red blood cell shapes as explained on the basis of curvature elasticity. *Biophys. J.* **16**, 861-868 (1976).
171. Canham, P. B. The minimum energy of bending as a possible explanation of the biconcave shape of the human red blood cell. *Journal of theoretical biology* **26**, 61-81 (1970).
172. Rawicz, W., Olbrich, K. C., McIntosh, T., Needham, D. & Evans, E. Effect of chain length and unsaturation on elasticity of lipid bilayers. *Biophysical journal* **79**, 328-339 (2000).
173. Steigmann, D. Fluid films with curvature elasticity. (1999).
174. Rangamani, P., Agrawal, A., Mandadapu, K. K., Oster, G. & Steigmann, D. J. Interaction between surface shape and intra-surface viscous flow on lipid membranes. *Biomechanics and modeling in mechanobiology* **12**, 833-845 (2013).
175. Jenkins, J. T. Static equilibrium configurations of a model red blood cell. *Journal of mathematical biology* **4**, 149-169 (1977).
176. Hassinger, J. E., Oster, G., Drubin, D. G. & Rangamani, P. Design principles for robust vesiculation in clathrin-mediated endocytosis. *Proceedings of the national academy of sciences* **114**, E1118-E1127 (2017).

177. Alimohamadi, H., Ovryn, B. & Rangamani, P. Modeling membrane nanotube morphology: the role of heterogeneity in composition and material properties. *Scientific reports* **10**, 1-15 (2020).
178. Rangamani, P., Mandadap, K. K. & Oster, G. Protein-induced membrane curvature alters local membrane tension. *Biophys. J.* **107**, 751-762 (2014).
179. Miao, L., Seifert, U., Wortis, M. & Dobereiner, H. G. Budding transitions of fluid-bilayer vesicles: The effect of area-difference elasticity. *Phys Rev E Stat Phys Plasmas Fluids Relat Interdiscip Topics* **49**, 5389-5407 (1994).
180. Mukhopadhyay, R., Lim, H. W. G. & Wortis, M. Echinocyte shapes: bending, stretching, and shear determine spicule shape and spacing. *Biophys J* **82**, 1756-1772 (2002).
181. Dobereiner, H. G., Evans, E., Kraus, M., Seifert, U. & Wortis, M. Mapping vesicle shapes into the phase diagram: A comparison of experiment and theory. *Physical Review E* **55**, 4458-4474 (1997).
182. Foret, L. Shape and energy of a membrane bud induced by protein coats or viral protein assembly. *The European Physical Journal E* **37**, 42 (2014).
183. Walani, N., Torres, J. & Agrawal, A. Endocytic proteins drive vesicle growth via instability in high membrane tension environment. *Proceedings of the national academy of sciences* **112**, E1423-E1432 (2015).
184. Agrawal, A. & Steigmann, D. J. Modeling protein-mediated morphology in biomembranes. *Biomechanics and modeling in mechanobiology* **8**, 371 (2009).
185. Alimohamadi, H., Vasan, R., Hassinger, J. E., Stachowiak, J. C. & Rangamani, P. The role of traction in membrane curvature generation. *Molecular biology of the cell* **29**, 2024-2035 (2018).
186. Agrawal, A. & Steigmann, D. J. Boundary-value problems in the theory of lipid membranes. *Continuum Mechanics and Thermodynamics* **21**, 57-82 (2009).
187. Delaunay, C. Sur la surface de révolution dont la courbure moyenne est constante. *Journal de mathématiques pures et appliquées*, 309-314 (1841).
188. Mladenov, I. New solutions of the shape equation. *The European Physical Journal B-Condensed Matter and Complex Systems* **29**, 327-330 (2002).
189. Zhanchun, T., Jixing, L. & Yuzhang, X. *Geometric Methods in Elastic Theory of Membranes in Liquid Crystal Phases*. Vol. 2 (World Scientific, 2017).
190. Djondjorov, P., Hadzhilazova, M., Mladenov, I. M. & Vassilev, V. in *Proceedings of the Eleventh International Conference on Geometry, Integrability and Quantization.* 108-117 (Institute of Biophysics and Biomedical Engineering, Bulgarian Academy of …).

191. Fosnaric, M. *et al.* Theoretical study of vesicle shapes driven by coupling curved proteins and active cytoskeletal forces. *Soft Matter* **15**, 5319-5330 (2019).
192. Callan-Jones, A. & Bassereau, P. Curvature-driven membrane lipid and protein distribution. *Curr Opin Solid St M* **17**, 143-150 (2013).
193. Bobrovska, N., Gozdz, W., Kralj-Iglic, V. & Iglic, A. On the Role of Anisotropy of Membrane Components in Formation and Stabilization of Tubular Structures in Multicomponent Membranes. *Plos One* **8** (2013).
194. Iglic, A., Slivnika, T. & Kralj-Iglic, V. Elastic properties of biological membranes influenced by attached proteins. *J Biomech* **40**, 2492-2500 (2007).
195. Kralj-Iglič, V., Heinrich, V., Svetina, S. & Žekš, B. Free energy of closed membrane with anisotropic inclusions. *The European Physical Journal B-Condensed Matter and Complex Systems* **10**, 5-8 (1999).
196. Walani, N., Torres, J. & Agrawal, A. Anisotropic spontaneous curvatures in lipid membranes. *Physical Review E* **89**, 062715 (2014).
197. Alimohamadi, H., Bell, M., Halpain, S. & Rangamani, P. Mechanical principles governing the shapes of dendritic spines. *bioRxiv* (2020).
198. Campelo, F. & Hernández–Machado, A. Polymer-induced tubulation in lipid vesicles. *Physical review letters* **100**, 158103 (2008).
199. Rangamani, P., Behzadan, A. & Holst, M. Local sensitivity analysis of the 'membrane shape equation' derived from the Helfrich energy. *arxiv* **https://arxiv.org/pdf/2005.12550.pdf** (2020).
200. Indrani, C. H. V. & Lipowsky, R. Membranes with anchored polymers at the adsorption transition. *EPL (Europhysics Letters)* **36**, 491 (1996).
201. Kim, Y. W. & Sung, W. Vesicular budding induced by a long and flexible polymer. *EPL (Europhysics Letters)* **47**, 292 (1999).
202. Ryan, V. H. *et al.* Mechanistic View of hnRNPA2 Low-Complexity Domain Structure, Interactions, and Phase Separation Altered by Mutation and Arginine Methylation. *Mol Cell* **69**, 465-+ (2018).
203. Goetz, R. & Lipowsky, R. Computer simulations of bilayer membranes: self-assembly and interfacial tension. *The Journal of chemical physics* **108**, 7397-7409 (1998).
204. Grafmüller, A., Shillcock, J. & Lipowsky, R. The fusion of membranes and vesicles: pathway and energy barriers from dissipative particle dynamics. *Biophysical journal* **96**, 2658-2675 (2009).
205. Helfrich, W. Amphiphilic mesophases made of defects. *Physics of defects*, 715-755 (1981).

206. Marsh, D. Lateral pressure profile, spontaneous curvature frustration, and the incorporation and conformation of proteins in membranes. *Biophysical journal* **93**, 3884-3899 (2007).
207. Fournier, J.-B. On the stress and torque tensors in fluid membranes. *Soft Matter* **3**, 883-888 (2007).
208. Szleifer, I., Kramer, D., Ben‐Shaul, A., Gelbart, W. M. & Safran, S. A. Molecular theory of curvature elasticity in surfactant films. *The Journal of chemical physics* **92**, 6800-6817 (1990).
209. Gompper, G. & Klein, S. Ginzburg-Landau theory of aqueous surfactant solutions. *Journal de Physique II* **2**, 1725-1744 (1992).
210. Lipowsky, R. & Döbereiner, H.-G. Vesicles in contact with nanoparticles and colloids. *EPL (Europhysics Letters)* **43**, 219 (1998).
211. Lipowsky, R. Spontaneous tubulation of membranes and vesicles reveals membrane tension generated by spontaneous curvature. *Faraday discussions* **161**, 305-331 (2013).
212. Vitkova, V., Meleard, P., Pott, T. & Bivas, I. Alamethicin influence on the membrane bending elasticity. *Eur Biophys J* **35**, 281-286 (2006).
213. Bouvrais, H., Pott, T., Bagatolli, L. A., Ipsen, J. H. & Meleard, P. Impact of membrane-anchored fluorescent probes on the mechanical properties of lipid bilayers. *Biochim Biophys Acta* **1798**, 1333-1337 (2010).
214. Arriaga, L. R. *et al.* Stiffening Effect of Cholesterol on Disordered Lipid Phases: A Combined Neutron Spin Echo plus Dynamic Light Scattering Analysis of the Bending Elasticity of Large Unilamellar Vesicles. *Biophys. J.* **96**, 3629-3637 (2009).
215. Doktorova, M., Harries, D. & Khelashvili, G. Determination of bending rigidity and tilt modulus of lipid membranes from real-space fluctuation analysis of molecular dynamics simulations. *Physical Chemistry Chemical Physics* **19**, 16806-16818 (2017).
216. Roux, A. *et al.* Role of curvature and phase transition in lipid sorting and fission of membrane tubules. *Embo Journal* **24**, 1537-1545 (2005).
217. McMahon, H. T. & Boucrot, E. Membrane curvature at a glance. *J Cell Sci* **128**, 1065-1070 (2015).
218. Jarsch, I. K., Daste, F. & Gallop, J. L. Membrane curvature in cell biology: An integration of molecular mechanisms. *J Cell Biol* **214**, 375-387 (2016).
219. Snead, W. T. & Stachowiak, J. C. Structure Versus Stochasticity-The Role of Molecular Crowding and Intrinsic Disorder in Membrane Fission. *J Mol Biol* **430**, 2293-2308 (2018).

220. Shurer, C. R. *et al.* Physical principles of membrane shape regulation by the glycocalyx. *Cell* **177**, 1757-1770. e1721 (2019).
221. Boeynaems, S. *et al.* Protein Phase Separation: A New Phase in Cell Biology. *Trends Cell Biol* **28**, 420-435 (2018).
222. Zeno, W. F. *et al.* Molecular mechanisms of membrane curvature sensing by a disordered protein. *Journal of the American Chemical Society* **141**, 10361-10371 (2019).
223. Stachowiak, J. C., Hayden, C. C. & Sasaki, D. Y. Steric confinement of proteins on lipid membranes can drive curvature and tubulation. *Proceedings of the National Academy of Sciences* **107**, 7781-7786 (2010).
224. Angelova, M. I. *et al.* pH sensing by lipids in membranes: The fundamentals of pH-driven migration, polarization and deformations of lipid bilayer assemblies. *Biochimica et Biophysica Acta (BBA)-Biomembranes* **1860**, 2042-2063 (2018).
225. Zhulina, E., Birshtein, T. & Borisov, O. Curved polymer and polyelectrolyte brushes beyond the Daoud-Cotton model. *The European Physical Journal E* **20**, 243-256 (2006).
226. Israels, R., Leermakers, F., Fleer, G. J. & Zhulina, E. B. Charged polymeric brushes: Structure and scaling relations. *Macromolecules* **27**, 3249-3261 (1994).
227. Borisov, O. & Zhulina, E. Effect of salt on self-assembly in charged block copolymer micelles. *Macromolecules* **35**, 4472-4480 (2002).
228. Zhulina, E. & Borisov, O. Polyelectrolytes grafted to curved surfaces. *Macromolecules* **29**, 2618-2626 (1996).
229. Evans, E. MECHANICS AND THERMODYNAMICS OF BIOMEMBRANES. II. (1979).
230. Evans, E. A. Bending resistance and chemically induced moments in membrane bilayers. *Biophysical journal* **14**, 923-931 (1974).
231. Zhu, C., Lee, C. T. & Rangamani, P. Mem3DG: modeling membrane mechanochemical dynamics in 3D using discrete differential geometry. *Biophysical reports* **2**, 100062 (2022).
232. McMahon, H. T. & Gallop, J. L. Membrane curvature and mechanisms of dynamic cell membrane remodelling. *Nature* **438**, 590-596 (2005).
233. Uversky, V. N. Intrinsically Disordered Proteins and Their "Mysterious" (Meta)Physics. *Frontiers in Physics* **7** (2019).
234. Xue, B., Dunker, A. K. & Uversky, V. N. Orderly order in protein intrinsic disorder distribution: disorder in 3500 proteomes from viruses and the three

domains of life. *Journal of Biomolecular Structure and Dynamics* **30**, 137-149 (2012).

235. Owen, D. J., Collins, B. M. & Evans, P. R. Adaptors for clathrin coats: structure and function. *Annual review of cell and developmental biology* **20**, 153 (2004).
236. Gómez-Puertas, P., Albo, C., Pérez-Pastrana, E., Vivo, A. & Portela, A. Influenza virus matrix protein is the major driving force in virus budding. *Journal of virology* **74**, 11538 (2000).
237. Saletti, D. *et al.* The Matrix protein M1 from influenza C virus induces tubular membrane invaginations in an in vitro cell membrane model. *Scientific reports* **7**, 1-14 (2017).
238. Strambio-De-Castillia, C., Niepel, M. & Rout, M. P. The nuclear pore complex: bridging nuclear transport and gene regulation. *Nature reviews Molecular cell biology* **11**, 490-501 (2010).
239. Rout, M. P. *et al.* The yeast nuclear pore complex: composition, architecture, and transport mechanism. *The Journal of cell biology* **148**, 635-652 (2000).
240. Denning, D. P., Patel, S. S., Uversky, V., Fink, A. L. & Rexach, M. Disorder in the nuclear pore complex: the FG repeat regions of nucleoporins are natively unfolded. *Proceedings of the National Academy of Sciences* **100**, 2450-2455 (2003).
241. Nag, N., Sasidharan, S., Uversky, V. N., Saudagar, P. & Tripathi, T. Phase separation of FG-nucleoporins in nuclear pore complexes. *Biochimica et Biophysica Acta (BBA)-Molecular Cell Research* **1869**, 119205 (2022).
242. Kratky, O. & Porod, G. Röntgenuntersuchung gelöster fadenmoleküle. *Recueil des Travaux Chimiques des Pays‐Bas* **68**, 1106-1122 (1949).
243. Neal, B., Asthagiri, D. & Lenhoff, A. Molecular origins of osmotic second virial coefficients of proteins. *Biophysical Journal* **75**, 2469-2477 (1998).
244. Quigley, A. & Williams, D. The second virial coefficient as a predictor of protein aggregation propensity: a self-interaction chromatography study. *European Journal of Pharmaceutics and Biopharmaceutics* **96**, 282-290 (2015).
245. Choi, U. B., McCann, J. J., Weninger, K. R. & Bowen, M. E. Beyond the random coil: stochastic conformational switching in intrinsically disordered proteins. *Structure* **19**, 566-576 (2011).
246. Derényi, I., Jülicher, F. & Prost, J. Formation and interaction of membrane tubes. *Physical review letters* **88**, 238101 (2002).
247. Mettlen, M., Chen, P.-H., Srinivasan, S., Danuser, G. & Schmid, S. L. Regulation of clathrin-mediated endocytosis. *Annual review of biochemistry* **87**, 871-896 (2018).

248. McMahon, H. T. & Boucrot, E. Molecular mechanism and physiological functions of clathrin-mediated endocytosis. *Nature reviews Molecular cell biology* **12**, 517-533 (2011).
249. Kaksonen, M. & Roux, A. Mechanisms of clathrin-mediated endocytosis. *Nature reviews Molecular cell biology* **19**, 313-326 (2018).
250. Chen, Z. & Schmid, S. L. Evolving models for assembling and shaping clathrin-coated pits. *Journal of Cell Biology* **219**, e202005126 (2020).
251. Traub, L. M. Tickets to ride: selecting cargo for clathrin-regulated internalization. *Nature reviews Molecular cell biology* **10**, 583-596 (2009).
252. Hicke, L. & Riezman, H. Ubiquitination of a yeast plasma membrane receptor signals its ligand-stimulated endocytosis. *Cell* **84**, 277-287 (1996).
253. Galan, J. M., Moreau, V., Andre, B., Volland, C. & Haguenauer-Tsapis, R. Ubiquitination Mediated by the Npi1p/Rsp5p Ubiquitin-protein Ligase Is Required for Endocytosis of the Yeast Uracil Permease (∗). *Journal of Biological Chemistry* **271**, 10946-10952 (1996).
254. Lin, C. H., MacGurn, J. A., Chu, T., Stefan, C. J. & Emr, S. D. Arrestin-related ubiquitin-ligase adaptors regulate endocytosis and protein turnover at the cell surface. *Cell* **135**, 714-725 (2008).
255. Dores, M. R., Schnell, J. D., Maldonado‐Baez, L., Wendland, B. & Hicke, L. The function of yeast epsin and Ede1 ubiquitin‐binding domains during receptor internalization. *Traffic* **11**, 151-160 (2010).
256. Tebar, F., Sorkina, T., Sorkin, A., Ericsson, M. & Kirchhausen, T. Eps15 is a component of clathrin-coated pits and vesicles and is located at the rim of coated pits. *Journal of Biological Chemistry* **271**, 28727-28730 (1996).
257. Sochacki, K. A., Dickey, A. M., Strub, M.-P. & Taraska, J. W. Endocytic proteins are partitioned at the edge of the clathrin lattice in mammalian cells. *Nature cell biology* **19**, 352-361 (2017).
258. Day, K. J. *et al.* Liquid-like protein interactions catalyse assembly of endocytic vesicles. *Nature Cell Biology* **23**, 366-376 (2021).
259. Wilfling, F. *et al.* A selective autophagy pathway for phase-separated endocytic protein deposits. *Molecular Cell* **80**, 764-778. e767 (2020).
260. Wilfling, F., Lee, C.-W., Erdmann, P. S. & Baumeister, W. Autophagy ENDing unproductive phase-separated endocytic protein deposits. *Autophagy* **17**, 3264-3265 (2021).
261. Shih, S. C. *et al.* Epsins and Vps27p/Hrs contain ubiquitin-binding domains that function in receptor endocytosis. *Nature cell biology* **4**, 389-393 (2002).

262. Hicke, L. & Dunn, R. Regulation of membrane protein transport by ubiquitin and ubiquitin-binding proteins. *Annual review of cell and developmental biology* **19**, 141-172 (2003).

263. Polo, S. *et al.* A single motif responsible for ubiquitin recognition and monoubiquitination in endocytic proteins. *Nature* **416**, 451-455 (2002).

264. Riezman, H. The ubiquitin connection. *Nature* **416**, 381-383 (2002).

265. Weinberg, J. S. & Drubin, D. G. Regulation of clathrin-mediated endocytosis by dynamic ubiquitination and deubiquitination. *Current Biology* **24**, 951-959 (2014).

266. Galan, J.-M. & Haguenauer-Tsapis, R. Ubiquitin lys63 is involved in ubiquitination of a yeast plasma membrane protein. *The EMBO journal* **16**, 5847-5854 (1997).

267. Huang, F. *et al.* Lysine 63-linked polyubiquitination is required for EGF receptor degradation. *Proceedings of the National Academy of Sciences* **110**, 15722-15727 (2013).

268. Erpapazoglou, Z., Walker, O. & Haguenauer-Tsapis, R. Versatile roles of k63-linked ubiquitin chains in trafficking. *Cells* **3**, 1027-1088 (2014).

269. Piper, R. C., Dikic, I. & Lukacs, G. L. Ubiquitin-dependent sorting in endocytosis. *Cold Spring Harbor perspectives in biology* **6**, a016808 (2014).

270. Cupers, P., ter Haar, E., Boll, W. & Kirchhausen, T. Parallel dimers and anti-parallel tetramers formed by epidermal growth factor receptor pathway substrate clone 15 (EPS15). *Journal of Biological Chemistry* **272**, 33430-33434 (1997).

271. Benmerah, A., Poupon, V., Cerf-Bensussan, N. & Dautry-Varsat, A. Mapping of Eps15 domains involved in its targeting to clathrin-coated pits. *Journal of Biological Chemistry* **275**, 3288-3295 (2000).

272. Santonico, E., Panni, S., Falconi, M., Castagnoli, L. & Cesareni, G. Binding to DPF-motif by the POB1 EH domain is responsible for POB1-Eps15 interaction. *BMC biochemistry* **8**, 1-14 (2007).

273. Lu, R. & Drubin, D. G. Selection and stabilization of endocytic sites by Ede1, a yeast functional homologue of human Eps15. *Molecular biology of the cell* **28**, 567-575 (2017).

274. Ehrlich, M. *et al.* Endocytosis by random initiation and stabilization of clathrin-coated pits. *Cell* **118**, 591-605 (2004).

275. Boulant, S., Kural, C., Zeeh, J.-C., Ubelmann, F. & Kirchhausen, T. Actin dynamics counteract membrane tension during clathrin-mediated endocytosis. *Nature cell biology* **13**, 1124-1131 (2011).

276. Collins, B. M., McCoy, A. J., Kent, H. M., Evans, P. R. & Owen, D. J. Molecular architecture and functional model of the endocytic AP2 complex. *Cell* **109**, 523-535 (2002).
277. Owen, D. J., Collins, B. M. & Evans, P. R. Adaptors for clathrin coats: structure and function. *Annu. Rev. Cell Dev. Biol.* **20**, 153-191 (2004).
278. Grimm, J. B. *et al.* A general method to improve fluorophores for live-cell and single-molecule microscopy. *Nature methods* **12**, 244-250 (2015).
279. Blondeau, F. *et al.* Tandem MS analysis of brain clathrin-coated vesicles reveals their critical involvement in synaptic vesicle recycling. *Proceedings of the National Academy of Sciences* **101**, 3833-3838 (2004).
280. Dao, T. P. *et al.* Mechanistic insights into enhancement or inhibition of phase separation by different polyubiquitin chains. *EMBO reports* **23**, e55056 (2022).
281. Stringer, D. K. & Piper, R. C. A single ubiquitin is sufficient for cargo protein entry into MVBs in the absence of ESCRT ubiquitination. *Journal of Cell Biology* **192**, 229-242 (2011).
282. Xu, P. *et al.* COPI mediates recycling of an exocytic SNARE by recognition of a ubiquitin sorting signal. *Elife* **6**, e28342 (2017).
283. Nielsen, C. P., Jernigan, K. K., Diggins, N. L., Webb, D. J. & MacGurn, J. A. USP9X deubiquitylates DVL2 to regulate WNT pathway specification. *Cell reports* **28**, 1074-1089. e1075 (2019).
284. Kattenhorn, L. M., Korbel, G. A., Kessler, B. M., Spooner, E. & Ploegh, H. L. A deubiquitinating enzyme encoded by HSV-1 belongs to a family of cysteine proteases that is conserved across the family Herpesviridae. *Molecular cell* **19**, 547-557 (2005).
285. Bolstad, M., Abaitua, F., Crump, C. & O'Hare, P. Autocatalytic activity of the ubiquitin-specific protease domain of herpes simplex virus 1 VP1-2. *Journal of virology* **85**, 8738-8751 (2011).
286. Komander, D. & Rape, M. The ubiquitin code. *Annual review of biochemistry* **81**, 203-229 (2012).
287. Chen, C. & Zhuang, X. Epsin 1 is a cargo-specific adaptor for the clathrin-mediated endocytosis of the influenza virus. *Proceedings of the National Academy of Sciences* **105**, 11790-11795 (2008).
288. Bugaj, L. J., Choksi, A. T., Mesuda, C. K., Kane, R. S. & Schaffer, D. V. Optogenetic protein clustering and signaling activation in mammalian cells. *Nature methods* **10**, 249-252 (2013).
289. Wendland, B. Epsins: adaptors in endocytosis? *Nature reviews Molecular cell biology* **3**, 971-977 (2002).

290. Hawryluk, M. J. *et al.* Epsin 1 is a polyubiquitin‐selective clathrin‐associated sorting protein. *Traffic* **7**, 262-281 (2006).
291. Chen, H. *et al.* Epsin is an EH-domain-binding protein implicated in clathrin-mediated endocytosis. *Nature* **394**, 793-797 (1998).
292. Aguilar, R. C., Watson, H. A. & Wendland, B. The yeast Epsin Ent1 is recruited to membranes through multiple independent interactions. *Journal of Biological Chemistry* **278**, 10737-10743 (2003).
293. Dupre, S., Urban-Grimal, D. & Haguenauer-Tsapis, R. Ubiquitin and endocytic internalization in yeast and animal cells. *Biochimica et Biophysica Acta (BBA)-Molecular Cell Research* **1695**, 89-111 (2004).
294. Taylor, M. J., Perrais, D. & Merrifield, C. J. A high precision survey of the molecular dynamics of mammalian clathrin-mediated endocytosis. *PLoS biology* **9**, e1000604 (2011).
295. Kennedy, M. J. *et al.* Rapid blue-light–mediated induction of protein interactions in living cells. *Nature methods* **7**, 973-975 (2010).
296. Aguet, F. *et al.* Membrane dynamics of dividing cells imaged by lattice light-sheet microscopy. *Molecular biology of the cell* **27**, 3418-3435 (2016).
297. Aguet, F., Antonescu, C. N., Mettlen, M., Schmid, S. L. & Danuser, G. Advances in analysis of low signal-to-noise images link dynamin and AP2 to the functions of an endocytic checkpoint. *Developmental cell* **26**, 279-291 (2013).